Permanent Magnet Assisted Synchronous Reluctance Machines for Electric Vehicle Traction Applications

By:

Panagiotis Lazari

A thesis submitted in partial fulfilment of the requirements for the degree of
Doctor of Philosophy

The University of Sheffield
Faculty of Engineering
Department of Electronic and Electrical Engineering

April 2018

Abstract

The thesis is an investigation into the performance of Permanent Magnet Assisted Synchronous reluctance Machines (PMA SynRM) employing rare earth-free/less permanent magnets for electric vehicle traction applications. The design optimisation methodology is based on the performance of the traction machine over specific driving cycles instead of conventionally adopted practices relying on optimisations at a specific operating condition. Albeit, requirements such as the maximum torque, maximum speed and cooling are taken into consideration. Therefore, a method for the selection of a finite number of energy-representative operating points characterising a given driving cycle is proposed. The technique can predict the energy loss over a driving cycle with high accuracy (i.e., error <6%), while only employing less than 5% of the total operating points of a driving cycle. This forms the basis upon which energy efficiency optimisation is undertaken.

A rare-earth-less PMA SynRM employing bonded NdFeB permanent magnets is designed and manually optimised, using an engineer-in-the-loop approach, to meet the specification of a personal mobility electric vehicle. All the multi-physical aspects of the design, i.e., electromagnetic, thermal, and mechanical are considered in an iterative process with the target of maximising the system's (i.e., machine and drive) energy efficiency over the NEDC, while meeting the specified torque-speed operating range. Energy efficiency higher than 94% is achieved for the traction machine operating over the NEDC. Special attention is also given to the reduction of the electromagnetic torque ripple through the introduction of special features in the rotor laminations and the step skewing of the rotor. A computationally efficient modelling technique for the estimation of the effect of skew on the torque ripple and the performance of the machine is proposed and validated using 2.5D multi-slice Finite Element Analysis (FEA).

Special consideration is given to the effects of the finite length of the machine, especially when step skewing is adopted. It is observed that the axial flux leakage at the boundaries between the skewed slices can significantly affect the torque ripple and hence the accuracy of the 2.5D multi-slice approach. Therefore, it is recommended that for PMA SynRM full 3D FEA may be required in order to

accurately predict the effects of skew on torque ripple. Furthermore, attention is also given to the effects of laser cutting on the magnetic properties of steel laminations and a method, which enables the assessment of these effects on the performance of the machine is proposed. It is shown that a substantial proportion of the discrepancy between the measured and predicted results can be attributed to these effects.

A multi-physics approach employing an algorithmic optimisation method is proposed. The technique employs sophisticated optimisation algorithms for efficient design space exploration combined with computationally efficient multi-physics models, thus considerably minimising the number of required FEA runs to reach the optimal designs. The method simultaneously takes into consideration of the main geometrical and topologic parameters of the PMA SynRM, as well as different permanent magnet materials properties. It is employed for the design optimisation of PMA SynRMs aiming to maximise energy efficiency against the NEDC, while meeting the specification requirements of the above-mentioned personal mobility EV. The resultant optimal designs are comprehensively compared against a set of indicative performance markers pertaining to EV traction. When compared to the manual optimisation method energy efficiency improvement in the region of 0.5% over a driving cycle is achieved.

Acknowledgments

The PhD journey has been a transformational experience for myself on both intellectual and personal levels. This would not have happened without the people who inspired, motivated and supported me during this challenging endeavour. I would like to take this opportunity to express my deepest gratitude to these people. First, I would like to thank the EPSRC for providing me with a PhD scholarship and the opportunity to carry out this research.

I would like to continue by thanking my supervisors, Prof Kais Atallah and Prof Jiabin Wang, for their support during my doctoral studies.

My sincere gratitude goes to my colleagues, Dr Xiao Chen, Dr Bhaskar Sen, Dr Vipul Patel, and Dr Liang Chen, Dr Chaohui Liu for our elaborate discussions and enlightening moments shared during our weekly technical meetings, and for the opportunity to collaborate on several technical publications. I am honoured to now have you as my dear friends as well.

Special thanks goes to Mr John Wilkinson, our research group lead technician, for his continuous support and valuable insights during the prototyping and test rig preparation process. I would like to thank our project partners from SIEMENS for their contribution in the prototype testing, and Dr Weiya Wang for her assistance with the preparation of the mechanical drawings for the prototype.

A special gratitude goes to my partner, Ms Claire Nicolaou, for her unconditional love and support in every aspect of my life.

I am also grateful to Dr Z. Halim for his tremendous efforts in supporting me during the period I was facing some severe health problems.

I am forever grateful to my family, who although far away in Cyprus, their presence was felt every part of the way. Thank you for providing me with the opportunity to pursue my choices in life.

Table of Contents

Chapter 1

Introduction

A worldwide campaign in the search for more energy efficient and environmentally friendly vehicles has gained increasing momentum during the past two decades due to increasing concerns on energy security and environmental pollution produced by fossil fuel engines. It has been widely recognized that electric vehicles (EVs) [1], [2] have the potential to offer an ultimate solution for sustainable personal mobility in the future, particularly if they can be powered by electrical energy generated from renewable sources, such as solar, wind, wave and tide stream. Thus, traction electrification could lead to a reduction in environmental pollution, CO_2 emissions as well as the reliance on fossil fuels.

1.1 Imminent need for worldwide transport electrification

The world's energy demands are becoming increasingly higher as populations grow and prosperity rises, especially in developing economies (such as Africa, Asia, and the Middle East) as can be observed from Figure 1.1, which illustrates the worldwide energy demands by region [3]. This situation places significant challenges on the future of global energy markets and energy security [3], [4]. The world energy demand has increased by more than ~40% in the past 30 years and is projected to grow further by ~21% in the next 20 years. About two-thirds of the growth is attributed to India, China and other nations outside of the Organisation for Economic Co-operation and Development (OECD) [3]. Energy security and pollutant emissions, along with their severe implications on the environment and climate change, constitute one of, if not, the most serious challenge facing humanity. Thus, this calls for the need for more stringent regulations by government bodies and organisations, and urgent deployment of effective solutions, in order to guarantee energy sustainability and prevent the catastrophic effects emanating from environmental pollution and climate change.
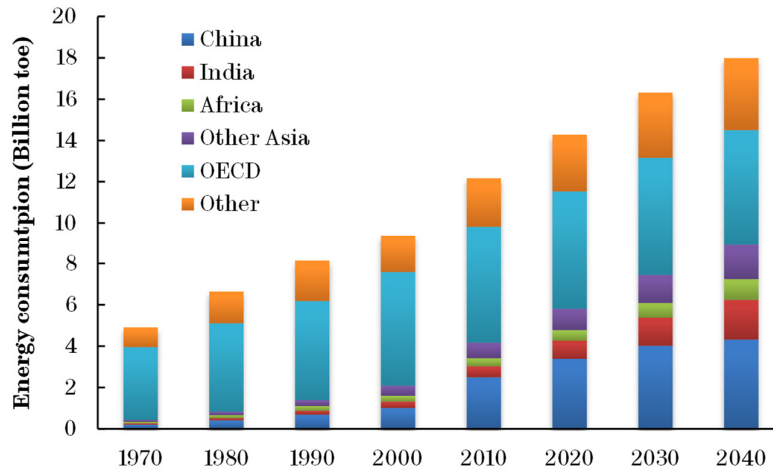
Figure 1.1. Worldwide primary energy demand by region [4].

Nowadays, environmental pollution is identified as the largest health hazard in the world and is responsible for the premature death of 9 million people in 2015 (i.e., 16% of all deaths worldwide) and the destruction of ecosystems as revealed in a recent report from the Lancet Medical Journal Committee [5]. The study highlights that environmental pollution kills more people every year than wars and other types of violence (viz., 15 times more), natural disasters, hunger, or smoking (viz., 1.5 time more), while also causing severe socio-economic damages, such as productivity and gross domestic product reduction, and increased health-care costs, resulting in yearly losses of ~6.2% in global economy. Countries with low-to-middle income account for 92% of pollution-related deaths, with air pollution being the leading cause of death followed by water pollution. Fuel combustion is the leading source of particulate matter (~85%) in the air and is responsible for approximately the entire pollution from nitrogen (NO_x) and sulphur (SO_x) oxides, while contributing a key share to the total greenhouse gas emissions (GHG) driving climate change worldwide [5].

In the European Union (EU), air pollution is classified as the most severe environmental health danger responsible for the premature death of hundreds of thousands despite recent improvements in air quality according to the European Environmental Agency (EEA) report [6]. The disease burden associated with air pollution is substantial, with stroke and heart disease contributing 80% of

premature deaths, followed by cancer and other respiratory diseases. The report argues that approximately 85% of urban residents in the EU have been exposed to levels of particle pollution that are considered hazardous to health by the World Health Organization (WHO). A major contributor to environmental pollution is the transport sector, and in particular, road transport, which in the EU is the largest source of NO_x, CO_2 and fine particulate matter ($PM_{2.5}$) emissions than any other mode of transport [6], [7].

As can be seen from Figure 1.2, transport is responsible for about a third of the total energy consumption in the EU with road transport representing the lion share of about 75% of total energy used by transport, Figure 1.3, and responsible for a similar proportion of the total GHG emissions from transport, Figure 1.4 [8]. Road transport is also responsible for a significant proportion of pollution in urban areas, as well as noise nuisance. In addition to pollution and energy requirements, road transport also affects the landscape, by dividing natural areas into smaller sectors affecting animals and plants.
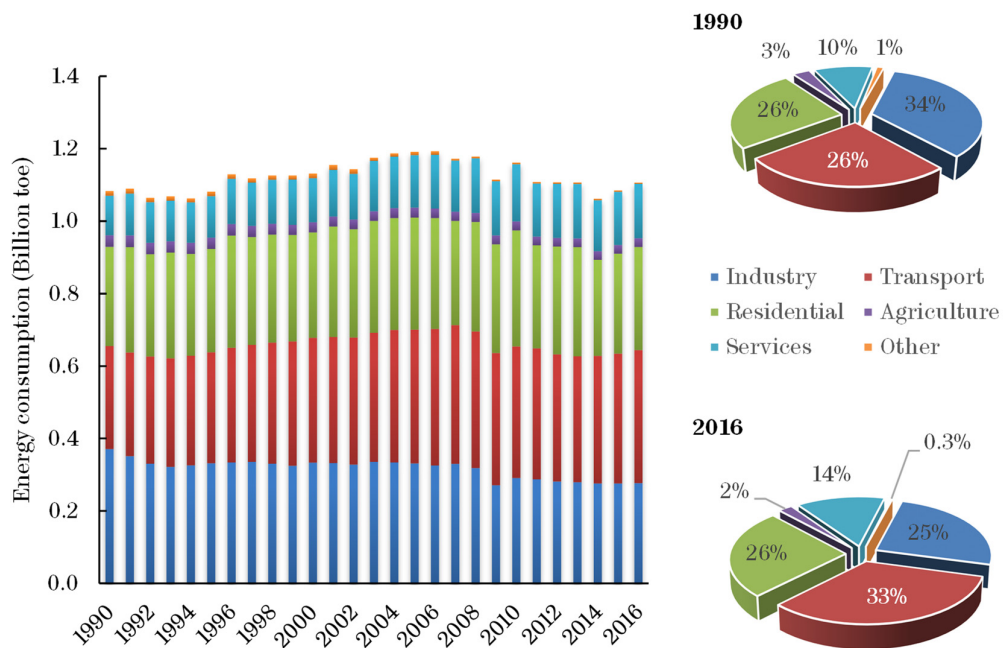
Figure 1.2. Evolution of energy consumption by end-use sector in the EU (left), and percentage contribution of each sector for years 1990 and 2016 (right) [7].
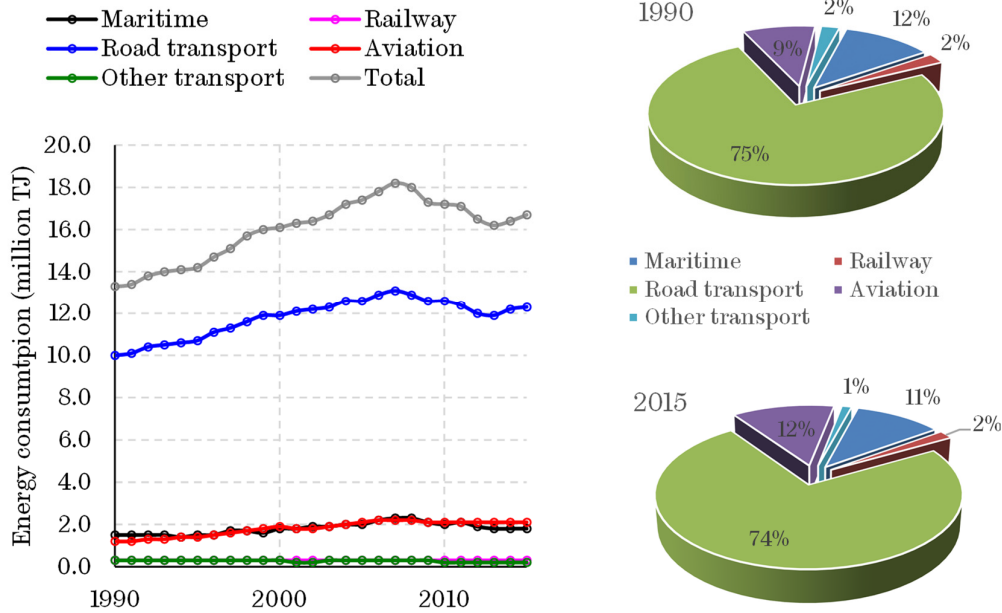
Figure 1.3. Energy consumption by transport mode in the EU (left), and contribution of each transport mode to the total energy consumption (right) [8].
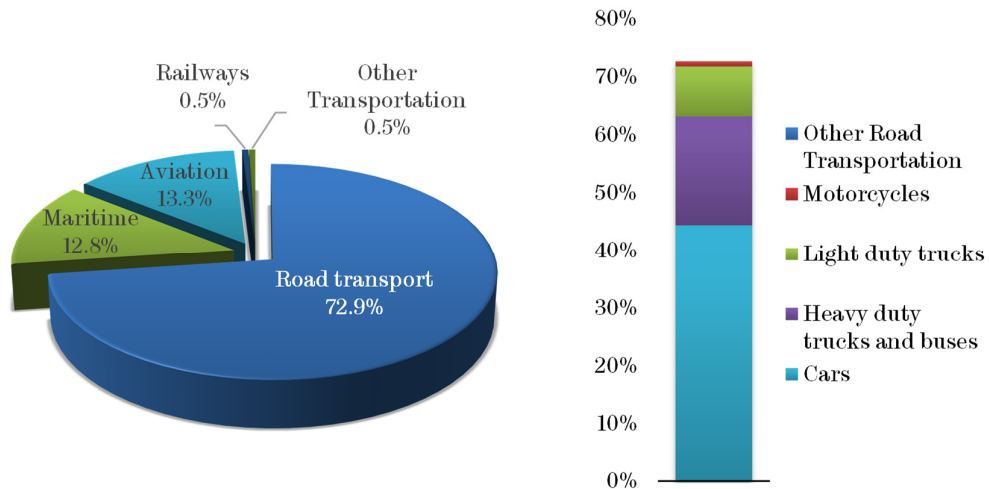
Figure 1.4. Contribution of different transport modes to the GHG emissions in Europe (left), and breakdown of total GHG emissions from road transport only (right) [8].

Consequently, the EU set several targets to reduce GHG emissions from transport. According to the 2011 white paper, by 2050 GHG are to be reduced by 60 % from 1990 levels [7]. Currently, the transport sector in the EU is dominated by oil, which accounts for 90% of its fuel, with road transport representing the largest share at 78% [9]. This implies that in the event of disruption in energy supply,

severe implications would arise on the economy and life quality in the EU. Therefore, plans to reduce the reliance of transport on oil consumption have been set in motion in the EU, aiming a reduction of ~70% in contrast to 2008 levels [7].

The testing procedures currently adopted in the EU — the New European Driving Cycle — are relative, and although this was updated in 1997, it was first introduced in 1970. Thus, they no longer represent real-world driving conditions in Europe, where traffic has changed, cars are heavier and faster and roads more congested [7]. These procedures give manufacturers flexibilities in setting testing parameters, such as mass, tyre pressure etc. Thus, vehicles emit significantly larger quantities of GHG and polluting emissions, and exhibit lower efficiencies in real-world conditions. Indeed, according to research by the International Council on Clean Transportation (ICCT) CO_2 emissions are up to 40% higher than those measured in testing laboratories [10]. Similar discrepancies also exist between real-world NOx emissions and laboratory measurements, with NOx emissions from diesel engines being up to seven times larger than the limits set by EURO 6 standard.

In January 2016, the European Commission introduced changes to the vehicle type-approval framework, in order to consolidate the independence of vehicle testing, and improve the enforcement and market surveillance regimes. A testing procedure known as the 'Worldwide Harmonized Light Vehicles Test Procedure' (WLTP) is being considered so that laboratory tests more accurately represent real-world conditions [7], [9]. In response to the imminent hazards arising from environmental pollution and climate change (which are intertwined), regulatory bodies around the globe have devised strict plans to tackle this problem. Transport is at the heart of every plan. Traction electrification is a major influence in all scenarios.

1.1.1   Electric vehicles – a promising pathway and their challenges

In response to the imminent consequences of climate change and energy supply security, regulatory bodies around the globe are creating new emissions and efficiency targets, with transport electrification being an important target at the core of every strategy, albeit the internal combustion engine and oil are predicted to remain important in transport until and beyond 2040 [3], Figure 1.5.
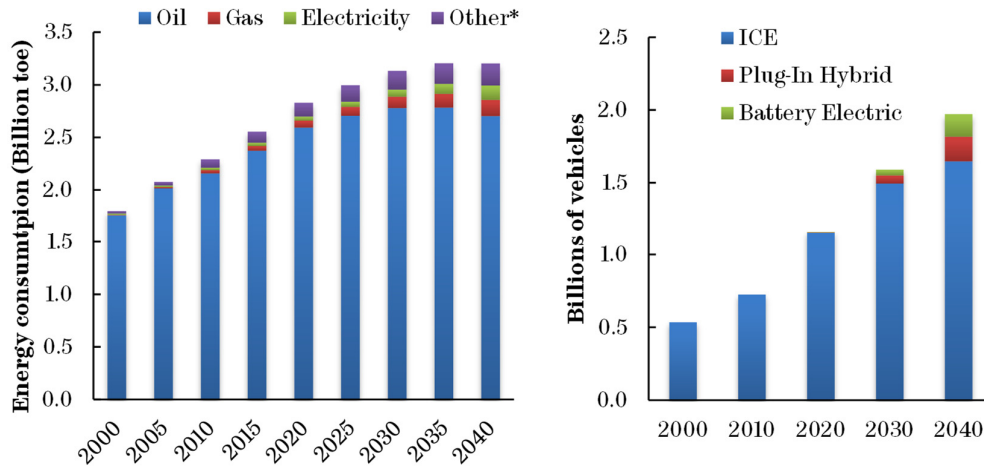
* ICE vehicles include hybrid vehicles which do not plug into the grid

Figure 1.5. Worldwide energy consumption in the transport sector (left), and passenger car number by type (right) [3].

1.1.1.1 Electrified drivetrains

Several electrified drivetrains have been proposed and implemented, varying from hybrid configurations to fully electric topologies [11], [12]. Hybrid drivetrains (HEV) can be grouped into three main topologies. Figure 1.6 shows a schematic of parallel hybrid drivetrain, where the electric traction machine and the ICE can share the input torque to the transmission. Such topology can be configured to operate in pure electric mode, pure ICE mode or in a hybrid mode, and can provide efficiency improving functions, such as re-generative braking.

Figure 1.7 shows a series hybrid configuration, where the engine is only used for the production of electrical power, and can therefore be controlled to operate at its maximum efficiency region. Similar to the parallel configuration, the series configuration also provides the possibility of driving the vehicle on pure electric mode and regenerative braking. However, due the fact that all components have to be rated to provide the total power, this configuration has always been considered to be more expensive. Lastly, Figure 1.8 shows the series/parallel drivetrain, which can operate in series, parallel or combined modes, and can offer the advantages of both the series and parallel configurations. This topology is adopted by Toyota and Ford automakers, and at the heart of the drivetrain, resides the planetary gear set,

which operates as a power-split device that enables the engine speed to be isolated from the vehicle speed.
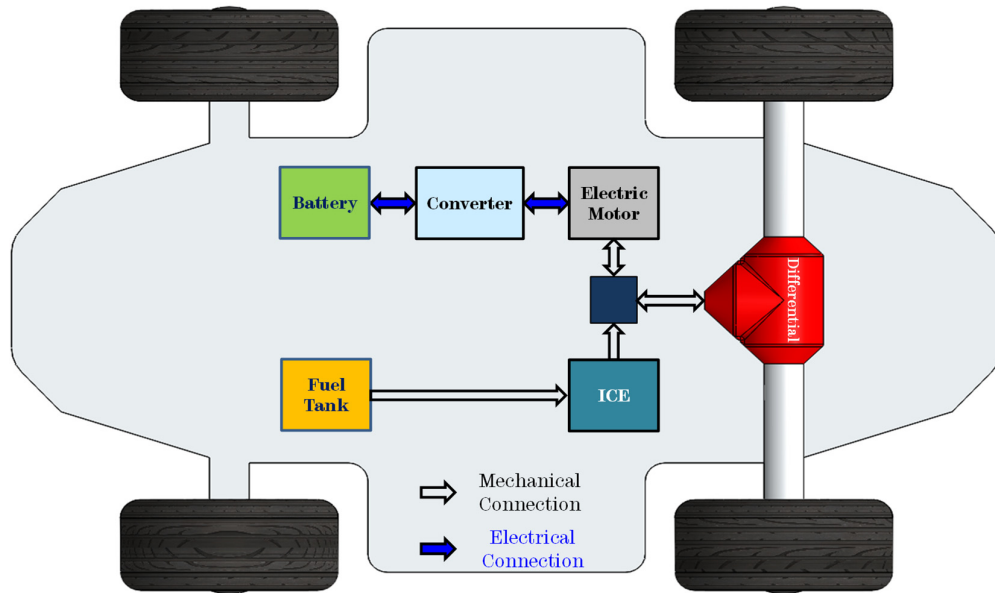
Figure 1.6. Hybrid electric vehicle - parallel architecture.
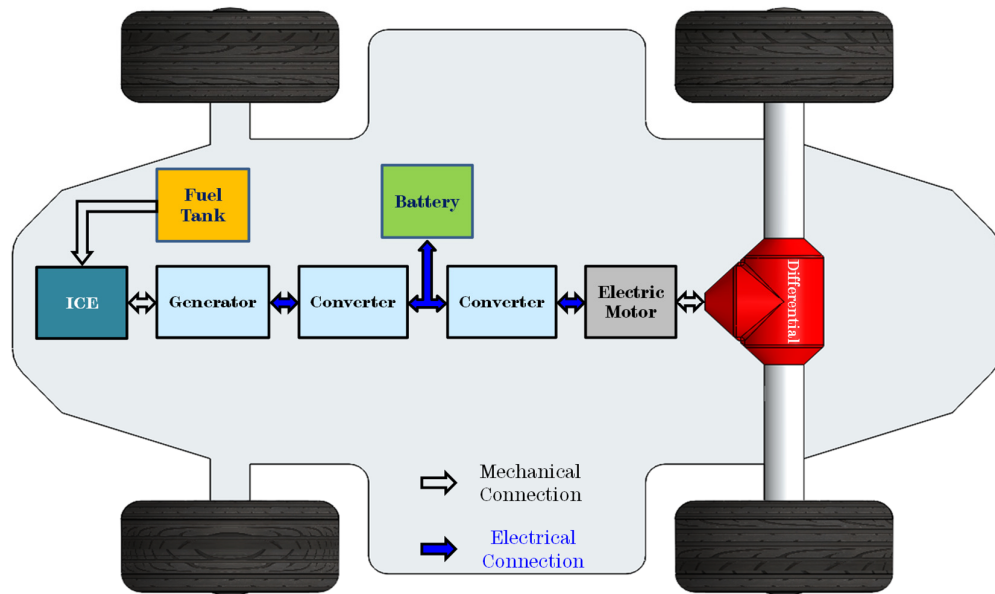
Figure 1.7. Hybrid electric vehicle - series architecture.
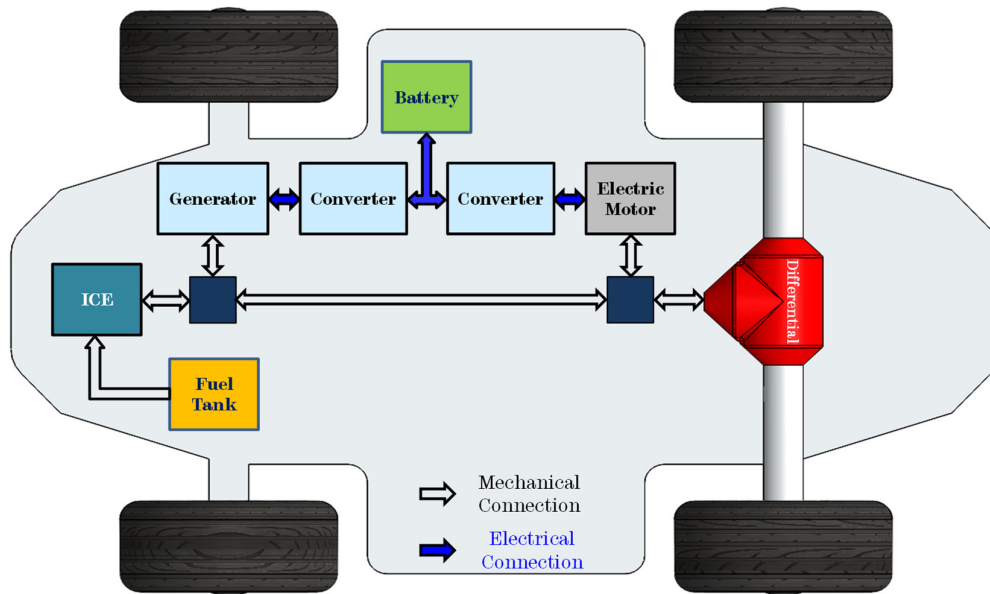
Figure 1.8. Hybrid electric vehicle – series/parallel (i.e., combined) architecture.

Pure electric drivetrain topologies (BEV) are relatively simple and consist of a battery pack, a converter and a traction machine, as seen in Figure 1.9. These are connected to the final drive/differential of the vehicle through a fixed-ratio gearbox. All the components are rated to provide the power required by the vehicle and the constant torque and constant power operations are achieved through the control of the traction machine, instead of the multi-ratio gearbox in conventional ICE drivetrains.

More advanced electric drivetrain configurations have been proposed, as can be seen in Figure 1.9. Such drivetrains can offer significant flexibility, albeit at an increased cost and complexity. For example, Figure 1.9 (d) shows 4-wheel, 4-motor electric drivetrain, where the wheels can be independently controlled, and the differential action can be electronically implemented.

The introduction of electric vehicles has the potential to significantly mitigate CO_2 emissions and air pollutants resulting from road transport. Nevertheless, the effectiveness of electric vehicles in reducing these emissions can be partially offset by the emissions produced by the generation of electricity required for powering them. It is projected, however, that despite this, by 2050 electrical vehicles will result in a net reduction in emissions in the EU, as can be

seen in Figure 1.10, partly due to the increase in the use of renewables for decarbonised electricity generation [13]. Note that the projections in Figure 1.10 are based on the assumption of a 30% and 80% EV market share for 2030 and 2050, respectively.
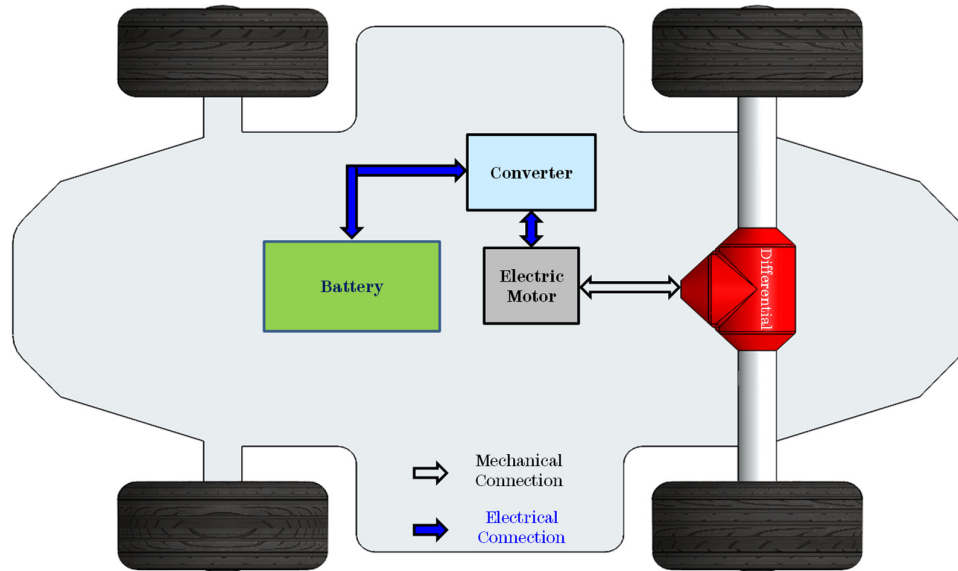
(a) BEV – one-motor concentrated powertrain
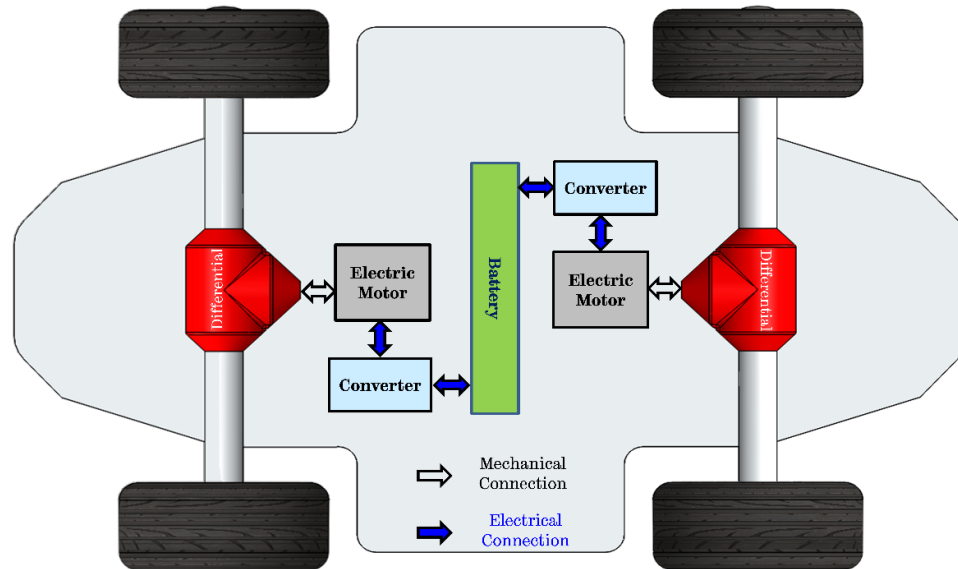
(b) BEV – two-motor distributed powertrain
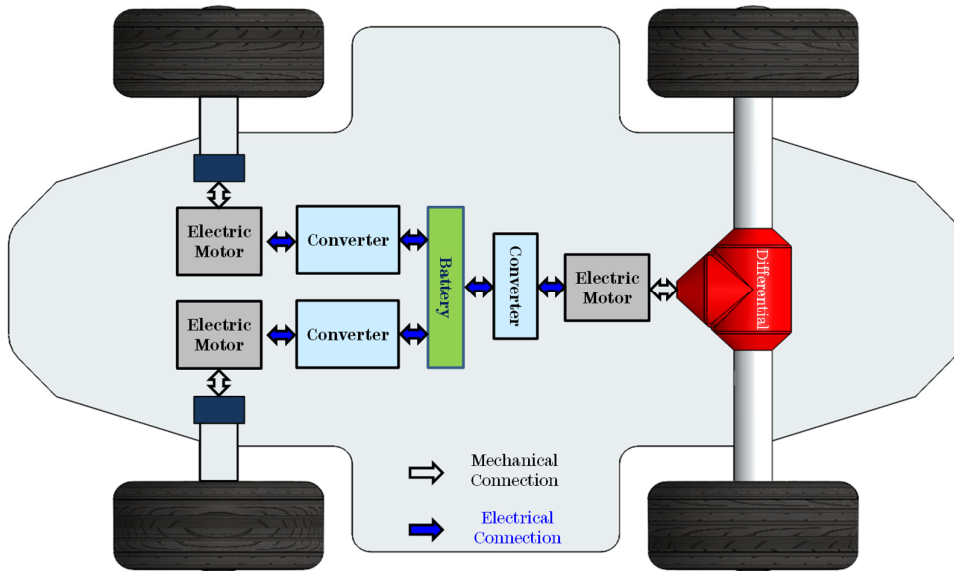
(c) BEV – three-motor distributed powertrain
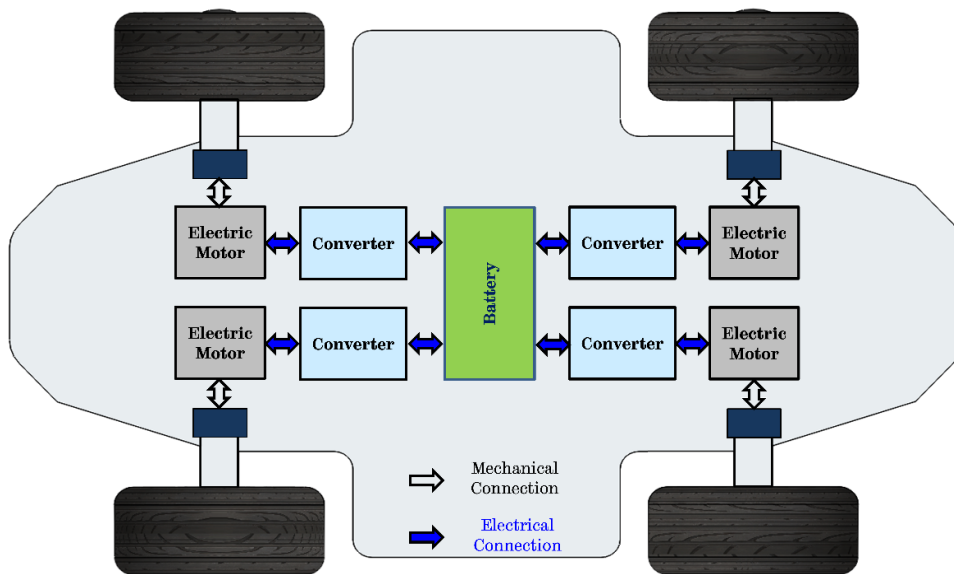
(d) BEV – four-motor distributed powertrain

Figure 1.9. Battery electric vehicle architectures with concentrated and distributed traction system.

A major issue for electric vehicle drivetrains remains the battery pack technology, in terms of cost and energy/power density, and by extension the achievable drive range that causes concerns to the consumers and considerably influences the mass deployment of EVs [14]. Figure 1.11 shows the trends in Lithium ion battery packs energy density and cost, where it can be seen that although

energy density exhibits continued improvements, cost reductions have plateaued in the last few years, albeit manufacturers, such as GM and Tesla reporting costs that are bucking the trend. Nevertheless, as can be seen in Figure 1.12, and based on different projection scenarios, from IEA RTS, IEA 2DS, IEA B2DS, Paris declaration, the market for electric vehicles is predicted to grow rapidly despite the currently low number of total EVs on the road [14]. The global electric car stock (EVs and plug-in HEVs) has reached 1.26m, with growth exceeding 77% in 2015.
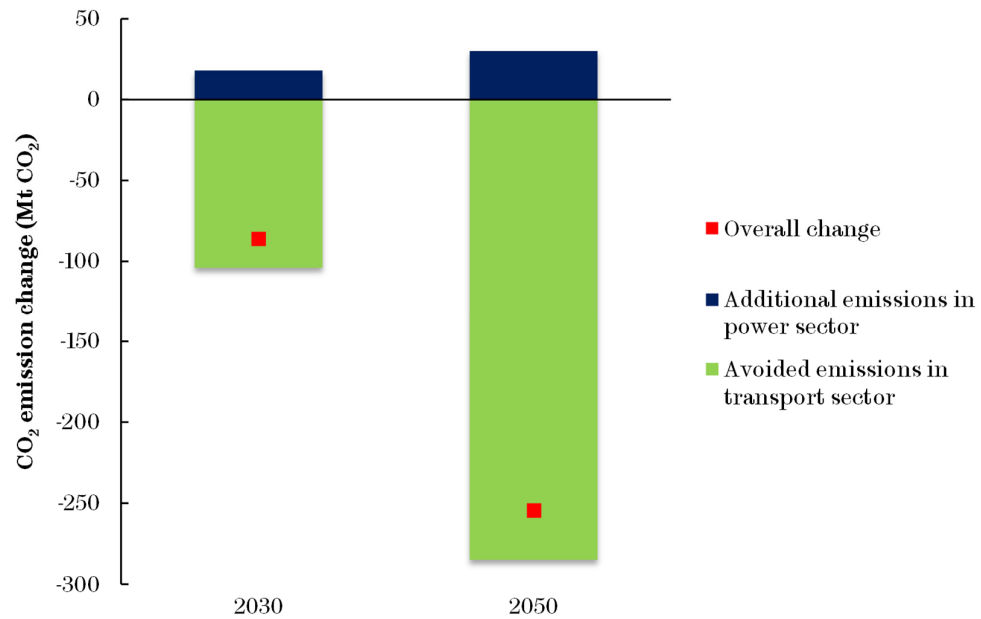
Figure 1.10. Future changes in CO_2 emissions in the energy and road transport sectors [13].
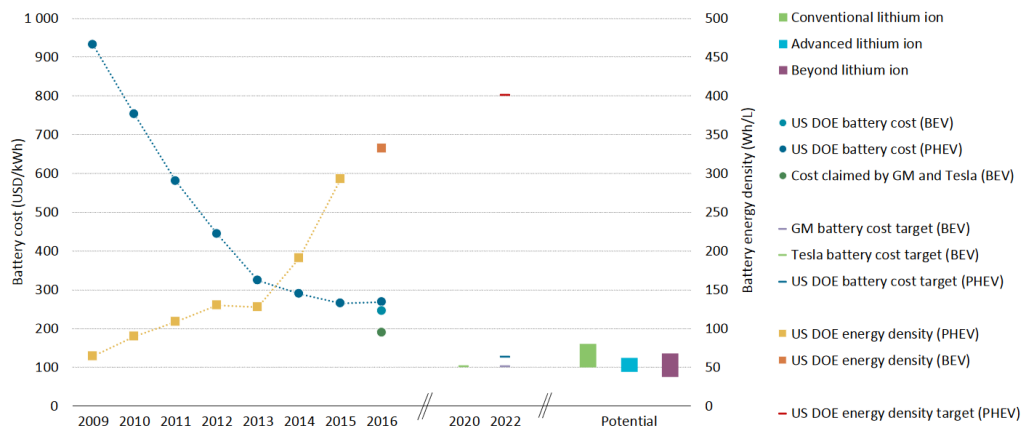
Figure 1.11. Evolution of battery energy density and cost [14].
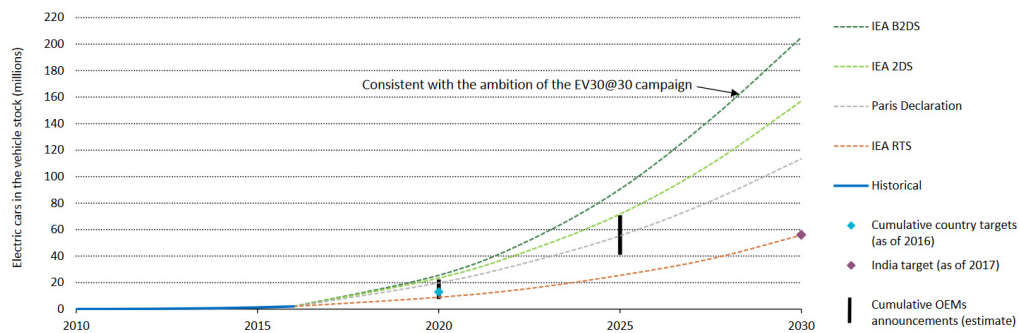
IEA – International Energy Agency

Figure 1.12. Deployment scenarios for the stock of electric cars up to 2030 [14].

1.2 Main traction machine technologies and topologies for EV applications

Electric traction machines are an intrinsic part of any electrified powertrain. Being the only tractive source in full-electric vehicles, the traction machine can have a significant impact on the mass, energy efficiency and cost of the EV powertrain. In fact, the traction machine incurs the largest share of losses among the different components of the EV powertrain [15]. The choice of a suitable traction machine technology/topology is a multi-faceted process and pertains to the challenging techno-economic requirements imposed by the vehicle application under consideration.

More specifically, the following machine design aspects can adequately represent these traction requirements [2], [16]–[21]:

- Packaging/space envelope (i.e., maximum outside diameter and maximum axial length) for the machine and/or the integrated drivetrain.
- The required torque-speed operating profile corresponding to both the peak and continuous power ratings.
- The cooling system requirements – liquid or air-cooling, which actually dictate the achievable torque and power density out of a particular machine technology/topology.

- The cooling system details, such as the flow rate and its control mechanism in relation to the operating profile of the vehicle, the inlet fluid temperature, and lastly the permissible ambient temperature range.

- The operating limits of the power electronics incorporated in the drivetrain – the DC-link voltage, the maximum fundamental frequency, and the maximum permissible open-circuit voltage necessary for the protection of the converter's power electronics.

- The maximum permissible winding temperature rise, which relates to the choice of the copper wire insulation grade, and dictates the lifecycle of the winding.

- The duty cycle for the considered application and the desired energy efficiency for operation over the duty cycle. The duty cycle can take the form of a single operating point, a driving cycle/mission profile or a map of operating points.

The above assertions are pivotal when it comes to the selection of an appropriate electric machine technology/topology and its design process for a given traction application.

Figure 1.13 shows representative torque-speed profiles for continuous and peak operation (in per-unit values) pertaining to current-state-of-art EV traction applications. These operating profiles represent the ideal variation of torque with speed for traction applications, and can be inherently achieved by a well-designed and controlled electrical machine. Whereas, in the case of ICE vehicles these ideal operating profiles are emulated through switching between multiple gears. The shape of the torque-speed operating profiles stems from the acceleration and gradeability (i.e., slope climbing) requirements of the vehicle that are used to determine the peak torque, and thereafter the peak power considering the maximum vehicle speed and selected gear ratio. The operating profiles consist of two distinct regions, i.e., the constant torque and constant power regions. The corner speed, at which operation changes from constant torque to constant power, is commonly referred to as the base speed. In broad terms, the constant torque region is limited by the maximum converter current limit and the constant power region is limited by the combination of both the maximum current and voltage

limits of the converter (however, this aspect has to do with the machine technology/topology under consideration and its design).

Typically, for EV application, the traction machine is required to exhibit a peak torque twice the continuous rating at low speeds or standstill to provide the required acceleration and gradeability. On the other hand, it also needs to deliver around twice the continuous power over a speed range 3-4 times the base speed [17], [21]. The wide torque-speed operating range places significant challenges on the selection and design of a appropriate traction machine technology/topology.
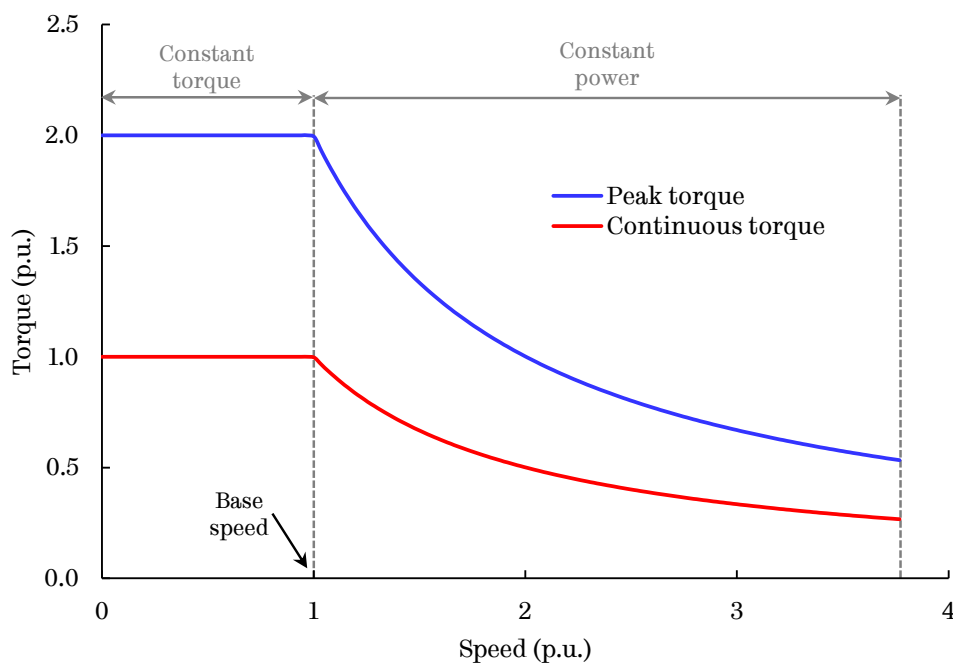
Figure 1.13. Typical torque-speed operating envelopes of the traction machine for EV applications.

1.2.1 Rare earth material resources – challenges and future implications on the EV automotive sector

Although several roadmaps and strategies have been set in motion toward a decarbonised and energy-sustainable transportation sector, it is essential to contemplate on the availability and supply security of the required material resources and their influence on the mass deployment of EVs in the future.

Currently, the electrified traction automotive industry relies heavily on rare earth elements, namely neodymium (Nd), dysprosium (Dy) and praseodymium (Pr), which are employed in NdFeB permanent magnets that play a key role in the development of torque/power-dense, lightweight and highly energy-efficient electrical traction machines (namely, permanent magnet machines – PMMs) [22].

Ever since the patenting of the strongest magnet material in the world, namely, sintered NdFeB, by M. Sagawa in 1983 the performance of electrical machines was revolutionised by the introduction of PMM technology [23]. The reason behind the drastic improvement in performance lies with the extremely high energy-product of NdFeB magnets in contrast to other magnet types, and their ability to exhibit high coercivity at relatively high temperatures without becoming demagnetised through the use of dysprosium (Dy) [24]. The extremely high energy density of NdFeBs enables the generation of a strong magnetic field in a smaller volume, in contrast to an electro-magnet. This can be visualised by Figure 1.14, where an NdFeB magnet with 5 times smaller area produces the same magnetic field as a 220-turn coil injected with 13A that also induces ~50W/m copper losses due to the wire resistance (assuming $10A/mm^2$ current density) [25]. Accordingly, this translates to a considerable reduction in the volume of a traction machine, thereby improving its torque density. More specifically, in [25] it is argued that for the case of an 80 kW traction machine the optimal use of NdFeB magnets would theoretically result ~20% volume reduction compared with the case where an electromagnet is employed for the generation of the equivalent magnetic field.
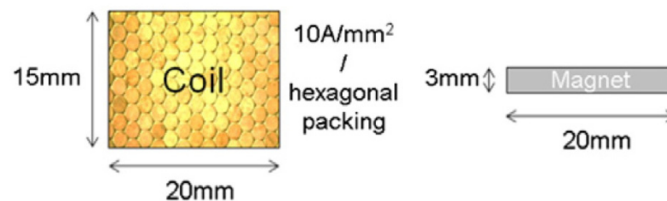
Figure 1.14. Surface area comparison between NdFeB magnet and electromagnet[25].

Undisputedly, the aforementioned qualities of rare earth magnets render them highly attractive, not only in the EV traction application, but also in other energy-critical applications such as wind turbines. Based on this, it is expected that

the demand for these rare earth materials would only increase in the future considering the drive toward a more energy sustainable and decarbonised future. The anticipation of this growth combined with other events (viz., China's threats in suspending international rare-earth supplies [26]) has had a substantial effect on the price of rare-earth materials, which saw an abrupt increase around 2011 with prices spiking 4-9 times higher than a year before. Although the prices have fallen since, they are still expected to grow higher, particularly for the case of dysprosium, due to the projections of mass deployment of EVs and wind energy in the future [22], [25].

In light of this, a drive to minimise or eliminate the use of rare-earth permanent magnets in electrical traction machines has been recently accelerated by the high cost, significant fluctuations in prices, and the potential restrictions on future supply [22], [23]. Figure 1.15 shows that the relative pricing of rare earth materials from 2008 demonstrates price fluctuations of up to a factor of 20. China produces more than 90% of rare earth materials, and dictates prices and availability [22], [27], [28]. China announced in October 2016 that it would limit annual mining by 2020. There are continuing difficulties in viable mining outside of China, which caused US mining firm Molycorp to file for bankruptcy in 2016.
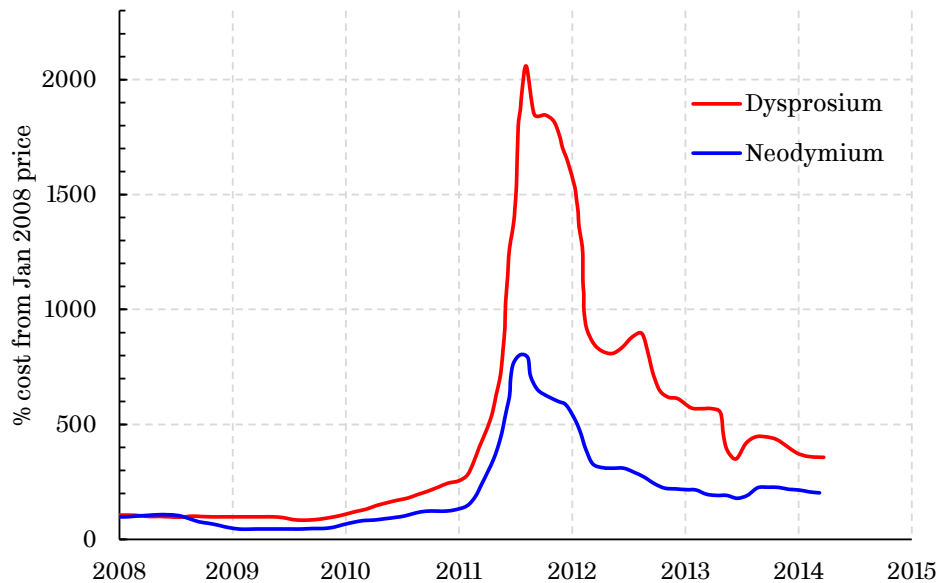
Figure 1.15. Price variability of neodymium and dysprosium rare earth elements [25].

In addition to supply chain and cost uncertainties, mining techniques have been reported to have significant environmental damage, and there are difficulties in recycling of rare earth materials [28]. These issues can have a large impact on the carbon footprint and lifecycle emissions of EVs. In a research project for the US Department of Energy [29], a breakdown of the material mass and cost of a permanent magnet motor was determined, Figure 1.16. Although the rare-earth magnets in the rotor account for only 3% of the motor's mass, they constituted 53% of the total motor cost, demonstrating that the total cost of the traction motor is severely influenced by fluctuations in the price of rare earth metals.
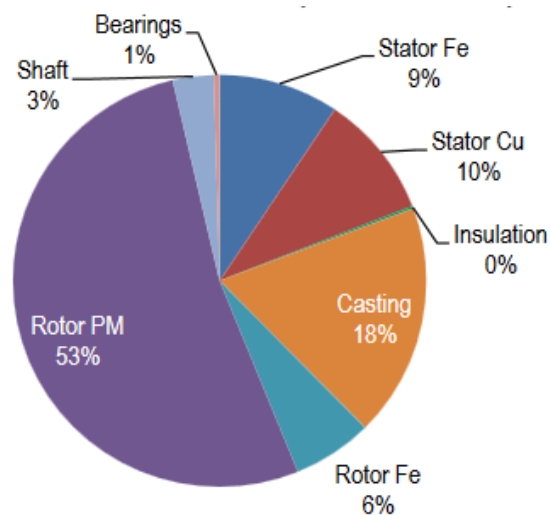
Figure 1.16. Breakdown of rare earth PM traction motor materials by cost [29].

Before 1989 EVs predominantly used DC motors. The first rare earth PM machine was used by Volkswagen in 1989, and the first induction motor (IM) by Ford in 1992 [30]. From that point onwards, IMs and PMs became common and DC machines receded, Figure 1.17. The EV automotive industry is now dominated by rare earth permanent magnet machines, predicted to increase to 90% market share in 2020 [31], due to their inherent torque/power density and energy efficiency advantages. Rare earth price fluctuations will therefore continue to have a significant effect on the EV industry. IDTechEx [32] warns that *"this is an industry structured for the past that is going to have a very nasty surprise when the future comes"*. For all of these reasons, other machine topologies that do not use rare earth materials (or limit their use significantly) are being actively considered as alternatives in

applications where rare-earth permanent magnet machines would normally be leading candidates. Another research direction involves the improvement of the magnet material efficiency, by achieving nearly identical magnetic strength with reduced quantity of rare earth elements through different manufacturing processes [22].

In this research, alternative rare earth-less and rare earth-free motor topologies are investigated, designed and optimised with the aim of achieving high energy efficiency of the EV drivetrain, thus, paving the way towards "future-proofing" the EV automotive industry in order to meet the increasing demand and cope with price fluctuations and supply restrictions in rare earth permanent magnets. The ferrite magnet material, for instance, provides an alternative to the rare earth magnet material for use in electrical machines. Ferrite magnets are still one of the most common magnet types, representing 85% of permanent magnets sold by weight. In 2016, raw material prices for ferrite magnets were forecasted to be \$5.26 per kg, as opposed to \$71.48 per kg for NdFeB magnets [33].
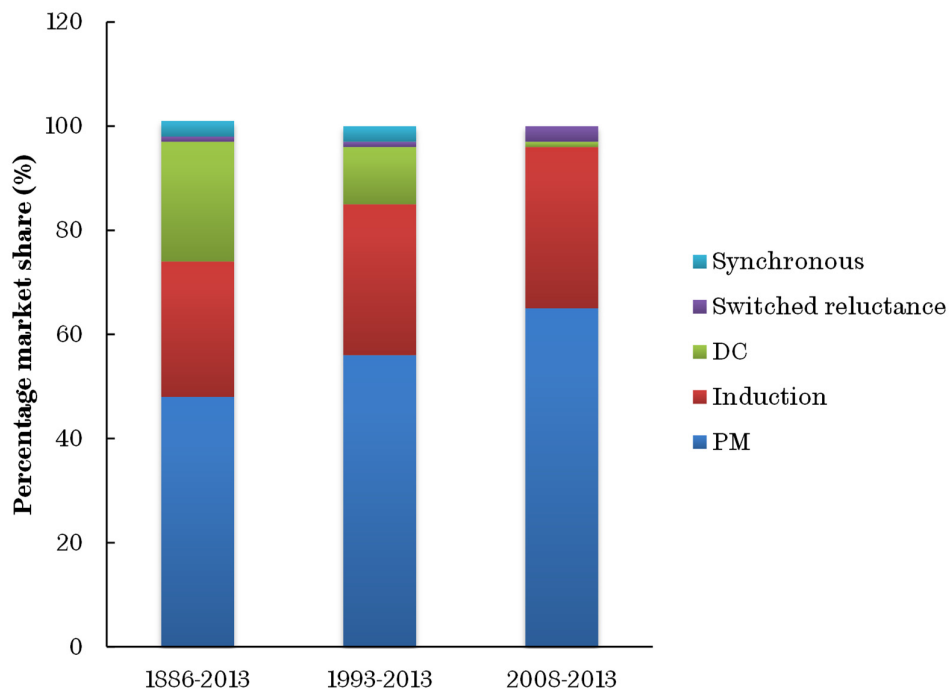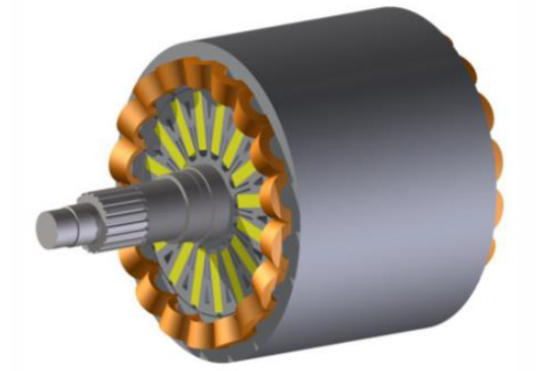
Figure 1.17. Change in the market share of EV motor technologies over time [30].

Ferrite magnets do not suffer from the same supply chain issues as rare earth materials. The essential components of hard ferrite magnets are iron oxide and either barium carbonate or strontium carbonate. Iron oxide and the alkali earth elements barium and strontium occur in nature in sufficient abundance. Iron oxide is also a by-product of industrial steel processing [34]. Although China dominates the production of ferrites, 40% of ferrites are produced outside China [27], including some prominent European manufacturers such as Magnetfabrik in Germany. Ferrites are employed in a variety of applications, of which 70% are electric motors. Traditionally, their application is limited to low-power and low-cost applications [33] due to lower energy density and potential for demagnetisation under high opposing fields. These shortcomings can be overcome using advanced machine topologies and design techniques.

A particular PMSM topology that facilitates the use of low remanence magnets, such as ferrites, or alternatively a substantial reduction in rare-earth magnets, is the Permanent Magnet Assisted Synchronous Reluctance Machine (PMA SynRM) [35]–[37], which is comprehensively investigated in this thesis. This characteristic pertains to the intrinsic torque production mechanism of this topology that mainly relies on the reluctance component of the torque due to its highly anisotropic rotor structure, while also having the assistance from the embedded permanent magnets (i.e., "torque hybridisation"). Under these circumstances, the assistive PM material embedded in the rotor can be of high quantity in the case of low remanence magnets (e.g., ferrites or bonded NdFeB), or of a substantially limited quantity in the case of high remanence rare earth magnets (e.g., sintered NdFeB). Torque hybridisation is a key contributing factor that enabled the mass deployment of interior-mounted PMSMs (IPMSMs) in various EV/HEV drivetrains [22], [25], [38], as it leads to an extended operating speed range with relatively high energy efficiency, as well as a high torque/power density. The degree of torque hybridisation, however, is significantly higher in the case of the PMA SynRM topology, thus, providing the potential to achieve comparable torque/power density and energy efficiency with limited or no use of rare earth magnets, when appropriately designed and optimised (as will be demonstrated in Chapters 3 and 7 for the specific EV application under study).

Table 1.1 summarises the main traction machine technologies/topologies employed or being considered (viz., received a high technological readiness level) by major automotive OEMs for pure EV applications. The table adopts a qualitative comparison of the key performance indicators and cost drivers. These include the energy efficiency, power density, and noise and vibration harshness (NVH), as well as cost and supply issues. As can be seen, rare earth PMSMs exhibit the best performance indicators despite the cost and supply chain issues associated with the rare-earth element found in rare-earth magnet materials, and are the preferred machine technology by various automotive OEMs.

Table 1.1. Main traction machine technologies/topologies employed or under consideration by automotive OEMs for pure EV traction applications

  • Maximum power: 80kW • Maximum torque: 280Nm	Rare-earth brushless machine: In use in a number of EVs including the Nissan Leaf [39] ✓ High efficiency ✓ High power density ✗ Supply chain issues with rare earth PMs ✗ Higher cost ✓ No specific NVH issues
  • Maximum power: 55kW • Maximum torque: 170Nm	Spoke type ferrite machine: E.U. funded Motorbrain ✗ Lower efficiency ✗ Lower power density ✓ No supply chain issues with materials ✓ Lower cost ✓ No specific NVH issues

 • Maximum power: 285kW • Maximum torque: 410Nm	Induction machine: In use by Tesla motors ✕ Lower efficiency ✕ Lower power density ✓ No supply chain issues with materials ✓ Lower cost ✓ No specific NVH issues
 • Maximum power: 80kW • Maximum torque: 260Nm	Alternative spoke type ferrite motor: Innovate UK Evoque_e project [40] ✕ Lower efficiency ✕ Lower power density ✓ No supply chain issues with materials ✓ Lower cost ✓ No specific NVH issues
 • Maximum power: 70kW • Maximum torque: 226Nm	Wound field synchronous machine: In use by Renault ✕ Lower efficiency ✕ Lower power density ✓ No supply chain issues with materials ✓ Lower cost ✓ No specific NVH issues

  • Maximum power: 60kW • Maximum torque: 400Nm	Synchronous reluctance machine: E.U. funded project Motorbrain ✖ Lower efficiency ✖ Lower power density ✓ No supply chain issues with materials ✓ Lower cost ✖ Potential NVH issues
  • Maximum power: 55kW • Maximum torque: 170Nm	Claw pole type ferrite machine: E.U. funded Motorbrain ✖ Lower efficiency ✖ Lower power density ✓ No supply chain issues with materials ✓ Lower cost ✓ No specific NVH issues
  • Maximum power: 85kW • Maximum torque: 215Nm	Switched reluctance machine: Innovate UK's RapidSR ✖ Lower efficiency ✖ Lower power density ✓ No supply chain issues with materials ✓ Lower cost ✖ Potential NVH issues

1.3 Thesis outline

The following will present the structure of this thesis by outlining the scope of each chapter.

1.3.1 Chapter 2

This chapter describes a new design technique for electric vehicle traction machines to achieve high energy efficiency against a defined driving cycle such as the New European Drive Cycle (NEDC) while satisfying the required torque-speed operating range, as well as other volumetric, electrical, thermal and mechanical design constraints. The work is undertaken as a part of the EU funded P-MOB (Personal Mobility) project. By analysing the energy distribution of a given driving cycle, the energy efficiency of the traction machine over the driving cycle can be characterised against a number of representative operating points, and thus, the design optimisation can be performed with respect to these points. This significantly reduces the computation time of the design optimisation process (using FEA), while improving the energy efficiency of the traction machines. The utility of the design technique is illustrated through design case studies and its effectiveness validated by experimental results.

1.3.2 Chapter 3

This chapter focuses on the design and performance evaluation of a rare-earth-less Permanent Magnet-Assisted Synchronous Reluctance Machine (PMA SynRM) for an EV traction application employing a distributed traction system (instead of a centralised system employing a single traction machine). The work undertaken is part of the European Green Vehicles Initiative FP7 Hi-Wi project.

The Hi-Wi EV employs a distributed traction powertrain consisting of multiple electrical machines of dissimilar technology or topology as a means to harness the inherent advantages of each machine. Such a powertrain implementation also enables the use of a dynamic torque distribution strategy between the front and rear-axle machines, which has the potential to further enhance the energy efficiency of the overall powertrain. The results from the investigation of different machine technology/topology combinations, as well as the application of a

dynamic torque distribution strategy, and their influence on the powertrain energy efficiency are presented and discussed.

Based on the results from the aforementioned investigations, a Permanent magnet assisted synchronous reluctance machine (PMA SynRM) has been identified as an ideal candidate for the rear wheels of the Hi-Wi EV, which form a key focus area of this chapter. Research is focused on the design and optimisation of this topology for the investigated traction application. The performance over representative driving cycles is incorporated in the design optimisation process to achieve a design pertaining toward real-world operation, while satisfying a set of electrical, thermal, volumetric and mechanical constraints. The multi-physical performance of the machine is comprehensively analysed, and special attention is paid into the minimisation of electromagnetic torque ripple and the demagnetisation-withstand ability of the machine against extreme operating conditions as the latter fall into the demerits of the PMA SynRM topology.

1.3.3 Chapter 4

This chapter exemplifies the influence of skew on the magnetic behavior (i.e. flux-linkages and inductances) and torque characteristic of a synchronous machine. Thereby, it proposes a computationally efficient semi-analytical technique to accurately derive the electromagnetic parameter model of a synchronous machine incorporating skew, whilst taking into account the effect of saturation and d-q axis cross-coupling. The proposed technique uses only one set of 2D finite element (FE)-computed data corresponding to the unskewed machine, and can be applied for the prediction of either average or instantaneous d- and q-axis flux linkages and torque of any synchronous machine with any number of skew slices and any skew angle. The validity of the technique is verified by FE analysis and measurements.

1.3.4 Chapter 5

This chapter focuses on the 3D effects associated with rotor step-skews performed in permanent magnet assisted synchronous reluctance machines (PMA SynRMs). It analyses and quantifies these effects via comparisons between 2D and

3D finite element analyses of skewed and unskewed machines. The 3D phenomena manifested in the skewed PMA SynRM are identified into end-effects and axial interactions between skewed steps, and their influence on its electromagnetic performance is examined under loaded and no-load conditions. The chapter exemplifies the significance of the skew-associated 3D effects, which can result in the decrease of the back-electro-motive-force (back-emf) and a substantially increased electromagnetic torque ripple. It, thereby, highlights the inability of the typically employed multi-slice 2D FEA or other existing 2D-based modelling techniques in taking the influence of these effects into account. The validity of the findings is experimentally verified with measurements acquired from a prototype PMA SynRM using skewed and unskewed shafts in the rotor.

1.3.5 Chapter 6

This chapter investigates the effect of laser cutting the stator lamination on the performance of a PMA SynRM. A technique for the modelling of the B-H curves of electrical steel laminations is described. It takes into account of the extent of degradation of the magnetic properties caused by laser cutting, reported in the literature, and assumes that the degree of damage is determined by the distance between the cut edges or the width of the strip. The technique is employed to predict the performance of the PMA SynRM, which exhibited significant discrepancies between measured and predicted performance assuming the ideal manufacturer's B-H curve. In the analysis, the machine is subdivided into regions characterized by the distance between the edges, and each region is assigned a corresponding B-H curve. Through comparisons between experimental measurements and predictions, the chapter highlights the potential adverse impact of laser cutting on the performance of electrical machines, especially those exhibiting a long cutting length per unit area of steel. Therefore, it demonstrates the necessity of incorporating such effects into the modelling in order to improve prediction accuracy.

1.3.6 Chapter 7

PMA SynRMs have the potential to substantially reduce or even eliminate the use of rare-earth magnets. Accordingly, this chapter conducts a comprehensive

investigation into topologic and parametric design optimisations of PMA SynRMs for EV traction applications, providing useful insights regarding their design for the specific application.

The design optimisations are conducted via an effective and computationally efficient optimisation platform, which facilitates fast multi-physics performance evaluations by using a set of finite-element characterised analytical machine models without sacrificing accuracy. It also enables multiple design optimisations with a large number of design parameters (>10) to be executed in a timely efficient manner through the integration of distributed computing capabilities. The employed optimisation platform maximises the system (machine plus inverter) energy efficiency against a given driving cycle by systematically evaluating a defined set of electrical, thermal and mechanical design constraints.

Against this background, the multi-physics design optimisation and performance of traction PMA SynRMs employing distributed windings and characteristically different magnet materials in the rotor (i.e., sintered NdFeB and ferrites) is comprehensively investigated. Optimal rotor structures that most effectively utilise the employed magnet material, while leaving the remaining performance virtually unaffected, are identified for each magnet type. Further, the multi-physics design optimisation of PMA SynRMs using fractional-slot windings is also investigated and benchmarked with the optimal configuration with a distributed winding. The attained optimal PMA SynRM designs are comprehensibly evaluated and compared against multiple indicative performance metrics including the energy efficiency against characteristically different driving cycles, reluctance torque capability, thermal behaviour, torque/power density and cost, with the aim of assessing their viability for (EV) traction applications.

1.3.7 Chapter 8

This chapter draws the general conclusions of the research undertaken in this doctoral thesis pertaining to the design, modelling and optimisation aspects of rare-earth-free/less PMA SynRMs for EV traction applications. It also discusses potential future work that further expands the scope of this research, with particular emphasis toward system integration and the interactions between the system components.

1.4 List of publications

1.4.1 Journal publications from the thesis

1. **P. Lazari**, J. Wang, and L. Chen, "A Computationally Efficient Design Technique for Electric-Vehicle Traction Machines," *IEEE Transactions on Industry Applications*, vol. 50, no. 5, pp. 3203–3213, Sep. 2014.
2. **P. Lazari**, J. Wang, B. Sen X. Chen "Accurate d-q axis modelling of synchronous machines with skew accounting for saturation," in *IEEE Transactions on Magnetics*, vol.50, no.11, pp.1,4, Nov. 2014.
3. **P. Lazari**, K. Atallah and J. Wang, "Effect of Laser Cut on the Performance of Permanent Magnet Assisted Synchronous Reluctance Machines," in *IEEE Transactions on Magnetics*, vol. 51, no. 11, pp. 1-4, Nov. 2015.
4. **P. Lazari**, J. Wang and B. Sen, "3-D Effects of Rotor Step-Skews in Permanent Magnet-Assisted Synchronous Reluctance Machines," in *IEEE Transactions on Magnetics*, vol. 51, no. 11, pp. 1-4, Nov. 2015.

1.4.2 Other journal publications

5. X. Chen, J. Wang, V. I. Patel and **P. Lazari**, "A Nine-Phase 18-Slot 14-Pole Interior Permanent Magnet Machine With Low Space Harmonics for Electric Vehicle Applications," in *IEEE Transactions on Energy Conversion*, vol. 31, no. 3, pp. 860-871, Sept. 2016.
6. B. Sen, J. Wang and **P. Lazari**, "A High-Fidelity Computationally Efficient Transient Model of Interior Permanent-Magnet Machine With Stator Turn Fault," in *IEEE Transactions on Industrial Electronics*, vol. 63, no. 2, pp. 773-783, Feb. 2016.
7. X. Chen, J. Wang, B. Sen, **P. Lazari**, and T. Sun, "A High-Fidelity and Computationally Efficient Model for Interior Permanent-Magnet Machines Considering the Magnetic Saturation, Spatial Harmonics, and Iron Loss Effect," *IEEE Transactions on Industrial Electronics*, vol. 62, no. 7, pp. 4044–4055, Jul. 2015.

1.4.3 Conference publications from the thesis

8. **P. Lazari**, J. Wang, X. Chen, and L. Chen, "Design optimisation and performance evaluation of a rare-earth-free Permanent Magnet Assisted Synchronous Reluctance Machine for electric vehicle traction," in *IET International Power Electronics, Machines and Drives Conference (PEMD)*, 8-10 Apr. 2014.
9. **P. Lazari**, J. Wang, and L. Chen, "A computationally efficient design technique for electric vehicle traction machines," in *International Conference on Electrical Machines (ICEM)*, Sept. 2012, pp.2596-2602.
10. **P. Lazari**, J. Wang, "Design Optimisation of Traction Motors for EV Applications," in *CEDRAT News Magazine, Issue 66,* June 2014.

1.4.4 Other conference publications

11. L. Chen, **P. Lazari** and J. Wang, and "Optimal power split ratio of a distributed electric vehicle traction system," in *IET International Power Electronics, Machines and Drives Conference (PEMD)*, 8-10 Apr. 2014.

12. L. Chen, X. Chen, J. Wang and **P. Lazari**, "A computationally efficient multi-physics optimization technique for permanent magnet machines in electric vehicle traction applications," *2015 IEEE International Electric Machines & Drives Conference (IEMDC)*, 2015, pp. 1644-1650.

13. X. Chen, J. Wang, **P. Lazari**, and L. Chen, "Permanent magnet assisted synchronous reluctance machine with fractional-slot winding configurations," in *IEEE International Electric Machines and Drives Conference (IEMDC)*, 2013, pp. 374–381.

14. L. Chen, J. Wang, **P. Lazari**, and X. Chen, "Optimizations of a permanent magnet machine targeting different driving cycles for electric vehicles," in *IEEE International Electric Machines and Drives Conference (IEMDC)*, 2013, pp. 855–862.

15. L. Chen, J. Wang, P. Lombard, **P. Lazari** and V. Leconte, "Design optimisation of permanent magnet assisted synchronous reluctance machines for electric vehicle applications," in *International Conference on Electrical Machines (ICEM)*, Sept. 2012, pp.2647-2653.

16. X. Chen, J. Wang, V. I. Patel, **P. Lazari**, L. Chen, and P. Lombard, "Reluctance torque evaluation for interior permanent magnet machines using frozen permeability," in *IET International Power Electronics, Machines and Drives Conference (PEMD)*, 8-10 Apr. 2014.

17. B. Sen, J. Wang, and **P. Lazari**, "A detailed transient model of Interior Permanent Magnet motor accounting for saturation under stator turn fault," in *2013 IEEE Energy Conversion Congress and Exposition (ECCE)*, 2013, pp. 3548–3555.

18. H. Aorith, J. Wang and **P. Lazari**, "A new Loss Minimization Algorithm for Interior Permanent Magnet Synchronous Machine drives," in *IEMDC*, 2013, pp. 526–533.

Chapter 2

A Computationally Efficient Design Technique for Electric Vehicle Traction Machines

This chapter describes a new design technique for electric vehicle (EV) traction machines to achieve high efficiency against a defined driving cycle such as the New European Drive Cycle (NEDC) while satisfying the required torque-speed operating range and space envelope as well as the thermal constraints. The work is undertaken as a part of the EU funded P-MOB (Personal Mobility) project. By analysing the energy distribution of a given driving cycle, the energy efficiency of the traction machine over the driving cycle can be characterised against a number of representative points, and the design optimisation can be carried out with respect to these points. This significantly reduces the computation time of the design optimisation process (using FEA), while improving the energy efficiency of the traction machines. The utility of the design technique has been illustrated through design case studies and its effectiveness validated by experimental results.

The author has published the main contents of this chapter in [41].

There is a drive towards the development of more efficient and environmentally friendly vehicles. It is widely accepted that electric vehicles (EVs) can be an important part of the solution which enables safeguarding of the environment and energy resources for future generations [1], [2]. Particularly if the electrical energy required for the propulsion of EVs is produced using renewable energy sources, such as wind, solar, tidal or wave power. Thus, traction electrification could lead to a reduction in environmental pollution, CO_2 emissions as well as the reliance on fossil fuels. The design requirements for the traction machine of EVs are highly demanding regarding efficiency, torque and power density, wide constant power operating range, overload capacity and cost-effectiveness [19].

Electric traction machines, being an intrinsic part of any drive, can have a significant impact on the energy efficiency and cost of the EV powertrain. In fact, based on recently performed studies [15], the traction machine incurs the most substantial amount of losses in the EV powertrain. Amongst the competing electrical machine technologies for traction applications, induction machines are potentially the lowest cost, simple to construct, and they can operate over a wide speed range with high reliability. However, they have a lower torque density and an inferior power factor making them less efficient compared to permanent magnet (PM) brushless machines, despite the use of any enhanced loss minimisation control algorithms [42]. Similarly, while switched reluctance machines are more robust and cost-effective than PM brushless machines, they have a higher torque ripple, and a poorer power factor potentially resulting in noise and vibration issues, and increased inverter cost. Thus, in general, brushless PM synchronous machines (PMSM) are preferred for traction applications, where energy efficiency and torque/power density are the most important attributes [19], [17], [20], [43]–[45], despite concerns about the price volatility of rare-earth materials[38]. PMSMs are particularly suited for applications (such as micro-sized vehicles), which have a restricted space envelope or require low machine power ratings. Nonetheless, it is important to note that efficiency is correlated with size and power rating scalability. Thus, the efficiency gap between other machine topologies and PMSMs could be reduced when moving towards higher power ratings or volume.

The challenge for the EV traction machine design is that it has to produce high torque, usually 2~3 times the nominal value, at standstill or low speed to provide the required acceleration and climbing capability. Conversely, the machine needs to output peak power close to twice the rated value at medium to high speeds. The wide torque and speed operating range place significant constraints on the attainable machine efficiency and power density using conventional design methodologies. Owing to the highly dynamic nature of EV traction applications, static efficiency maps, which reflect power efficiency, are an inadequate performance metric for traction machines [42]. Instead, the concept of energy efficiency should be employed to evaluate their performance with respect to a

particular mission profile. This concept will, in fact, indicate at which regions of the efficiency map the traction machine most frequently operates when the vehicle is operating over its corresponding driving cycle.

Since an EV operates over a wide torque-speed range in response to various driving conditions, the machine design should be aimed to achieve overall energy saving over a driving cycle. The high efficiency operating region of current state-of-the-art PM brushless machines for EV traction is typically designed around the rated (specific: continuous at base speed) and/or the maximum speed operating points [44] or a few points around the rated point [46]. However, despite the need for high torque to satisfy the acceleration and curb climbing requirements, EV traction machines during a typical urban or suburb driving frequently operate in the low torque region where the efficiency is much lower [15], [21], [47]. The mismatch between the regions of high efficiency and high operating duty with the existing PM brushless traction drives results in lower overall energy efficiency, higher energy consumption, and reduced vehicle range.

Recently, several authors started acknowledging the significance of energy efficiency in traction machines and begun to assess and evaluate their performance over driving cycles [42], [48], [49]. However, the traction machine design still relies on the conventional design approaches. The integration of driving cycles in the design optimisation of traction machines has to date received limited attention in the literature. The challenges associated with the realisation of such a design approach are computational time and loss calculation accuracy (due to the large number of cycle operating points), where the two form a trade-off depending on the simplification assumptions on loss modelling. Authors who attempted to realise such an optimisation, reported enormous computational time [50] or ended up simplifying the calculations to the extent where accuracy is sacrificed [51]. This calls for the need to develop a viable and computationally efficient motor design method, allowing for minimising the total energy loss over a driving cycle rather than at a few operating points. This approach constitutes a crucial step in the development and swift realisation of EVs in an industrial market where low cost and high energy efficiency are the most dominant factors [45].

This chapter describes design techniques for EV traction machines to achieve high efficiency against a defined driving cycle, such as the New European Drive Cycle (NEDC) while satisfying the required torque-speed operating range and maintaining high fidelity calculations with a low computational time cost. The methods described in this chapter are machine topology and driving cycle independent. Thus, they can be extended to other machine topologies and technologies, and different driving cycles.

This chapter is structured as follows: §2.1 describes the procedure to derive the motor torque-speed envelope based on the investigated vehicle parameters and the defined driving cycle. Further, this section analyses the motor energy consumption distribution over the NEDC and exemplifies that the motor's energy efficiency over the cycle can be characterized against a finite number of representative points, which will be used as design targets in the optimisation process. §2.2 identifies the constraints that should be considered for the design optimisation of a surface-mounted PM traction motor (SPM), and illustrates the significance of optimising for maximum energy efficiency against a driving cycle through design case studies. A fractional-slot concentrated winding (FSCW) SPM, designed based on the proposed techniques, was manufactured and its predicted performance is validated through experimental test results presented in §2.3.

2.1 Energy consumption distribution over a reference driving cycle

2.1.1 Investigated vehicle and motor design specification

The NEDC, illustrated in Figure 2.1, has been extensively employed during the past decades by manufacturers for the purpose of testing the vehicle's energy consumption and polluting emissions, as it represents the typical usage of light-duty vehicles in Europe [52]. It consists of four recurring ECE-15 city driving cycles along with an extra-urban driving cycle (EUDC) with a maximum speed of 120 km/h. The NEDC has a duration of ~20 minutes, within which a total distance of ~11km is covered.
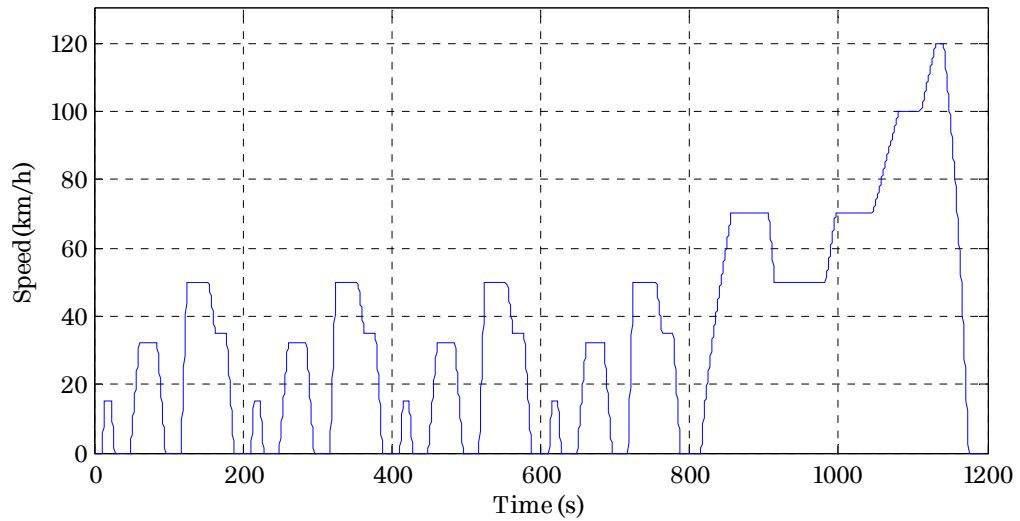
Figure 2.1. NEDC velocity profile.

The investigated electric vehicle is a micro-sized (two-seater) car with a distributed drivetrain. The drivetrain employs two identical motors coupled to the front and rear axles, respectively, via two differentials as shown in the schematic of Figure 2.2. Two separate inverters are used to feed and control the traction motors. This approach enables a degree of redundancy and safety in the event of a fault during driving in either of the two drive systems. It also facilitates the potential to improve driving efficiency and vehicle stability, via intelligent dynamic traction torque distribution between the rear and front wheels according to various operating conditions and considering the interactions of the tires with the road surface [15]. The detailed parameters of the investigated vehicle are provided in Table 2.1, as defined by the OEM as part of the EU-funded P-MOB project.
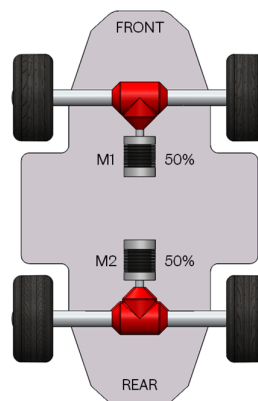
Figure 2.2. Schematic of the investigated vehicle with front and rear drivetrain.

Table 2.1. Investigated EV specification (Micro-sized vehicle)

Parameter (Unit)	Symbol	Value
Tire size	-	165/50 R15
Radius of wheels (m)	r_w	0.273
Vehicle mass (kg)	m	500
Gravitational acceleration (m/s^2)	g	9.807
Rolling resistance coefficient	k_r	0.007
Product of drag coefficient and front area (m^2)	A	0.6
Wind drag coefficient	c_d	0.5
Air density (kg/m^3)	ρ	1.250
Efficiency of differential	η_{dif}	0.980
Differential Gear Ratio	G_r	4:1
Maximum vehicle speed (km/h)	-	120.0

Based on the vehicle data, a simplified vehicle dynamics model is established, following the procedure described in [21], for the purpose of estimating the continuous and peak output power ratings of the drivetrain, where the NEDC is considered as a reference. The required output power over the NEDC, together with the acceleration and curb-climbing requirements, would lead to determining the design specification of the drivetrain's traction machines.

The interactions of the vehicle with the surrounding air and the road are considered in the vehicle dynamics model to calculate the various types of resistance forces acting on the vehicle during driving. These resistance forces include the vehicle's inertia (F_i), the rolling resistance (F_{roll}) and the air drag force (F_{air}). Ultimately, this enables to calculate the total tractive force (F_t) required from the vehicle's drivetrain to overcome the drive resistance, as expressed by (2.1). Note that the influence of slip between the tyre and the road is not considered in this steady-state vehicle dynamics equation. However, based on simulations conducted on a more complex vehicle dynamic model that considers the effect of tyre slip, [53] it has been identified that, compared to the model that neglects tyre slip, the total tractive power required from the machines was increased by only 1% for a front-rear distributed traction system, such as the one considered in this chapter. Whereas, in the case of a concentrated traction system (where only one machine is

employed) the increase in the required tractive power was 9.5%, which is non-negligible. This outcome highlights the benefits of employing a distributed traction system and its impact on the traction machine sizing and cost.

$$F_t = F_i + F_{roll} + F_{air} \qquad (2.1)$$

According to Newton's second law of motion, a mass under acceleration, will resist its acceleration with a force of inertia (F_i) described by (2.2).

$$F_i = m \cdot \frac{dv}{dt} \qquad (2.2)$$

where m is the vehicle's mass, v and dv/dt are the vehicle's velocity and acceleration, respectively, which are defined based on the velocity profile of the NEDC shown in Figure 2.1.

The rolling resistance, expressed in (2.3), is proportional to the rolling resistance coefficient (k_r). The coefficient (k_r) is a function of the normal force that is applied on the tyre and the deformation of the tyre (which is dependent on the vehicle's velocity and the tyre's structure) [21].

$$F_{roll} = m \cdot g \cdot k_r \qquad (2.3)$$

where g is the gravitational acceleration.

The air drag, described by (2.4), is proportional to the product of the drag coefficient (c_d) and the vehicle's frontal area (A), the mass density of air (ρ) and the square of the vehicle's velocity (v) (viz., the wind speed is neglected [21]).

$$F_{air} = \frac{1}{2} \cdot c_d \cdot A \cdot \rho \cdot v^2 \qquad (2.4)$$

Now that the total tractive force (F_t) required from the vehicle's drivetrain is obtained via (2.1)-(2.4), the torque (T_w) and angular speed (ω_w) of the wheel can be calculated via (2.5) and (2.6), respectively.

$$T_w = F_t \cdot r_w \qquad (2.5)$$

$$\omega_w = \frac{v}{r_w} \qquad (2.6)$$

where r_w is the radius of the wheel.

Accordingly, the total torque (T_m) and angular speed (ω_m) of the two traction machines can be obtained from the torque and angular speed of the wheel, considering the gear ratio (G_r) and efficiency (η_{dif}) of the differential, as shown by (2.7) and (2.8) respectively.

$$T_m = \frac{T_w}{G_r \cdot \eta_{dif}} \ , \quad for \ T_w > 0$$

$$(2.7)$$

$$T_m = \frac{T_w \cdot \eta_{dif}}{G_r} \ , \quad for \ T_w < 0$$

$$\omega_m = \omega_w \cdot G_r \qquad (2.8)$$

Having defined the resistive forces of the vehicle dynamics model, the NEDC velocity profile (shown in Figure 2.1) is used as the model input, in order to calculate the angular speed and the required torque and power for each traction motor over the NEDC as shown in Figure 2.3. The calculation assumes that the traction torque is shared equally between the front and rear motors of the vehicle's distributed drivetrain.

Based on the velocity profile of the NEDC and the vehicle's dynamic model, the required torque and power over the NEDC can be calculated. These results will be used to determine the peak and continuous torque and power ratings of the drivetrain's traction machines. As can be observed from Figure 2.3, the maximum traction torque required over the NEDC is ~35 N·m. The steady-state peak and continuous power at the maximum NEDC speed of 120 km/h, indicated as P_{pk} and P_c in Figure 2.3, is ~6.5 kW and ~4.1 kW respectively.
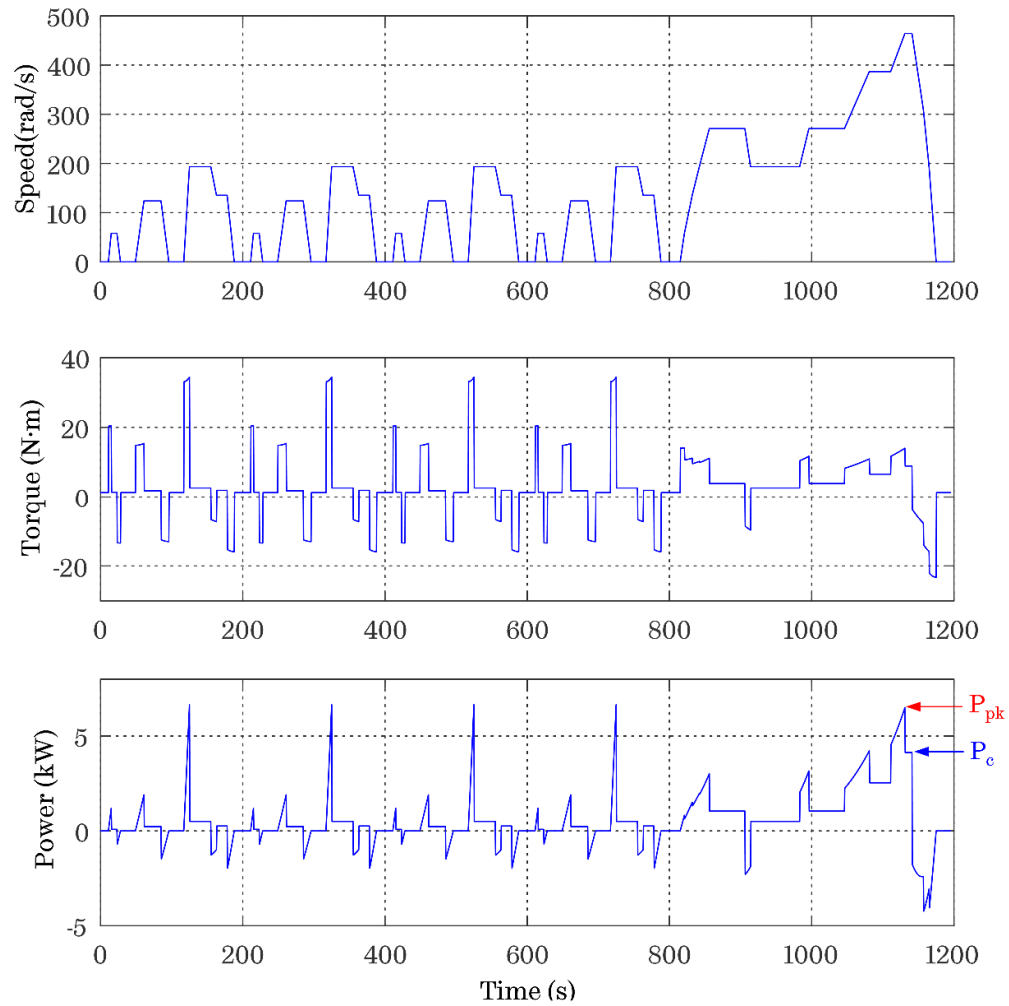
Figure 2.3. Torque-speed envelope requirement for one motor.

The maximum motor operating speed is defined based on the maximum cruise speed over the NEDC (i.e., 120 km/h), through equations (2.6) and (2.8). An extra margin of 2% is considered to account for the effect of tyre slip, resulting in the maximum cruise speed of 4500 r/min. The peak and continuous power of the traction machines, at their maximum operating speed, is thus defined by the derived peak and continuous steady-state power required from the drivetrain at the maximum NEDC speed (as indicated in Figure 2.3 by P_{pk} and P_c, respectively). To factor in any potential losses due to variations in the vehicle dynamics, such as higher rolling resistance and/or aerodynamic air drag, and to facilitate a degree of power redundancy, an additional 7.5%, and 15% margin is considered when defining the peak and continuous power ratings of the traction machines, respectively. The

resulting peak and continuous power ratings of each traction machine at the maximum operating speed amount to 7.0 and 4.75 kW, respectively. Accordingly, the peak (T_{ms}) and continuous (T_{cms}) torque at the maximum cruise speed (ω_{ms}) are defined by the ratio of power over the angular speed. These operating points are plotted on the torque-speed plane overlaid by iso-power lines, as illustrated in Figure 2.4, which will assist in creating the operating envelopes of the traction machines.
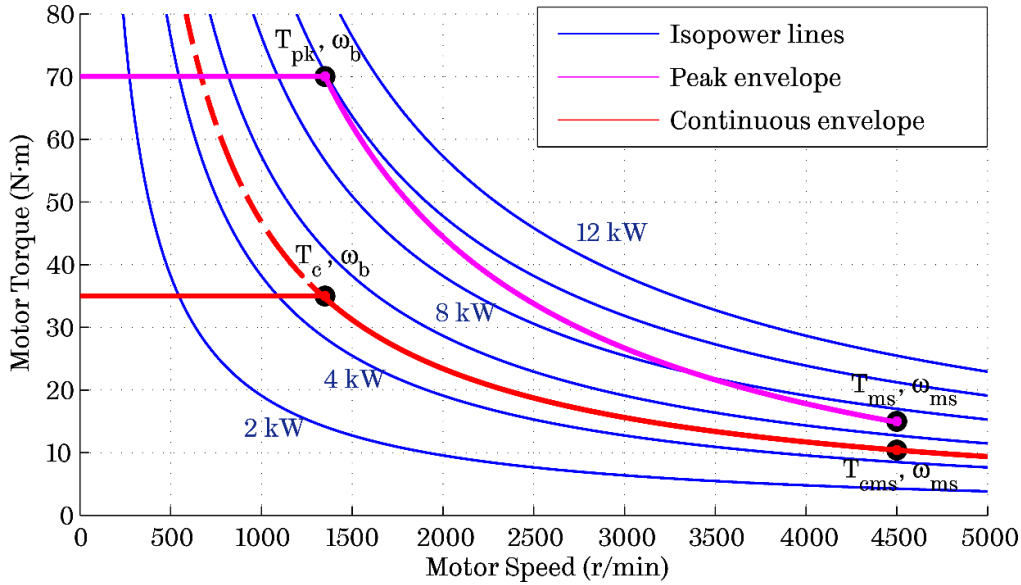
Figure 2.4. Derivation of the torque-speed envelope requirements for one motor.

The ratio of the continuous steady-state power to the maximum torque required over the NEDC determines the base speed of the traction machines (viz., frequently expressed as rated speed). Again, a 2% margin is considered to account for the effect of tyre slip, resulting in the base speed of 1350 r/min. The process of determining the base speed can be visualised from the plot of Figure 2.4 by observing the intersection of the maximum NEDC torque with the 5kW iso-power line. The projection of the intersection point to the x axis leads to the base speed. The continuous torque of the traction machines (T_c) at and below the base speed (ω_b) is set equal to the peak torque required over the NEDC. This would ensure continuous operation over the NEDC without the risk of violating the traction machine's thermal limit. As can be seen from Figure 2.4 the continuous operating envelope of the traction machines is formed, with the constant torque region below

the based speed, and the constant power region (field-weakening region) above the base speed.

The peak torque required over the NEDC (i.e., 35 N·m), however, is insufficient in providing drive-away acceleration or curb-climbing capability to the vehicle. Therefore, to account for that, the peak (or overload) torque of the traction machines at and below the base speed (T_{pk}) was set to the double of the maximum torque required over the NEDC (T_c), according to the provided specification of P-MOB project. The peak power rating of each traction machine is, thus, defined by the product of the peak torque and the base angular speed, amounting to 9.9 kW. This operating point (T_{pk}, ω_b) is plotted on the torque-speed plane of Figure 2.4, and enables the formation of the peak operating envelope of the traction machines.

A transient calculation of the vehicle's aerodynamics equation (2.1) with a torque contribution of 70 N·m from each traction motor was performed to identify the drive-away capability of the two-seater micro-sized vehicle. Please note that a total mass of 680 kg has been used in the model, assuming two passengers weighing 90 kg each. Under this scenario, it has been found that with the selected peak torque of 70 N·m the vehicle achieves 0-60 km/h in 6.6 sec and 0-100 km/h in 8.6 sec. Given that the traction machine size and inverter VA rating scale with the peak torque of the drivetrain, any additional increase in the peak torque will result into a cost increase of the electric traction drive, where the two form a trade-off.

The continuous and peak torque-speed envelopes for one traction machine sharing 50% of the traction torque, overlaid with the torque-speed trajectory over the NEDC, are illustrated in Figure 2.5. The continuous and peak torque-speed envelopes are adequately defined by the previously derived continuous and peak torque operating points at the base (T_c / T_{pk}, ω_b) and maximum (T_{cms} / T_{ms}, ω_{ms}) speed, respectively. These operating points are indicated in the plot of Figure 2.5, which also includes the torque-speed trajectory of one traction machine over the NEDC for comparative purposes. As it can be observed, the majority of the torque-speed trajectory over the NEDC is covered by the continuous torque-speed envelope, thus implying that the machine could continuously operate over the NEDC without exceeding its thermal limit. More detailed requirements pertaining

to the design of the traction machine can be acquired from Figure 2.5 and they are summarised together with other machine design specification in Table 2.2.
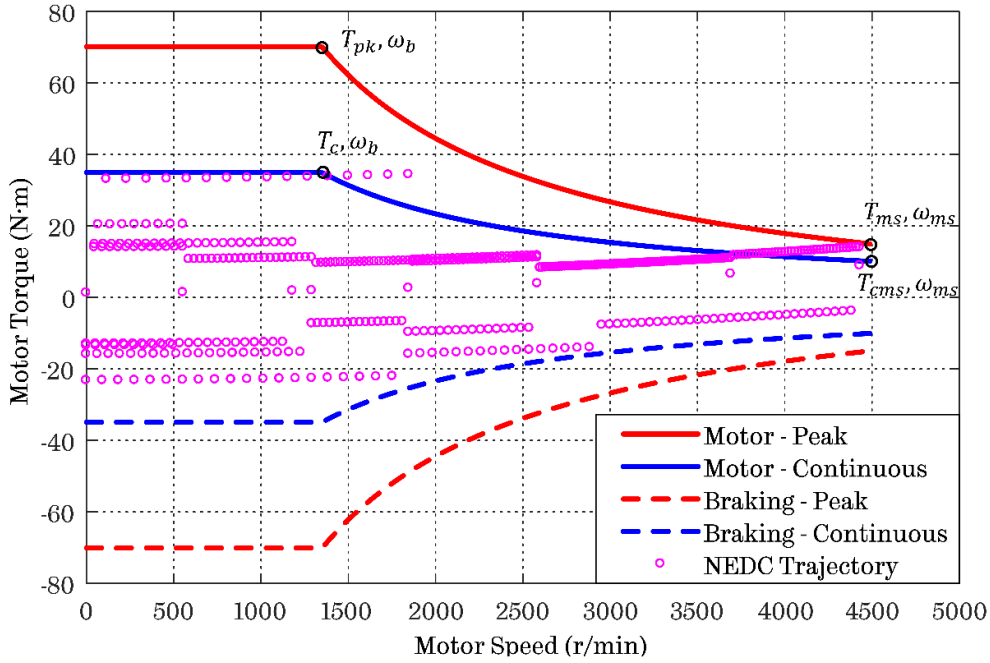
Figure 2.5. Torque-speed envelope requirement for one motor.

Table 2.2. Motor design specification

Parameter (Unit)	Symbol	Value
Base speed (r/min)	ω_b	1350
Maximum cruise speed (r/min)	ω_{ms}	4500
Maximum speed (r/min)	ω_{max}	5050
Peak torque below and at base speed (N·m) for 120s	T_{pk}	70.0
Continuous torque below and at base speed (N·m)	T_c	35.0
Peak torque at maximum cruise speed (N·m)	T_{ms}	15.0
Peak power (kW)	P_{pk}	9.9
Peak power at maximum cruise speed (kW)	P_{ms}	7.0
Continuous power below and at base speed (kW)	P_c	5.0
Continuous power at maximum cruise speed (kW)	P_{cms}	4.7
Nominal DC link voltage (V)	V_{dc}	120
Maximum permissible line-to-line voltage (V)	E_{max}	< 250 (for safety)
Ambient Temperature (ºC)	T_{amb}	45.0
Cooling type	-	Air-cooled

2.1.2 Energy consumption distribution over the NEDC

Since traction applications are characterised by highly dynamic torque-speed combinations, which consequently have a significant impact on motor efficiency, it is important to analyse and understand how the energy consumption of a driving cycle is distributed within the torque-speed operating range of the traction machine. Without loss of generality, this chapter investigates the energy consumption over the NEDC, since (at the time of conducting/writing this work) it has formed the certification standard for light-duty vehicles in Europe. However, we acknowledge that standardised driving cycles, such as the NEDC, have been increasingly criticised as being unable to truly emulate real-world driving conditions leading to underestimation of power and energy demand during cruise, acceleration or stop-and-go activities of the vehicle [54]. More specifically, the aggressiveness of the driver in accelerating or decelerating the vehicle which is conducive to increased energy consumption [55]. Recent studies concluded that there is a lack of a single, widely accepted driving cycle in the literature.

As a result, research is performed to model and develop more realistic driving profiles from real-world collected data [45], [54], [56], [57]. Based on this notion is the development of the Worldwide Harmonised Light Vehicles Test Procedure (WLTP cycle) by the members of the 1998 UN/ECE (i.e., Europe, USA, China, Japan, Russia, India, and more) [7], which is currently approaching the completion of its final phases. The WLTP cycle aims to more realistically represent the actual driving characteristics (spanning from urban to motorway driving) of a vehicle/driver worldwide, and thus comprising a universally accepted solution to the issues pertaining to vehicle testing and certification that currently characterise the automotive industry. It should be noted that, in this chapter, NEDC is only used as a reference cycle, against which the machine design optimisation should be performed. The subsequent analysis and described techniques can be applied to any given driving cycle.

Based on the plots of Figure 2.3, for a given time instant, $t = t_i$, the corresponding angular speed, torque, power and energy consumption are $\omega_m(t_i)$, $T_m(t_i)$, $P_m(t_i)$ and $\Delta t_i P_m(t_i)$, where Δt_i denotes the interval of time over which

$\omega_m(t_i)$ and $T_m(t_i)$, are assumed to be constant. Therefore, the energy consumption for each motor of the drivetrain can be calculated for any time instant during the NEDC, and plotted as a function of the torque and speed, as illustrated in Figure 2.6. It is evident that the energy consumption is distributed to hundreds of operating points over the torque and speed range. However, one can observe from Figure 2.6, that there exist six operating points at which the energy consumption is significantly higher compared to the remaining operating points of the driving cycle.
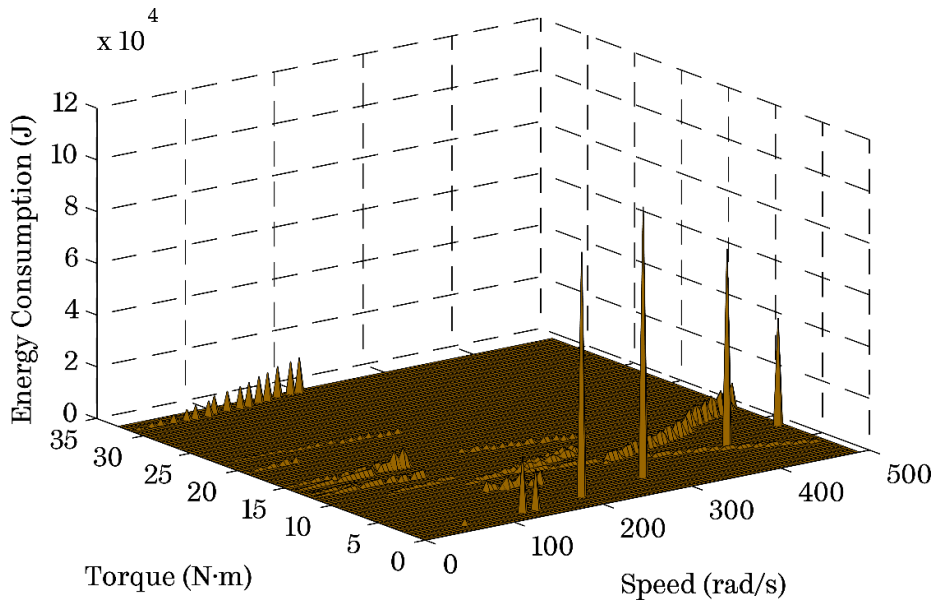
Figure 2.6. Energy consumption distribution over the NEDC plotted as a function of torque and speed.

These operating points, associated with the six higher peaks of Figure 2.6, correspond to the constant speed operations of the driving cycle where the time duration is relatively long, and the torque is relatively low, as also indicated by Figure 2.3. Therefore, the traction motor's efficiency over these operating points is of key importance. Figure 2.7 shows the energy consumption distribution over the torque-speed range when these six operating points are excluded. Since the energy levels at these widely distributed operating points are relatively low, it is possible to lump a cluster of operating points together according to the energy distribution pattern within the torque-speed range, and thus calculate their equivalent "*energy centre of gravity*".
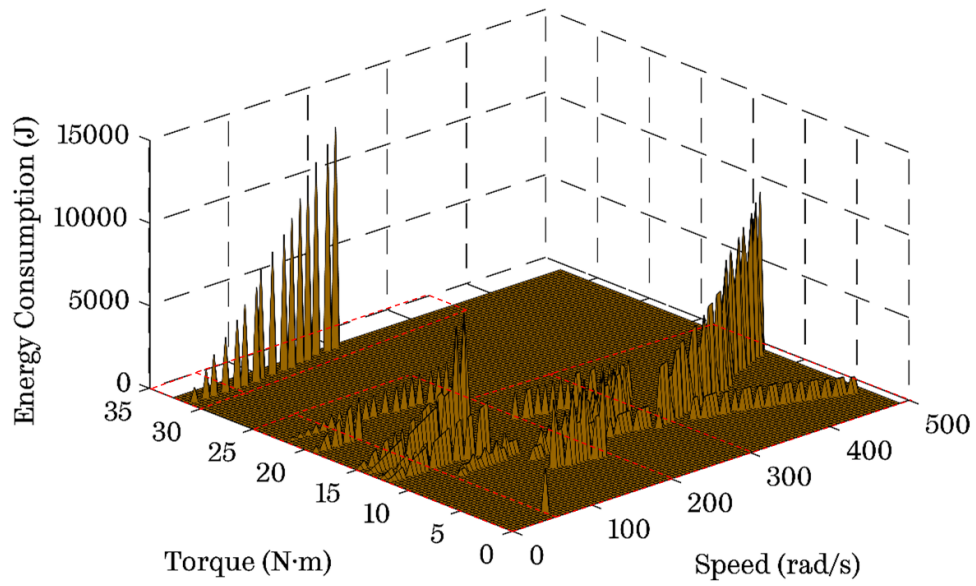
Figure 2.7. Energy consumption distribution over the NEDC, after excluding the six highest energy consumption points. Please observe the red dashed lines dividing the torque-speed plane into the selected sub-regions.

Without loss of generality, the torque-speed region in Figure 2.7 is divided into six sub-regions as shown in Table 2.3. For each sub-region, the energy consumption is represented by the energy sum of

$$E_i = \sum_{j=1,2\ldots}^{N_i} E_{ij} \tag{2.9}$$

centred at ω_{mc_i} and T_{mc_i} given by,

$$\omega_{mc_i} = \frac{1}{E_i} \sum_{j=1,2\ldots}^{N_i} E_{ij}\, \omega_{m_{ij}} \tag{2.10}$$

$$T_{mc_i} = \frac{1}{E_i} \sum_{j=1,2\ldots}^{N_i} E_{ij}\, T_{m_{ij}} \tag{2.11}$$

where N_i, is the number of operating points in the ith region.

Table 2.3. Torque and speed range of six sub-regions

Region number	T_m (N·m)	ω_m (rad/s)
Region 1	$30 - 35$	$0 - 50$
Region 2	$30 - 35$	$50 - 250$
Region 3	$0 - 25$	$0 - 50$
Region 4	$0 - 25$	$50 - 200$
Region 5	$0 - 20$	$200 - 300$
Region 6	$0 - 20$	$300 - 500$

The total twelve operating points and their corresponding energy consumption are shown in Table 2.4. The first six operating points are those previously shown in Figure 2.6, at which the energy level is relatively high. The remaining six operating points represent the equivalent energy consumption for the six torque-speed sub-regions. It is evident, from Table 2.4, that the six high-energy consumption operating points, together with other equivalent operating points, with torque below 17 N·m (i.e. approximately half of the continuous torque, T_c), account for 89.56 % of the total energy consumption over the NEDC. This indicates that the energy efficiency during low-load operation, particularly at the middle-to-high speed operating range, is critical for the enhancement of driving range or the reduction of battery capacity [21], [47]. Thus, the traction machine optimization should consider these operating points.

Table 2.4. Equivalent energy consumption points over the NEDC

ω_m (rad/s)	T_m (N.m)	E_m (kJ)	Normalized to total energy	Percentage of total energy
269.1	3.784	104.4	0.0982	
190.2	2.408	94.41	0.0888	
385.1	6.536	76.11	0.0716	
459.3	8.600	41.27	0.0388	
120.6	1.720	21.39	0.0201	**< 17 N.m**
134.6	1.720	15.49	0.0146	**89.56 %**
32.10	15.92	36.91	0.0347	
119.4	12.96	203.7	0.1917	
248.6	10.89	122.2	0.1150	
387.5	10.56	235.8	0.2219	
33.88	33.03	8.006	0.0075	**>17 N.m**
139.0	33.64	103.0	0.0969	**10.44 %**

Based on the preceding analysis, it follows that the vehicle's energy consumption over the NEDC can be represented by twelve operating points. This would significantly reduce the number of calculations for the evaluation of the motor's energy efficiency during a design optimisation process [particularly when Finite Element Analysis (FEA) is employed].

2.1.3 Validation of the 12 energy consumption representative operating points

To validate the above representation, the energy loss (*EL*) over the NEDC is calculated according to (2.12) for all the operating points in Figure 2.3 using a reference efficiency map for the traction motor topology under investigation. The design specification and corresponding efficiency map of the FSCW SPM motor are shown in Table 2.2 and Figure 2.8, respectively.

$$EL = \sum_{j=1,2\ldots}^{N} \omega_m(t_i) \cdot T_m(t_i) \cdot \Delta t_i \cdot \frac{(1-\eta_i)}{\eta_i} \qquad (2.12)$$

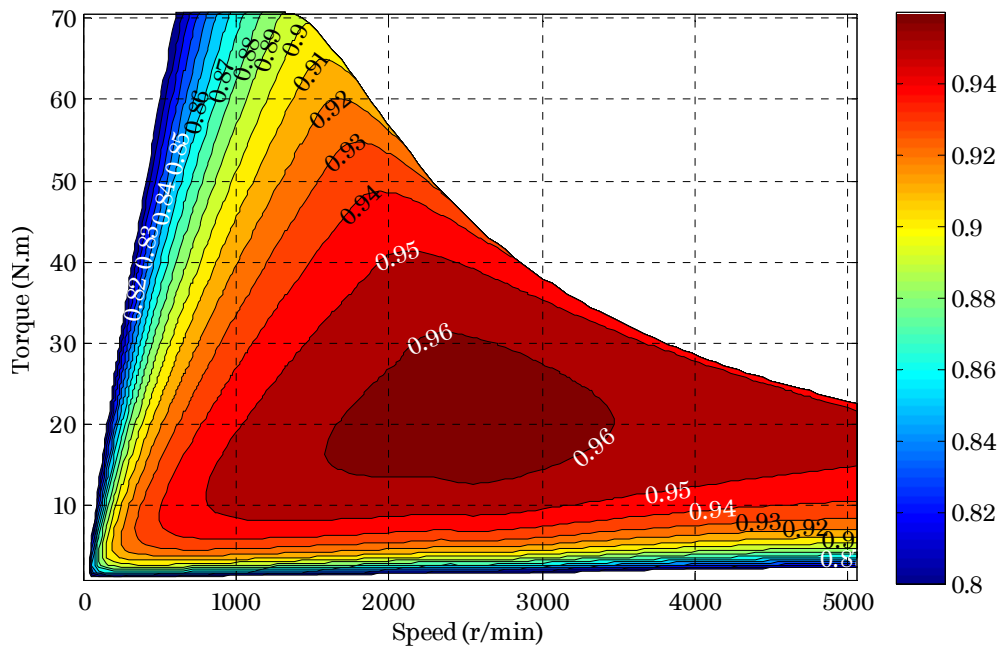where η_i is the motor's efficiency at $\omega_m(t_i)$ and $T_m(t_i)$ on the efficiency map.

Figure 2.8. Predicted efficiency map (in per unit values) of a reference FSCW SPM traction machine.

The energy loss over all the operating points of the NEDC is compared to the energy loss calculated using the twelve representative operating points of Table 2.4 and the same efficiency map. The result is shown in Table 2.5.

Table 2.5. Motor energy loss comparison obtained using the 12 representative and all NEDC operating points

Parameter	Value
Energy loss over all points in NEDC cycle (kJ)	88.35
Energy loss over the 12 points of Table 2.4 (kJ)	86.55
Percentage difference	2.1 %

As it can be observed, the 12 operating points listed in Table 2.4 can adequately provide a good representation of the total energy loss of the motor over the NEDC cycle calculated by (2.13).

$$EL = \sum_{j=1,2\ldots}^{12} E_{n_j} \cdot \frac{(1 - \eta_i)}{\eta_i} \qquad (2.13)$$

where E_{n_j} and η_j is respectively the energy consumption and efficiency, at the jth operating point. Thus, the traction machine design optimisation over the NEDC can now be conducted against the twelve representative operating points.

2.1.4 Torque-speed plane segmentation principle

In order to derive the "*energy centre of gravity*" (i.e., representative) operating points, the torque-speed plane is divided into a number of sub-regions. The weighted means of the torque and speed of all energy consumption points within a sub-region result into an energy centre of gravity operating point (ω_{mc_i}, T_{mc_i}), which represents the energy intensity in that region [viz., the process described by equations (2.9) to (2.11)].

The number of torque and speed segments (i.e., the number of selected sub-regions) will influence the number and accuracy (or effectiveness) of the representative operating points. The effectiveness of the energy centre of gravity

points in representing the energy consumption of a particular driving cycle is reflected through energy loss calculations based on a predetermined efficiency map, representing the traction machine under consideration. The loss calculated from all operating points of the cycle is iteratively compared to that obtained from the representative points until the number (i.e., minimum) versus accuracy of the gravity operating points is optimised.

The selection of torque and speed segments strongly depends on the distribution of the driving cycle's energy consumption within the torque-speed range (e.g. energy more concentrated in specific regions or widely distributed across the torque-speed plane). However, since the accuracy of the gravity points is reflected through the use of a representative efficiency map, the shape of the map (i.e. loss distribution over the torque-speed range) will influence the division selection process in determining the gravity points. It is important to note that traction machines (and particularly PMSM traction machines – widely reported in the literature) are characterised by a distinctive efficiency map shape that does not drastically change through parametric design modifications. In other words, it can only be optimised, but not changed.

An already derived set of energy centre of gravity operating points will still accurately represent the driving cycle's energy consumption even if a different efficiency map of another design is used. In fact, when this was implemented by using two different representative efficiency maps, from SPM and IPM machine topologies, the deviation of the error in the cycle energy loss representation was in the vicinity of 1%, which in turn validates the above assertion. Thus, a representative efficiency map for the selected machine technology [e.g., PMSM, induction machine (IM), switched reluctance machine (SRM)] should be employed in this process.

As indicated by the shape of the efficiency map (viz. Figure 2.8), the efficiency variation is more significant when the speed or torque is low. In these regions, more segments or representative points are required for increased accuracy. The torque-speed plane division can be implemented in the form of a regular or irregular grid, with the latter achieving the same accuracy with a reduced number of energy

centre of gravity operating points compared with the former. It is important to note the trade-off between computational cost (i.e., the number of gravity points) and accuracy since this cycle quantification process aims in representing the cycle's energy consumption with a drastically reduced number of operating points while maintaining the cycle characteristics.

In the case of the NEDC analysis, described in §2.1.2, the majority of most energy intensive cycle operating points of Figure 2.7 are located in regions where the efficiency variation is small. Thus, a relatively low number of torque-speed segments (i.e. six sub-regions) are required to represent the energy loss of the driving cycle accurately. To illustrate the utility of the proposed technique to other legislative driving cycles (e.g., ARTEMIS, FTP75, US 06 etc.), the previously described mathematical model was employed to analyse their energy consumption distribution. Table 2.6 contains the results obtained from the analysis of the considered driving cycles.

Table 2.6. Energy distribution analysis for various legislative driving cycles (using irregular grid segmentation)

Driving Cycle	Total No. of points/ Cycle duration (s)	Non-zero energy points	Representative points	Error in cycle loss representation	Potential computational cost savings
FTP75	1372	833	56	-5.64 %	93.28 %
Artemis Urban	993	581	45	-5.78 %	95.47 %
Artemis Rural	1082	706	45	-3.57 %	93.63 %
Artemis Motorway	1068	619	17	-5.60 %	97.25 %
US 06	600	452	23	-5.05 %	94.91 %
US Motorway	765	461	18	-5.13 %	95.66 %

The proposed technique also extends to other driving cycles where the torque and speed variation can be more aggressive compared to the moderate NEDC. As indicated by Table 2.6, there is a substantial reduction from the original driving

cycle operating points to a finite number of representative (energy centre of gravity) operating points ranging from ~10 to 60, depending on the energy consumption distribution pattern of the investigated cycle. This results in a reduction of at least 90% in computational cost. The negative percentage of the error in the cycle energy loss representation in Table 2.6 indicates an underestimation compared with the loss calculated by using all of the cycle's operating points.

2.2 Design technique for EV traction machines

The electric vehicle weight and cost are fundamentally related to the driving range or the required battery capacity, which in turn are significantly influenced by the motor energy efficiency. It is therefore indispensable to emphasise the significance of optimising a traction machine over its corresponding driving cycle for maximum energy efficiency or minimum energy loss.

Optimisation against the rated power point (i.e. conventional design method) will not necessarily yield the maximum attainable efficiency over the driving cycle. The validity of this assertion can be understood by observing the distribution of the twelve representative points of the NEDC under the motor's peak and continuous torque-speed envelope requirements, as shown in Figure 2.9. Note that the energy weight (i.e., a specific amount of energy consumed over the driving cycle) for each of the representative points of Figure 2.9 is represented by its equivalent marker diameter, which is normalised to the operating point with the maximum energy weight over the NEDC.

It can be observed, from Figure 2.9, that there is a mismatch between the locations of the most energy-intensive driving cycle operating points and the rated and/or peak torque operating points, which are mainly utilised for short transients when hill climbing or acceleration is required during driving. The high energy consumption over the NEDC, as can be verified from Table 2.4, is dominated by low torque, and particularly middle-to-high speed operating points where the time duration is longer. It should be noted that this trend is not only observed in the NEDC, but also in other typical legislative driving cycles used in the automotive industry, such as the CADC and FTP72 [47].
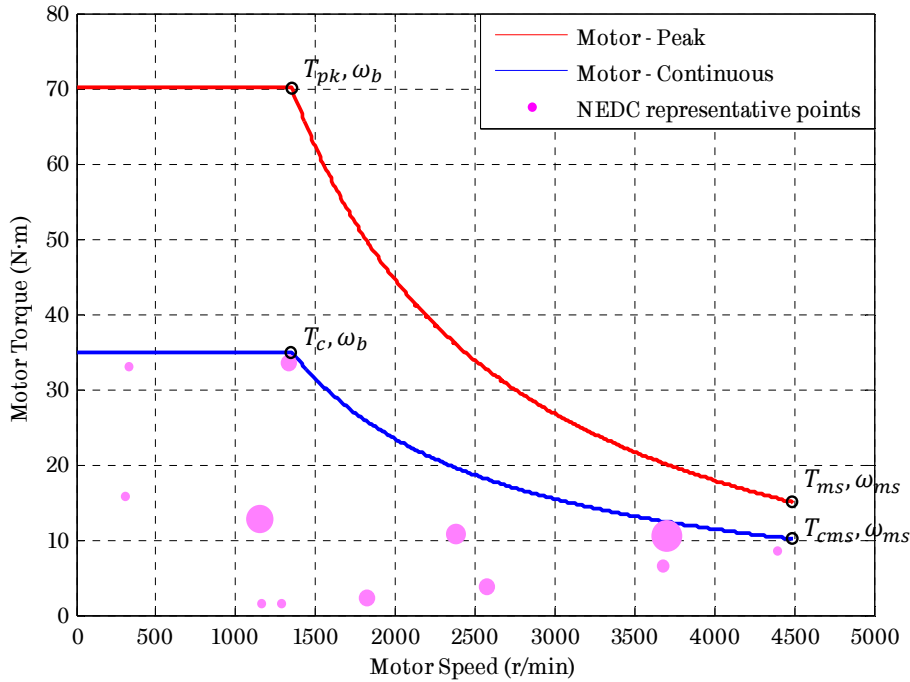
Figure 2.9. Distribution of twelve NEDC points under the peak and continuous torque-speed envelopes of the investigated traction motor.

Hence, a trade-off is imposed on the selection of a suitable optimisation strategy. To demonstrate the difference between optimisation at the rated point and over the NEDC cycle, two design case studies were considered, and their corresponding design constraints and loss components distribution will be described in the following sections of this chapter.

2.2.1 Traction machine optimisation against driving cycle

When selecting the most suitable machine topology, the choice of the best candidate, which meets the desired objectives while satisfying the design constraints, ultimately depends on a careful evaluation of the performance requirements related to the particular application under consideration.

In the case of the application investigated in this chapter, the maximum speed requirement for the traction motors of the micro-sized vehicle is relatively low (i.e. 4500 rpm), resulting from a single stage reduction gear ratio (i.e. 1:4) and the employment of a distributed traction drive (front and rear). FSCW SPM is well known to exhibit high torque and power density, high efficiency, excellent field

weakening capability, inherently low cogging torque, reduced risk of an interphase fault, and distinctive advantages in manufacturability (due to the use of concentrated coils – encircling a single tooth) [58]–[60]. All of these attributes are highly desirable in EV traction applications. The disadvantages of FSCW SPM are the lack of reluctance torque as well as the induced eddy current losses in the rotor magnets [48], which significantly scale at higher rotating speeds. However, since the maximum cruise speed in this particular application is relatively low (i.e. 4500 rpm), the eddy current losses in the rotor magnets are significantly reduced by simple segmentation of the magnets (at the expense of a small cost increase in manufacturing).

2.2.1.1 Leading design parameters and EV traction machine design constraints

Without loss of generality, two three-phase FSCW SPM motors were optimised with respect to a set of leading design parameters [59] including, the pole-slot number combination, the magnet pole arc (α_m) to pole-pitch ratio, the tooth width (T_w), the back iron width (H_j), the magnet thickness (H_m) and the split ratio (i.e., the ratio of the rotor diameter to the outer stator diameter - R_m/R_e), as illustrated in the schematic of Figure 2.10. The coil turn number (TN) and axial stack length (L_a) were additional optimising parameters. The airgap length (G) was assumed fixed at 1mm to ensure sufficient margin for the manufacturing tolerances and the carbon-fibre banding layer thickness, which is necessary to protect and retain the magnets in place at high rotating speeds.

The optimisation was conducted through the use of both analytical and Finite Element Analysis (FEA) methods since the SPM topology exhibits less complex field distribution. However, when optimising a nonlinear machine topology, such as an interior PM machine (IPMSM), the use of FEA is considered mandatory due to the inherent salient structure. One machine, denoted as "Design I" was optimised over the NEDC cycle and the other denoted as "Design II", was optimised against the rated operating point. The optimisation target in both design cases was the maximum attainable efficiency under a given set of electrical, thermal and volumetric constraints. In order to acquire the optimal machine

designs, several design constraints, which derive from the defined machine design specification listed in Table 2.2, should be satisfied during the optimisation process of the leading design parameters (to deliver the defined performance requirements).
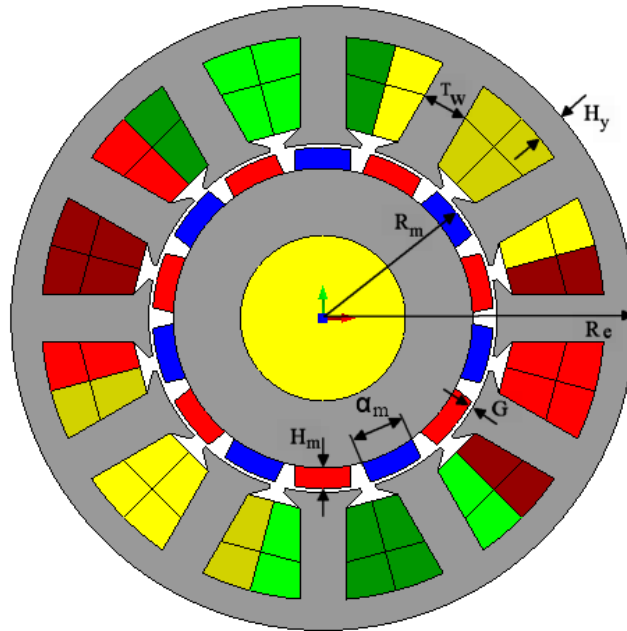

Figure 2.10. Key design geometrical parameters of FSCW SPM motor.

The required peak torque, at both base (T_{pk}, ω_b), and maximum cruise speed (T_{ms}, ω_{ms}), should be obtained without exceeding the inverter VA rating. Further, an important aspect pertaining to the design of PM traction machines, which are required to deliver constant power over a wide speed range, is their field-weakening (FW) capability that is, in turn, largely influenced by the ratio of the permanent magnet flux linkage (ψ_m) to the d-axis inductance (L_d) [58], [61]. Thus, the respective maximum and minimum limits of the d-axis inductance (L_d) for a given number of pole-pairs (p) can be determined against the machine specifications shown in Table 2.2, ensuring the required performance targets [59]. A constant power speed ratio of 3.33 must be achieved within the inverter VA rating for the investigated application.

The back-EMF induced at the maximum speed (ω_{max}) of the SPM machines must be limited below the maximum permissible line-to-line peak voltage (E_{max})

for safety, as the permanent magnet (PM) field cannot be turned off during an intermittent inverter fault.

$$E = p \cdot \psi_m \cdot \omega_{max} \cdot \frac{2\pi}{60} \leq \frac{E_{max}}{\sqrt{3}} \qquad \text{or} \qquad p \cdot \psi_m \leq \frac{E_{max}}{\sqrt{3} \cdot \omega_{max} \cdot \frac{2\pi}{60}} \qquad (2.14)$$

where p is the pole pair number and ψ_m is the no-load magnet flux linkage. The electromagnetic torque (T) of an SPM machine, assuming zero magnetic saliency (which is typically the case), is given by:

$$T = \frac{3}{2} \cdot p \cdot \psi_m \cdot I_q \qquad (2.15)$$

where I_q is the q-axis current of the machine. Inspection of (2.14) and (2.15) indicates a trade-off on the demand of $p \cdot \psi_m$ – where a large value is desired for high torque production, and in turn, high efficiency, while a relatively small value is preferable to ensure a low induced back-EMF at the maximum speed for safety.

To achieve the defined peak torque requirement (T_{pk}), the required maximum motor phase current (I_{max}) must satisfy the following condition, which can be derived using (2.14) and (2.15):

$$T = \frac{3}{2} \cdot p \cdot \psi_m \cdot I_{max} \geq T_{pk} \qquad \text{or} \qquad I_{max} \geq \frac{2}{\sqrt{3}} \cdot \frac{\omega_{max} \cdot 2\pi/60 \cdot T_{pk}}{E_{max}} \qquad (2.16)$$

The minimum inverter VA rating can, therefore, be defined as shown in (2.17), based on the maximum required peak phase current (I_{max}) derived in (2.16) and the DC-link voltage (V_{dc}), which in turn defines the maximum achievable peak phase voltage ($V_{max} = V_{dc}/\sqrt{3}$).

$$\frac{3}{2} \cdot V_m \cdot I_m \geq \frac{3}{2} \cdot \frac{V_{dc}}{\sqrt{3}} \cdot I_{max} = \frac{V_{dc}}{E_{max}} \cdot \omega_{max} \cdot \frac{2\pi}{60} \cdot T_{pk} \qquad (2.17)$$

To meet the required peak torque (T_{pk}) at base speed (ω_b) within the inverter VA rating, the subsequent voltage constraint, described by (2.18), must be satisfied:

$$\left(p \cdot \omega_b \cdot \frac{2\pi}{60} \cdot I_{max} \cdot L_d \right)^2 + \left(p \cdot \omega_b \cdot \frac{2\pi}{60} \cdot \psi_m + I_{max} \cdot R_{ph} \right)^2 \leq V_m^2 \qquad (2.18)$$

This condition, in turn, introduces a maximum limit on L_d, i.e. $L_{d_{max}}$, which, by neglecting the influence of phase resistance (R_{ph}), is described by (2.19).

$$L_{d_{max}} = \frac{\sqrt{V_m^2 - \left(\frac{E_{max}}{\sqrt{3}} \cdot \frac{\omega_b}{\omega_{max}} \right)^2}}{p \cdot \omega_b \cdot \frac{2\pi}{60} \cdot I_{max}} \qquad (2.19)$$

Likewise, to meet the peak torque requirement (T_{ms}) at the maximum cruise speed (ω_{ms}), within the inverter VA rating, the L_d of the traction machine must exceed a minimum inductance limit, i.e. $L_{d_{min}}$, which can be obtained by:

$$I_{q_{ms}} = \frac{2}{3} \cdot \frac{T_{ms}}{p \cdot \psi_m} \quad , \quad I_{d_{ms}} = \sqrt{I_{max}^2 - I_{q_{ms}}^2}$$

$$(2.20)$$

$$L_{d_{min}} = \frac{-\psi_m \cdot I_{d_{ms}} - \sqrt{\left(\psi_m \cdot I_{d_{ms}} \right)^2 - I_{max}^2 \cdot \left[\psi_m^2 - \left(\frac{V_m}{p \cdot \omega_{ms} \cdot 2\pi/60} \right)^2 \right]}}{I_{max}}$$

The variation of the minimum and maximum L_d with the pole pair number of an SPM machine, derived using (2.14)-(2.20) for the specification listed in Table 2.2, is illustrated in Figure 2.11. For a given number of pole pairs, the d-axis inductance of the FSCW SPM traction machines should reside within the defined maximum and minimum limits of L_d in order to deliver constant power over the required speed range, and meet the peak torque requirements at the base and maximum cruise speed within the minimum inverter VA rating. In the literature[58], [59], [61], superior field-weakening capability is frequently associated with the condition $L_d \geq \psi_m/I_{rated}$, where I_{rated} is the rated phase current of the machine. Based on this condition, it can be inferred that as the d-axis inductance approaches $L_{d_{max}}$, a lower current would be required during field weakening operation leading to a reduction in high-speed copper loss and, thus, to improved efficiency while delivering the required peak torque within the defined inverter VA

rating. It is important to note, though, that an increase in the d-axis inductance leads to a decrease of the power factor.
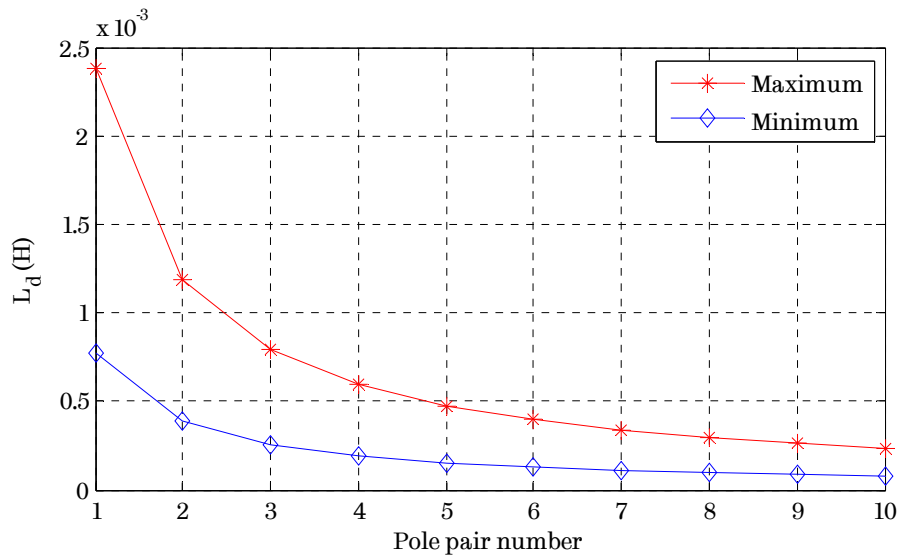

Figure 2.11. Minimum and maximum d-axis inductance variation with the pole pair number.

In addition to the electrical design constraints pertaining to the torque-speed range and FW requirements, the outer stator diameter for both designs is set to 150mm and the maximum axial (i.e. active) length is limited below 135mm (due to available space envelope restrictions in the vehicle imposed by the OEM as part of the project). Further, the machines should be enclosed by a finned aluminium cooling shell, which is air-cooled with no additional cooling fan. The maximum winding temperature limit is set to 150°C, according to the insulation class of the employed copper material. The magnets should be able to withstand the armature reaction field at both base and maximum cruise speeds, with peak torque, in order to avoid irreversible demagnetisation at the worst temperature condition. Moreover, the torque ripple should be limited to <5% of the peak torque to meet the requirements for EV traction applications.

An important point to note is the time required for the finite element calculations over the driving cycle. In fact, according to [50], several months would be required to obtain FE results for a design optimisation performed against the hundreds of operating points over the NEDC. However, this limitation is effectively

removed using the twelve representative operating points derived through the technique already presented in §2.1.2. The cross sections and flux density plots of the two optimised motors along with their dimensions and key design parameters are shown in Figure 2.12 and Table 2.7, respectively. The resulting trend of the leading design parameters will assist in the analysis of the energy loss distribution and efficiency of the two optimised designs, described in the following section.
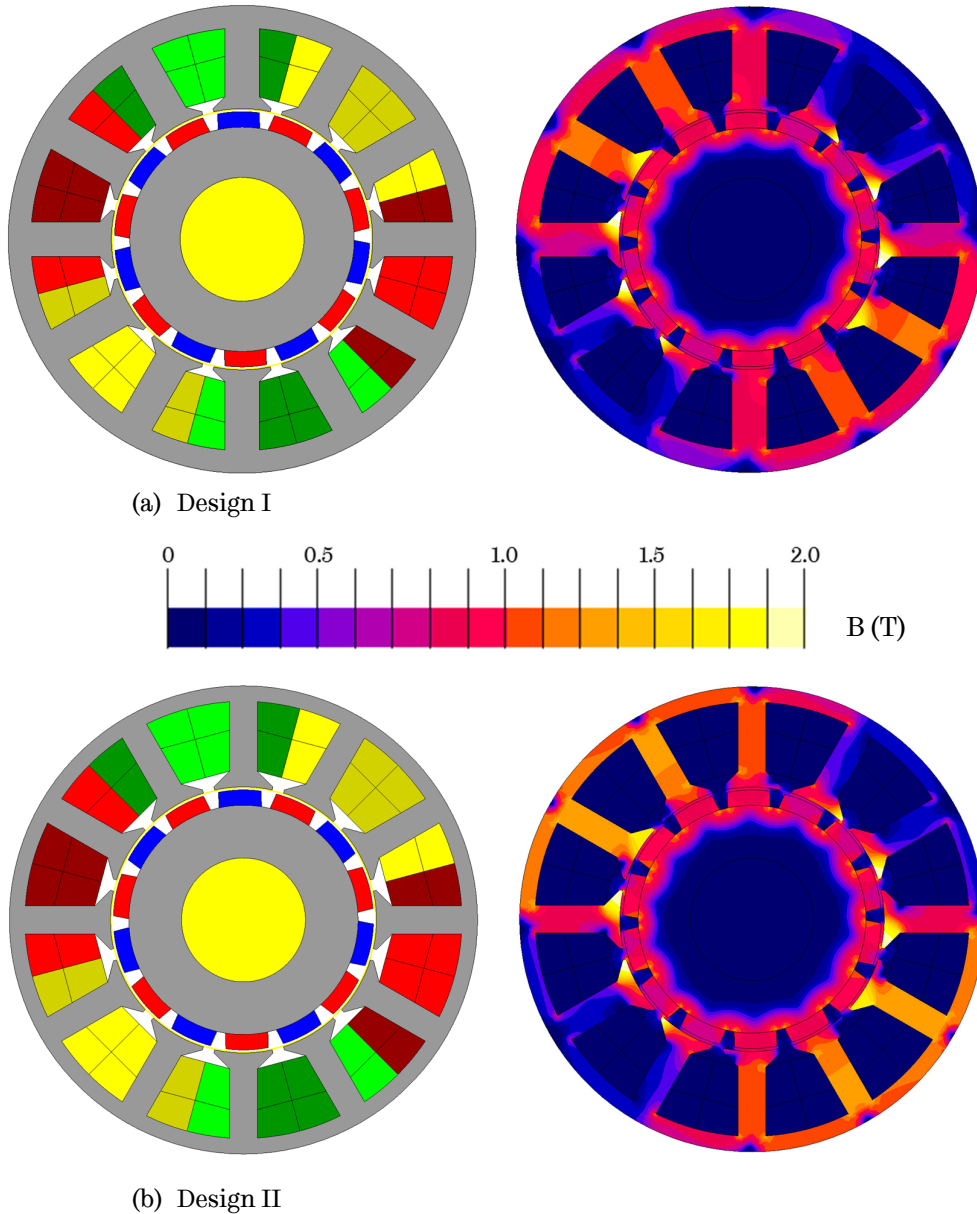

(a) Design I

(b) Design II

Figure 2.12. Cross sections and flux density plots (at T_c, ω_b) of optimized FSCW SPM traction motors.

Table 2.7. Optimised FSCW SPM Motors Data

Parameter (Unit)	Design I	Design II
Pole number	14	
Slot number	12	
Outside Diameter (mm)	150	
Stack Length (mm)	118	135
Split Ratio	0.55	0.56
Air gap Length (mm)	1.0	
Slot Opening (mm)	3.75	
Magnet Material	NdFeB (N35EH)	
Magnet mass (kg)	0.89	1.02
Number of turns per coil	8	7
Number of Phases	3 – Star Connected	
Number of coils per phase	4	
Fundamental Winding Factor	0.933	
Slot-fill factor	0.4	
Phase resistance at 120 ºC (mΩ)	20.8	14.4
Synchronous inductance (mH)	0.335	0.281
Flux Linkage per phase (mWb)	39.5	39.1
Torque Ripple at T_{pk}, ω_b	1.03%	1.15%
I_{rated} at T_c, ω_b (A,pk)	79.0	78.5
I_{pk} at T_{pk}, ω_b (A,pk)	166	171
J_{rms} at T_c, ω_b (A$_{rms}$/mm^2)	5.4	3.9
J_{rms} at T_{pk}, ω_b (A$_{rms}$/mm^2)	11.3	8.5
V_{dc} at T_{pk}, ω_b and T_{ms}, ω_{ms} (V,pk)	≤ 120	

2.2.2 Analysis and comparison of major loss components

The results summarised in the tables of this section were obtained through the utilisation of finite element analysis (FEA) tools for the two machines under investigation. A breakdown of the main loss components will assist in a quantitative understanding of the impact of the different optimisation strategies on design outcomes of electric machines targeted for traction applications.

The copper and iron losses for both traction motors were calculated against the rated and peak power operating points indicated in Figure 2.9, and are presented in Table 2.8 and Table 2.9 along with their corresponding efficiencies. The eddy current losses are not considered in the loss evaluation, since as already

explained, the magnets of the investigated FSCW SPM are axially and circumferentially segmented and, hence, the resulting eddy current losses are in turn negligible.

Table 2.8. Energy loss components and efficiency at the rated and peak power points at the base speed

Parameter (Unit)	Design I	Design II
Copper loss at T_c, ω_b (W)	198.0	133.0
Copper loss at T_{pk}, ω_b (W)	857.0	627.0
Iron loss at T_c, ω_b (W)	43.6	59.6
Iron loss at T_{pk}, ω_b (W)	64.5	78.2
Efficiency at T_c, ω_b	95.3 %	96.3 %
Efficiency at T_{pk}, ω_b	91.5 %	93.4 %

Table 2.9. Energy loss components and efficiency at the rated and peak power points at the maximum cruise speed

| Parameter (Unit)	Design I	Design II
Copper loss at T_{cms}, ω_{ms} (W)	136.8	124.5
Copper loss at T_{ms}, ω_{ms} (W)	184.6	153.3
Iron loss at T_{cms}, ω_{ms} (W)	90.4	127.5
Iron loss at T_{ms}, ω_{ms} (W)	93.9	130.4
Efficiency at T_{cms}, ω_{ms}	95.4 %	95.1 %
Efficiency at T_{ms}, ω_{ms}	96.2 %	96.1 %

Since copper loss is dominant under these operating conditions (i.e., T_{pk} or T_c at ω_b), it is evident that the machine (Design II) optimised against the rated point has ~1% higher efficiency compared with that (Design I) optimised against the NEDC. The efficiency difference grows up to ~1.8% as the torque increases towards its peak value. The optimisation for Design II was mainly made to minimise the copper losses in the windings. Therefore, the slot area was maximised whereas the saturation level in the stator teeth and back iron was designed in the vicinity of 1.4 – 1.5 T, under rated torque conditions, as it can be seen from Figure 2.12. In addition, Design II uses one less turn per coil compared with the motor optimised over NEDC for the purpose of further reducing the winding resistance, whereas its

axial length is 17mm longer in order to achieve the required torque production capability within the inverter current limit of 175A. Note that the winding resistance is proportional to the square of the coil turn number, but linearly proportional to the axial length. Consequently, the motor optimised against the rated point has a larger slot area with more conductors leading to a lower current density and thus lower copper loss. Conversely, (as expected) a higher iron loss occurs in this machine since its magnetic saturation levels are higher as also is its axial length/volume. However, the trend of loss distribution changes for the two motors once they are evaluated over the twelve NEDC operating points, since, as already explained the highest energy consumption predominantly occurs at low-load, middle-to-high speed operating conditions. The cycle energy efficiency and accumulated energy loss components are summarised in Table 2.10 for the two investigated designs.

Table 2.10. Loss components and energy efficiency over the twelve points of NEDC (with and without inverter losses)

| Parameter (Unit)	Design I	Design II
Copper loss (kJ)	24.6	19.3
Iron loss (kJ)	36.4	54.2
Inverter loss (kJ)	55.6	59.0
Efficiency without inverter loss	94.7 %	93.6 %
Efficiency with inverter loss	90.2 %	89.0 %

As can be seen from Table 2.10, for the case of FSCW SPM, the iron loss becomes the most dominant loss component during the NEDC, and therefore the motor optimised over the driving cycle achieves ~1.1% higher energy efficiency. The higher iron loss of Design II, evidently, penalises its energy efficiency over the driving cycle. It can be clearly observed that there is a trade-off between the static efficiency at the rated power operating point and the energy efficiency over the driving cycle. In order to further clarify this trade-off, the efficiency distribution of the two designs is illustrated in their corresponding efficiency maps overlaid with the previously derived twelve NEDC operating points of Table 2.4, as shown in Figure 2.13 (a) and (b) for Design I and II, respectively.
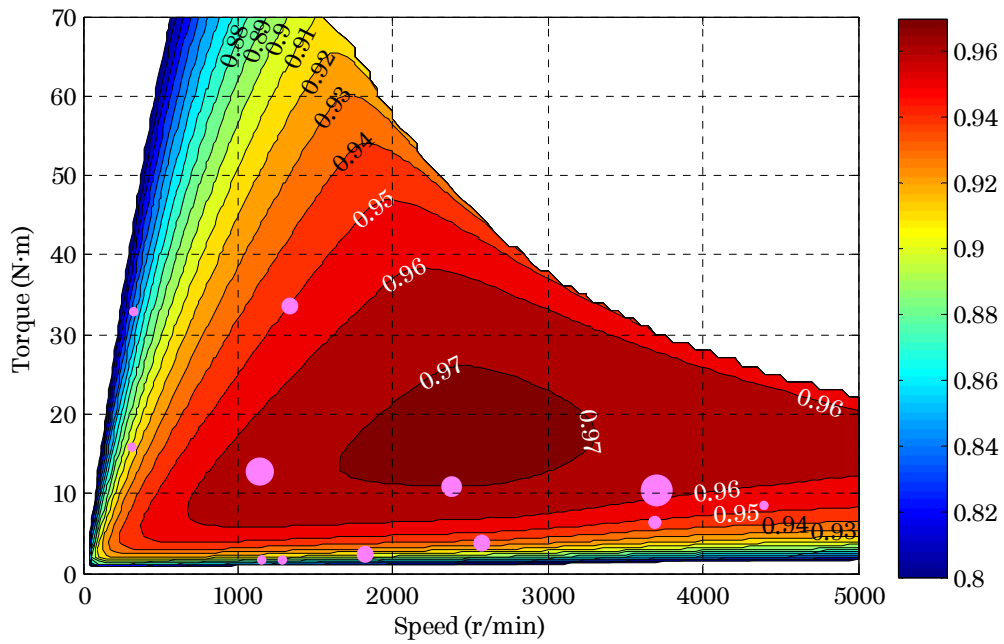
(a) Machine efficiency map (in per unit values) of Design I.
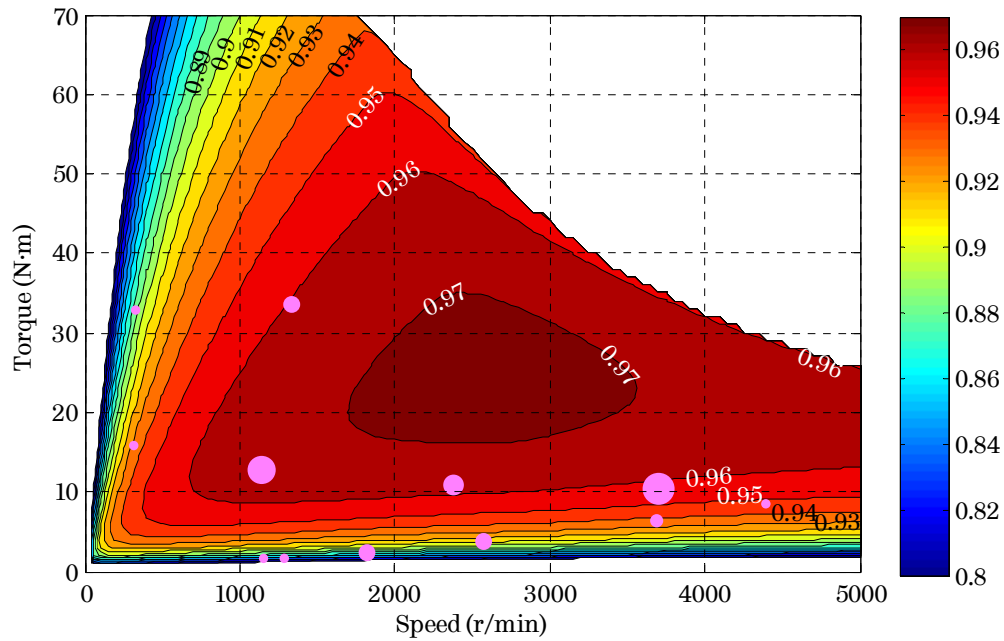
(b) Machine efficiency map (in per unit values) of Design II.
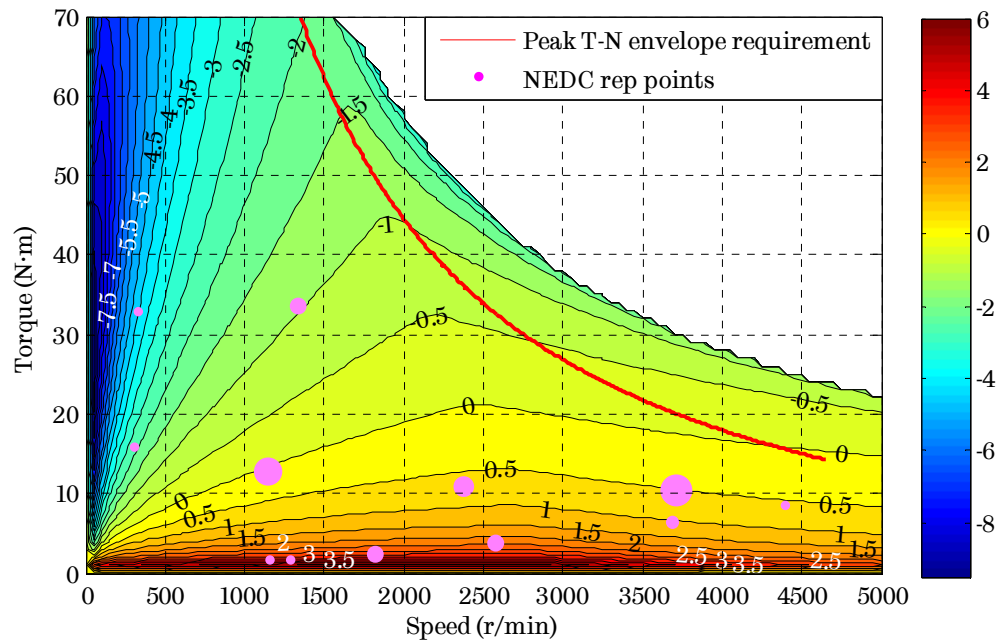
(c) Efficiency difference map (in %) between the two machines.

Figure 2.13. Efficiency and efficiency-difference maps of the optimised designs overlaid with the NEDC representative operating points.

These, indeed, are static efficiency maps, but the locations of the representative NEDC operating points, along with their energy consumption weight, can easily provide an indication of the high energy efficiency regions when the motors are operated over the cycle. Furthermore, Figure 2.13 (c) demonstrates the efficiency difference between the two machines over the entire torque-speed operating range, where positive percentage indicates superior performance for Design I and *vice versa*.

Design I, which was optimised over the NEDC cycle, outperforms Design II in terms of energy efficiency over the NEDC since particular attention was paid to minimising the losses over the twelve representative operating points of Table 2.4 during the design optimisation process. These twelve points significantly influenced the selection of the appropriate set of leading design parameters. Therefore, the lower saturation levels in the stator laminations (resulting from the thicker tooth and back iron) in combination with the shorter axial length, justify the considerably lower iron loss of Design I over the driving cycle. Further, Design I does not use the full available axial length (as is the case for Design II), but an

axial length proportionally reduced to increase its coil turn number to 8, while still satisfying the maximum permissible line-line back-EMF limit.

This is, in turn, conducive to an increase in synchronous inductance, given that inductance is proportional to the product of the square of the coil turn number and the axial length, whereas the permanent magnet flux linkage is only proportional to the product of the coil turn number and the axial length. This has led to the synchronous inductance of Design I, which approximately equals to $L_{d_{max}}$ limit shown in Figure 2.11, being higher compared with that of Design II. As already explained in §2.2.1.1, the higher synchronous inductance of Design I (see Table 2.7) is conducive to enhanced FW capability, and, consequently, leads to a lower current under these operating conditions. This can be clearly observed in Figure 2.14, which compares the d-q axis current trajectories of the two optimised designs during FW operation over the continuous and peak torque-speed envelopes, and during operation over the NEDC's representative operating points.
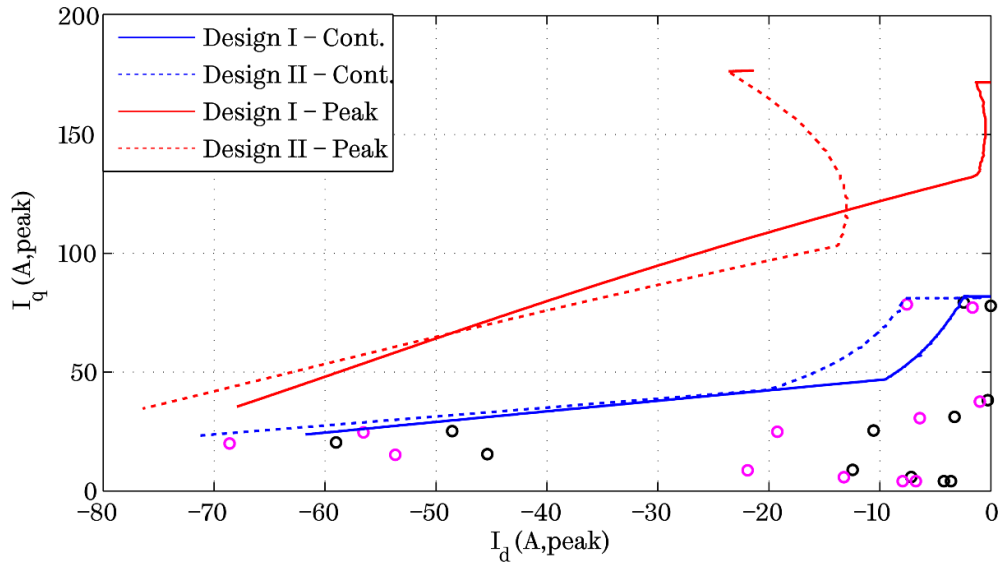

*Figure 2.14. d- and q-axis current trajectories of the two optimised designs during field weakening operation over the continuous and peak T-N envelopes, and over the NEDC representative points (Note: **black** circles– Design I, and magenta circles– Design II).*

It can be seen that Design I (with the higher synchronous inductance) requires a lower d-axis current for the majority of operating points compared with

Design II, while both designs exhibit comparable q-axis currents. On the other hand, the thicker tooth and back iron, as well as the higher coil turn number of Design I, result in a higher phase resistance compared with Design II. This is conducive to higher copper losses that, as previously described, penalise its efficiency against the rated operating point. Nevertheless, the superior FW capability of Design I partially compensates for its higher phase resistance in regards to copper loss production during operation over the NEDC, where high energy consumption is concentrated at low-load, middle-to-high speed operating points. Hence, the considerably lower iron losses in combination with the enhanced FW capability of Design I have enabled it to achieve a superior energy efficiency against the NEDC.

It becomes apparent, from Figure 2.13 (c), how the high-efficiency regions of Design I have evolved during the optimisation process to cover the most energy significant and frequently operated driving cycle operating points. Despite the fact that both designs exhibit comparable efficiencies at the extremes of the torque-speed envelope of Figure 2.5 (i.e., T_{cms} or T_{ms} at ω_{ms}), Design I still exhibits a higher driving cycle energy efficiency, as shown in Table 2.9 and Table 2.10, respectively.

In order to further assess the two designs at a system level, the inverter loss was calculated using a loss model described in [62]. It is important to note that the efficiency of the drivetrain components is interlinked, and thus, the performance of the motor would significantly influence the losses generated by the inverter. The inverter employed in the P-MOB project uses IGBT switches with a rated collector current of 300 A, a DC-link voltage of 120 V, a rated diode current of 200 A, and a switching frequency of 10 kHz. The inverter loss (consisting of conduction and switching losses) is calculated from the model using the amplitude of the phase current, the power factor and the modulation index, which are defined by d- and q-axis currents and voltages. The energy loss data and the system energy efficiency (i.e., machine + inverter) of the two machines are also shown in Table 2.10, and were obtained using their respective phase voltages and currents over the twelve NEDC operating points, under both the maximum-torque-per-ampere (MTPA) and FW operating modes.

The efficiency difference between the two machines grows moderately to ~1.2%, after considering the inverter losses. It can be seen that Design I yields slightly lower inverter loss, despite the fact that its winding resistance is much higher when compared with that of Design II. Again, this is due to its higher synchronous inductance as observed in Table 2.7. The machine with lower inductance requires a higher phase current during the FW operation [58], [59] (viz., Figure 2.14). This is, in turn, conducive to an increase in current-induced losses, i.e., the copper and inverter loss. For instance, a 10% increase in current would result in about 20% increase in copper loss.

2.2.2.1 EV range estimation for back-to-back runs over the NEDC

The EV range difference between the two designs was estimated for back-to-back runs over the NEDC assuming 4.9 kWh available battery capacity, which corresponds to 70% of battery SOC (state of charge) with a single charge in order to avoid significant degradation of battery life from deep discharge.

As can be observed from the EV range calculations listed in Table 2.11, Design I, which is optimised over the NEDC, achieves ~17% lower motor energy losses (viz., ~12% including inverter loss) compared with Design II, and can extend the EV range by ~2.3 km. Although the range extension for a single battery charge does not appear to be large, it should be noted that Design I also yields ~14% lower material usage. This translates to the same amount of cost, size and weight reduction, while achieving ~14% higher torque density compared to Design II as a result of employing the proposed design technique. Evidently, the higher cost of Design II, which uses the full length to maximise the efficiency at the rated operating point, does not yield better energy efficiency over the NEDC.

Table 2.11. EV Range Calculation for the two Designs

Parameter (Unit)	Unit	Design I	Design II
Battery capacity (per motor)	kWh	4.90	
Motor output energy for NEDC	kWh	0.295	
NEDC distance	km	11.02	
Motor loss	kWh	0.0169	0.0204
Inverter loss	kWh	0.0154	0.0164
EV range	km	**164.9**	**162.6**

Based on the preceding analysis and discussion, it can, therefore, be deduced that the optimisation of a traction machine over a defined driving cycle is of paramount importance, as inappropriate design optimisation techniques may lead to low energy efficiency over the driving cycle and higher cost. It has been demonstrated that the energy consumption of several driving cycles can be quite accurately represented by a finite number of equivalent energy-centre of gravity points (i.e., representative operating points). Although this chapter focuses exclusively on the NEDC, design optimisations against other driving cycles have also been conducted, and the results have further confirmed the preceding findings. These findings will be discussed in subsequent chapters of the thesis.

2.3 FSCW SPM motor prototype and validation through experimental results

The FSCW SPM motor optimised against the twelve representative operating points of NEDC (i.e., Design I) has been manufactured. The stator with the concentrated windings, the rotor before the placement of the carbon fibre banding layer of 0.4 mm thickness, as well as the complete motor assembly are shown in Figure 2.15.

As it can be observed from Figure 2.15 (b), the rotor magnets were segmented into four pieces circumferentially, and three pieces axially. The segmentation enables to achieve a reduction in the eddy currents induced in the rotor magnets due to the magneto-motive force harmonics occurring in typical FSCW winding slot/pole configurations [63], [64].

A test rig has been established to measure the motor performance in the defined torque and speed range. The schematic of the motor test system is shown in Figure 2.16. In the test rig, a bi-directional four-quadrant converter-controlled dynamometer drives the traction machine at a specified speed. It supplies the load torque when a load test is performed. A dedicated converter, operating in torque control mode and capable of realising field-weakening during high-speed operation, is employed for the control of the traction machine. A bi-directional power supply is used to provide the DC-link power to the converter. The test rig employs voltage

and current transducers of high precision and bandwidth in order to accurately measure the power fed to the traction machine from the converter through a power analyser (viz., Yokogawa WT3000). An in-line MAGTROL torque transducer is employed to acquire the output power of the traction machine through measurements of the speed and torque. The test rig illustrated in Figure 2.16 enables direct measurements of the traction machine's efficiency.
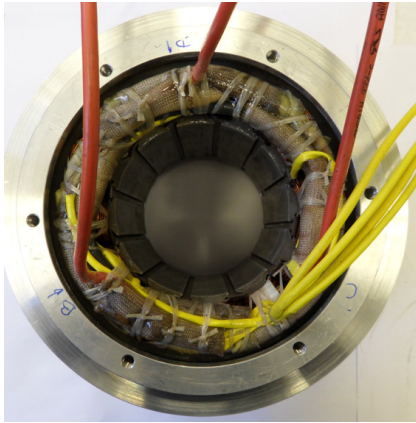
(a) Shrink-fitted stator with concentrated coils

(b) SPM rotor with segmented magnets
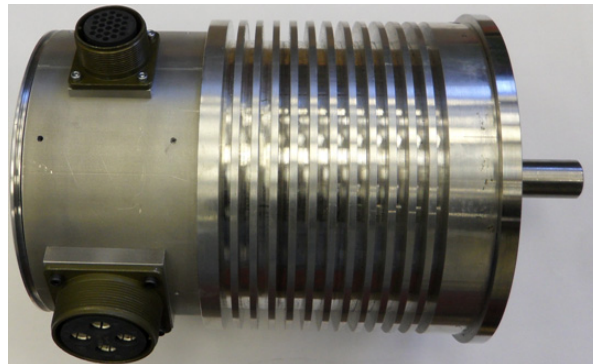
(c) Final motor assembly with shrink fitted aluminium cooling shell

Figure 2.15. Prototype FSCW SPM motor parts.

Figure 2.17 shows the measured motor efficiency map when the DC-link voltage is 120V. In comparison to the predicted efficiency map shown in Figure 2.13 (a), the measured efficiency is about 0.8~1.3% lower. This is due to a number of factors. First, the end winding of the prototype motor is slightly longer, and together with the three-phase cable leads, which are not included in the prediction, result in ~9% increase in winding resistance. Further, the iron loss is affected by

the manufacturing process and is about 35% higher than the prediction according to no-load loss measurements at various operating speeds. The permanent magnet eddy current losses (although significantly low due to magnet segmentation), as well as the mechanical and windage losses, are present in the measurement but are neglected in the prediction. In addition, the errors in speed and torque measurements may also contribute to the difference.
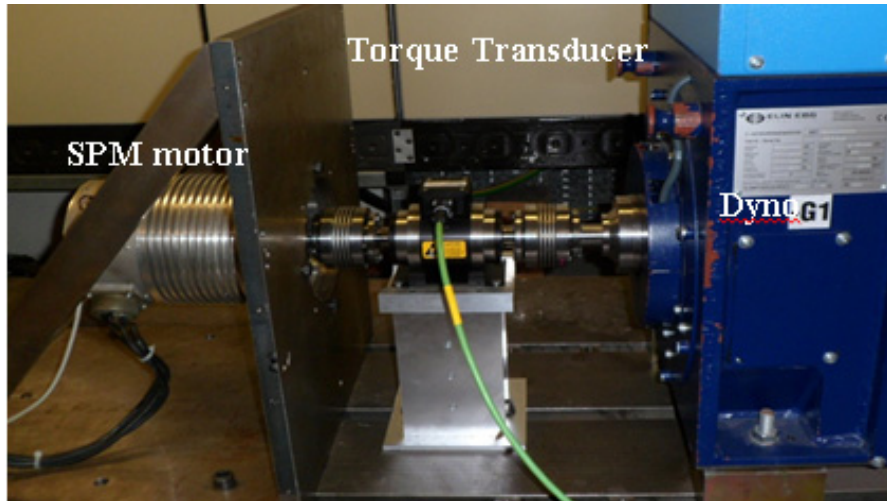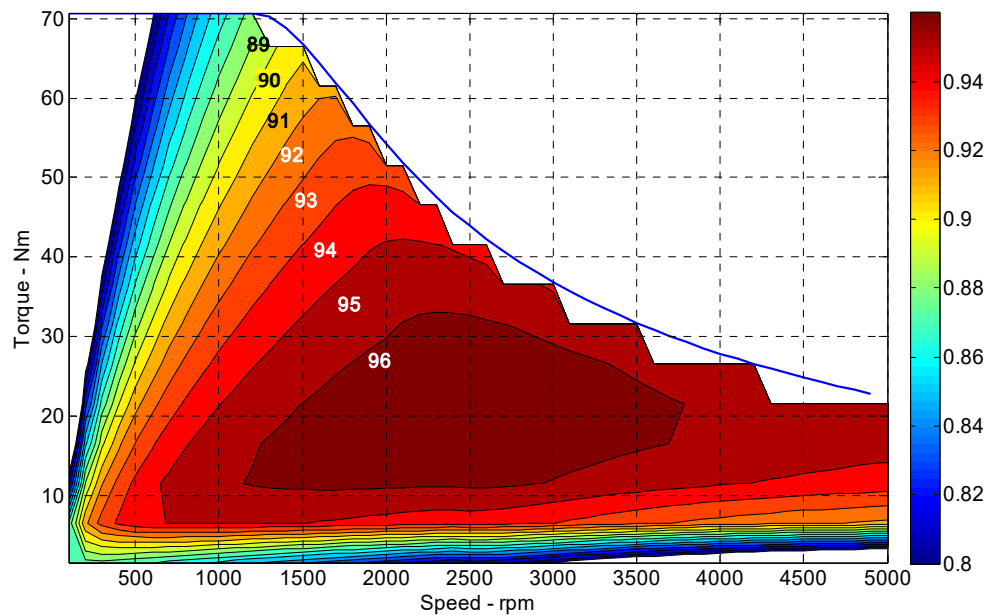

Figure 2.16. Dynamometer test system arrangement.

Figure 2.17. Experimentally measured efficiency map.

2.4 Remarks

A new design technique has been presented in this chapter for maximising the energy efficiency of EV tractions over a defined driving cycle. It has been shown that the energy distribution of the traction machine over the NEDC can be represented by twelve operating points through a clustering process. The design optimisation can, therefore, be made against these representative points. This dramatically reduces the computation time required for the design optimisation process, particularly in the case where FEA is employed. Additionally, the utility of the technique has been demonstrated for other driving cycles with different energy consumption distributions compared to that of the NEDC. It has also been shown that a design optimised against a few points close to the rated operating condition will not yield optimal results against a driving cycle, as in real driving conditions the traction machine frequently operates over a wider speed range and at low torque (partial load) for a considerable part of its lifespan. The proposed design technique is validated by design case studies and measurement results from a prototype permanent magnet machine.

Chapter 3

A Rare-Earth-Less PMA SynRM Topology for an Electric Vehicle with Distributed Powertrain

This chapter focuses on the design and performance evaluation of a Permanent Magnet-Assisted Synchronous Reluctance Machine (PMA SynRM) for an EV traction application employing a distributed traction system. The work undertaken is part of the European Green Vehicles Initiative FP7 Hi-Wi project, where the objective is the enhancement of energy efficiency for both the electrical traction machines and drive systems while minimising the reliance upon the vulnerable and volatile rare-earth supply chains.

In order to meet these objectives the Hi-Wi EV employs a distributed traction powertrain employing multiple electrical machines of dissimilar technology or topology as a means to harness the inherent advantages of each machine, which are more adept towards certain operating modes over the torque-speed operating range. On that basis, the electromagnetic performance of each machine should complement that of the other, thus enabling to achieve an expanded high-efficiency operating region of the overall powertrain system. Such a powertrain implementation also enables the use of a dynamic torque distribution strategy between the front and rear-axle machines, which has the potential to further enhance the energy efficiency of the overall powertrain. The results from the investigation of different machine technology/topology combinations, as well as the application of a dynamic torque distribution strategy, and their influence on the powertrain energy efficiency are presented and discussed.

Based on the results from the aforementioned investigations, a Permanent magnet assisted synchronous reluctance machine (PMA SynRM) has been identified as an ideal candidate for the rear wheels of the Hi-Wi EV, which form a key focus area of this chapter. The primary reasons behind this choice pertain to the significantly low idling losses of this topology, as well as its ability to exhibit relatively high efficiency especially toward low-load and high-speed operation while using low-remanence, cheap magnets in the rotor. In view of this, key research is focused on the design and optimisation of this topology for the investigated traction application. The performance over representative driving cycles is incorporated in the design optimisation process to achieve a design pertaining toward real-world operation, while satisfying a set of electrical, thermal, volumetric and mechanical constraints. The multi-physical performance of the machine is comprehensively analysed, and special attention is paid into the minimisation of torque ripple and the demagnetisation-withstand ability of the machine against extreme operating conditions as the latter fall into the demerits of the PMA SynRM topology.

Contents of this chapter are published by the author in [65],[66].

3.1 Concept of investigated EV traction application

The machine design work undertaken in this chapter is part of the European Green Vehicles Initiative FP7 **Hi-Wi** project (the acronym stems from **Hi**gh efficiencies over a **Wi**de torque-speed operating range concept). Currently, EV traction machines typically exhibit high efficiency over a narrow speed range (approximately 1/4th to 1/3rd of their maximum angular speed) and a limited ideal torque region. However, as demonstrated in the previous chapter, while operating under real-word driving (typically emulated by driving cycles) the traction machine frequently operates over a wide speed region and under low torque (partial-loads) resulting in a mismatch between the regions of high operating duty and those of high efficiency of existing traction motors [41].

As the project's name suggests, the Hi-Wi project focuses on addressing this mismatch by developing a novel powertrain approach, and advancing the design and manufacture of traction machines in order to achieve high energy-efficient operation over a wide operating torque-speed range. An additional goal of the project is to achieve this while reducing the reliance on rare-earth materials, which are characterised by high price-volatility and availability issues due to their uneven distribution in the world and the resulting market monopolisation problems emanating from the rapidly growing anticipation of EV penetration in the automotive sector [2], [23], [38].

Similar to the case with the previously described P-MOB EV concept, which made a strong case in favour of a distributed traction drive due to its enhanced energy efficiency and operational safety, the proposed Hi-Wi powertrain is also distributed. An additional benefit emanating from distributed powertrains, consisting of more than one traction machines, is the ability to apply a dynamic torque distribution strategy between the traction machines to achieve further improvements in the combined powertrain energy efficiency. In [15] it has been exemplified that the optimal torque distribution that yields maximum performance in the case of the P-MOB two-motor (front & rear axle-mounted) distributed powertrain with identical PMSM topologies, occurs at 50% split

between the two traction machines. The reason behind this outcome is that despite not assigning any load to one of the machines (when thermal limitations allow it) for the sake of improving efficiency, the unloaded machine still exhibits idling losses (iron and mechanical losses), as well as copper loss associated with the need for field-weakening at high speed. These power losses, however, still contribute to the system's total efficiency and, thus, alleviate any potential benefits. Unless, of course under these circumstances, the traction machine is disengaged from the system by means of a clutch for example, which, however, may not be desirable as it can potentially increase the complexity and/or cost of the system.

To eliminate this restriction, in this case, the front and rear traction machines are of different machine technology/topology, and not identical as was the case with P-MOB project. The idea behind such an implementation is to purposely harness the inherent benefits of different machine technologies/topologies, which are more adept toward certain operating modes over the torque-speed operating range.

Against this background, the electromagnetic performance of each machine should complement the other, and thus enable to achieve an enhanced overall powertrain energy efficiency. This can be achieved by tuning their individual efficiency map to exhibit high efficiency regions in different locations within the defined torque-speed operating range. This concept can be visualised by the schematic of Figure 3.1. One traction machine is mounted on the front axle and is responsible for the high torque operations, while the rear wheels are mounted with two identical traction machines adept toward partial-load, high-speed operations with low idling losses. This approach lays the ground to applying a dynamic torque distribution strategy [15] for further maximisation of the powertrain's overall energy efficiency while operating over a given driving cycle. Different gear ratios have been selected for the front and rear motors in order to realise the torque-speed profiles illustrated in Figure 3.1, namely 1:4 for the front motor and 1:7 for the rear motors. More details regarding the Hi-Wi EV are provided in the following section.
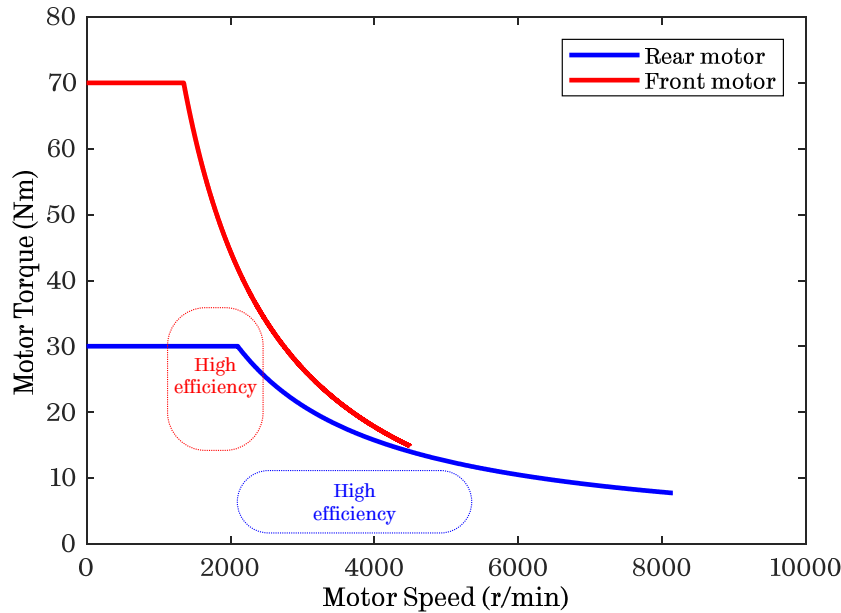
Figure 3.1. Hi-Wi distributed powertrain concept demonstrated by the operating envelopes of the front and rear motors.

A reasonable combination of dissimilar machine technologies/topologies, with the potential to resolve the issue encountered in the distributed powertrain with two identical PMSMs, would be a conventional PMSM topology with either SPM or IPM rotor configuration paired with a permanent magnet-assisted synchronous reluctance machine (PMA SynRM) or a purely synchronous reluctance machine (SynRM). The major reason pertaining to this choice is that PMA SynRM or SynRM, respectively, exhibit very low or zero no-load loss at idling, respectively, and are both relatively efficient at low-load and high-speed operation. Whereas, the conventional PMSM machine will be more capable in handling high-load operation with higher efficiency (viz., more torque-dense) due to its intrinsic characteristics and the use of high-energy NdFeB magnets.

The choice of SynRM/PMA SynRM aligns well with the intentions of the project in reducing the reliance on rare-earth materials since both topologies provide the flexibility of not using magnets at all, or employ low-remanence cheap ferrites or injection-moulded NdFeB magnets with minimal rare-earth utilisation. Whereas, for the case of the conventional PMSM, to be mounted to the front wheels, great efforts have been directed (by the project partners) into producing high-

energy NdFeB magnets with greatly reduced dysprosium content (viz., around 80% reduction), through the development of nanostructure magnet architectures and the deposition of dysprosium via the Cold Spay process that facilitates mass manufacturing [67].

The influence of dissimilar machine topology/technology combinations on the overall powertrain energy efficiency were investigated by the author and his co-authors in [66]. Without loss of generality, the aforementioned work, considered a two-motor (front and rear mounted) distributed powertrain with identical torque-speed envelopes like the P-MOB EV, instead of the three-motor distributed powertrain of the Hi-Wi EV, for simplicity in demonstrating the findings. Several traction machine combinations for the front and rear wheels were examined; these include a fractional-slot SPMSM and a fractional-slot IPMSM for the front-wheel motor, and a PMA SynRM or SynRM candidate for the rear-wheel motor.

The SPM machine (similar to the one discussed in Chapter 2) uses a 14-pole/12-slot configuration, and the IPM uses a novel 8-pole/18-slot configuration proposed in [68]. All traction machine candidates for the front wheels employ high-energy density NdFeB magnets. As for the rear-wheel candidate machines, the PMA SynRM has a 4-pole/36-slot configuration and uses ferrite magnets, while the SynRM uses a 6-pole/36-slot configuration without magnets at all. The 14-pole/12-slot SPM, 8-pole/18-slot IPM and the PMA SynRM have been preliminary optimised based on a 50:50 power distribution between the front and rear wheels such that they exhibit a high efficiency over the NEDC. Whereas, the 6-pole/36-slot SynRM has been designed such that it achieves the required torque-speed operating range, with the minimum possible axial length subject to the thermal, current and voltage constraints. All other traction machine candidates have the same outer diameter and axial length, but the SynRM could not compete with their torque and power density due to the absence of magnets, and, therefore, its axial length has been increased by 30% to achieve that.

A dynamic torque distribution strategy between the front and rear machines has been applied, using all possible machine combinations for the front and rear wheels, with the aim of investigating the potential overall energy

efficiency increase when the powertrain operates the NEDC. To demonstrate an example, one could observe the movement of the NEDC representative points in Figure 3.2, when the optimal torque distribution is applied to the front and rear machines instead of the default 50:50 ratio. The illustrated results correspond to the combination of the SPM machine (front wheel) with the PMA SynRM (rear wheel), and are displayed on the efficiency map of the SPM design.
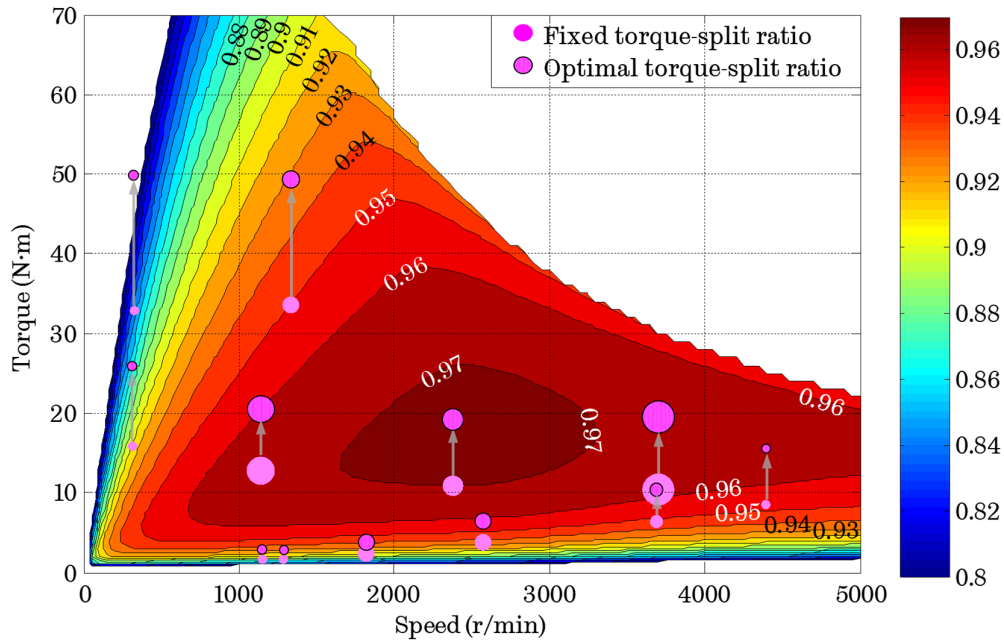

Figure 3.2. Efficiency map of P-MOB SPM overlaid with the location of the NEDC representative operating points when the power is distributed between the P-MOB SPM and PMA SynRM machine combination with a 50:50 ratio and with the optimal ratio [66].

All NEDC representative points appear to move toward higher torque in the efficiency map, indicating that generally higher torque is allocated to the front SPM machine at variable rates, while 75% of the points are moved toward a higher efficiency region. This outcome is attributed to the substantially lower iron loss of the PMA SynRM. It has been found that when torque is below ~15 N·m the optimal torque distribution for the front motor lies around 0.8 for the entire speed range, implying that the rear motor either operates at very low load or it is idling. As the torque increases, however the optimal torque distribution between the front and rear machines leans toward 50:50 as the thermal limitations are approaching as

well. The energy efficiency gain over the NEDC, resulting from the application of a dynamic torque distribution strategy to this particular machine combination, is ~1%, which is significant as it translates to ~20% decrease in energy loss. The power efficiency gains over the entire efficiency map were in the range of 1-3% compared to the case where a fixed 50:50 torque distribution is applied to the front and rear machines. The obtained results for all the possible machine combinations for the front and rear wheels are listed in Table 3.1.

Table 3.1. Energy efficiency over the NEDC for different traction machine combinations for the front and rear wheels of the distributed powertrain, with and without optimal torque distribution ratio [66]

Parameter	Identical machines at 50:50 ratio	Paired with PMA SynRM		Paired with SynRM	
		50:50	Optimal	50:50	Optimal
14-pole/12-slot SPMSM	94.5%	94.0%	95.1%	94.1%	95.1%
8-pole/18-slot IPMSM	94.3%	93.9%	94.5%	94.1%	94.7%

The results indicate considerable energy efficiency improvements over the NEDC when an optimal torque distribution strategy is applied compared with using a fixed 50:50 ratio for dissimilar machine topology combinations, leading to ~10%-20% energy loss reduction. Moreover, improved energy efficiency is obtained even when compared with the case where two identical conventional PMSMs with a fixed power distribution ratio of 50:50 are employed. This outcome indicates that an enhanced energy efficiency can be achieved with a relatively reduced powertrain cost and rare earth material reliance by pairing the conventional PMSM with either a PMA SynRM or a SynRM and applying a dynamic torque distribution strategy.

Although the fractional-slot SPMSM exhibits a higher energy efficiency when combined with a PMA SynRM or SynRM with optimal torque distribution, the 8-pole/18-slot IPMSM was selected for the design of the front-wheel motor as it uses ~40% less NdFeB magnet material. As for the rear-wheel motor, which is the topic of investigation in this thesis chapter, the following trade-offs were considered in selecting the most appropriate topology. The results from Table 3.1 indicate that comparable performances occur for the cases where a conventional

PMSM for the front wheels is paired with either a PMA SynRM or a SynRM for the rear wheels. However, the PMA SynRM appears as the best candidate topology to use for the rear wheels of the Hi-Wi EV due to the inadequacy of the SynRM in achieving the required torque-speed operating range within the volumetric, electrical and thermal design constraints of the application.

For this reason, its axial length has been accordingly extended, resulting in 30% more volume, in order to deliver the required performance while satisfying the electrical and thermal constraints. A primary reason pertaining to this issue is the poorer power factor of the SynRM that hinders it from achieving the required constant-power speed range during FW operation within the specified inverter VA limit [35], [69]. The fact that relatively inexpensive ferrite magnets can be employed in the rotor of the SynRM to essentially form a PMA SynRM, leading to a more torque- and power-dense traction machine with a greatly improved power factor [35], [70]–[72], further supports this choice. An additional attractive attribute of the PMA SynRM is the relatively reduced uncontrolled current in the event of an intermittent inverter fault, leading to increased safety during high-speed operation, due to the weak embedded magnets. This is a challenging aspect in the design of traction PMSMs employing high-energy density NdFeB magnets [73], [74]. The selected machine topologies for the front and rear wheels form an ideal combination for the objectives that the distributed traction system of the Hi-Wi EV has set out to achieve.

3.2 EV and traction machine specification

Figure 3.3 illustrates a schematic of the investigated Hi-Wi EV, which is classified as a class-2 vehicle. In contrast to concentrated traction systems, employing a distributed traction system leads to enhanced operational safety and energy efficiency due to the fact that it eliminates the effect of tyre slip [53] and provides redundancy in the event of a fault [15].

The distributed traction drivetrain comprises of three motors, with one motor mounted on the front axle and contributing nominal 40% of the total traction power, and two identical motors mounted on the rear axle, each providing 30% nominally, as per the Hi-Wi project specifications. All three motors are

coupled to their corresponding axle via a differential with a gear ratio of 1:4 and 1:7 for the front and rear motors, respectively. Detailed vehicle parameters are given in Table 3.2.
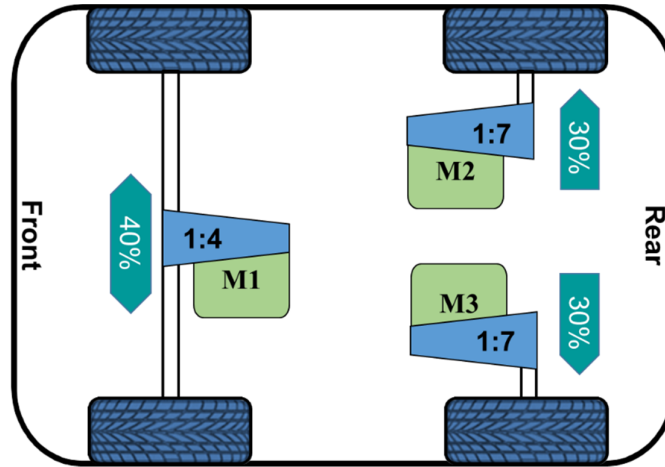
Figure 3.3. Powertrain schematic of Hi-Wi EV – class 2 vehicle.

Table 3.2. Electric vehicle specification

Parameter	Symbol	Value
Tire size	-	165/50 R15
Effective rolling radius of wheels (m)	r_w	0.273
Vehicle mass (kg)	m	800
Rolling resistance coefficient	c_r	0.007
Front area (m²)	A	0.7
Wind drag coefficient	c_d	0.5
Air density (kg/m³)	ρ	1.250
Efficiency of differential	η_{diff}	0.980
Gear Ratio	G_r	1:7 rear/ 1:4 front
Maximum vehicle speed (km/h)	v_{max}	120.0

3.2.1 Torque-speed envelopes and driving cycles

This chapter investigates the design of the vehicle's rear motors with a 1:7 reduction gear (see Figure 3.3). Compared with that of the front motor (i.e., single-stage reduction of 1:4), the higher gear ratio translates to a flatter (lower torque) and wider (higher speed) operating envelopes (viz., Figure 3.1). The resultant shape

of the torque-speed envelopes correlates well with the attributes of the selected PMA SynRM topology, which is known to exhibit higher power density (viz., extended speed operation) rather than torque density due to the weak embedded magnets [36], [75].

Based on a vehicle dynamics model established from the data of Table 3.2, the power requirements for operation over the NEDC, as well as the vehicle acceleration and hill-climbing ability, the peak and continuous torque-speed profiles for each of the rear traction motors are derived, as shown in Figure 3.4, following the process described in Chapter 2. More specific design requirements for the traction machine can be established from Figure 3.4, and they are listed in Table 3.3 together with other volumetric, electrical and thermal design requirements as specified by the project's consortium.
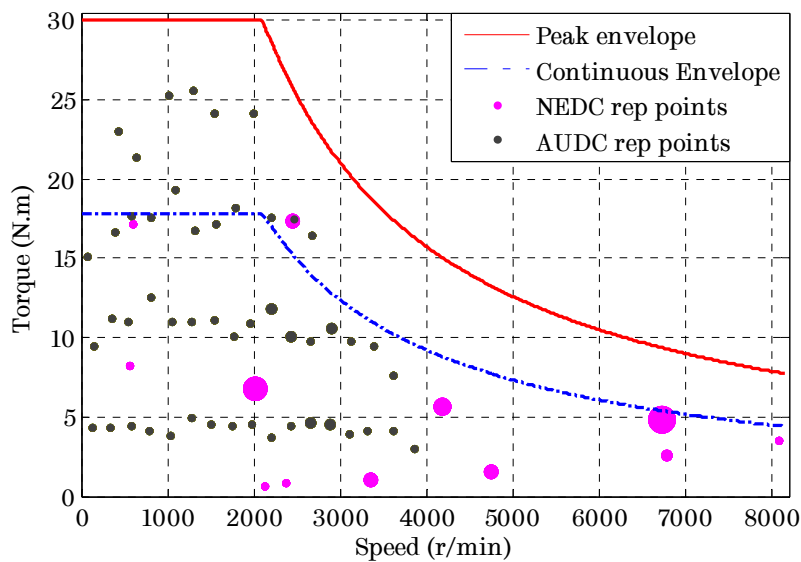
Figure 3.4. Torque-speed envelope overlaid by NEDC and AUDC representative points.

Owing to the dynamically varied torque-speed combinations characterising traction applications, which significantly influence the traction machine's energy efficiency and hence the attainable EV range, it is essential to consider the performance over representative driving cycles, such as the NEDC, during the design optimisation process of the traction PMA SynRM. As highlighted in Chapter 2 this will enable to acquire designs exhibiting superior energy efficiency against driving conditions pertaining to real-world operation (rather than a few operating

points, which are typically used in short transients for acceleration or hill-climbing activities of the vehicle, as is frequently the case in the literature) [41]. Nonetheless, the incorporation of driving cycles (consisting of hundreds of operating points) in the design optimisation process imposes prohibitive computational time costs, particularly when high-fidelity FEA is required to characterise the performance of the machine, such as is the case of the highly anisotropic PMA SynRM topology investigated in this chapter.

Table 3.3. Traction machine design specification

Parameter	Symbol	Value
Active axial length (mm)	L_s	105
Stator outside diameter (mm)	D_o	120
Base speed (rpm)	ω_b	2100
Maximum cruise speed (rpm)	ω_{ms}	8200
Peak torque below and at base speed for 120 s (N.m)	T_{pk}	30.0
Continuous torque below and at base speed (N.m)	T_c	17.0
Peak torque at maximum cruise speed (N.m)	T_{ms}	7.4
Continuous torque at maximum cruise speed (N.m)	T_{cms}	4.4
Peak power (kW)	P_{pk}	6.6
Continuous power below and at base speed	P_c	3.75
Nominal DC link voltage (V)	V_{dc}	120
Maximum inverter current (A)	A_{pk}	120
Maximum permissible line-to-line voltage (V)	E_{max}	<250
Slot-fill factor (net)	-	0.4
Ambient Temperature (ºC)	T_{amb}	45
Thermal limit for continuous operation (ºC)	-	120
Maximum thermal limit (ºC)	-	150
Cooling method	-	Air-cooled

Therefore, to enable the performance evaluation of the machine over driving cycles within realistic computational times during the design optimisation process, the technique devised in Chapter 2 is employed to characterise the energy consumption over driving cycles by only a finite number of representative operating points (i.e., "energy gravity centres") without compromising accuracy in energy loss representation [41]. The derived representative operating points for the

NEDC and the AUDC (viz., Artemis Urban driving cycle [76], [77]) are illustrated under the operating envelopes in Figure 3.4 for comparative purposes. The instantaneous operating profiles of the NEDC and AUDC corresponding to the investigated EV specification are shown in Figure 3.5. The number of the representative operating points is dependent on the energy consumption distribution of a given driving cycle over the torque-speed plane. Each of the operating points in Figure 3.4 represents a torque-speed combination at which a specific amount of energy, referred to as energy weight, is consumed over the driving cycle. The energy weight of each representative point is indicated by its equivalent marker diameter, which is normalised to the point with the maximum energy weight over both driving cycles.

As can be seen in Figure 3.4 and Figure 3.5, the two considered driving cycles emulate different driving modes according to their energy consumption distribution. In the case of the NEDC, which is represented by 12 operating points, the major energy consumption occurs in the low-torque middle-to-high speed operating region, equivalent to sub-urban and highway driving. The AUDC on the other hand, is characterised by 50 representative points (in order to accurately represent the energy losses) due to its widely distributed energy consumption in the middle-to-high torque and low-speed operating region, reflecting the frequent stop-and-go activities and hard accelerations of the vehicle during urban driving. The AUDC consists of five distinct cycles to more accurately emulate urban driving – an urban dense, free-flow urban, congested stops, congested low-speed, and a flowing-stable cycle [76]. It is characterised by a 17.7 km/h average speed and lasts for ~4.9 km distance. Further, the NEDC is an artificially created driving cycle, whereas the AUDC is created through the processing of data measured from real-world driving patterns.

As can be observed from Figure 3.4, all of the NEDC representative operating points are covered by, or are in very close proximity to the continuous operating envelope, implying that the machine could be continuously operated over NEDC without exceeding its rated thermal limit. That is to be expected as the continuous operating envelope has been derived in accordance to the torque and

speed requirements of the NEDC for the specified EV. The vast majority of the AUDC representative operating points are also covered by the continuous operating envelope, although there is a small number of high-torque operating points outside the continuous envelope, indicating relatively higher temperatures during operation over repeated AUDC cycles.
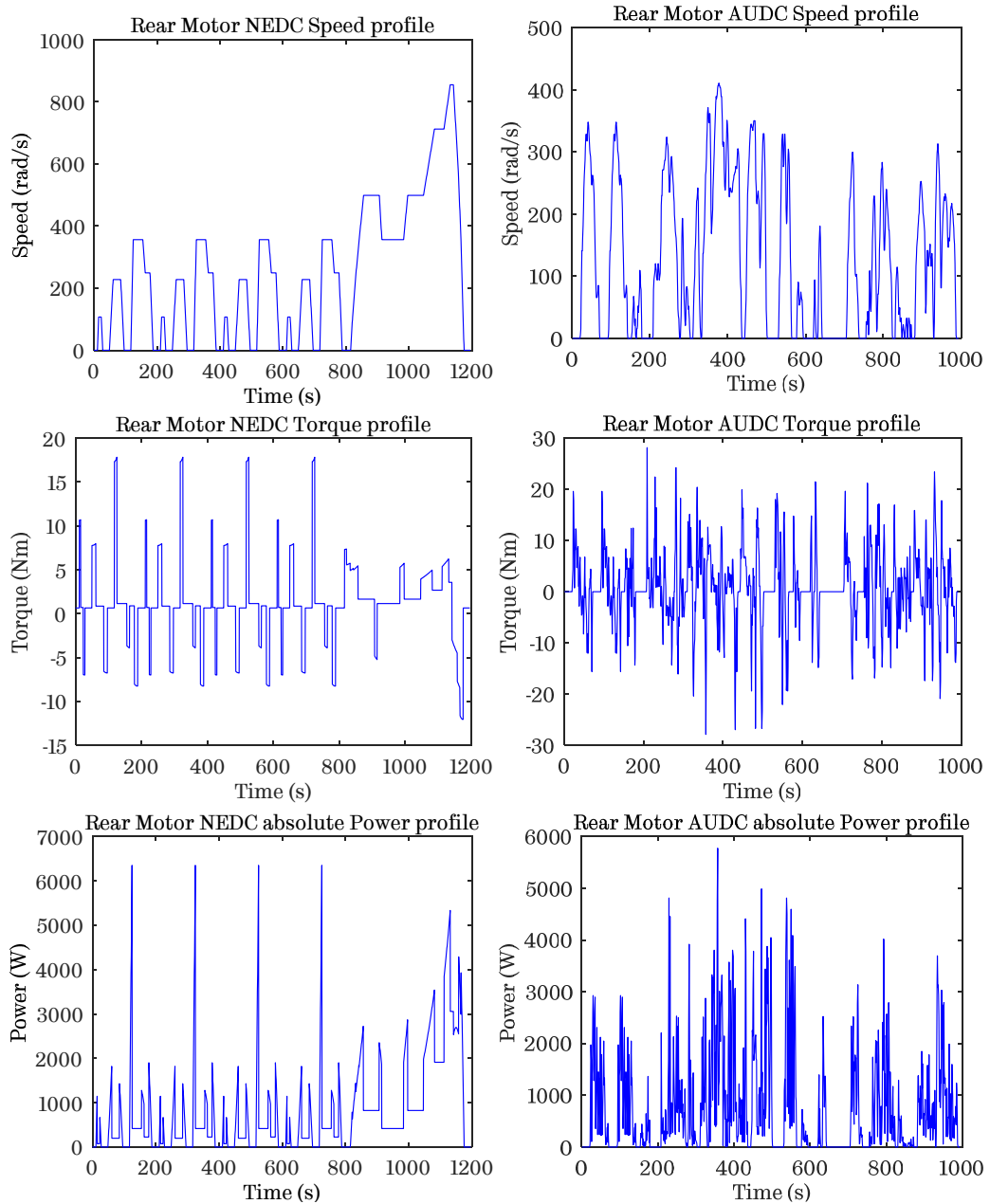
Figure 3.5. Speed, torque and absolute power profiles of the rear motors over the NEDC (left column) and AUDC (right column).

Referring back to Figure 3.4, one can observe the mismatch between the operating regions where high energy consumption is concentrated over the two driving cycles, and the locations of the machine's rated and peak operating points (i.e., T_{pk}, T_c, T_{ms}, T_{cms}), which are primarily utilised in short transients during driving for acceleration and hill-climbing purposes. This mismatch highlights the significance of incorporating representative driving cycles into the design optimisation process of traction machines, which is in turn critical for the enhancement of the driving range on a single battery charge or the reduction of battery capacity.

Without loss of generality, the NEDC, which currently forms the standard for energy efficiency certification of vehicles in Europe, has been selected as the reference cycle against which the design optimisation should be conducted as specified by the Hi-Wi project consortium. Acknowledging, however, the universally criticised inability of the NEDC in adequately emulating real-world driving conditions [7], [9], especially those pertaining to urban driving with frequent accelerations and stop-and-go activities [76], the AUDC has been also considered as an indicative performance metric for the performance evaluation of the final design.

3.3 Design process

Although no formal method (i.e., algorithmic) has been used, the PMA SynRM has been optimised using an iterative process involving the best engineering practices applicable to the design of traction machines and the PMA SynRM in particular. The process starts with an initial sizing exercise based on typical shear stresses, current densities, and split ratios for the selected number of poles. This provides the initial design to be analysed and refined using 2D electromagnetic FEA. Thermal and mechanical stress analyses are then undertaken on the selected design, and the results from these analyses are employed for further electromagnetic performance refinement. Typically, few iterations of this process are required to achieve the final design.

3.3.1 Optimisation objective and constraints

Without loss of generality, the optimisation objective is to maximise the energy efficiency (or minimise the energy losses) over the target driving cycle (i.e., NEDC), whilst satisfying the required torque-speed operating range and a given set of electrical, thermal, mechanical and volumetric constraints specified by the project consortium.

The selection of the final design is ultimately subjected to the fulfilment of the defined design constraints. The machine should deliver the peak (overload) torque at both ω_b and ω_{ms} within the specified inverter VA rating, i.e., $120\ A_{pk}$ and $120\ V$ dc-link, whilst not exceeding the maximum line-line back-EMF limit of $250\ V_{pk}$ at maximum speed in order to ensure safety in the case of an intermittent inverter fault. The machine should deliver constant power over a wide speed range, i.e., ~4 times the base speed. The rotor magnets should endure irreversible demagnetisation against the worst-case overload condition of the defined operating range (i.e., T_{pk}, ω_b or T_{ms}, ω_{ms}), while operating under their corresponding critical temperature condition where the demagnetisation knee-point is more evident (viz., high temperature for bonded NdFeB, whereas sub-zero temperature for ferrites).

The mechanical stress exhibited at the rotor bridges, when the rotor is rotated at 1.5 times the maximum speed (ω_{ms}), should not exceed the yield strength limit ($450\ Mpa$) of the employed lamination electrical steel grade, namely M270-35A, to avoid the rotor deformation which would compromise the airgap. The traction machine of the investigated EV application is air-cooled, totally enclosed by a radial-finned aluminium jacket with an ambient temperature of 45ºC. The copper winding and magnet temperatures should be limited below 120ºC (considering the selected insulation class and a safety margin to prolong lifetime) when operating over the entire continuous torque-speed envelope, where the worst-case operating conditions typically reside at the extremities of the envelope, i.e., T_{pk}, ω_b or T_{ms}, ω_{ms}.

The torque ripple exhibited by the machine should be sufficiently low in order to ensure comfort during cruise. The torque ripple at T_{pk}, ω_b is typically considered as the worst-case scenario. The percentage of peak-peak torque ripple

over the peak torque requirement should be limited below 5%, according to the project specification. This particular requirement frequently appears in the literature for EV traction applications, such as for the next generation EV project (Freedom car 2020) [78].

3.3.2 Leading design parameters of investigated PMA SynRM

A three-phase transversally laminated PMA SynRM with 6-pole and 36-slot configuration was selected for the design investigation using a classical single-layer distributed winding. This slot/pole configuration was selected considering the trade-off between high torque production capability at low speed, and low iron loss generation at high speed [79]. Further, the choice of distributed winding configuration with integral slot-per-pole-per-phase allows for the full exploitation of the reluctance torque component, which is typically known to considerably deteriorate when fractional slot-per-pole configurations are paired with highly anisotropic rotor structures [80]–[82]. This aspect is critical in enhancing the torque and power density of this topology, especially when low-remanence magnets are employed in the rotor. The lack of low order space harmonics (i.e., low total harmonic distortion in the MMF of this configuration), combined with the multilayer rotor, lead to low iron loss production under high-speed operation [83].

The selection of three embedded layers and a cutout in the rotor leads to enhanced magnetic anisotropy [84], and hence reluctance torque capability, whilst ensuring good structural integrity and manufacturability of the rotor based on the specified machine space envelope. Further, the selection of three layers ensures thick enough magnets capable of withstanding irreversible demagnetisation during overload. A schematic of the investigated PMA SynRM topology is illustrated in Figure 3.7. The rotor layers are almost entirely filled the with low-remanence magnets to fully exploit their contribution in enhancing the torque density and power factor (considering the relatively small machine space envelope), while a small portion at the sides of each layer is left empty so as to prevent flux leakage. The investigated design has been intended for use of ferrite magnets in the rotor. However, the prohibitive tooling costs, as well as the inability to guarantee acceptable manufacturing tolerances, for producing bespoke-shaped

ferrite magnets have led to the decision to employ injection-moulded bonded NdFeB magnet material. An equivalent, low-remanence magnet grade has been selected based on availability from the magnet supplier.
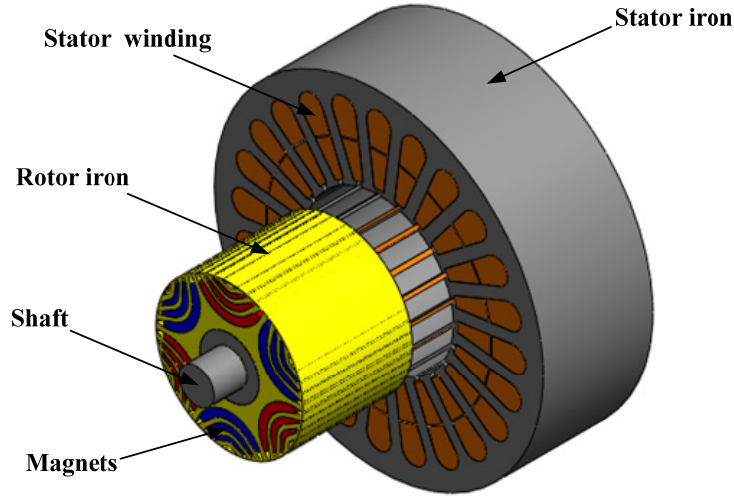
Figure 3.6. Schematic of PM assisted synchronous reluctance machine.

Owing to the complexity of the rotor structure of the PMA SynRM, its geometry consists of a relatively large number of design parameters that need to be tuned to enhance the energy efficiency against the NEDC, while satisfying the specified design constraints. A primary set of design parameters, which most significantly influence the electromagnetic performance of this topology has been identified and the leading design parameters are illustrated on the schematic of Figure 3.7.

The motors were optimised with respect to the leading design parameters of Figure 3.7, viz., the tooth width (T_w), the stator yoke width (H_y), the ratio of the rotor radius to the stator outer radius, abbreviated as split ratio ($\frac{R_i}{R_o}$), the magnet depth (d_m), the coil turn number (TN), and the ratio of air/magnet-to-silicon steel in the rotor, abbreviated as insulation ratio (k_{ins}) and described by equation (3.21). A secondary set of geometrical parameters, such as the individual flux barrier thickness in the rotor and the flux barrier angles, are considered in subsequent iterations of the design cycle for further fine-tuning of the design in terms of torque ripple minimisation and demagnetisation withstand capability for instance.

$$k_{ins\_mid} = \frac{\sum_i h_{m_i} + h_n}{d_m} \qquad (3.21)$$

where the subscript i denotes the number of each flux barrier in the rotor.
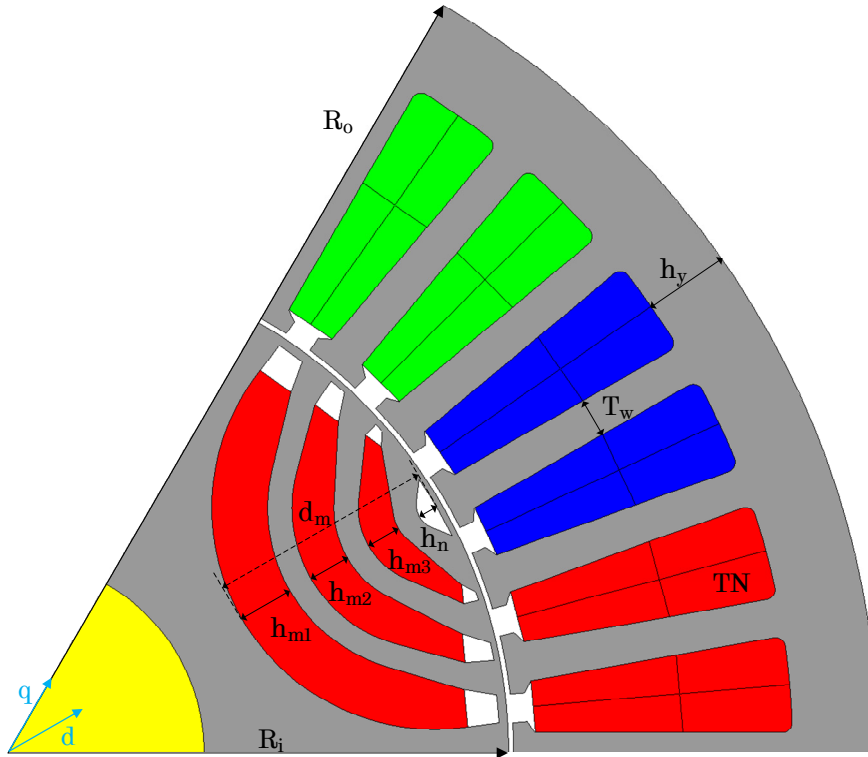
Figure 3.7. Leading design optimisation parameters of a typical PMA SynRM schematic with circular magnets embedded in the rotor (viz., the magnetisation direction is set parallel to the d-axis).

The split ratio is a fundamental design parameter for the sizing of the rotor and stator for a given space envelope, as it determines the machine losses for a given power output, and there always exists an optimum ratio for which the losses are minimum. However, in practice initial split ratios are usually selected based on the number of poles of the machines. The insulation ratio is a critical parameter pertaining to the design of the PMA SynRM topology as it regulates the saturation level in the rotor and it is responsible for the enhancement of magnetic anisotropy (i.e., d- and q-axis inductance difference), and hence the reluctance torque capability of the machine [69], [85]. The insulation ratio should be optimised in

alignment with the back iron and tooth thickness, which define the flux density levels in the stator lamination, in order to fine tune the flux circulation between rotor and stator iron cores for optimal electromagnetic performance. Unlike the conventional SynRM, the insulation ratio also controls the thickness of the magnets embedded in the rotor for the case of the PMA SynRM.

The magnet depth (d_m) controls the area occupied by the magnet/air layers and iron flux guides in the rotor, and the distance between adjacent poles (viz., thickness of iron flux guide on the high permeance q-axis). Thereby, also influencing the magnetic anisotropy and reluctance torque capability of the machine as a high amount of magnetic flux flows through that path. Lastly, the coil turn number is tuned accordingly to adhere to the specified current and voltage limits of the converter. Due to the use of low-remanence embedded magnets, the airgap thickness has been set to 0.35mm to minimise the reluctance in the magnetic circuit, whilst ensuring the mechanical integrity of the machine. The described parameters pertaining to the design of the PMA SynRM have been iteratively modified with the aim of maximising the energy efficiency over the NEDC (i.e., optimisation target), while satisfying the specified electrical, thermal and mechanical design constraints.

3.4 Design details and performance evaluation of optimised PMA SynRM

3.4.1 Geometric parameters and schematics of selected design

The schematics of the rotor and stator stacks, as well as the basic geometrical parameters of the optimised PMA SynRM design are illustrated in Figure 3.8, Figure 3.9 and Table 3.4, respectively.
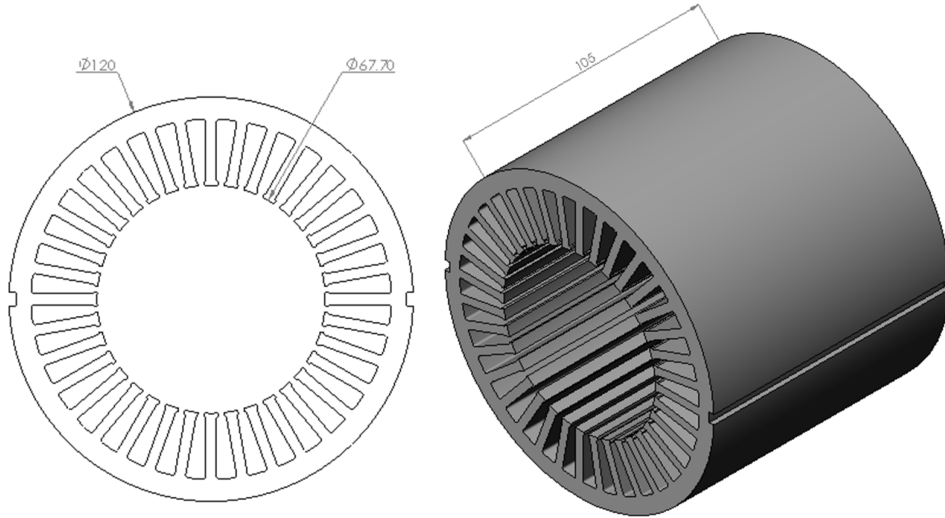
Figure 3.8. Stator design schematics of rear PMA SynRM traction machine.
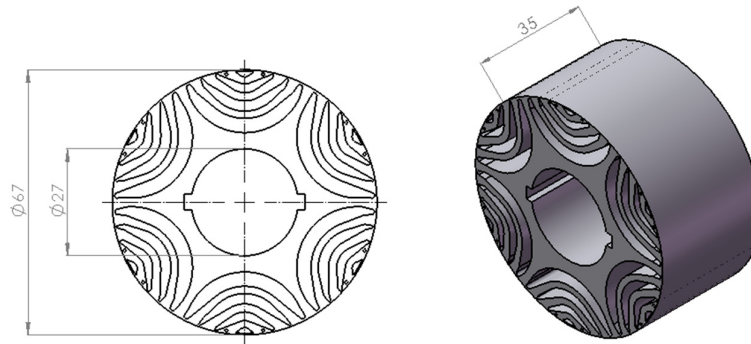
Figure 3.9. Rotor design schematics for one stack of the rear PMA SynRM traction machine (due to skew there are three stacks that complete the rotor).

Table 3.4. Design parameters of optimised PMA SynRM

Parameter (Unit)	Value
Stator outer radius (mm)	60.0
Rotor outer radius (mm)	33.5
Air-gap thickness (mm)	0.35
Shaft radius (mm)	13.5
Stack length (mm)	105.0
Stator slot number	36
Pole pair number	3
Phase number	3
Coil number per phase	6
Turn number per coil	7

3.4.2 Active material usage

The materials employed for the active parts of the traction machine along with their corresponding usage are shown in Table 3.5. The non-oriented silicon steel used for the stator and rotor lamination has a thickness of 0.35mm and typical loss data of 2.47 W/kg at 1.5T and 50Hz frequency. The stator winding uses copper wire of class F insulation thermal rating.

The material selected for the embedded rotor magnets is injection-moulded bonded NdFeB. Bonded NdFeB is essentially a mixture of NdFeB powder with a polymer binder, thus being cheap and flexible to produce in various shapes when injection moulding is employed. A compression moulding process also exists, and can produce bonded NdFeB magnets of higher remanence. However, for the case of the investigated design, which employs arc-shaped magnets, injection moulding is the preferred manufacturing method. Further, a higher remanence is not required for the investigated design, for which a lower magnetic remanence closer to that of ferrite magnets was purposely selected based on availability from the supplier, since the tooling costs to produce ferrite magnets of this shape were prohibitive.

Table 3.5. Material type and usage employed for the active parts of the traction machine

Parameter (Unit)	Employed Material	Material usage (kg)
Stator lamination	M270-35A	3.72
Rotor lamination	M270-35A	1.39
Rotor Magnets	Bonded NdFeB (injection-moulded)	0.66
Stator winding wire	Copper	1.79

3.4.3 Stator winding schematic

The distributed winding type employed in the rear traction motor is classified as a Tier Winding. The distributed coil arrangement for each of the three phases and their connections are illustrated by the schematic of Figure 3.10. The basic stator winding design parameters are given in Table 3.6. Each coil consists of 7 turns, where each turn is made of 25 individual strands with bare copper

diameter of 0.5mm, assuming a gross slot-fill factor of 0.4 in the calculation performed to identify the ideal wire gauge and strand number for each coil turn. The aforementioned strand number and wire gauge were selected with manufacturability in mind, in that the resultant turn with an *x* number of strands should be pliable enough to achieve a compact end-winding to satisfy the given space envelope in the vehicle, and also achieve a phase resistance as close to the predicted one as possible.
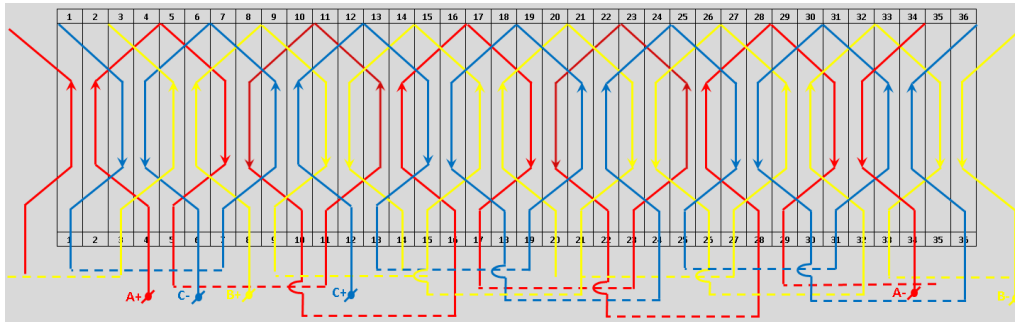
Figure 3.10. Winding layout schematic of selected PMA SynRM.

Table 3.6. Stator winding design parameters

Parameter	Value	Parameter	Value
Number of pole-pairs	3	**Turns / phase**	42
Number of slots	36	**Winding Layers**	1
Winding type	Distributed	**Slots/pole/phase**	2
Connection type	Star	**Slot-fill factor**	0.40
Coil pitch	5	**Bare wire diameter (copper)**	0.5 mm
Number of turns per coil	7	Number of strands per turn	25

3.4.4 Predicted electromagnetic performance

3.4.4.1 Electrical parameters

The fundamental electrical parameters of the selected traction machine at typical operating points are listed in Table 3.7. These include the phase resistance (R_{ph}) at 120ºC, the corresponding d and q-axis inductances (L_d, L_q), the magnet flux

per pole ($p\Psi_m$), the inductance difference per pole $((L_q - L_d)p)$ as well as the saliency ratio $(\frac{L_q}{L_d})$. The last two parameters provide an indication of the reluctance torque capability of the PMA SynRM. Note that p denotes the pole pair number.

Table 3.7. Equivalent electrical parameters of PMA SynRM at characteristic operating points of the torque-speed envelope

Parameter	Unit	T_{pk} at ω_b	T_c at ω_b	T_{cms} at ω_{ms}
Rph	Ohm		0.0679	
Ld	mH	0.569	0.607	0.673
Lq	mH	2.084	2.596	3.496
$(L_q - L_d)p$	mH	4.545	2.50E-03	8.469
$\dfrac{L_q}{L_d}$	-	3.663	5.997	5.195
$p\Psi_m$	V.s	0.117	0.124	0.129

3.4.4.2 Variation of flux-linkage with inductance with current

The equivalent electromagnetic parameters of the final design have been derived through FEA simulations for the purpose of modelling and dynamic simulation of the drive system. The stator phase windings are excited with 3-phase balanced sinusoidal currents of the same magnitude and frequency, but with a phase shift of 120° (electrical) with respect to each other. The classical voltage and torque equations, shown in (3.22) and (3.23), and the corresponding 3-phase to *d-q* transformation, and its inverse, are employed for the calculation of the equivalent electromagnetic parameters of the 3-phase PMA SynRM.

The *d*- and *q*-axis model of the machine is given by:

$$L_d \frac{di_d}{dt} + R_{ph}i_d = v_d + \omega L_q i_q$$

$$L_q \frac{di_q}{dt} + R_{ph}i_q = v_q - \omega L_d i_d - k_e \omega_m$$

(3.22)

where, i_d and i_q are the *d*- and *q*-axis currents, v_d and v_q are the *d*- and *q*-axis voltages. L_d and L_q are respectively the *d*- and *q*-axis inductances, ω_m and ω are

the mechanical and electrical angular velocities, respectively, R_{ph} is the phase resistance, p is the pole pair number, ψ_m is the phase flux-linkage from the field of the magnets embedded in the rotor, and $k_e = p\psi_m$ is the back-electromotive-force (back-emf) constant. The output electromagnetic torque defined in the d- and q-axis frame is expressed by

$$T_e = \frac{qp}{2}\left[\psi_m i_q + (L_d - L_q)i_d i_q\right]$$

(3.23)

where, q is the phase number, which in the case of the investigated PMA SynRM is equal to 3.

The 3-phase to d-q axes transformation employed in the analysis is given by

$$C_{dq \leftarrow 3ph} = \frac{2}{q}\begin{bmatrix} -\cos\theta & -\cos(\theta - 120^o) & -\cos(\theta + 120^o) \\ \sin\theta & \sin(\theta - 120^o) & \sin(\theta + 120^o) \end{bmatrix}$$

(3.24)

The inverse transformation, for the case of dq to 3-phase, is given by

$$C_{3ph \leftarrow dq} = \frac{2}{q}\begin{bmatrix} -\cos\theta & \sin\theta \\ -\cos(\theta - 120^o) & \sin(\theta - 120^o) \\ -\cos(\theta + 120^o) & \sin(\theta + 120^o) \end{bmatrix}$$

(3.25)

The mechanical equation representing the system is given below

$$J\frac{d\omega_m}{dt} = (T_e - T_L - B\omega_m)$$

(3.26)

where, J is the system's moment of inertia, T_L is the load torque, T_e is the traction machine's output electromagnetic torque, and B is the coefficient of viscous friction.

The derivation of the equivalent electromagnetic parameter model of the PMA SynRM is carried out using time-stepped FEA with the rotor rotating over the span of one sixth of the electrical cycle (i.e., 120° mechanical), which is equivalent to one torque ripple period. This is due to the symmetry of a balanced 3-phase system, and enables a proportional saving in computational time.

The variation of L_d and L_q with the d- and q-axis currents is illustrated in the plots of Figure 3.11. Figure 3.12 shows the variation of ψ_m with I_q (where, $I_d = 0$), which represents the cross-saturation effect in permanent magnet machines. It should be noted that the cross-coupling effect between the d- and q- axes has been taken into consideration in the calculation process of the equivalent circuit parameters. The high non-linearity of the PMA SynRM, stemming from its intrinsically high anisotropy due to its unique rotor structure, can be observed from the plot of Figure 3.12, where the PM-flux initially increases, and then reduces as the I_q becomes higher. Note that the maximum variation of ψ_m is in the vicinity of 6%, which is relatively low. This can be explained by the low magnet remanence of the embedded bonded NdFeB magnetic material, but also the fact that the stator has been purposely design to not be heavily saturated.
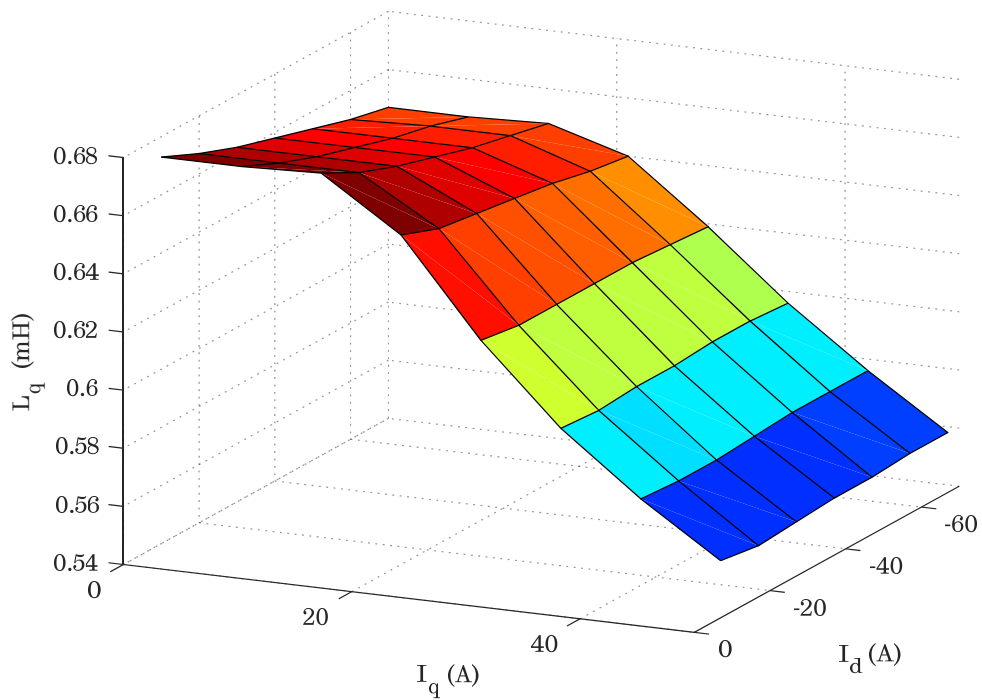
a) L_d variation with I_d and I_q
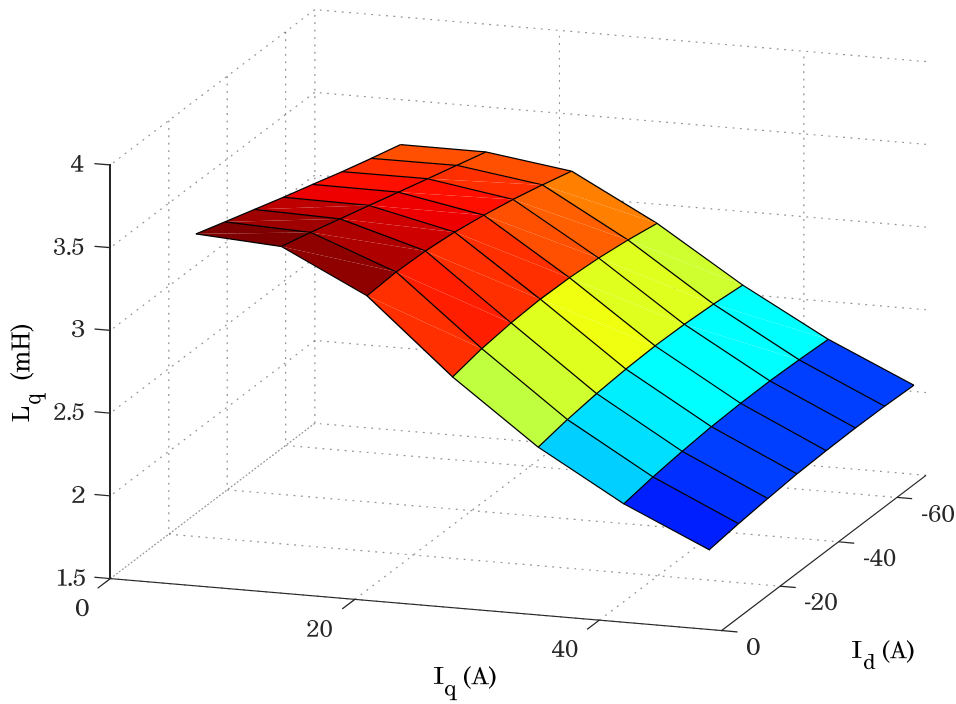
b) L_q variation with I_d and I_q

Figure 3.11. Variation of L_d and L_q with the d- and q-axis currents.
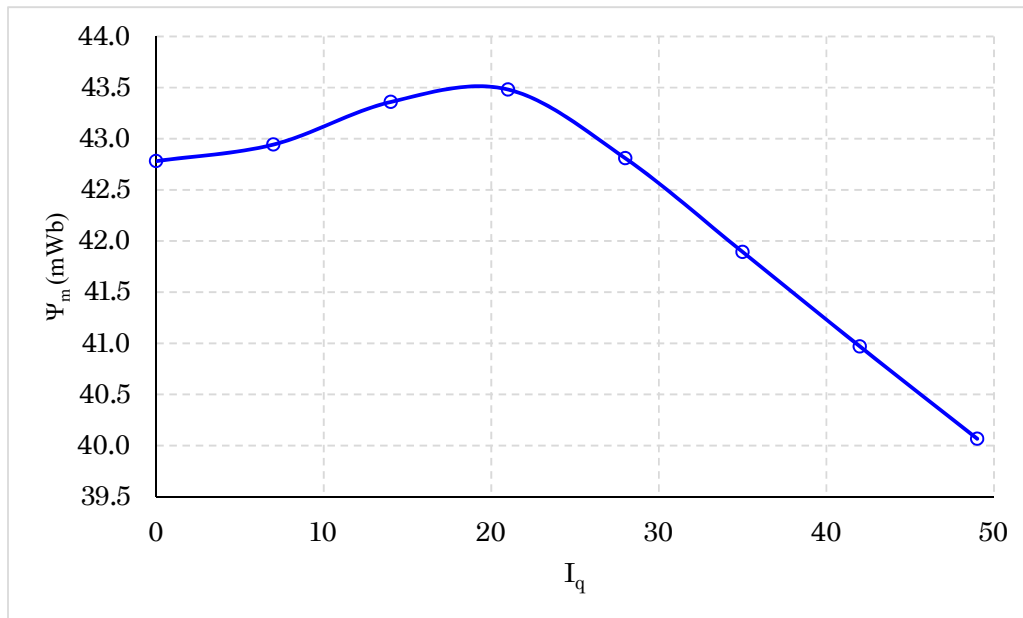
Figure 3.12. Variation of ψ_m with I_q, with $I_d = 0$.

The accuracy of the obtained equivalent circuit electromagnetic parameter model has been verified through comparison between the results from FEA simulations and those calculated from the model. Table 3.8 demonstrates that the torque calculation from the electromagnetic parameter model is almost identical to that obtained from the FEA, with the error in prediction being less than ~0.6%. The model has also been employed for calculation at other operating points and exhibited comparable accuracy.

Table 3.8. Comparison of calculated and FEA-predicted electromagnetic torque

Parameter	Unit	T_c at ω_b	T_{pk} at ω_b
I_d	A	-35.5	-66.7
I_q	A	31.8	45.8
Ld	mH	0.605	0.563
Lq	mH	2.75	2.14
$\dfrac{L_q}{\Psi_m}$	-	4.55	3.80
	mWb	42.23	40.40
T_e from FEA	N·m	16.96	30.00
T_e from model	N·m	17.07	30.17
% error between FEA and model	-	-0.65 %	0.56 %

3.4.4.3 Efficiency maps and energy consumption over driving cycles

The energy efficiency and energy consumption of the PMA SynRM over the NEDC and AUDC are shown in Table 3.9 and Figure 3.13, respectively. The energy efficiency over the combination of both driving cycles is also included in Table 3.9 for the purpose of completeness. The predicted results are based on a winding temperature of 120°C and a magnet temperature of 100°C.

The energy consumption is broken down to the main energy loss components generated by the traction machine along with the associated converter losses (calculated using the same approach as Chapter 2 and the given inverter specification) to consider the performance at a system level. The copper and iron losses are classified as low- and high-speed, where low-speed corresponds to maximum-torque-per-ampere (MTPA) operation, and high-speed corresponds to field weakening operation over the driving cycles. Owing to their distinct characteristics, the two driving cycles subject the drivetrain to different torque-

speed combinations, thereby, resulting into different energy loss distributions as can be seen from Figure 3.13. Energy loss associated with copper losses remains the loss component for both driving cycles for the case of PMA SynRM topology.

As can be observed, the optimised PMA SynRM design exhibits a relatively high energy efficiency of ~94.4% over the NEDC, which was set as the design objective, with a system energy efficiency (machine and converter) in excess of 90%. The efficiency over the AUDC is relatively lower due to the relatively higher torque demand associated with this driving cycle, which is conducive to higher copper loss, a characteristic of PMA SynRM over these driving cycles.

Table 3.9. Energy efficiency of optimised PMA SynRM over driving cycles

Parameter	NEDC	AUDC	Combined
Efficiency (without converter loss)	94.37%	92.79%	93.70%
Efficiency (with converter loss)	90.44%	88.06%	89.36%
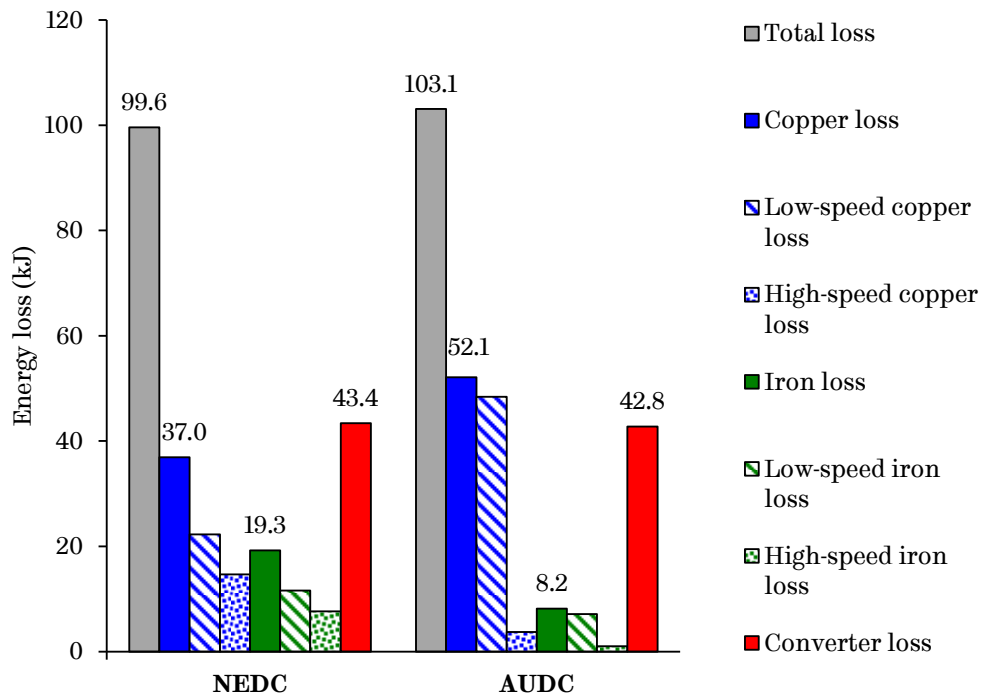
Figure 3.13. Energy loss components over NEDC and AUDC.

For completeness, Figure 3.14 and Figure 3.15 show the efficiency maps of the traction machine alone, and the combined traction machine and converter, respectively, employed for the determination of the energy losses over the driving cycles. As can be observed, the majority of the driving cycles' operating points lie over the high-efficiency regions.
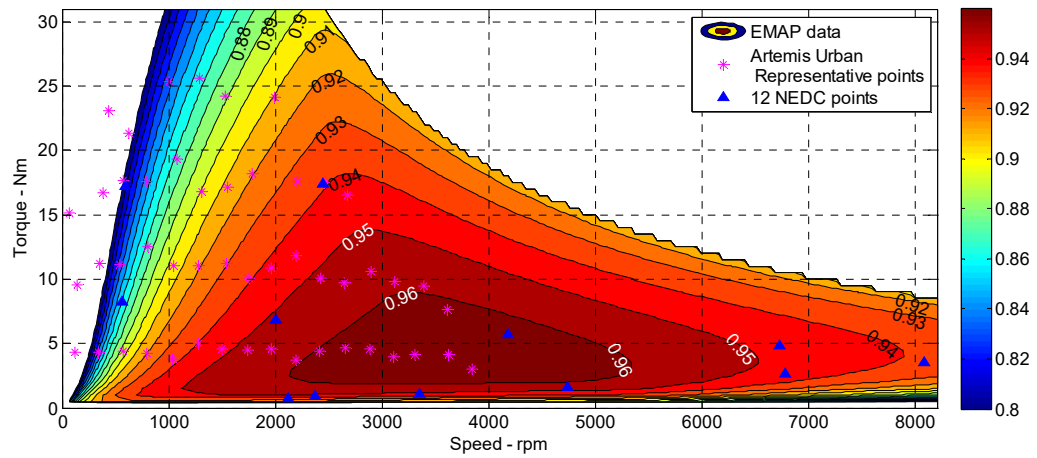
Figure 3.14. Efficiency map (in per unit values) of traction machine.
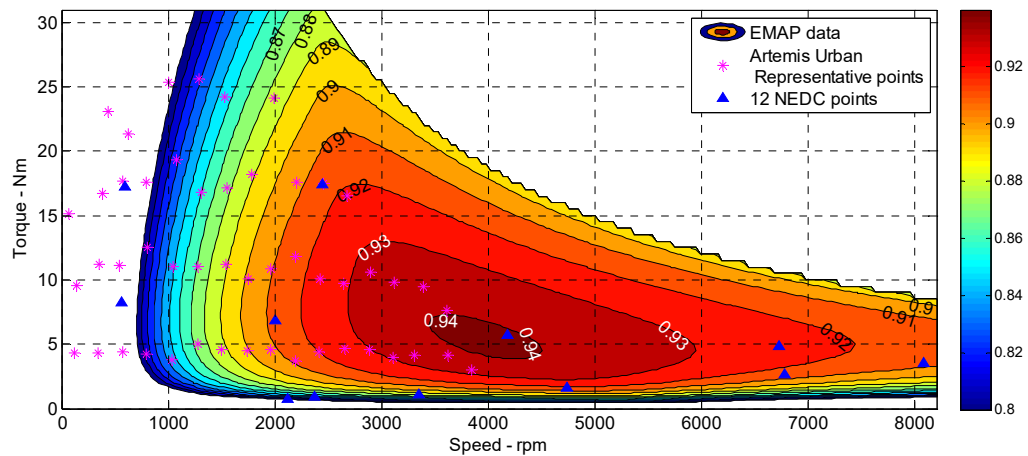
Figure 3.15. Efficiency map (in per unit values) of combined machine and converter.

3.4.5 Torque ripple analysis

Intrinsically high torque ripple is one of the demerits of the PMA SynRM topology due to its highly salient nature that underlines its operating principle. However, numerous techniques are now available that can rectify the high torque

ripple by means of skewing [86], flux barrier pairing and shaping [36],[37], [87]–[89], whilst leaving the remaining performance virtually unaffected (since torque ripple is more sensitive to minor geometrical modifications, such as the flux barrier angles and their opening). Further, in [90] a circular flux barrier has been introduced deep in the q-axis of the rotor (i.e., between adjacent poles) for the purpose of reducing the torque ripple of a fractional slot IPMSM. The aforementioned techniques can also be combined for more effective torque ripple reduction. Other approaches for the torque ripple reduction by means of control algorithms also exist. Therefore, torque ripple minimisation is considered as a post-process, applied once the design sample that exhibits optimised performance with respect to the defined design objectives and constraints has been identified.

The total electromagnetic torque ripple consists of three components:

- The cogging torque, which results from the interaction of the magnets in the rotor with the stator teeth as the rotor rotates.
- The interaction of the stator magneto-motive-force (mmf) with the magnets in the rotor
- The interaction of the stator mmf with the rotor saliency, which typically contributes the largest share in the total torque ripple in electrical machines that exhibit high reluctance torque.

The torque ripple requirement for EV applications should be as low as possible to avoid unwanted excessive noise and vibrations. For the investigated application a maximum limit of 5% is specified. However, the initial torque ripple of the optimised design was in the region of 22%. Therefore, additional torque ripple minimisation techniques are investigated in order to meet the design requirements. Initially, the flux barrier angles of alternate poles are varied and the torque ripple is examined as proposed by [36], [88]. This technique only resulted in a small torque ripple reduction for the employed rotor topology in the investigated EV application. In order to better understand the origins of the torque ripple, a technique proposed in [91], which enables the determination of the contribution from individual harmonics to the electromagnetic torque has been employed. The contribution from the nth harmonic is given by equation (3.27).

$$T_n = \frac{4\pi l_a r^2}{\mu_0} B_{r_n} B_{\theta_n} \cos(\phi_n) \qquad (3.27)$$

where, r is the airgap radius and l_a is the active axial length. B_{r_n} and B_{θ_n} are the magnitudes of the nth harmonic of the airgap radial and circumferential flux densities, respectively.

Figure 3.18 shows the contribution from the dominant harmonics to the total torque under the peak torque condition. As can be seen the 11th and the 13th harmonics in the airgap field are the largest contributors to the torque ripple, and are responsible for the 12th harmonic of the torque. Therefore, a significant reduction in torque ripple can be achieved by increasing the reluctance in the path of these harmonics through the introduction of features close to the surface of the rotor, given the short wavelength of these harmonics.
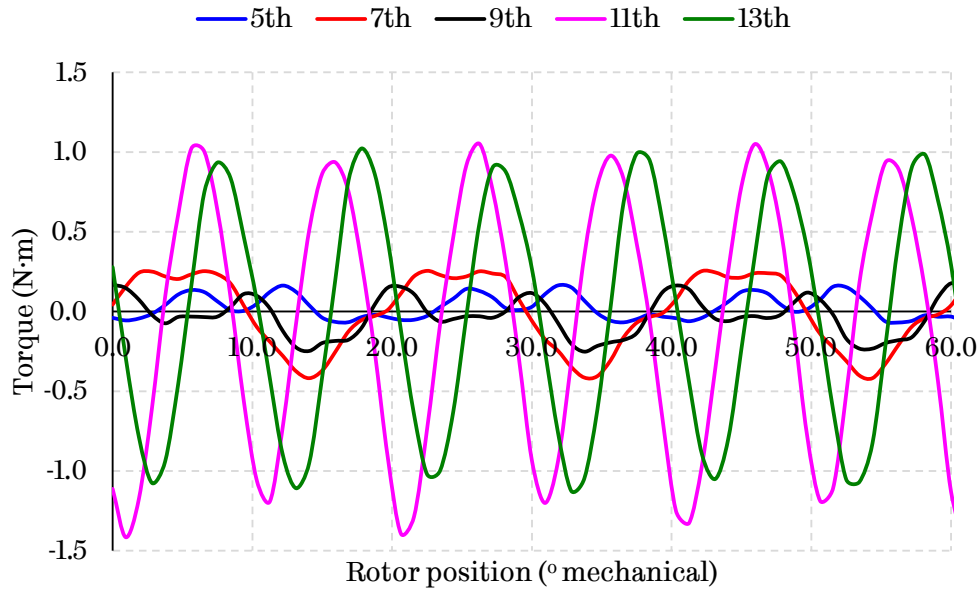
Figure 3.16. Variation of torque harmonics with rotor position for the design case without holes in the rotor steel.

Figure 3.17 shows the proposed circular features to be inserted in the rotor and their geometrical parameters, which need to be tuned accordingly in order to minimise torque ripple while taking the mechanical constraints into consideration. Figure 3.18 shows the effect of the holes inserted in the rotor on the

contribution of the major harmonics to the torque ripple. It can be observed that the contribution from the 11th and the 13th is significantly reduced.
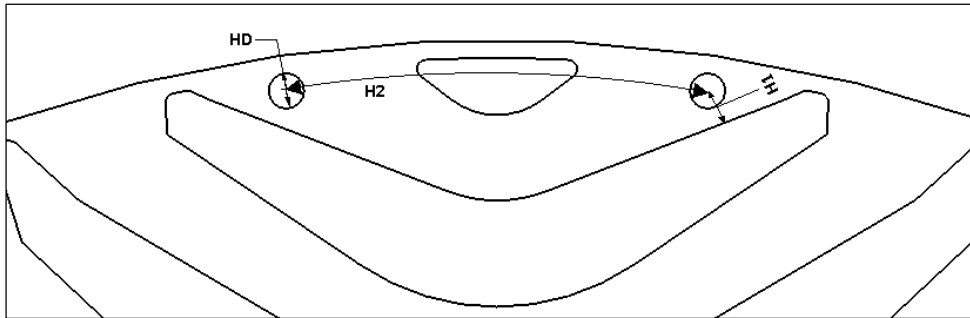
Figure 3.17. Geometrical parameters for the optimal sizing and position of the holes in the rotor steel for torque ripple minimisation.
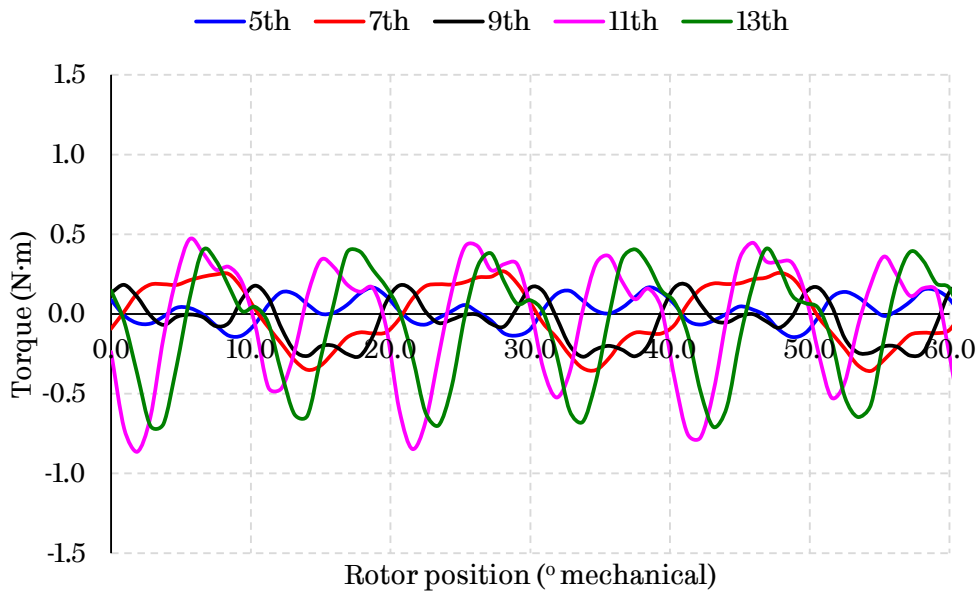
Figure 3.18. Variation of torque harmonics with rotor position for the design case with holes inserted in the rotor steel.

The comparison between the resultant instantaneous torque and the initial one prior to the insertion of the holes, as well as the corresponding torque harmonic spectrums are displayed in Figure 3.19 and Figure 3.20, respectively. It can be observed that there is a great reduction in the 12th torque harmonic, which is the most dominant in the torque ripple of the initial waveform. Note that the mean output torque remains largely unchanged after introducing the holes near the rotor surface (viz. <1% reduction).
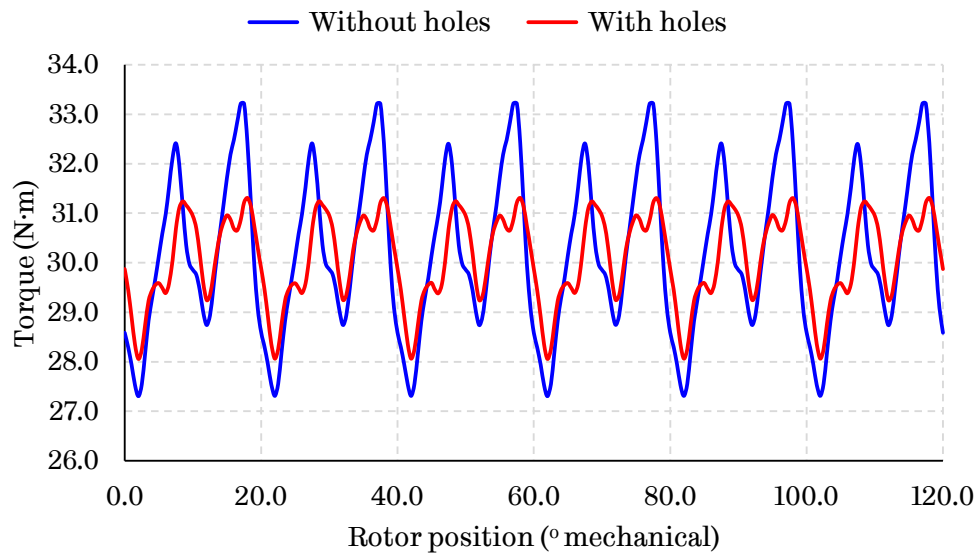
Figure 3.19. Comparison of instantaneous torque over one electrical cycle, prior and after the introduction of the circular features in the rotor.
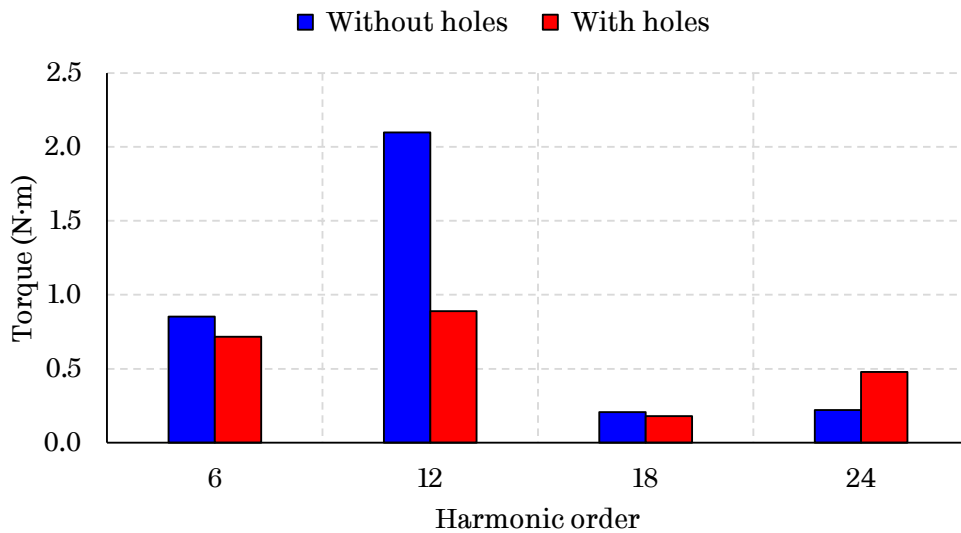
Figure 3.20. Comparison of major torque harmonics, prior and after the introduction of the circular features in the rotor.

Although the insertion of the holes nearly halved the torque ripple (viz., ~11%), in order to meet the design requirement (i.e., <5%) the use of rotor step-skew is still necessary. Therefore, different skew combinations were considered in order to achieve a torque ripple below 5%. The skew combinations as well as the obtained results are listed in Table 3.10. The commonly used half-slot skew was inadequate

to meet the given requirement, and therefore, a 7° mechanical 3-step skew has been selected. Table 3.11 summarises the final torque ripple for different torque-speed conditions at the extremities of the peak and continuous operating envelopes.

Table 3.10. Rotor step skew combinations

Number of steps	Skew angle (° mechanical)	Torque ripple (%)
2	5.0	9.1
3	5.0	6.3
3	**7.0**	**4.0**

Table 3.11. Torque ripple at critical operating points of torque-speed envelopes

Operating point	Torque ripple without skew	Torque ripple with skew
T_{pk} at ω_b	11.5%	4.0%
T_c at ω_b	9.8%	1.5%
T_{ms} at ω_{ms}	5.7%	2.7%
T_{cms} at ω_{ms}	3.1%	1.2%

3.4.6 Thermal analysis

The rear motor should be air-cooled with a totally enclosed non-ventilated cooling shell (TENV). The thermal requirements for continuous operation at the maximum cruise speed, derived from the NEDC power profile, should be satisfied in order to ensure safe thermal operation without excessive winding temperatures and magnet material degradation. Therefore, the maximum winding and magnet temperatures should be limited below 120°C. The ambient temperature in the model is set to 45°C.

A static thermal analysis was performed using MotorCad software [92]. The losses generated during continuous operation at the rated and maximum speed have been input to the software in order to produce the corresponding thermal models shown in Figure 3.21 and Figure 3.22, respectively. When the vehicle is driven at the maximum speed, an air velocity of 10 m/s is assumed for the forced motor cooling. The calculated model temperature at various parts of the motor is shown in Figure 3.21. As it can be observed, the winding and rotor temperatures

are well below the limit of 120°C, since PMA SynRM is characterised by an excellent field-weakening capability as well as inherently low iron loss. However, when operating at the base speed/continuous torque (Figure 3.22), where the air-velocity is scaled to 2.56 m/s, the temperatures are elevated but maintained below the temperature limit. This is mainly due to the rise in copper losses, since torque density is not a key trait of this topology (viz. weak magnets).

Based on these results, the thermally worst operating condition for this particular topology appears to be at the base speed with continuous torque for the investigated application, in contrast to the maximum speed with continuous torque, which is typically the case with conventional PMSMs. This can be attributed to the inherently low iron losses generated in the PMA SynRM topology, which do not significantly contribute to the temperature rise at maximum speed, as is the case with conventional PMSMs (also employing a distributed winding). An additional factor that may contribute to this outcome may be the relatively lower torque density of the PMA SynRM, which leads to increased temperature rise over continuous operation at base speed.
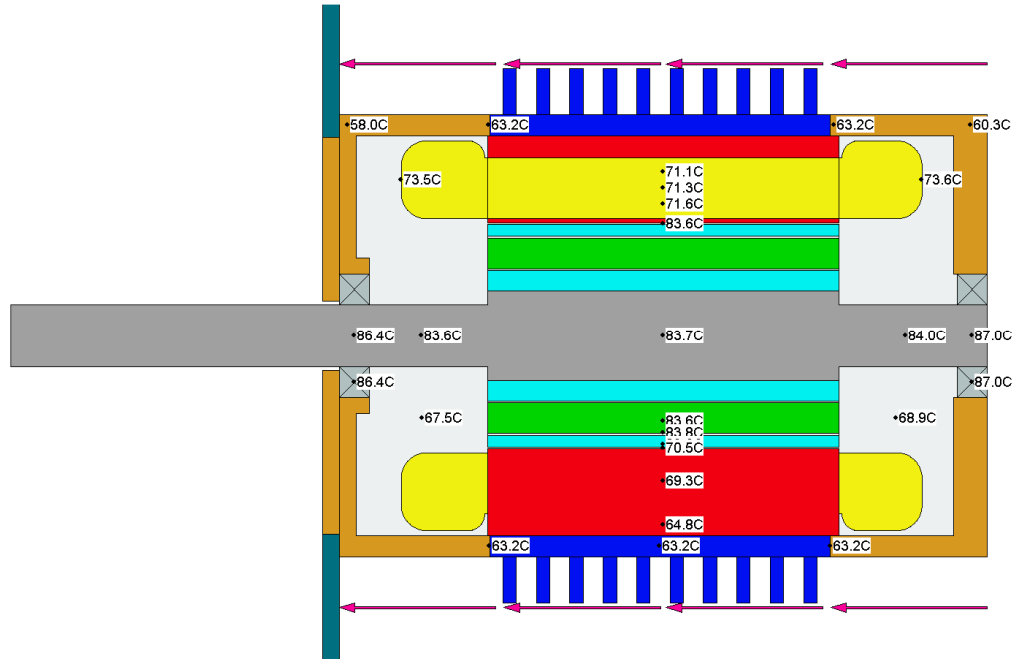
Figure 3.21. Steady-state temperature prediction at T_{cms} and ω_{ms} (i.e., 4.4Nm, 8200r/min).
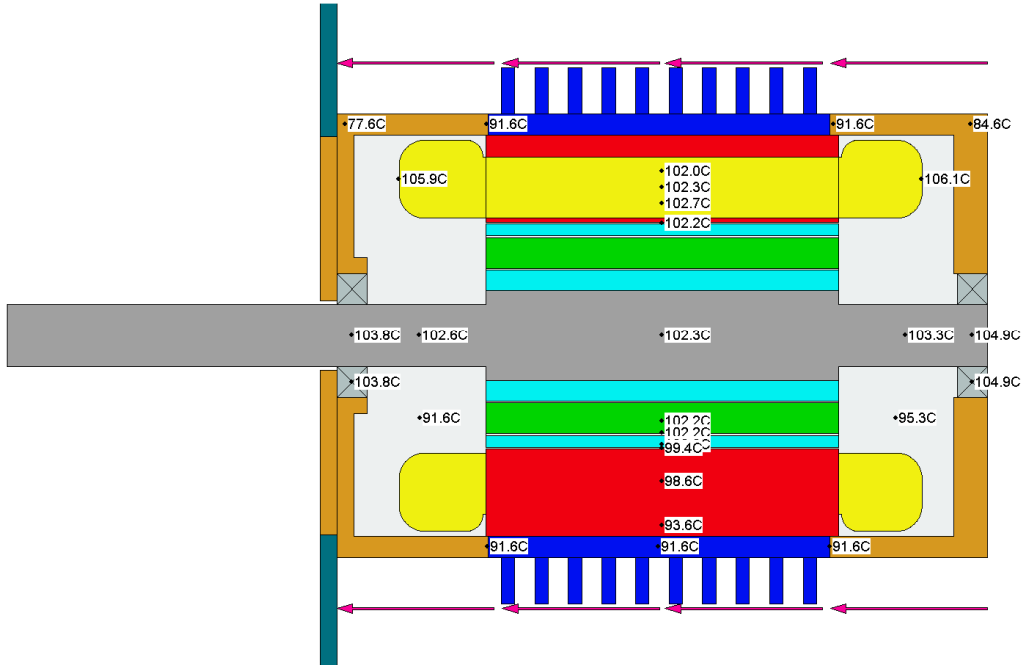
Figure 3.22. Steady-state temperature prediction at T_c and ω_b (i.e., 17Nm, 2100rpm).

The transient thermal model for peak torque operation at base speed is illustrated in Figure 3.23. This effectively represents the acceleration or curb-climbing operations of the vehicle. The maximum temperature rise above the ambient (reference) becomes 24°C at the end windings after 90 seconds of operation and 2.56 m/s air velocity (cooling). It is evident that copper loss is the dominant cause of temperature rise under this operating condition. The temperature rise for other motor parts during the transient operation are also illustrated in Figure 3.23. Figure 3.24 shows the instantaneous temperature variation of the rotor and windings when the traction machine operates over repeated driving cycles for the case of the NEDC and AUDC. The cooling air velocity is set as a function of the operating speed with 10 m/s corresponding to the maximum rotating speed. As can be seen, the steady-state temperatures over the two driving cycles are well within the specified thermal limit. As expected, the temperatures obtained while operating over the more aggressive AUDC are higher than those obtained while operating over the more moderate NEDC. The characteristically different energy loss distributions over the two driving cycles are reflected by the instantaneous temperature variation of the rotor and stator windings.
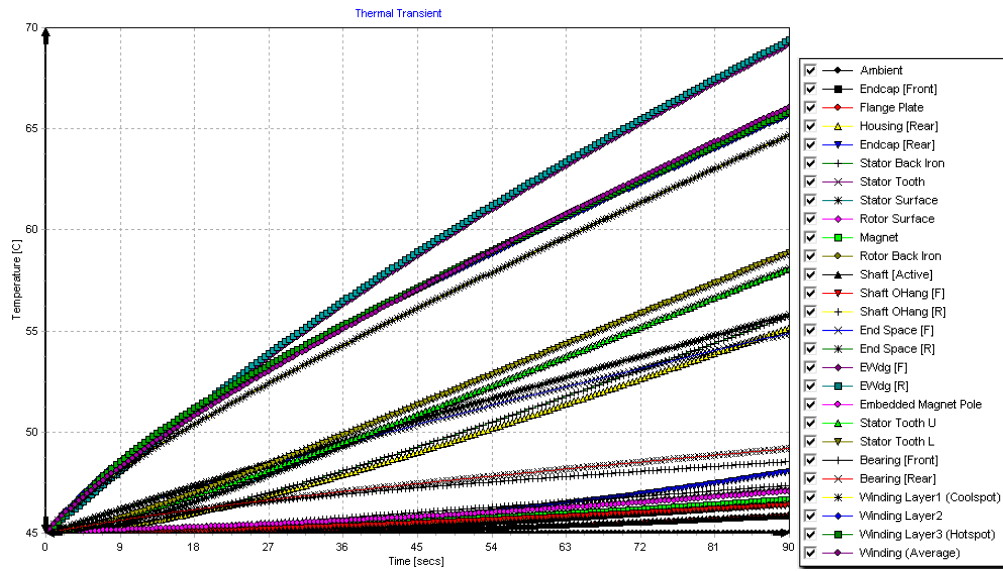
Figure 3.23. Transient temperature prediction for T_{pk} and ω_b (i.e., 30Nm, 2100rpm).
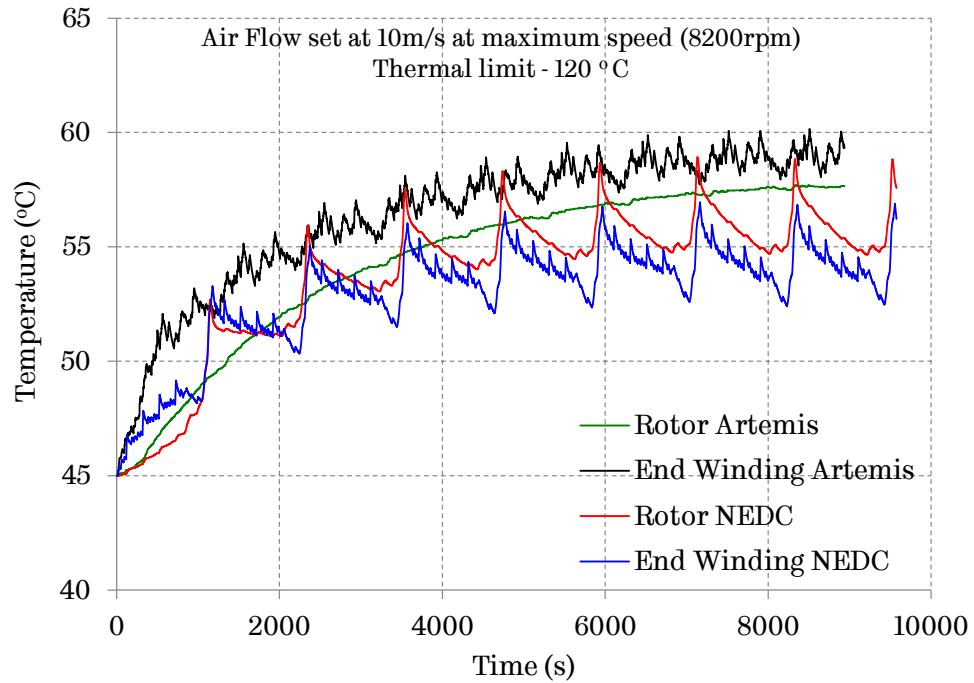
Figure 3.24. Transient variation of temperature when the machine operates through
several NEDC and AUDC cycles until the temperatures approaches steady-state.

3.4.7 Demagnetisation analysis

The armature reaction field in this particular machine topology is strong, since a large current is required in order to obtain the high torque (typically required for acceleration and overtaking during driving), due to the weak embedded magnets. Thereby, the low remanence bonded NdFeB magnets employed in the machine are subject to a strong demagnetisation field resulting from the armature reaction. The risk of irreversible demagnetisation becomes high, when an excessive armature reaction occurs, causing the magnet operating point to move over the knee of the demagnetisation characteristic. Consequently, the magnet is unable to recover to its original state leading to permanent performance deterioration.

The degree of performance deterioration is dependent on the severity of permanent demagnetisation under a particular operating scenario. This causes an avalanche effect, where a higher current will be required to deliver the same torque, leading to increased temperature and thermal stress to the winding insulation, which in turn shortens the lifespan of the machine. Thus, it was essential to consider the demagnetisation effect during the designing process in order to ensure the motor's performance under different operating conditions. The aim of the analysis was to identify the worst operating condition, where the magnets are more vulnerable to demagnetisation, and evaluate the effect on the machine's electromagnetic performance.

The demagnetisation analysis was conducted considering a common failing mechanism of traction machines, where a large current increase occurs when the saturating voltage at the controllers' switches exceeds a pre-set limit and the controller (trying to protect itself) drops the DC link voltage. The generated current, resulting from the voltage difference, can be very similar to the transient short circuit current of the motor. In order to simulate such a condition using the finite element method, the motor is initially operated in steady-state until suddenly a three phase short circuit is triggered. This simulation was performed against the peak torque at both base and maximum speed operating points of the torque-speed envelope. The first considers the operation under maximum-torque-

per-ampere (MTPA), while the second condition represents the field weakening operation.

Unlike ferrite, bonded NdFeB magnets are more prone to demagnetisation at elevated temperatures where the knee point becomes more prevalent. The presence of a polymer binder in this type of material increases its strength against any external demagnetising field making it more difficult to get demagnetised when compared to sintered NdFeB magnets. According to the thermal analysis results illustrated in the previous section, the maximum operating magnet temperatures lie near 100°C. At this temperature, the knee point on the demagnetising (B-H) curve of bonded NdFeB magnet material appears to be below 0T as observed by the B-H characteristics of Figure 3.25. Therefore, during the analysis, any magnet region with a flux density below 0T is considered irreversibly demagnetised.
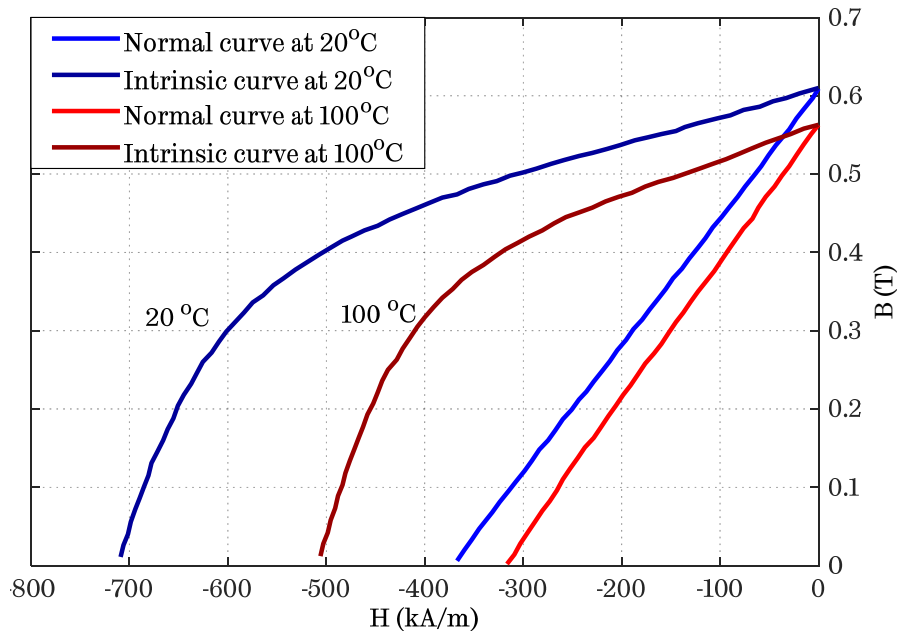
Figure 3.25. B-H characteristics of employed bonded NdFeB at different temperatures.

Demagnetisation studies were performed prior and after the optimisation process. The preliminary studies were done in order to ensure the magnet's ability to withstand demagnetisation through appropriate geometry modifications and prepare the model for performance optimisation. The transient *d-q* current vector trajectories against the two operating conditions under consideration are shown

in Figure 3.26 and Figure 3.27, respectively. As it can be observed, the current vector follows a spiral trajectory in the clockwise direction after the short circuit is triggered until it reaches steady-state represented by the core of the spiral.

The amplitude of the short circuit current vector at the condition where the motor is operating at T_{pk} , ω_b is 40% larger compared to that at T_{ms} , ω_{ms} operation. This can be attributed to the low magnet remanence, which implies that a lower demagnetising current is required during field weakening operation at high speeds, and a higher current requirement during MTPA operation. Therefore, the most severe demagnetisation occurs at T_{pk} , ω_b operating point for this motor topology. Under this operating condition, the coils were already energised with a high current required to produce the peak torque while an additional current component (resulting from the back-emf) is added after the short circuit is triggered. Consequently, the increased energy stored in the coils has to interact with the rotor magnets thereby causing irreversible demagnetisation. The instantaneous currents as well as the generated torque, prior and after the short circuit, are illustrated in Figure 3.28 and Figure 3.29, respectively.
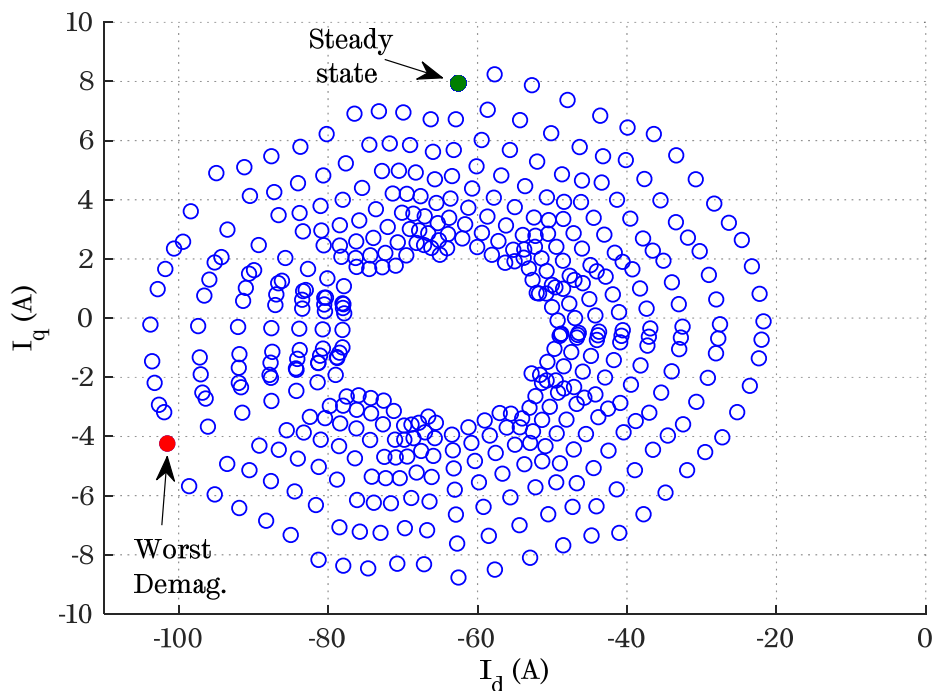
Figure 3.26. Transient d-q current trajectory at T_{ms} and ω_{ms} under short circuit fault.
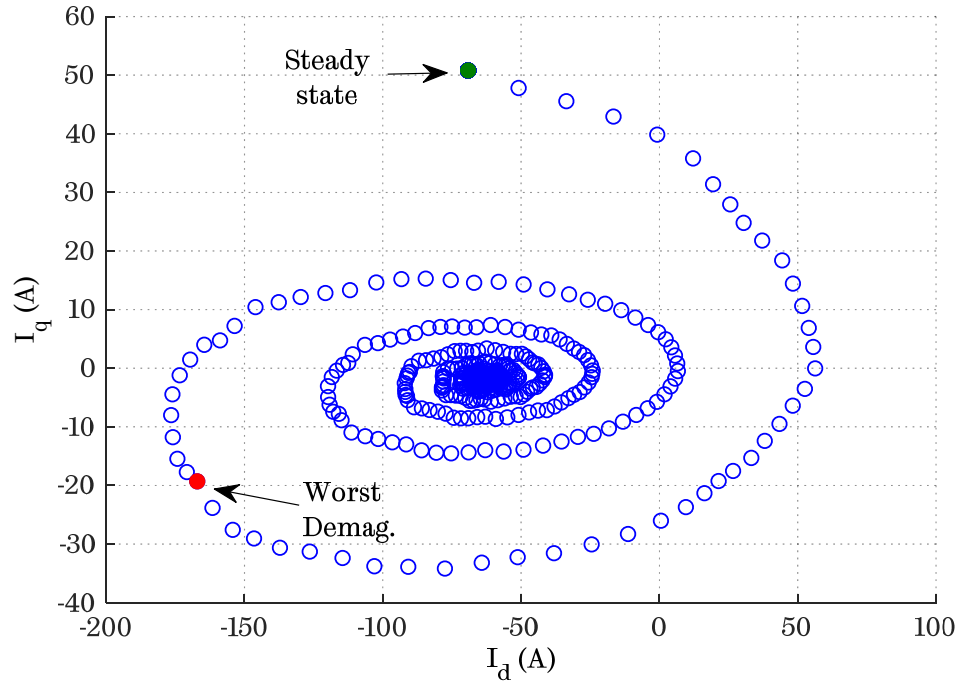
Figure 3.27.   Transient d-q current vector trajectory at T_{pk} and ω_b under short circuit fault.
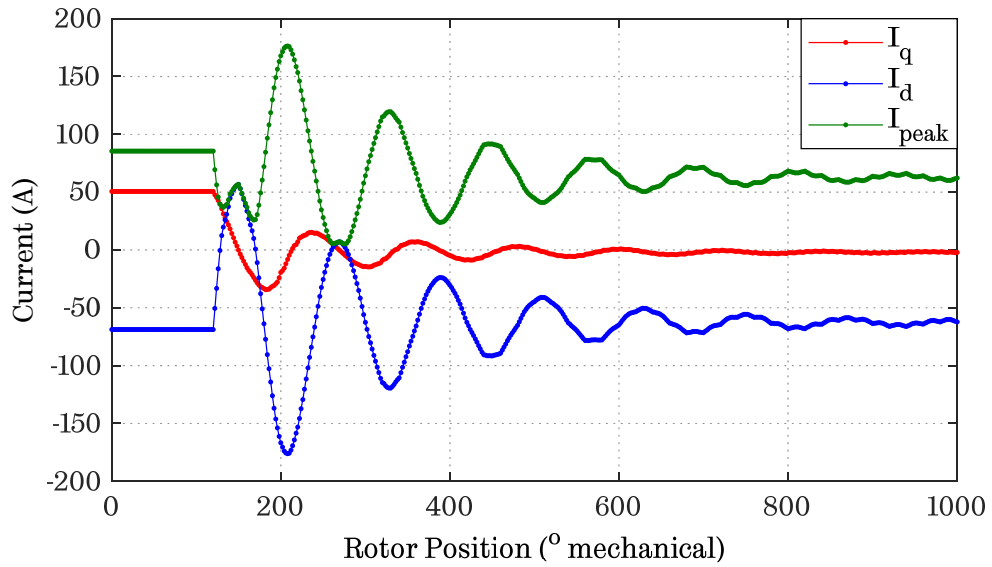
Figure 3.28.   Instantaneous current prior, and after short circuit at T_{pk} and ω_b.
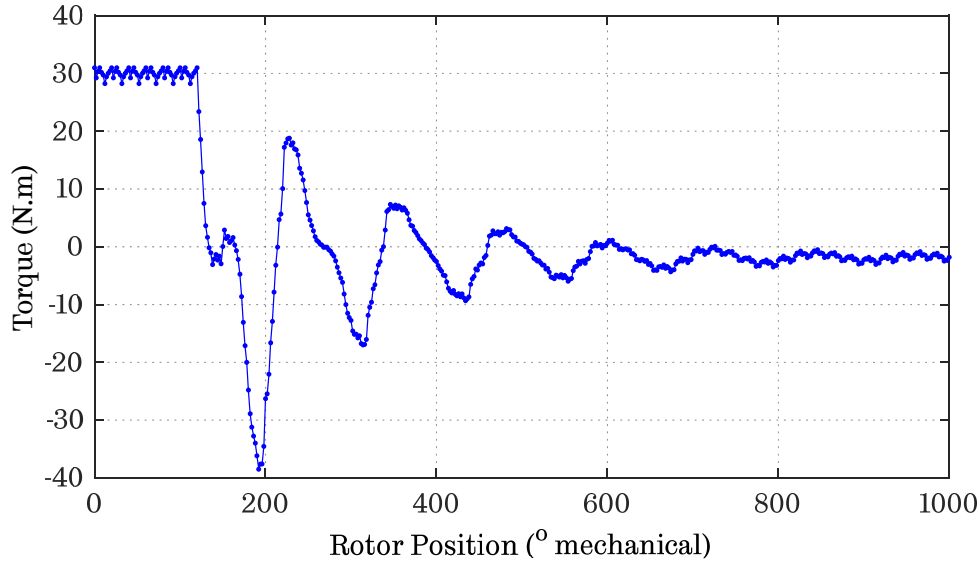
Figure 3.29. Instantaneous torque prior, and after short circuit at T_{pk} and ω_b .

The demagnetisation is evaluated by calculating the projection component of the magnet flux density (B_d) with respect to the magnetisation direction at each rotor position as shown by equation (3.28).

$$B_d = B_x \cos(magnet\ direction + rotor\ position)$$
$$+ B_y \cos(magnet\ direction + rotor\ position) \qquad (3.28)$$

This is performed for each node of the magnet surface. When the field projection (B_d) is lower compared to the knee point, the magnet element is judged to be irreversibly demagnetised. The projection component of the flux density in the magnets of the optimised PMA SynRM, when the machine is exhibited under the two different operating conditions, are shown by the contour plots of Figure 3.30. The demagnetisation analysis results obtained from the simulations under different operating scenario are summarised in Table 3.12. As shown by the data of Table 3.12, it can be deduced that there is no risk of irreversible demagnetisation under steady-state operation along the full range of the peak torque-speed envelope.

However, in the case of a short circuit fault or a controller failure the peak generated current can become two times the steady state peak current at T_{pk} and ω_b. Consequently, a small portion of the outer magnet layer becomes irreversibly demagnetised. The magnet sides close to the flux barriers are more influenced by

demagnetisation, since the opposing armature reaction flux tends to flow around the flux barrier region where the reluctance path is smaller, as indicated in Figure 3.31. This is because the flux barrier thickness is smaller compared to that of the magnet. Therefore, during the design and optimisation process, the magnet thickness of the outer layer was sufficiently increased, and the flux barriers were tapered, in order to guide the armature reaction flux away from the magnets and, thus, enhance the demagnetisation strength of the motor [71], [79], [93].

a) Worst case demagnetisation at T_{pk} and ω_b

b) Worst case demagnetisation at T_{ms} and ω_{ms}
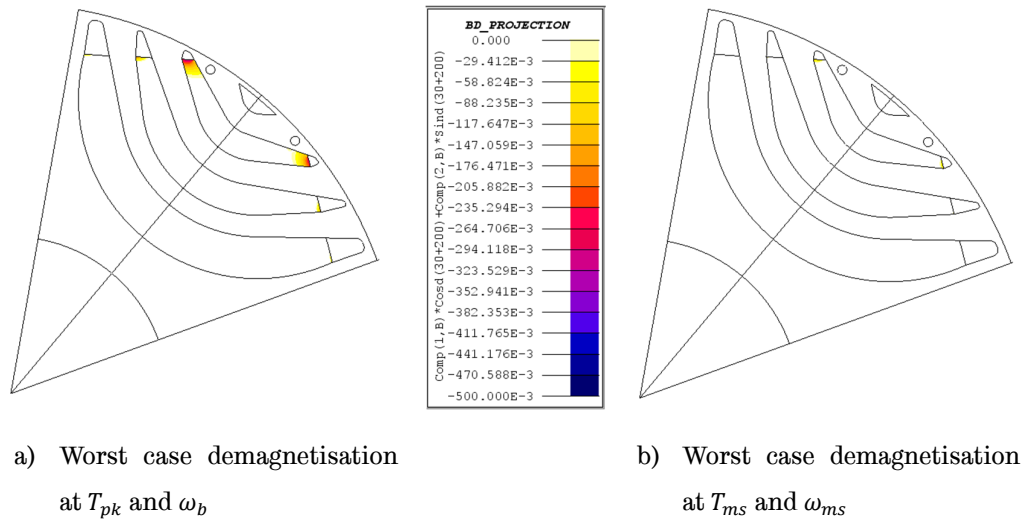
Figure 3.30. Contour plots of magnetic flux density projection on the rotor magnets, under the two extreme operating points of the torque-speed envelope.
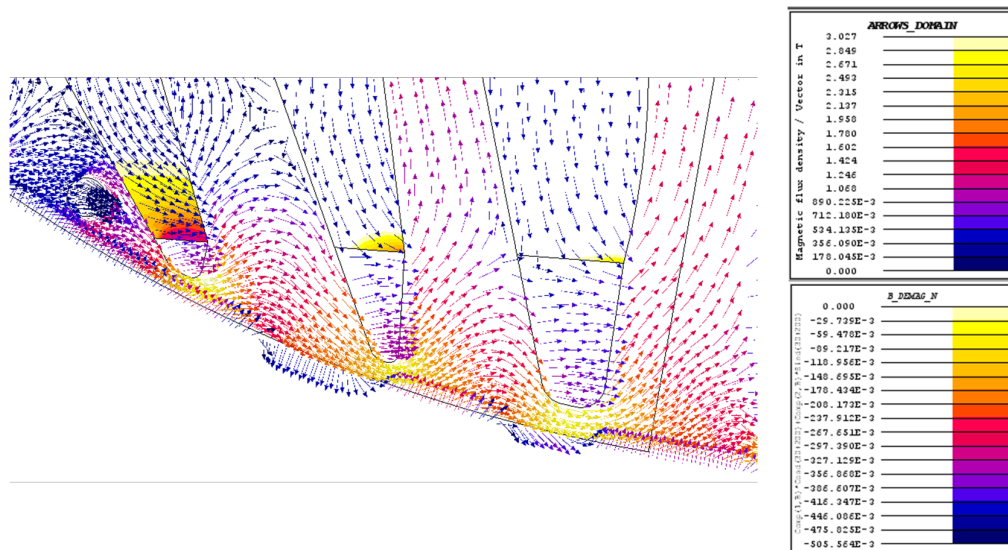
Figure 3.31. Flux density distribution at the worst-case rotor position (i.e., 200°), while operating at T_{pk} and ω_b.

Table 3.12. Demagnetisation analysis results during transient and steady-state operation

Parameter	Unit	T_{pk} at ω_b transient	T_{ms} at ω_{ms} transient	T_{pk} at N_b steady-state
Max. number of demagnetised nodes	-	234	30	4
% of demagnetised magnet area	-	6.4 %	0.8 %	0.1 %
Min. demagnetisation flux density	T	-0.34	-0.15	-0.07
Rotor position at worst demagnetisation	°mech.	200	200	every 20°
Worst demagnetising I_d	A	-166.73	-101.40	-68.80
Worst demagnetising I_q	A	-19.45	-4.23	50.63

In order to evaluate the effect of demagnetisation on the motor performance, the irreversibly demagnetised portion of each magnet layer under the worst case scenario displayed in Figure 3.30 (a) (i.e., T_{pk} and ω_b), was replaced by air and a new back-emf was obtained. The comparison between the back-emf spectra prior and after irreversible demagnetisation is illustrated in Figure 3.32. The fundamental back-emf component has been decreased by ~2.9%, indicating a reduction of the same amount on the alignment torque component (i.e., the torque contributed by the rotor magnets), which comprises ~30% of the total output torque in this motor topology. Given, however, the ratio of the torque components in the investigated PMA SynRM, the influence of the slightly reduced back-emf is expected to be minimal on the total output torque due to the significant reluctance torque component. Thereby, the traction machine could virtually continue operating as normal, even after the occurrence of such a fault. This can be classified as one of the attractive attributes of this topology.
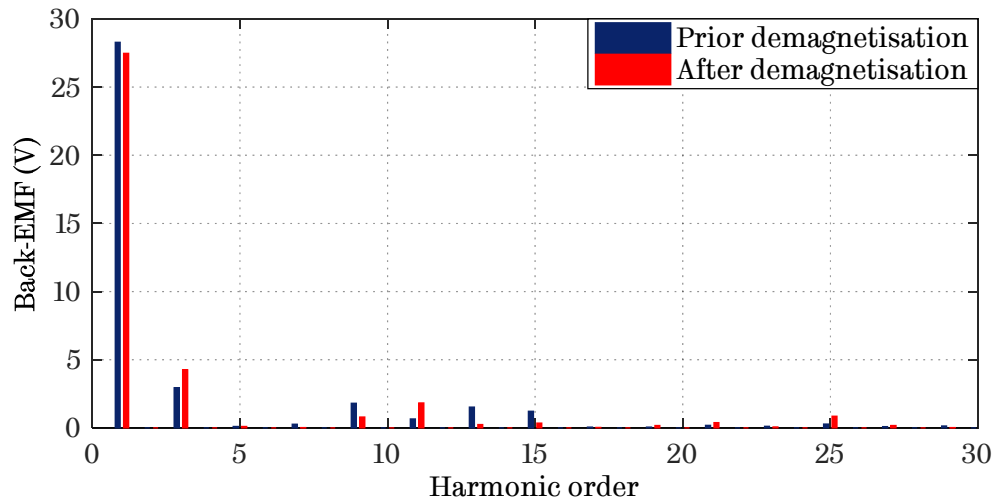
Figure 3.32.   Comparison of phase back-emf spectra prior and after demagnetisation .

3.4.8 Mechanical stress analysis

In order to finalise the optimised design and proceed to prototyping, several design iterations were conducted to satisfy all the required design constraints. The mechanical stress at the bridges of each magnet layer, resulting from the centrifugal forces generated while the rotor is rotating, should be analysed to guarantee the mechanical integrity of the rotor at maximum speed operation. According to the yield strength of the lamination material used, the stress level should be maintained below 450 MPa at 1.5 times the maximum operating speed (i.e. 12300 rpm).

There is always a trade-off between the mechanical strength and the magnet flux leakage at the rotor bridges. Therefore, the bridge thickness of each rotor layer was optimised in order to satisfy the mechanical stress requirement while keeping the thickness to a minimum. The analysis results are shown in Table 3.13. The selected bridge thicknesses, starting from the outer rotor layer and moving inwards, are 0.4, 0.4 and 0.6 mm respectively. The maximum stress level of 438 MPa occurs at the inner layer bridges, which have the largest mass to support as it can be observed by Figure 3.33 and Figure 3.34. In addition, the low mass density of the employed magnet material (viz. bonded NdFeB) circumvented the need for a middle bridge and consequently, the requirement of two magnet blocks per rotor layer.

Table 3.13. Mechanical stress analysis for tuning the bridge thickness of each rotor layer

First layer thickness (mm)	Second layer thickness (mm)	Third layer thickness (mm)	Maximum stress (MPa)	Maximum stress location
0.20	0.20	0.20	1120	third layer bridge
0.30	0.30	0.50	691	third layer bridge
0.37	0.37	1.80	408	second layer bridge
0.35	0.40	1.20	352	second layer bridge
0.30	0.40	1.00	365	first layer bridge
0.32	0.40	0.90	360	first layer bridge
0.32	0.40	0.70	380	third layer bridge
0.32	0.38	0.80	366	first layer bridge
0.32	**0.38**	**0.60**	**438**	**third layer bridge**
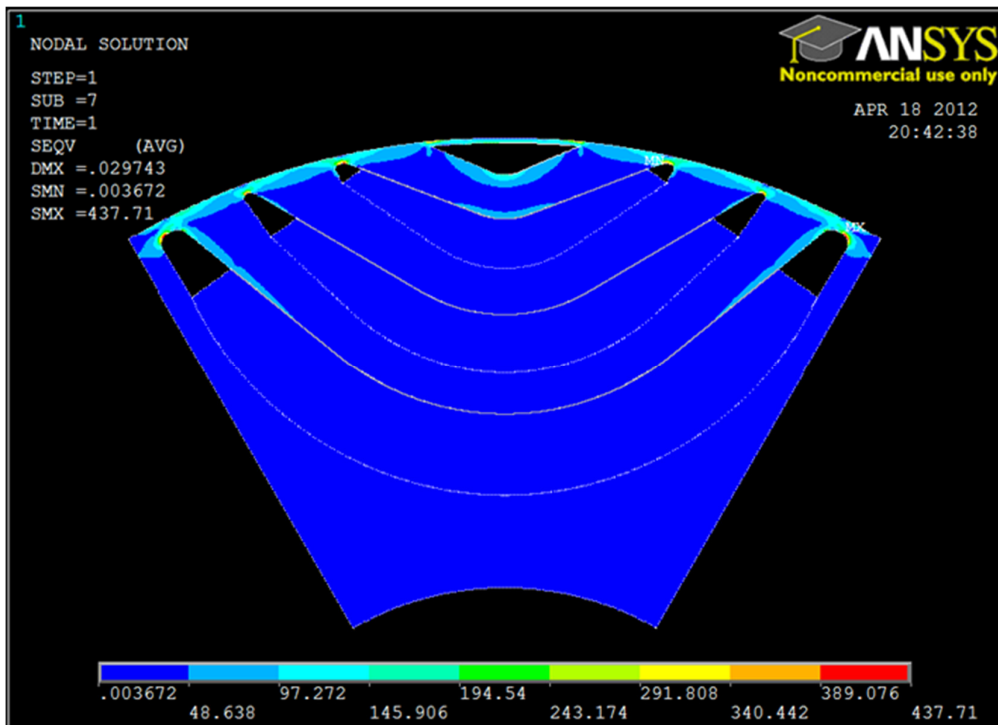
Figure 3.33. Von mises stress contour plot – rotor overview.
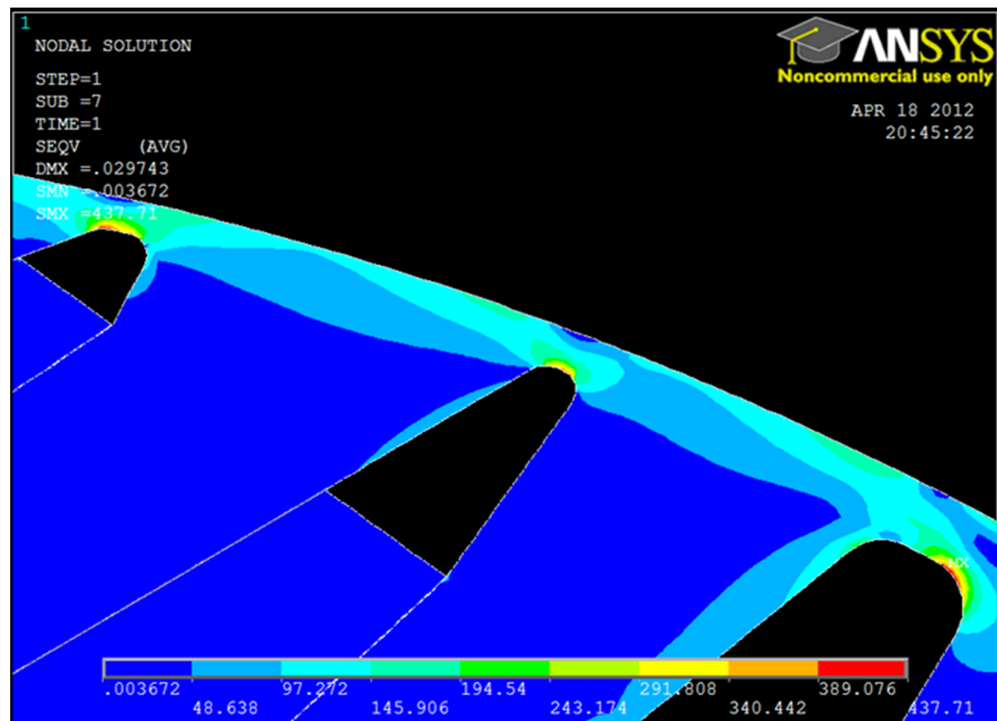
Figure 3.34. Von mises stress contour plot – zoomed detail at rotor layer bridges.

3.5 Remarks

The potential energy efficiency gains arising from the combination of dissimilar machine topologies/technologies and the application of a dynamic torque distribution strategy to the front- and rear-wheel motors in a distributed traction powertrain is discussed and quantified. It is shown that such an implementation, combined with a dynamic torque distribution strategy, can lead to energy efficiency improvements of around 1 % when the powertrain operates over the NEDC.

A key focus of this chapter is the design of the rear-wheel machines of the Hi-Wi EV. A thorough investigation is conducted for the design of the traction PMA SynRM, with the aim of optimising its performance over the NEDC while satisfying the torque-speed requirements. The selected design is subjected to an iterative comprehensive multi-physics analysis including electromagnetic, thermal, and mechanical. An energy efficiency in excess of 94% is achieved over the NEDC.

Several design techniques are investigated and combined to minimise the intrinsically high torque ripple of this machine topology. The output torque at the operating condition, where the torque ripple is most severe, is decomposed based on the airgap field harmonics to better understand its source. In combination with rotor step-skew, the torque ripple has been minimised below the 5% requirement, frequently associated with EV traction applications.

Chapter 4

Accurate *d-q* axis Modelling of Synchronous Machines with Skew Accounting for Saturation

*This chapter exemplifies the influence of skew on the magnetic behavior (i.e. flux-linkages and inductances) and torque characteristic of a synchronous machine. Thereby, it proposes a computationally efficient semi-analytical technique to accurately derive the electromagnetic parameter model of a synchronous machine incorporating skew, whilst taking into account the effect of saturation and d-q axis cross-coupling. The proposed technique uses only one set of 2D finite element (FE)-computed data corresponding to the unskewed machine, and can be applied for the prediction of either average or instantaneous d-q axis flux linkage and torque of any synchronous machine with an **n** number of skew slices and any skew angle. The validity of the technique is verified by FE analysis and measurements obtained from a prototype Permanent Magnet Assisted Synchronous Reluctance machine (PMA SynRM) developed for a traction application.*

The main contents of this chapter are published by the author in [94].

Stator or rotor skewing, one of the most effective and frequently employed techniques to minimize cogging torque, electromotive force (emf) harmonics and electromagnetic torque ripple, influences the machine's electromagnetic behaviour, i.e. flux-linkages and inductances, which are most commonly used to predict the motor's performance. Numerous analytical, semi-analytical and FE-based methods have been developed for the prediction of parameters in a machine's electromagnetic model with due account of the influence of skew. Analytical techniques are often unable to emulate the non-linearities exhibited in machines characterized by high magnetic saturation, thus numerical (FE) computations are deemed necessary for high accuracy. FE-based methods, being the most computationally intensive, make use of 3D or 2D analysis. In the case of 3D analysis, the computational time and numerical memory costs remain the highest, while in the case of 2-D analysis, multiple-slice solutions along the skew

axis, coupled by means of the electric circuit, are required to effectively represent skew [95], [96].

Although the computational time for the most commonly used, multi-slice 2D model is relatively reduced compared to 3D FEA, it still remains computationally intensive as the problem linearly scales with the number of slices employed in the machine model [97]. Semi-analytical methods appear to be the most viable, considering the trade-off between computational time and accuracy. The semi-analytical method proposed in [98] does not consider the influence of d-q axis cross-coupling on the machine's parameter model. Whilst this was improved in [98], the methods presented in both [98] and [99] make use of a skew factor to account for the effect of skew on the electromagnetic parameter model of the machine, and thus, through assumptions, neglect the effect of axial variation in magnetic saturation introduced by skew [100]. In cases where high magnetic anisotropy is exhibited or the skew angle is relatively large, this effect can significantly influence the saturation-dependent electromagnetic parameters of the skewed machine. Employing a skew factor to modify the machine's electromagnetic parameters does not inherently account for this effect. Further, neither [98], nor [99] consider the prediction of instantaneous variation of flux linkage and torque with rotor position in their proposed models.

This chapter proposes a simple and computationally efficient semi-analytical technique for the accurate derivation of a machine's electromagnetic parameter model by incorporating the effect of skew, and accounting for both axial variations in saturation and d-q axis cross coupling. The proposed method is applicable for the prediction of either average, or instantaneous d-q axis flux linkage and torque of any synchronous machine (provided that no damper bars are used in the rotor) with an n number of skew slices and any skew angle. Its effectiveness is validated by multi-slice FE computations and measurements obtained from a prototype motor developed for a traction application.

4.1 Influence of skew on the machine's electromagnetic behaviour

Skew causes axial variation of airgap flux density, and can therefore result in variation of saturation in both stator and rotor lamination along the axial length of the machine. The saturation-dependent electromagnetic parameters (i.e. equivalent circuit parameters) will, thus, be altered when the machine is skewed and as a result, the performance of the machine may change [86], [100]. It is therefore important to examine the effect of skew on the electromagnetic parameters, with the aim of developing a technique, which can include these effects and provide improved accuracy, while being computationally efficient, in predicting the equivalent-circuit parameters and performance of synchronous motors employing skew.

Without loss of generality, the results provided in this and following sections are for the 3-phase, 6-pole and 36-slot PMA SynRM developed in Chapter 3 for the Hi-Wi EV application, which employs a rotor skewed in three steps by an angle of 7° mechanical (viz., -3.5^o, 0°, $+3.5^o$). The traction motor has outside diameter and axial length of 120mm and 105mm, respectively, and should deliver a power of 3.75kW under continuous and 6.6kW under peak operation. This motor topology inherently exhibits high magnetic anisotropy, which translates to a high degree of non-linearity, and thus was considered as a suitable design case for the analysis conducted in this chapter. The high magnetic anisotropy of this machine topology (PMA SynRM) stems from the rotor structure, where multiple air flux barriers are located in the direction of the d-axis introducing high reluctance in that path, whereas no barriers exist in the q-axis path. Note that d-axis represents the magnetisation direction of the embedded magnets. The absence of flux barriers in the q-axis thereby translates to high permeance (i.e., low reluctance) in that path. The difference in reluctance between the d- and q-axis is characterised as magnetic anisotropy.

Figure 2.2 illustrates the relative magnetic permeability (μ_r) distribution in the stator and rotor electrical steel laminations of each slice at different axial position of the skewed PMA SynRM, when the peak current (viz., 97A) is injected to

the stator windings. The degree of variation in magnetic permeability (μ_r), and hence saturation, along the skew axis (i.e., z-axis) of the simulated machine can be clearly observed. This variation results from the alteration of the current phase angle with respect to the d- or q-axis at different slices of the skewed machine along the axial co-ordinate. The influence of such axial variation in saturation on the machine's d- and q-axis inductances, L_d and L_q, over the entire d- and q-axis operating current ranges, I_d and I_q, is quantified in Figure 4.2 with data obtained from multi-slice FE analysis. Note that the cross-coupling between the d and q axes was taken into account in the calculation process employed to derive L_d and L_q.
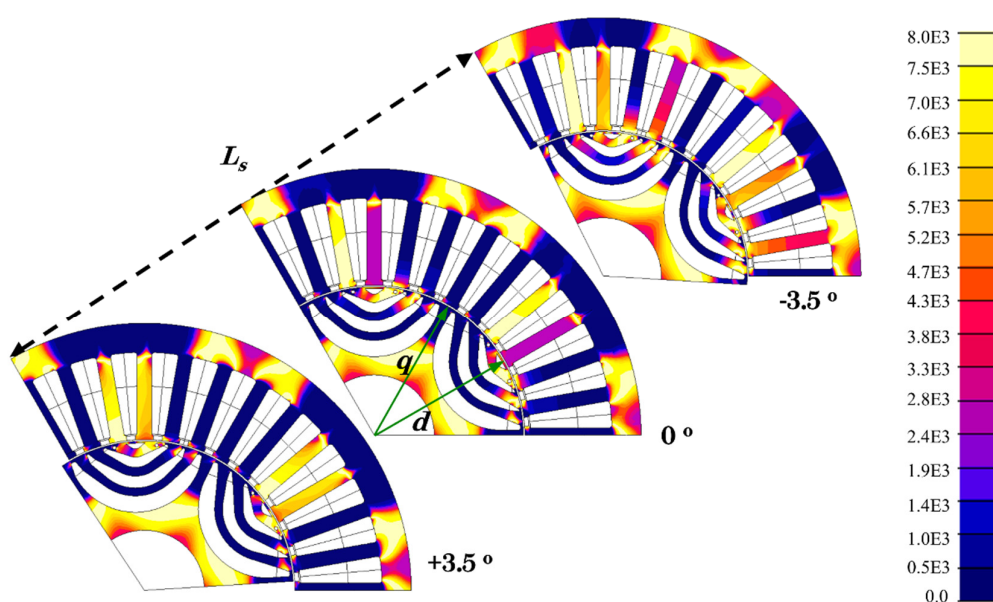
Figure 4.1. Variation of magnetic permeability (μ_r) along the axial direction of the skewed PMA SynRM, with the peak current of 97A (i.e., I_d=-80A, I_q=55A) injected to the stator windings.

It is evident that skew can, indeed, result in considerable variation of d- and q-axis inductances under certain d-q axis current combinations, which can exceed 15% in some cases. The degree of variation in magnetic flux density, and hence inductances, due to skew is dependent on d-q axis current excitation levels which in turn define the saturation level in the core. More specifically, the variation in both L_d and L_q is more aggravated when I_q is relatively low ($I_q < 40A$), which translates to lower core saturation that is, in turn, conducive to larger inductance

deviations resulting from the change of the current phase angle at each skew slice. As I_q increases, the d-q axis inductance variation reduces since saturation starts to occur.
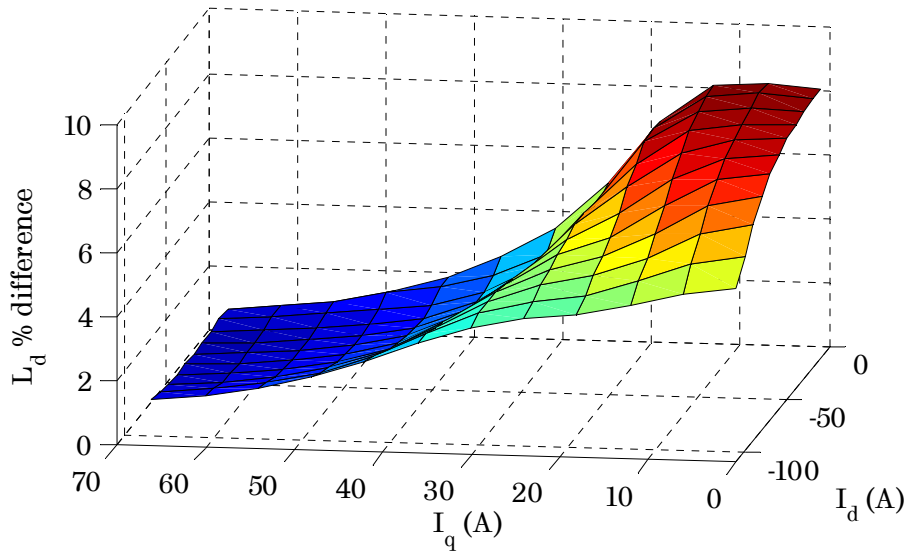
(a) d-axis inductance – L_d
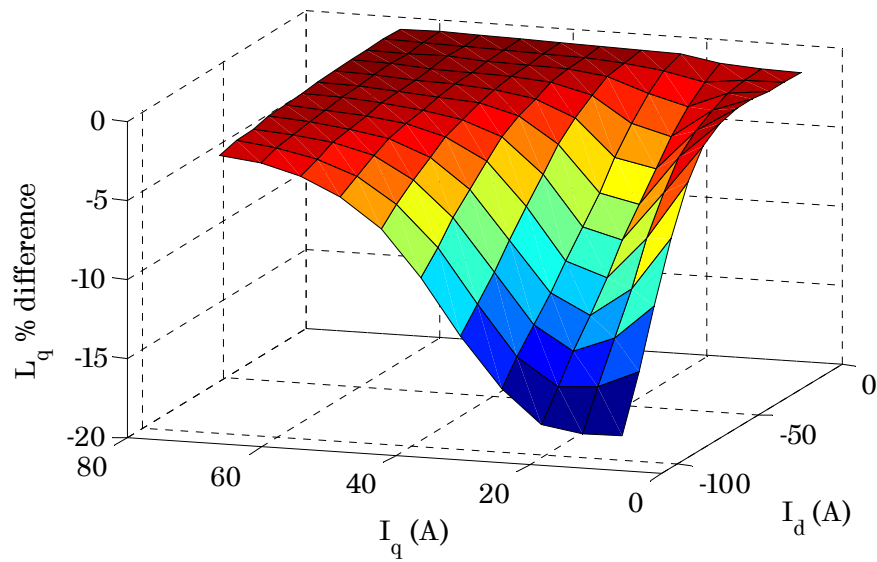
(b) q-axis inductance – L_q

Figure 4.2. Percentage change of d- and q-axis inductances resulting from skew (with respect to the machine without skew).

In summary, skew causes L_d to increase, while L_q decreases. This trend results in a reduced saliency ratio (i.e., L_q/L_d) and inductance difference (i.e., $L_d - L_q$), and thus inferior reluctance torque production (for the same input current) is to be expected compared with the case of the unskewed machine. In addition, the field weakening (FW) capability of the skewed machine can be affected as skew leads to a change in the value of magnet flux linkage (Ψ_m) and L_d, the ratio of which defines the steady-state short-circuit current (I_{sc}) of the machine (i.e., I_d at which d-axis flux linkage, $\Psi_d = 0$, hence, $I_{sc} = \Psi_m/L_d$). The ratio of I_{sc} over the rated current of the machine is frequently used in the literature to characterize the FW capability of the machine [74]. For instance, in the case where the ratio ψ_m/L_d normalized to the rated current equals to the optimal value of 1.0 (which theoretically infers infinite speed), the FW capability would deteriorate as L_d tends to increase and ψ_m reduces after skew. Note from Figure 4.2 (a), that the largest increase in L_d due to skew occurs at low I_q values for all I_d range, which corresponds to the current trajectory under FW operation.

The above assertions can be verified by the plots of Figure 4.3 and Figure 4.4. Figure 4.3 shows the ratio of inductance difference of the skewed machine over that of the unskewed one (i.e., $\frac{L_{d_{sk}} - L_{q_{sk}}}{L_{d_{unskew}} - L_{q_{unskew}}}$) as a function of the d- and q-axis current. Where, a value < 1 indicates a lower inductance difference for the skewed machine and vice versa. This particular plot is indicative of the reluctance torque capability of an IPMSM considering that the product of inductance difference by the d- and q-axis currents represents the reluctance torque component of total torque based on the classical 2D analytical torque equation (4.29) of an IPMSM [101]. Whereas, the product of q-axis current by Ψ_m represents the torque contributed by the magnets in the rotor.

$$T = \frac{m}{2}p(\Psi_m I_q + (L_d - L_q)I_d I_q) \qquad (4.29)$$

where, m is the number of phase and, p is the pole pair number.
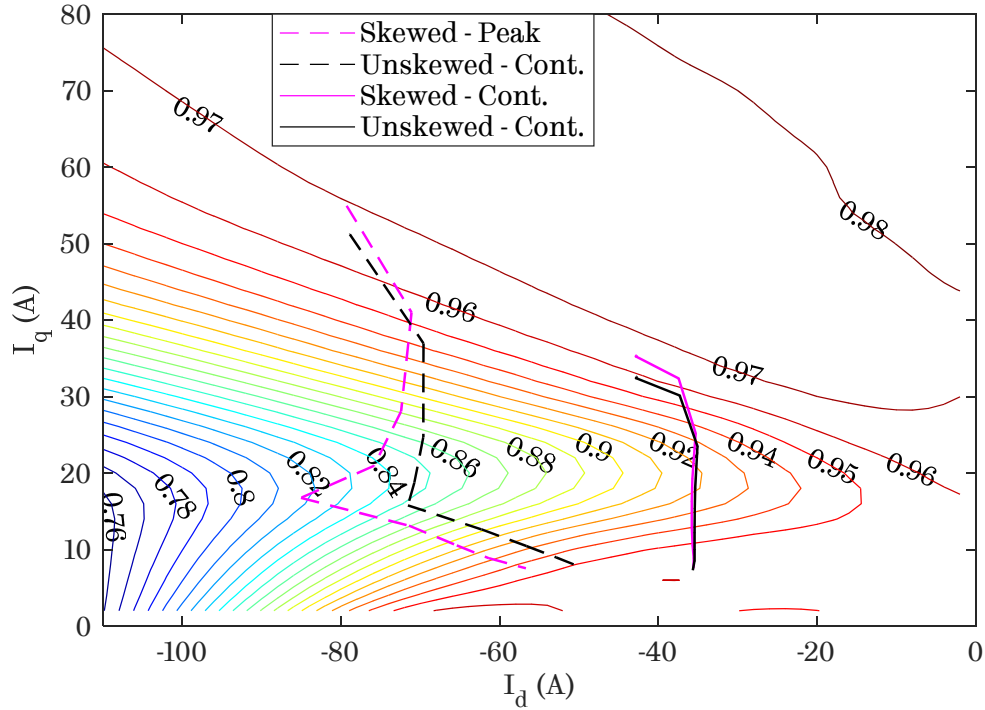
Figure 4.3. Ratio of inductance difference of the skewed machine over the unskewed one

(i.e., $\frac{L_{d_{sk}} - L_{q_{sk}}}{L_{d_{unskew}} - L_{q_{unskew}}}$) as a function of d- and q-axis current.

Based on the plots of Figure 4.3, it can be clearly seen that the skewed machine sees a reduction in its inductance difference, which infers a diminished reluctance torque capability. Particularly in the current region where I_q <30A and $I_d < -30$A. A reduction of reluctance torque capability of up to 24% is visible. This correlates well with the plots of Figure 4.4, which show the ratio of output torque produced by the skewed machine over that of the unskewed one as a function of I_d and I_q for the total, as well as the reluctance and magnet torque components. Where, values <1 indicate a lower output torque of the skewed machine. A close inspection of the plots reveals that the major contributor to the total torque reduction due to skew is the reluctance torque component. Whereas, the torque reduction attributed to the magnet torque component is <1.2%. This occurs because the magnetic insulation between the d and q axes becomes compromised when skew is introduced. As a result, the inductance difference between the two axes, which is responsible for the reluctance torque production, reduces after skew as previously demonstrated.
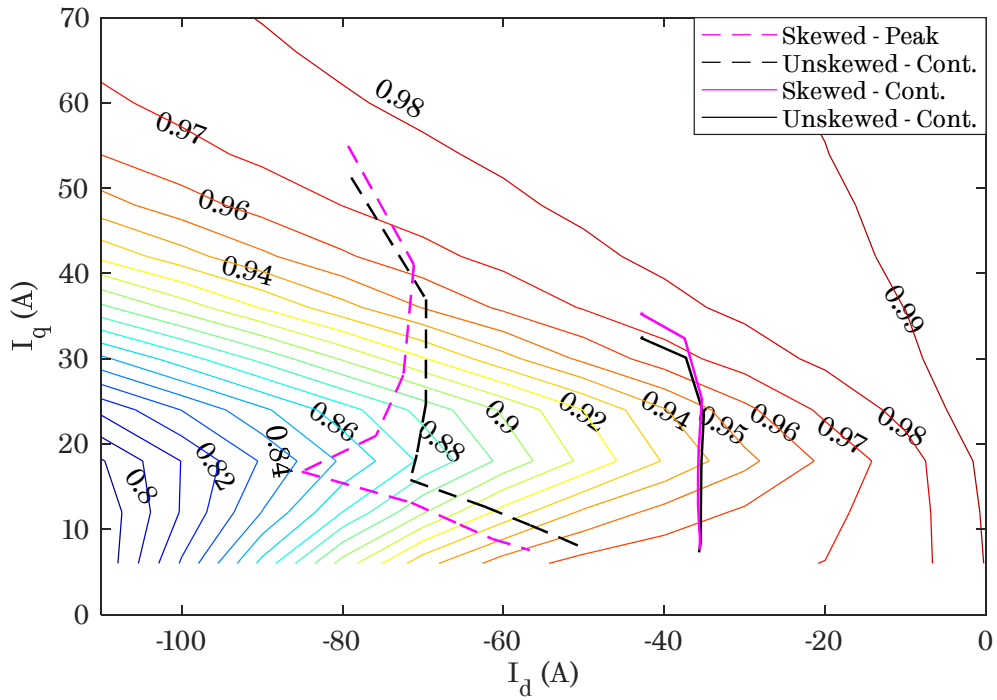
(a) Total torque variation
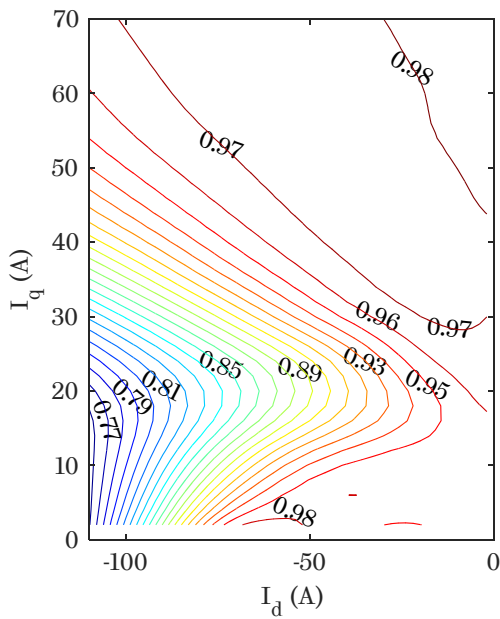
(b) Reluctance torque
variation
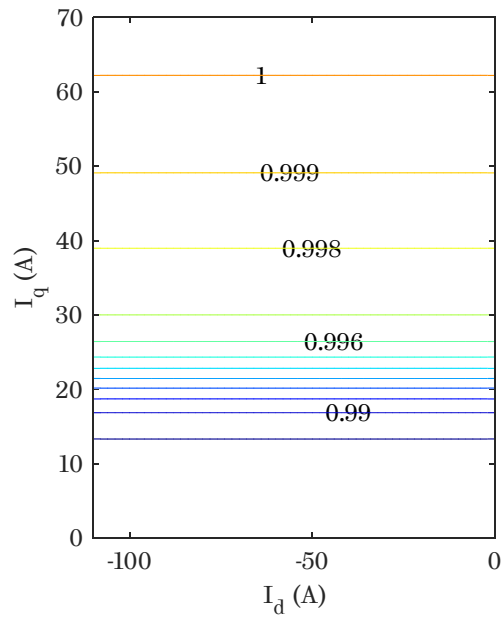
(c) Magnet torque variation

*Figure 4.4. Ratio of output torque produced by the skewed machine over the unskewed
one as a function of the d- and q-axis current.*

The reduced reluctance torque capability in combination with the slight reduction in PM-flux and the increase of L_d, due to skew, cause the maximum-torque-per-volt (MTPV) operating mode to kick-in at an earlier speed since more current is now required to deliver the same torque, while the voltage limit remains the same. Thus, influencing considerably the FW operation of the machine after skew, with increased energy loss over the operating envelopes and lower maximum attainable torque under the same dc-link voltage. The deterioration of the FW performance is more pronounced when the machine operates towards the peak torque-speed envelope, where the machine is pushed to its limits.

This can be clearly observed through a comparison between the d- and q-axis current trajectories of the skewed and unskewed machines corresponding to the peak operating envelope in the plot of Figure 4.4 (a). On the other hand, the FW performance over, and below, the continuous operating envelope is on par between the skewed and unskewed machines, as can be observed by comparing their corresponding current trajectories. This is due to the fact that the difference between their reluctance torque capability reduces towards that operating region (viz., Figure 4.3). The current amplitude required to deliver the torque in the lower speed region (MTPA operation), however, is consistently higher for the skewed machine over both the continuous and peak operating envelopes. The aforementioned effects will ultimately translate into an efficiency reduction for the case of the skewed machine.

Figure 4.5 illustrates the efficiency difference map between the unskewed and skewed machine, where a positive value indicates a higher efficiency for the unskewed machine and vice versa. The skewed machine exhibits a lower efficiency throughout the majority of the operating range. The highest difference in efficiency, however, manifests in the operating regions where the speed is relatively low, and where the machine operates toward its maximum torque trajectory under FW. This aligns well with the trends explained above. The progressively higher efficiency difference exhibited in the lower speed region (i.e., <1500rpm) can be primarily attributed to the fact that the iron loss is very low in that operating region. Hence, the energy efficiency is now largely dictated by the copper loss, which is directly influenced by the diminished reluctance torque capability of the skewed machine.

Additionally, the relatively low output power, at such low operating speeds, also contributes to this result.
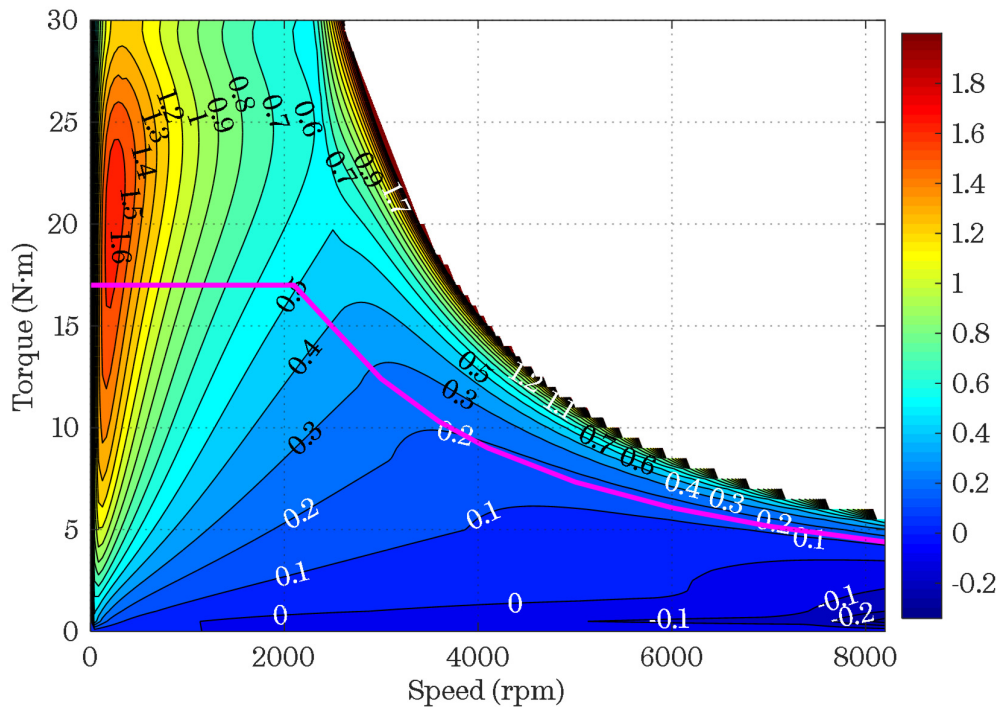
Figure 4.5. Efficiency difference map between the unskewed and skewed machine
(i.e., $\eta_{unskewed} - \eta_{sk}$) in percentage.

The investigation into the effects of skew on the performance of the studied traction machine highlights the importance of incorporating such effects in the prediction of the machine's electromagnetic parameter model during the design and optimization process. The multi-slice FE method automatically considers the effect of skew, but it still remains computationally intensive due to the numerical solution of multiple skew slices. The existing computationally efficient method to account for the effect of skew employs a skew factor (k_{sk}), which is used to modify the electromagnetic parameters obtained from a single set of 2D FEA calculations corresponding to the unskewed machine [98], [99]. However, the modification of the electromagnetic parameters by means of a skew factor (k_{sk}) does not intrinsically account for the effect of axial variations in saturation introduced by skew [100], which in turn result into the aforementioned changes in flux linkage and inductance.

To perform a comparison between the two methods, the semi-analytical model proposed in [99] was employed to predict the d- and q-axis inductances of the skewed PMA SynRM under consideration. The percentage error resulting from the prediction of L_d and L_q by employing a skew factor, with respect to the results obtained from the multi-slice FEA, is quantified over the entire d-q axis current range in the surface plots of Figure 4.6.
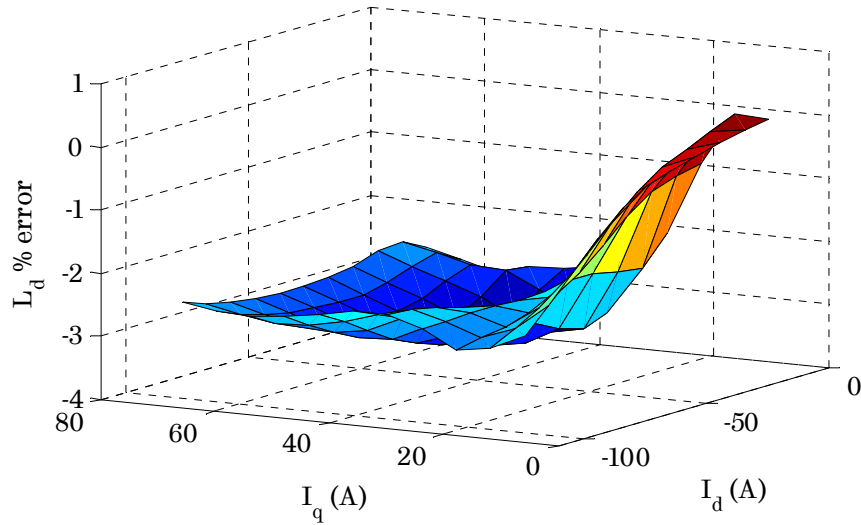
(a) d-axis inductance – L_d
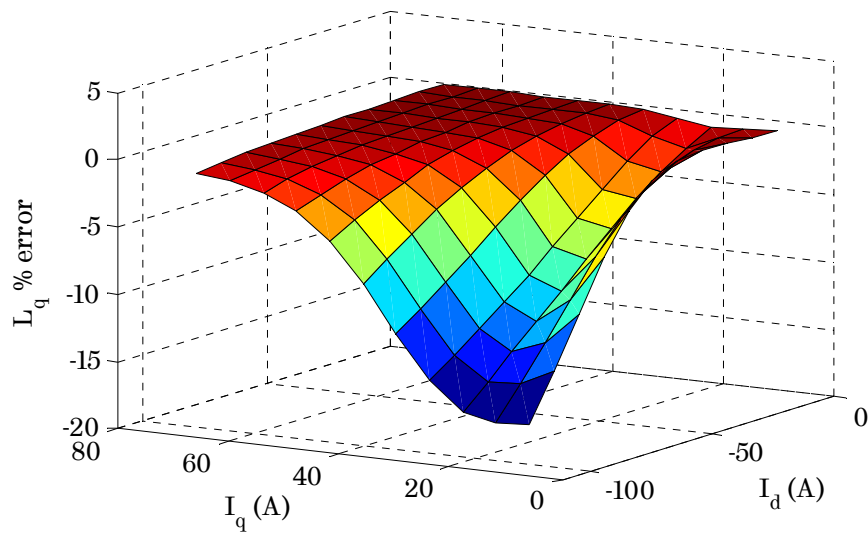
(b) q-axis inductance – L_q

Figure 4.6. Percentage error in predicting the d-q axis inductances of the skewed machine by employing a skew factor (k_{sk}).

As can be observed from Figure 4.6, the prediction of L_d is not far from the results predicted from the multi-slice FEA, with the absolute percentage error being up to ~4%. However, in the case of L_q the prediction error remains relatively large (viz. up to 18% maximum error) as the q-axis (i.e., high permeance axis) is more sensitive, and hence more influenced by variations in magnetic saturation. Now that the influence of skew on the machine's electromagnetic parameters has been examined and quantified, the proposed computationally efficient model that can account for its effects will be described and compared with the multi-slice FEA method in the following section.

4.2 Proposed technique for the prediction of d-q axis electromagnetic parameter model accounting for skew

The proposed model is based on a single 2D FE-computed look-up table (LUT), corresponding to the unskewed machine, in the form of d-q axis flux linkage variations, ψ_d and ψ_q, with d-q axis currents, I_d and I_q, which includes all non-linearities and saturation effects present in the 2D domain. As this method explicitly relies on 2D domain for the FE computations, end-effects and axial leakage flux components present in the 3D domain are not considered. It should be noted that the skew does not influence the effect of end-winding but does affect the axial flux leakages between skewed slices. The influence of such 3D effects on the performance of step-skewed PMA SynRM machines will be discussed in Chapter 5. The model uses complex vector notation and for the purpose of simplicity in explaining the proposed technique, a 2-slice skewed machine example is considered.

The vector diagrams illustrated in Figure 4.7 provide a visual interpretation of the d-q axis current and flux linkage vectors corresponding to the skewed and unskewed slices, and will assist in the derivation of the mathematical model. At first, the average flux linkage vector as functions of d- and q-axis currents is established from transient or multi-static FE solutions over one electrical cycle, or one sixth of the electrical cycle (due to symmetry exhibited in the case of a balanced

3-phase system). The average flux linkage is subsequently used as the reference to account for the effect of skew by employing the technique described below.
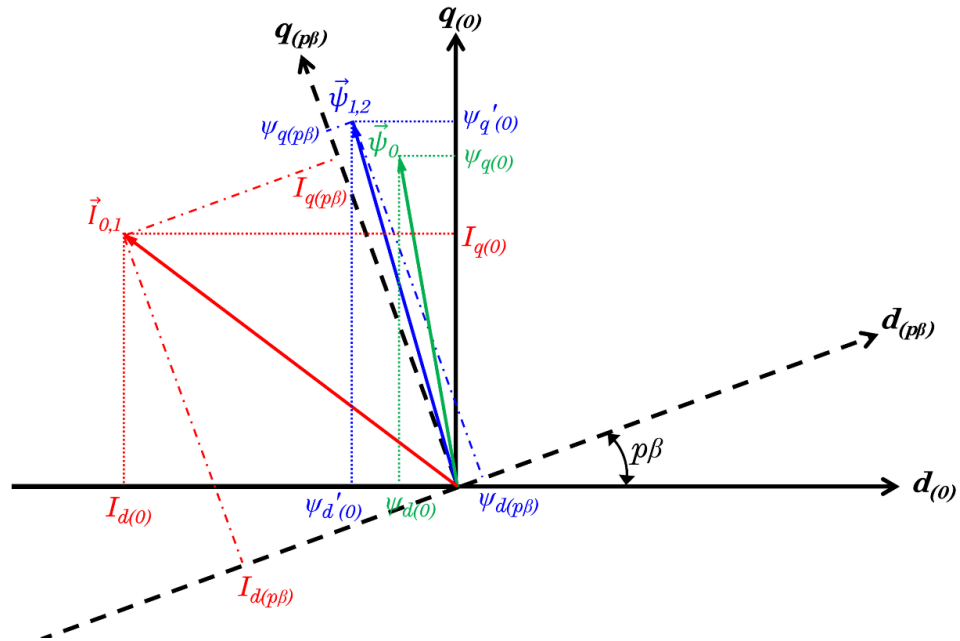
(a) Step 1: Unskewed and skewed slice current and flux linkage vectors referred to unskewed (i.e., reference) d-q axes
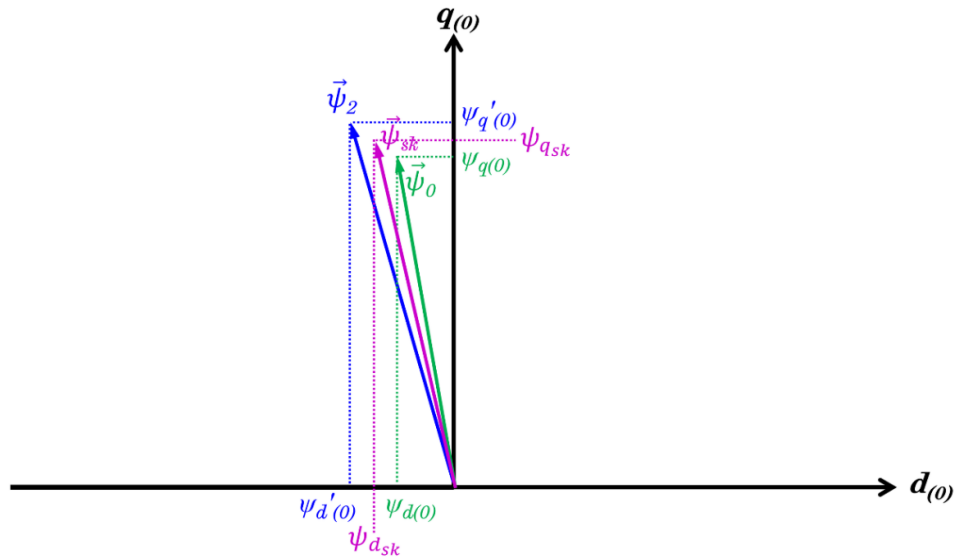
(b) Step 2: Total skewed flux linkage vector referred to unskewed (i.e., reference) d-q axes

Figure 4.7. Flux and current vectors diagrams illustrating the derivation process of the electromagnetic parameters of a machine employing a rotor skewed by angle β.

For a given stator current in (4.30) referred to the $d_{(0)}$-$q_{(0)}$ axis (i.e., reference axis) corresponding to the unskewed rotor,

$$\vec{I_0} = I_{d(0)} + jI_{q(0)} \tag{4.30}$$

the flux linked by the stator winding coils can be calculated from

$$\vec{\Psi_0} = \Psi_d(I_{d(0)}, I_{q(0)}) + j\Psi_q(I_{d(0)}, I_{q(0)}). \tag{4.31}$$

When the rotor is skewed by a β mechanical angle, the d- and q- axes of the skewed slice become shifted (i.e. $d_{(p\beta)}$ – $q_{(p\beta)}$) by $p\beta$ with respect to the stator magneto-motive-force (MMF) axis, as shown in Figure 4.7 (a), where p is the number of pole-pairs. Clearly, the skewed slice will have a different current phase angle for the same input current magnitude, implying that the d-q axis current components seen by the skewed rotor, $I_{d(p\beta)}$ and $I_{q(p\beta)}$, will be altered compared to those of the unskewed rotor, $I_{d(0)}$ and $I_{q(0)}$. The current vector of the skewed slice and its d-q axis components referred in the skewed $d_{(p\beta)}$ – $q_{(p\beta)}$ system are described by (4.32) and (4.33), respectively.

$$\vec{I_1} = \vec{I_0}\, e^{-jp\beta} \tag{4.32}$$

$$\begin{aligned} I_{d(p\beta)} &= \Re\left(\vec{I_1}\right) \\ I_{q(p\beta)} &= \Im\left(\vec{I_1}\right) \end{aligned} \tag{4.33}$$

where the operators $\Re$ and $\Im$ denote the real and imaginary parts of a complex vector, respectively. Note that the negative sign in the exponent of (4.32) indicates positive rotor rotation (i.e., anti-clockwise).

The new d-q axis currents of the skewed slice, $I_{d(p\beta)}$ and $I_{q(p\beta)}$, are then used to calculate the effective d-q axis flux linkage from the pre-computed reference LUT ($\Psi_{d(p\beta)}$, $\Psi_{q(p\beta)}$) as shown in the diagram of Figure 4.7 (a) and described by equation (4.34).

$$\overrightarrow{\Psi_1} = \Psi_d\big(I_{d(p\beta)}, I_{q(p\beta)}\big) + j\Psi_q\big(I_{d(p\beta)}, I_{q(p\beta)}\big) \qquad (4.34)$$

It should be noted that this is a critical step in the process, as the axial variations in saturation precisely occur due to the alteration in the d-q axis currents (or the current phase angle) of the skewed slice. The obtained flux linkage vector, $\overrightarrow{\Psi_1}$, is then referred back to the reference $d_{(0)}$-$q_{(0)}$ axes (i.e., unskewed rotor) using (4.35), as illustrated in Figure 4.7 (a), and its d-q axis flux linkage components, $\Psi'_{d(0)}$ and $\Psi'_{q(0)}$, can be calculated with (4.36).

$$\overrightarrow{\Psi_2} = \overrightarrow{\Psi_1}\, e^{jp\beta} \qquad (4.35)$$

$$\Psi'_{d(0)} = \Re\big(\overrightarrow{\Psi_2}\big)$$
$$\Psi'_{q(0)} = \Im\big(\overrightarrow{\Psi_2}\big) \qquad (4.36)$$

Finally, the d-q axis flux linkage vectors obtained for individual skew slices, $\overrightarrow{\Psi_0}$ and $\overrightarrow{\Psi_2}$, are vectorially added yielding the combined flux linkage vector of the skewed machine, $\overrightarrow{\Psi_{sk}}$, as illustrated in Figure 4.7 (b). The combined flux linkage vector and its d-q axis components, $\Psi_{d_{sk}}$ and $\Psi_{q_{sk}}$, can be derived using (4.37) and (4.38), respectively. The combined d-q axis flux linkage LUTs, describing the electromagnetic behaviour of the skewed machine, can therefore be derived for the entire range of d-q axis currents.

$$\overrightarrow{\Psi_{sk}} = \frac{\overrightarrow{\Psi_0} + \overrightarrow{\Psi_2}}{2} \qquad (4.37)$$

$$\Psi_{d_{sk}} = \Re\big(\overrightarrow{\Psi_{sk}}\big)$$
$$\Psi_{q_{sk}} = \Im\big(\overrightarrow{\Psi_{sk}}\big) \qquad (4.38)$$

The described process can be generalized to predict the total flux linkage LUTs, $\Psi_{d_{sk}}$ and $\Psi_{q_{sk}}$, of any synchronous motor employing an n number of skew slices and any skew angle. Since this technique involves interpolation, it should be noted that in order to avoid any error due to extrapolation, appropriate ranges for the minimum and maximum d-q axis currents, I_d and I_q, should be considered in

the process of constructing the reference LUT, in alignment with the selected skew angle value. For instance, when a relatively large skew angle is considered, the *d-q* axis current ranges defined in the process of building the reference LUT should be relatively larger compared to those selected for a case where a smaller skewing angle is employed.

The percentage error in the prediction of the average flux linkage of the skewed machine using the proposed technique, with respect to the results obtained from the multi-slice FEA model, is illustrated in the surface plots of Figure 4.8 (a) and (b) for the *d-q* axis flux linkage, Ψ_d and Ψ_q, respectively. The results indicate a very good agreement between the proposed (semi-analytical) and multi-slice FEA models against the entire *d-q* axis operating current range, with the prediction error being less than 0.7%.

The presented model, (4.30)–(4.38), which exhibits high accuracy in predicting the average skewed flux linkage, can also be extended to provide predictions for the instantaneous flux linkage and torque of the skewed machine. The concept remains similar to the case where the average flux linkage is considered, with the only difference being that the current and flux linkage phasors in the diagrams of Figure 4.7 synchronously rotate.
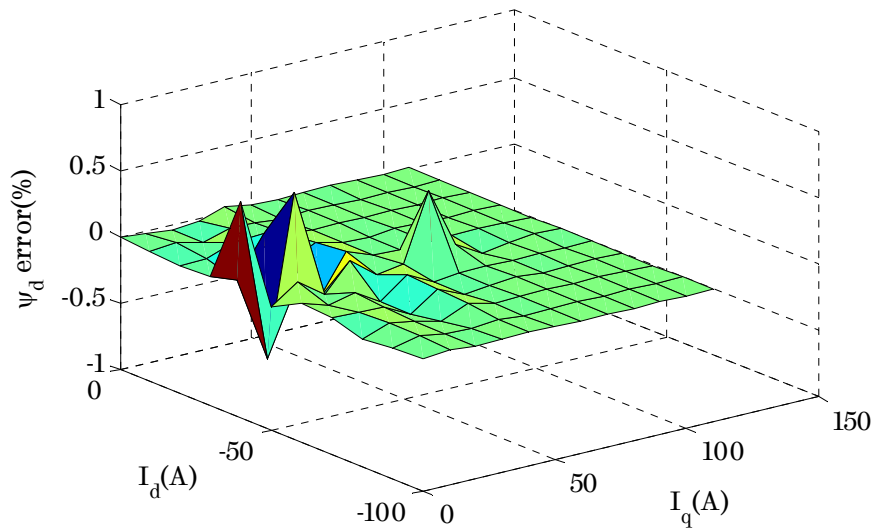
(a) *d*-axis flux linkage – ψ_d
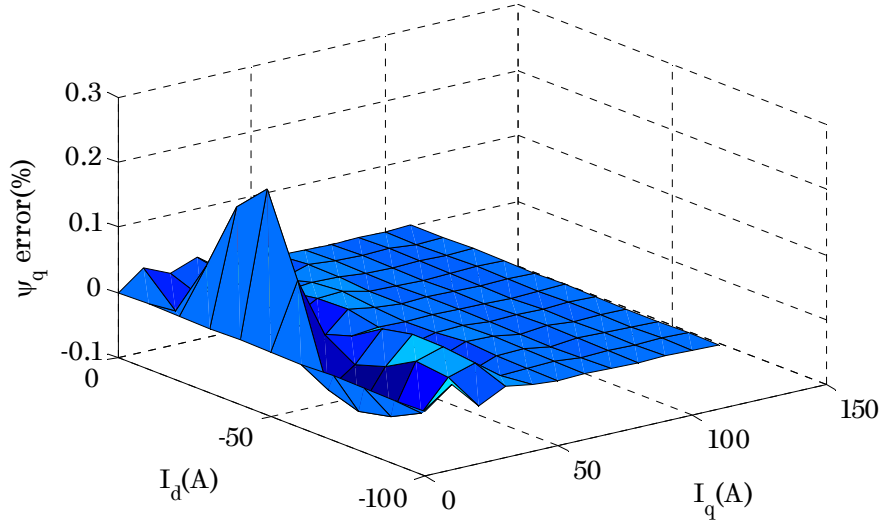
(b) *q*-axis flux linkage – ψ_q

Figure 4.8. Average flux linkage prediction error between multi-slice FEA and proposed semi-analytical technique over the entire d-q axis current range.

To account for this, the same set of pre-calculated data is used in the model. However, in this case the electrical rotor position (θ_e) is also included as an additional parameter in the reference LUTs, which now take the form of $\Psi_d(I_d, I_q, \theta_e)$, $\Psi_q(I_d, I_q, \theta_e)$ and $T_0(I_d, I_q, \theta_e)$. For a given rotor position, the effective instantaneous flux linkage vector of the skewed slice, $\overrightarrow{\Psi_1}$, can be calculated by (4.39) using the shifted *d-q* axis currents, $I_{d(p\beta)}$ and $I_{q(p\beta)}$, given in (4.34), and a rotor position angle shifted based on the selected skew angle ($\theta_e + p\beta$). The obtained flux linkage vector is then referred back to the reference *d-q* axes ($d_{(0)} - q_{(0)}$) using (4.40), where it can be vectorially added with the flux linkage vector of the unskewed slice in order to acquire the total flux linkage of the skewed machine as illustrated in the previous process for the average flux linkage predictions.

$$\overrightarrow{\Psi_1} = (\Psi_d(I_{d(p\beta)}, I_{q(p\beta)}, \theta_e + p\beta) + j\Psi_q(I_{d(p\beta)}, I_{q(p\beta)}, \theta_e + p\beta)) \tag{4.39}$$

$$\overrightarrow{\Psi_2} = \overrightarrow{\Psi_1}\, e^{jp\beta} \tag{4.40}$$

The instantaneous torque corresponding to the skewed slice can be calculated in a similar manner as the instantaneous flux linkage using (4.41), from the torque data contained in the reference LUT $T_0(I_d, I_q, \theta_e)$. Only in this case, the obtained torque, T_1, need not be referred to the reference $d_{(0)} - q_{(0)}$ axes, since torque is not a vector but a scalar quantity. Likewise, the torque of the skewed slice can then be added to that of the unskewed one to obtain the total instantaneous torque of the skewed machine, T_{sk}, as shown in (4.42).

$$T_1 = T_0(I_{d(p\beta)}, I_{q(p\beta)}, \theta_e + p\beta) \qquad\qquad (4.41)$$

$$T_{sk} = \frac{T_0 + T_1}{2} \qquad\qquad (4.42)$$

As previously explained, since this technique involves interpolations from a reference LUT, one should consider selecting sufficiently large ranges (minimum and maximum values) for the d-q axis currents when building the reference LUTs based on the selected skew angle, in order to avoid any errors due to extrapolation. Theoretically, the same applies for the rotor position angle range in the reference LUTs for the case of instantaneous predictions using the proposed technique. This directly implies increased computation FE time in obtaining the data of the reference LUT, which note that now is three-dimensional. This problem can be avoided, however, with appropriate data manipulation coding owing to the periodicity of flux linkage and torque over an electrical or mechanical cycle.

To demonstrate the accuracy of the proposed model in predicting the instantaneous flux linkages and torque of a skewed machine, the d-q flux linkages and torque calculated under no-load and load conditions, are provided in Figure 4.9 for each skew slice of the 3-step-skewed PMA SynRM (i.e., -3.5º, 0 º, +3.5 º). The data predicted via the multi-slice FEA technique are also provided in Figure 4.9 for comparative purposes. As can be observed, a very close match is achieved between the results predicted by the proposed model and those obtained from multi-slice FEA, with the proposed technique essentially replicating the results from the multi-slice FEA. Based on the above assertion, the proposed technique can

comprise an attractive solution for the rapid evaluation of different skew angles with various skew arrangements (ranging from step-skewed rotors or continuously skewed stators) on the electromagnetic torque ripple, which is known to be significantly influenced by axial variations in saturation under different load conditions [86].

In addition to this, the technique also allows to simultaneously evaluate the impact of the different skew angles and arrangements on the output torque-speed characteristic (MTPA and FW), enabling to identify the optimal skew configuration of the machine in a computationally efficient manner. As a result, the technique can be integrated with an iterative global design optimisation process of the machine, where torque ripple can be set as a design constraint and the skew configuration parameters can be set as optimising parameters. This, in turn, enables systematic optimisation of the machine performance without penalising the computational time.

The presented results demonstrate the capability of the proposed technique in achieving high accuracy under any mode of operation spanning from low to high saturation levels, while being computationally efficient, thus alleviating the need for multi-slice FEA for skewed synchronous motors (without damper bars in the rotor).
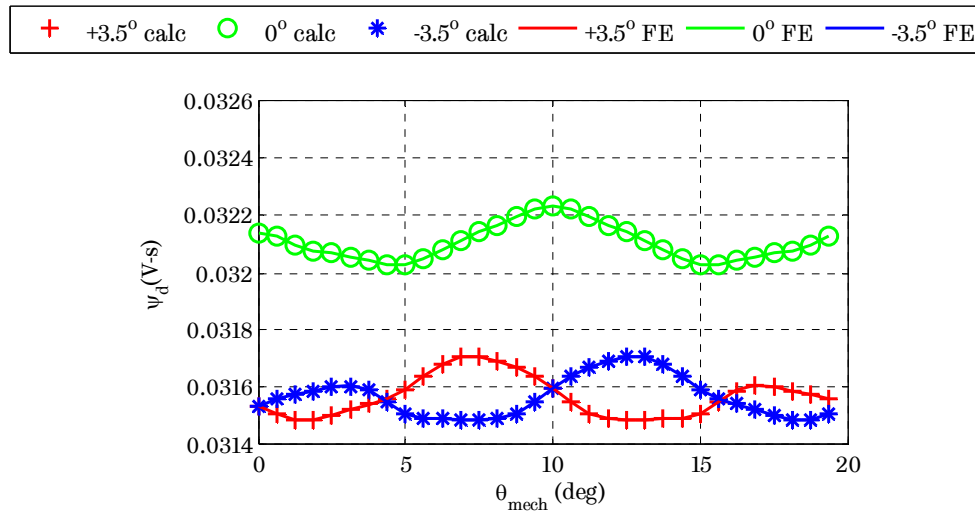
(a) ψ_d (I_d=0A, I_q=0A)
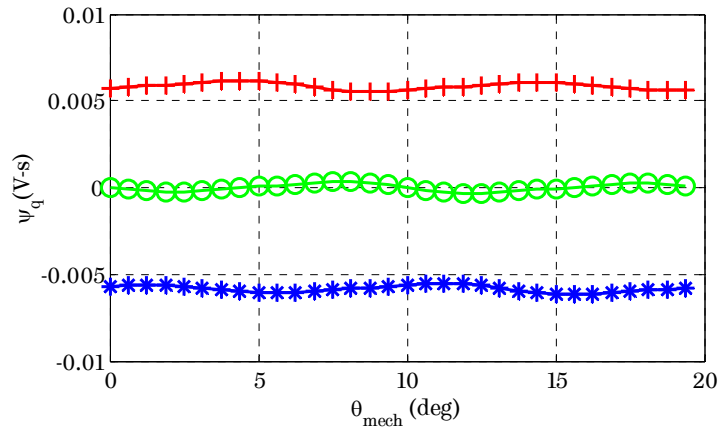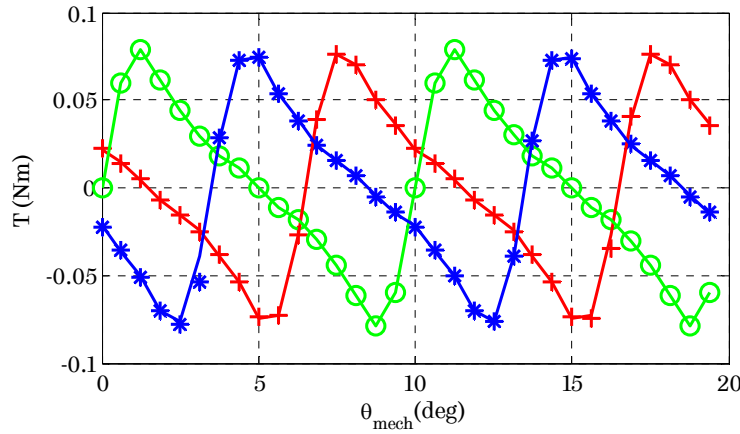
(b) ψ_q (I_d=0A, I_q=0A)

(c) Cogging torque (I_d=0A, I_q=0A)

+ $+3.5^o$ calc   ◯ 0° calc   ✳ -3.5^o calc   —— $+3.5^o$ FE   —— 0° FE   —— -3.5^o FE
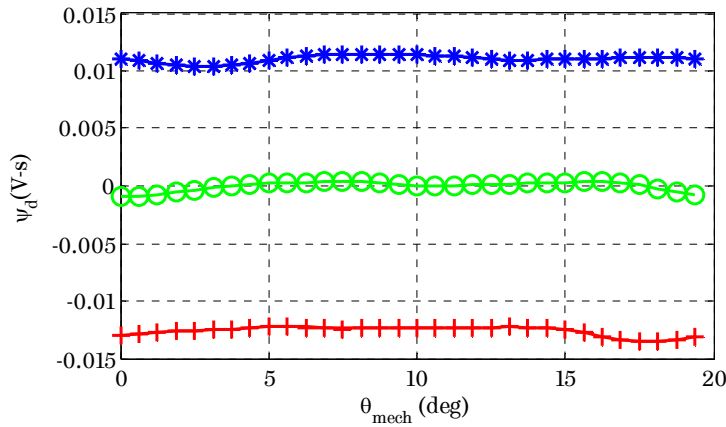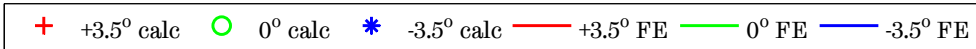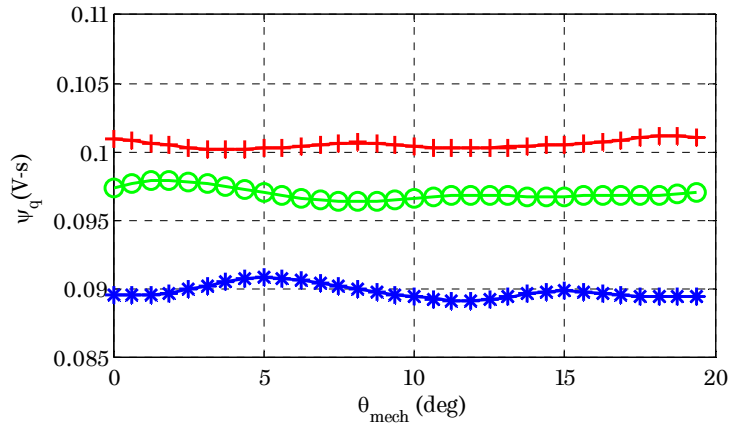
(d) ψ_d (I_d=-50A, I_q=50A)
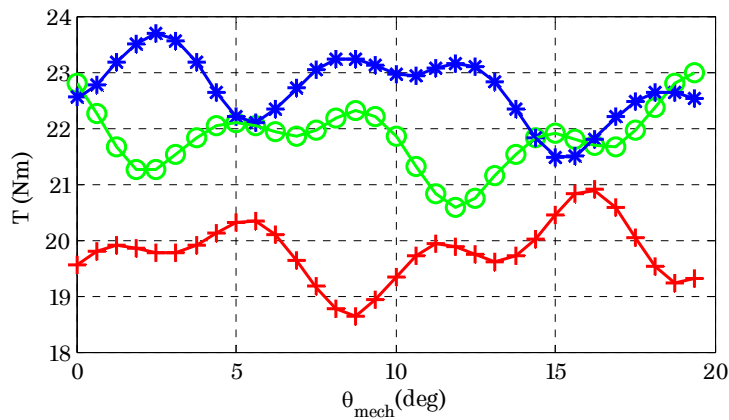
(e) ψ_q (I_d=-50A, I_q=50A)

(f) Torque (I_d=-50A, I_q=50A)

Figure 4.9. Comparisons between FE and predicted (denoted as "calc") instantaneous results corresponding to each slice of the skewed rotor (i.e. -3.5º, 0º and +3.5º).

4.3 Experimental validation

A prototype PMA SynRM machine has been manufactured and experimentally tested through locked rotor tests. From these tests the angle dependence of the motor torque at different phase current amplitudes, as well as the saturation behavior of the motor can be determined. The machine under test was mechanically connected to a dynamometer (load) machine and was energized with two constant DC current sources. The load machine was speed-controlled and programmed to perform two revolutions with a very low speed of 3 r/min with long cooling periods between the testing of different load points. This is to ensure the temperature of each test point is kept very close. The motor output torque was

measured through an in-line torque transducer (KISTLER - type 4503A). The experimental test-rig setup for the locked rotor tests is illustrated in Figure 4.10.
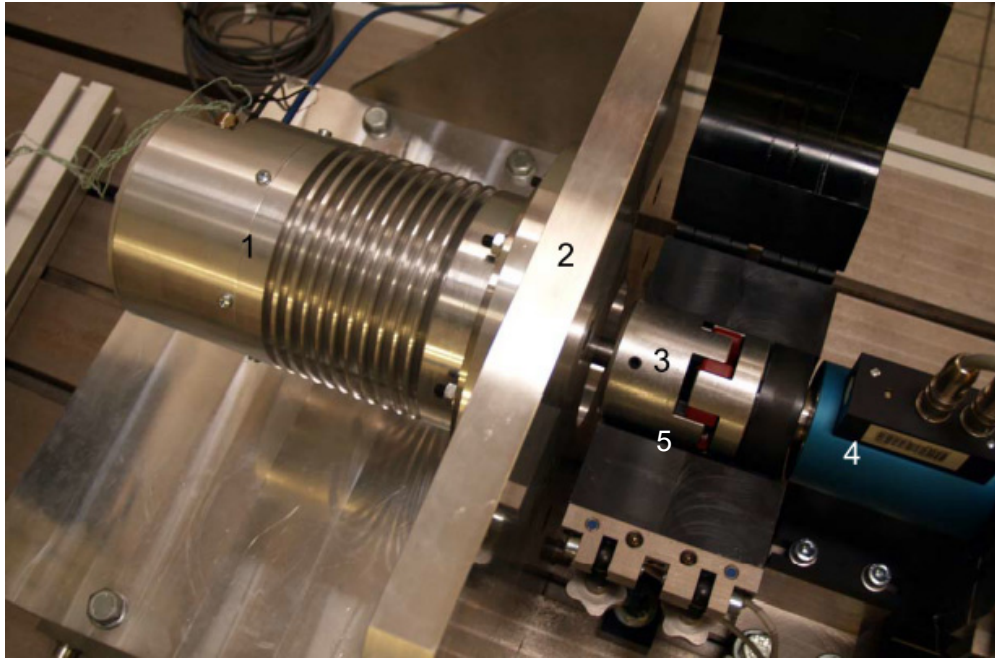
1: PMA SynRM   2: Mounting plate

3: Coupling   4: KISTLER torque transducer

5: Rotor locking mechanism

Figure 4.10. Test-rig setup for the locked-rotor tests.

Figure 4.11 shows the variations of the measured and predicted back-emf with speed. It can be seen that the measured back-emf is about 22% lower than the predicted one using 2D FEA, despite the fact that the B-H characteristic of the magnet material has been experimentally checked, and the manufacturing tolerances have been determined using a special purpose microscope and considered in the modelling. Figure 4.12 shows the gap between the permanent magnets and the rotor steel laminations caused by manufacturing tolerances. However, these tolerances have been taken into consideration in the 2D FE modelling. Therefore, the discrepancy between the measured and predicted back-emf can be attributed to 3D effects and the damage caused by using laser to cut the lamination of the stator. These effects are addressed in subsequent chapters of the thesis. Nevertheless, for the purpose of the initial analyses these effects are

represented by an equivalent reduction in the properties of the permanent magnets (viz., B_r), which represents a reduction in the magnetic loading of the magnetic circuit.
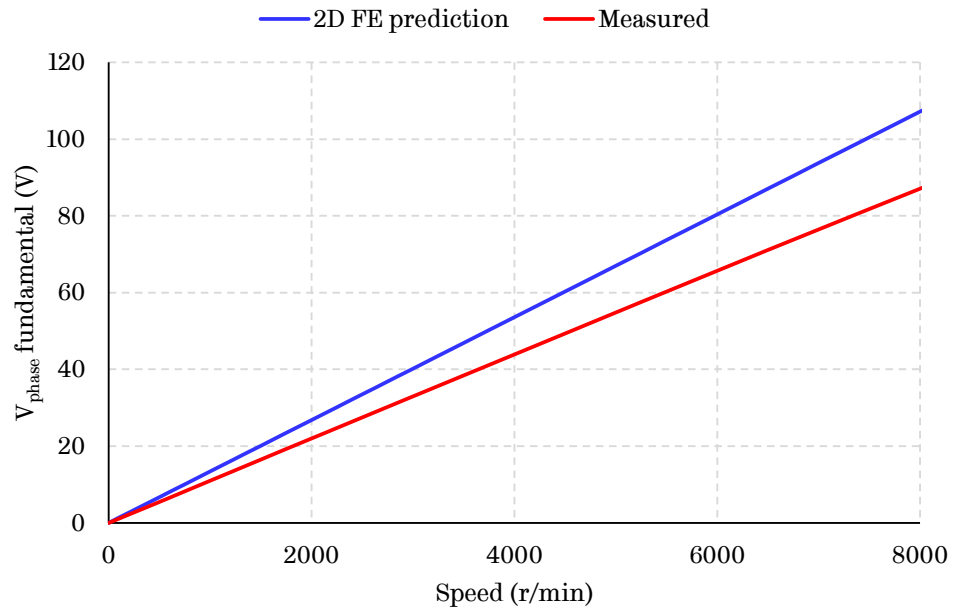
Figure 4.11. Variation of back-emf with speed.
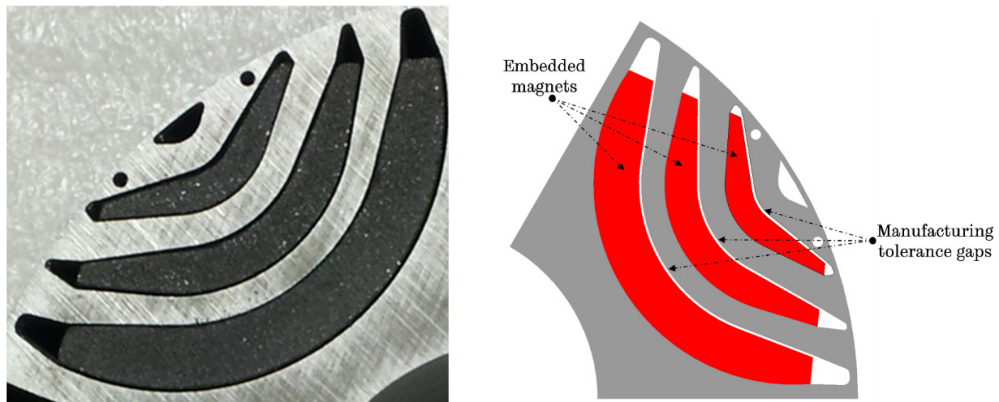
Figure 4.12. Mechanical tolerances on PMA SynRM rotor.

Figure 4.13 shows the measured and predicted variation of output torque with the current phase angle under different load current amplitudes representing low to high saturation operating conditions. Note that the current phase angle in the plot is the angle starting from the *q*-axis of the machine (i.e., the high

permeance axis). Figure 4.14 shows the measured and predicted variation of torque with the current amplitude, under maximum-torque-per-ampere (MTPA) operation, where the optimal current phase angle is selected for each input current amplitude to maximise the output torque. A direct comparison between the predicted and measured torque indicates a very good agreement against both current phase angle and current amplitude variation, as illustrated by Figure 4.13 and Figure 4.14, respectively. The slight difference between the results can be attributed to a number of factors. First, the end-effects and axial flux leakage components are present in the measurement, but are neglected in the prediction. Second, the errors of torque and rotor position angle measurements may also contribute to the difference. Lastly, the friction torque, which is not accounted in the prediction, will also contribute to the difference.
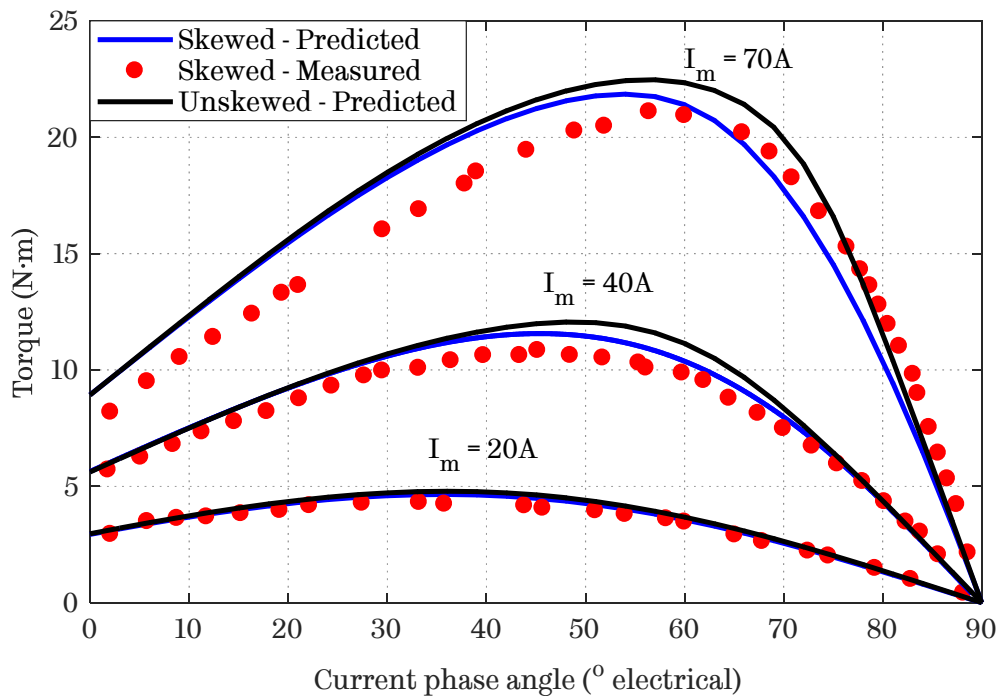
Figure 4.13. Average torque against current phase angle at various current amplitudes.
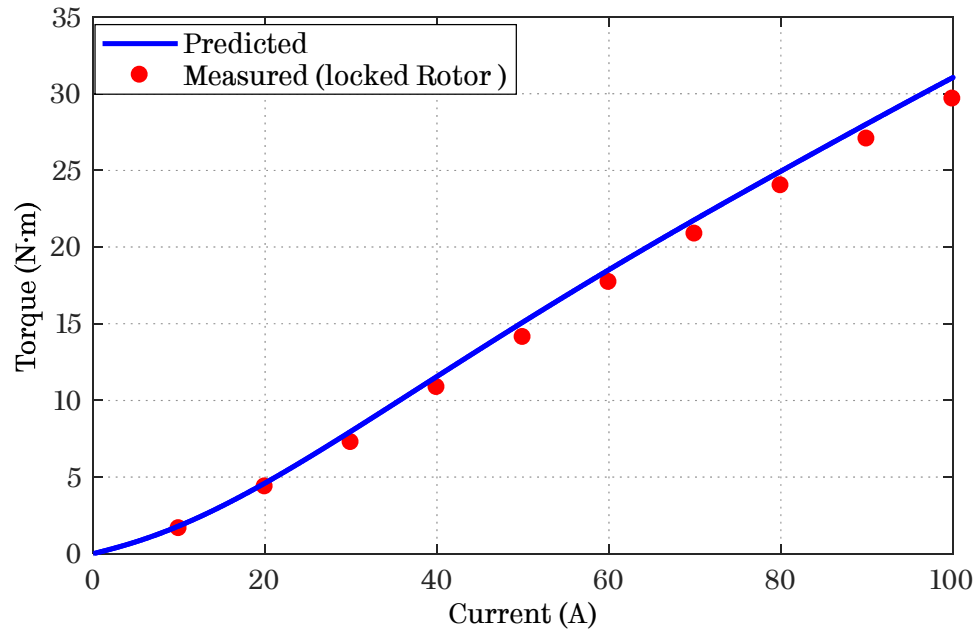
Figure 4.14. Comparison of measured and predicted torque under maximum torque per ampere (MTPA) operation of the skewed machine.

4.4 Remarks

The effect of axial variations in saturation, introduced by skew, on the electromagnetic parameters (i.e., flux linkages and inductances) of the machine was examined and quantified. It was found that the electromagnetic parameters can significantly vary under certain operating conditions, after skew is introduced. A computationally efficient semi-analytical technique, that can account for these axial variations in saturation and the d-q axis cross-coupling has been presented, and its ability to accurately predict the equivalent-circuit parameters of a skewed synchronous machine has been validated through multi-slice FEA and measurements obtained from a prototype motor. The computational cost-savings resulting from the proposed technique, against the multi-slice FEA method, are linearly proportional to the number of skew slices employed in the skewed machine.

Chapter 5

3D Effects of Rotor Step-skews in Permanent Magnet Assisted Synchronous Reluctance Machines

This chapter focuses on the 3D effects associated with rotor step-skews performed in permanent magnet assisted synchronous reluctance machines (PMA SynRMs). It analyzes and quantifies these effects via comparisons between 2D and 3D finite element analyses (FEA) of skewed and unskewed machines. The 3D phenomena manifested in the skewed PMA SynRM are identified into end-effects and axial interactions between skewed steps, and their influence on its electromagnetic performance is examined under loaded and no-load conditions. The chapter exemplifies the significance of the skew-associated 3D effects, which can result in considerable decrease of the back-electro-motive-force (back-EMF) and a substantially increased electromagnetic torque ripple. It, thereby, highlights the inability of the typically employed multi-slice 2D FEA or other existing 2D-based modelling techniques in taking their influence into account. The validity of the findings is experimentally verified with measurements acquired from a prototype PMA SynRM using skewed and unskewed shafts in the rotor.

The main contents of this chapter have been published by the author in [102].

Permanent magnet assisted synchronous reluctance machines (PMA SynRM), stemming from the combination of synchronous reluctance and interior PM machine topologies, have recently gained increasing popularity as a viable candidate for electric vehicle traction applications due to concerns regarding the price volatility of rare-earth magnet materials [36]. Their attractiveness can be mainly attributed to their distinct torque production mechanism, which essentially relies on the reluctance torque component, enabling the use of less expensive ferrite or bonded NdFeB magnet solutions whilst exhibiting comparable efficiency, torque and power density typically found in conventional PM machines. A drawback often associated with this machine topology is high torque ripple emanating from its intrinsically high salient nature [36], [88]. Among several available machine design techniques to mitigate the high torque ripple, skewing is

known to be one of the most effective and frequently incorporated solutions, which can also be combined with other techniques for more effective torque ripple reduction [86], [88]. Rotor step-skew, in particular, is often employed as a more viable alternative to stator or rotor continuous skew considering manufacturability and cost reduction [86], [103]–[105].

When a skew is performed, it causes variation of the magnetic flux density along the axial (skew) direction, and thus influences the machine's electromagnetic behavior, i.e. flux-linkage and torque [86], [94], [96]. This effect is, indeed, exhibited due to the alteration of the current phase angle at different skew slices (or steps). Numerous methods are available in literature to investigate and take into account of the effects of skew using (either) 2D or 3D numerical finite element analysis (FEA), analytical, or semi-analytical approaches, where the trade-off in each case being the computational time versus accuracy. Albeit the least computationally intensive, analytical approaches are commonly unable to represent the non-linearities exhibited due to magnetic saturation under loaded conditions [86], [94].

On the other hand, due to the increased complexity and prohibitive computational time and numerical memory costs of 3D FEA, the analysis of a skewed machine's electromagnetic performance typically relies on 2D domain-based techniques, such as the widely employed multi-slice 2D FEA (often mentioned as 2.5D) [95], [97] or more computationally efficient semi-analytical techniques [94] exhibiting comparable accuracy. A common limitation associated with these techniques, however, is their inability to capture certain 3D phenomena, namely the end-effects and axial interaction between skewed steps, since they explicitly rely on the 2D domain for their analysis [106]. The significance of such 3D effects can be influenced by the ratio of axial length to the airgap length (viz. end-effect), the number of skewed steps, the skew angle, and the structure of the machine topology under consideration. The quantification, and particularly experimental verification, of the 3D effects associated with skewed PMA SynRMs has received limited attention in literature to date.

Accordingly, this chapter investigates and quantifies the 3D effects exhibited in a PMA SynRM with step-skewed rotor under loaded and no-load conditions. It

thereby, through comparisons between 2D and 3D FEA-acquired results, exemplifies the inability of multi-slice 2D FEA, or other 2D-based modeling techniques, in accurately predicting the skew-induced 3D effects, which as will be shown, can have a considerable impact on the machine's electromagnetic performance; namely the back-electro-motive force (EMF) and output torque characteristics. The findings of the study are validated through measurements from a prototype PMA SynRM, developed for a traction application, using skewed and unskewed shafts in the rotor.

5.1 Machine specification and skew modelling

5.1.1 Machine specification

The investigation is undertaken on a 3-phase, 6-pole and 36-slot PMA SynRM, illustrated in Figure 5.1, with three embedded bonded NdFeB magnet layers and an airgap length of 0.35mm. The PMA SynRM, developed for a traction application, is characterized by 3.75kW continuous, and 6.75kW peak power rating, respectively. The rotor is skewed in three steps by 7° mechanical (i.e., -3.5°, 0°, $+3.5^{\circ}$) for the purpose of reducing the intrinsically high electromagnetic torque ripple.
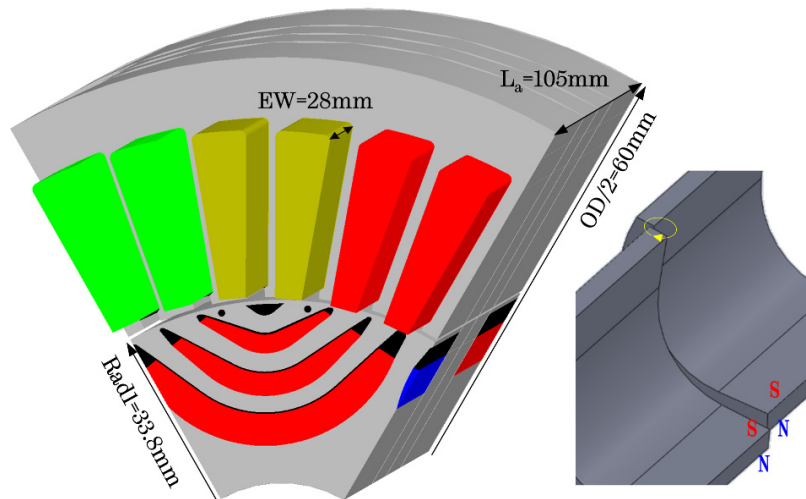
Figure 5.1. 3D geometry schematic, skewed magnets detail indicating the axial interaction between skewed steps.

5.1.2 Skew modelling

When skew is implemented along the machine's axial co-ordinate, the translatory symmetry assumed by 2D FEA is no longer valid as the problem now becomes three-dimensional. In the case of the widely employed multi-slice FEA model, the 3D problem is discretized into a number of 2D problems (i.e., skewed slices), coupled by means of the electric circuit [95], [97]. Ultimately, the solution is found by linear addition of the multiple 2D slices. As this skew modeling approach discretizes the problem with the aim of reducing the long computational times required for 3D FEA, it still has its limitations owing to the fact that it explicitly relies on the 2D domain. The same applies to other 2D-based semi-analytical approaches, such as [94], which fundamentally rely on the combination of 2D FEA and analytical calculations emulating the accuracy of the multi-slice FEA, whilst alleviating the increased computational time associated with the numerical FE solution of multiple skew slices.

Inspection of Figure 5.1 provides a visual interpretation of the axial interaction between adjacent step-skewed magnets, where in the case of embedded magnet machines the presence of laminations provides a flux leakage path. This effect can be accentuated with larger number of skew steps, larger skew angles and in cases where multiple magnet layers are embedded, such as in PMA SynRM. Under these circumstances the overlapping area between skewed parts typically increases. However, owing to the high degree of magnetic anisotropy exhibited in these machines, it is expected that the iron core's magnetic saturation level may influence the significance of such effects under different operating conditions.

5.1.3 3D FEA modelling

To examine and quantify the 3D effects exhibited in the machine under consideration, skewed and unskewed 3D models were created using a commercial FEA package (CEDRAT Flux) [107]. It should be noted that the step-skewed 3D model (Figure 5.1) was created through extrusions from a complex 2D geometry containing the faces of all skew steps as illustrated in Figure 5.2. This allowed achieving a continuous geometry along the axial co-ordinate, i.e. without interface

gaps between the skewed steps, and the use of extrusive mesh for the volumes. To appropriately select a sufficient amount of axial mesh divisions ensuring high accuracy for the 3D modelling, a 3D unskewed machine model with tangential field boundary conditions imposed at its axial ends (viz. neglecting the end effect) was used as a guiding reference based on FEA result comparisons with its 2D counterpart (i.e., the 2D unskewed model). The axial mesh density of the reference 3D model was iteratively adjusted until the difference between its results and those from the 2D unskewed model was reduced to a minimum. The mesh was made progressively denser near the skew boundaries and the machine ends for the purpose of achieving higher fidelity (viz., Figure 5.3).
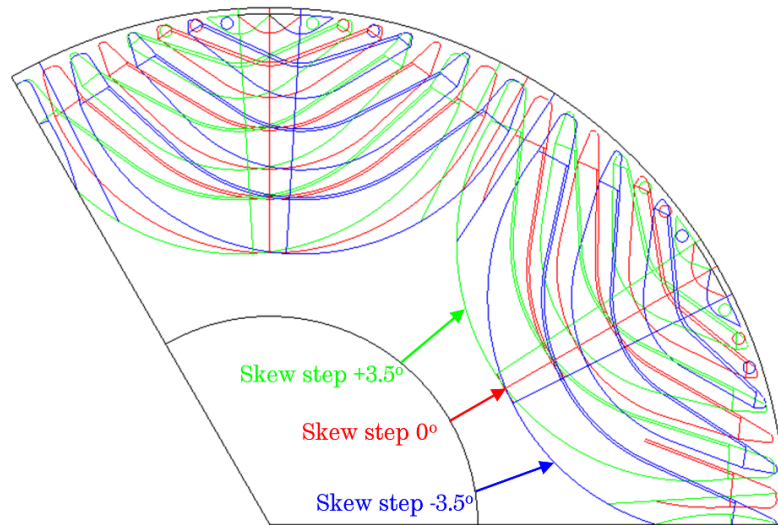
Figure 5.2. Complex 2D rotor geometry schematic containing all skew steps.

The end-winding was also modelled in order to factor in its contribution to the flux linkage and torque. A simplified end-winding model was adopted, using meshed coils rather than non-mesh coils to represent the end-windings for higher accuracy. The tradeoff in this case, however, is the neglecting of the end-winding overlapping parts due to the prohibitive complexity involved for their representation in the 3D FE domain with the employed software package. Note that the end-winding axial length (i.e., extruding from the stator core) incorporated in the 3D model is representative of that measured from the manufactured prototype PMA SynRM.
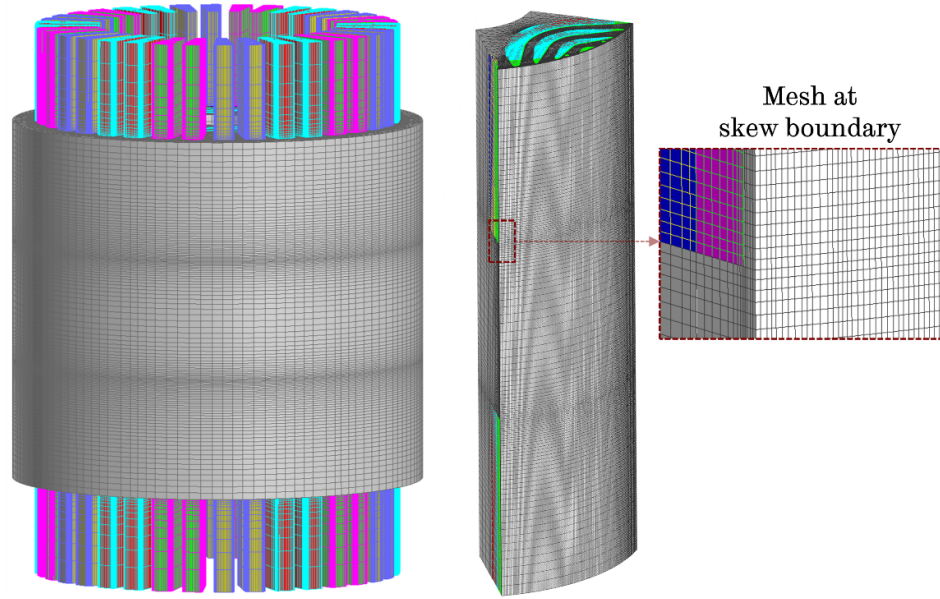
Figure 5.3. 3D mesh detail of skewed PMA SynRM – stator (left) and rotor (right).

5.2 3D effects manifestation under no-load

After establishing a qualitative understanding of the mechanism underlying the 3D effects exhibited in a step-skewed PMA SynRM, as well as the limitations associated with 2D-based modeling techniques, the quantitative results acquired via 2D and 3D FEA simulations are introduced in this and following sections for comparative purposes.

Figure 5.4 (a) illustrates the variation of the magnitude of no-load flux density along the angular direction at the middle of the airgap of the unskewed machine, computed with 2D FEA. A number of points from the flux density profile of Figure 5.4 (a) are selected for the purpose of examining their variation along the axial direction for the case of the unskewed and skewed machines using both 2D and 3D FEA. This will assist in identifying the influence of the different 3D effects, namely the end-effect and axial interaction between skewed steps. The presence of the end-effect is clearly manifested in Figure 5.4 (b), which compares the flux density variation with axial position for point, P1, predicted by 2D and 3D FEA for the unskewed machine. Its influence, however, is not substantial as the axial-to-airgap length ratio of the considered machine is relatively large.

(a) Along the angular direction (2D FEA)

(b) Along the axial direction for point P1
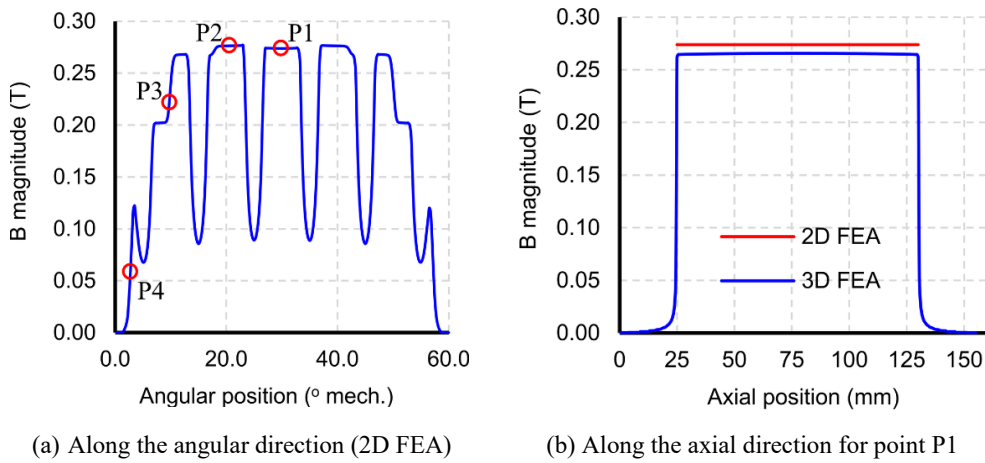
Figure 5.4. No-load flux density magnitude variation of unskewed machine at the middle of the airgap and 0° rotor position.

(a) Along the axial direction for point P1

(b) Along the axial direction for point P2

(c) Along the axial direction for point P3

(d) Along the axial direction for point P4
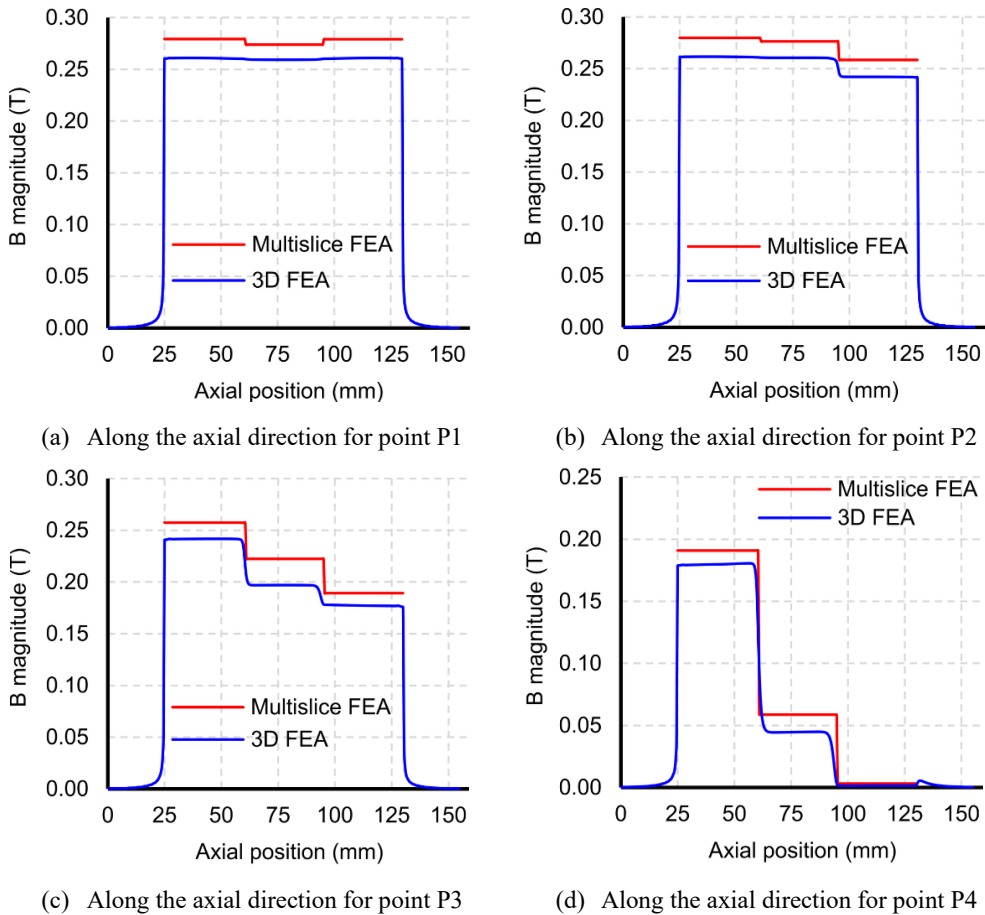
Figure 5.5. No-load flux density magnitude variation along the axial direction of skewed machine for the points indicated in Figure 5.4(a), predicted by multi-slice and 3D FEA.

Figure 5.5 shows the axial flux density variation, predicted by 2D multi-slice and 3D FEA, of all four points indicated in Figure 5.4 (a), for the case of the skewed machine, which includes the influence of both 3D effects. A direct comparison between the unskewed (Figure 5.4 (b)) and skewed (Figure 5.5 (a)) axial flux density variation of point, P1, reveals that the difference between 3D and 2D results is noticeably larger for the case of the skewed machine. This suggests that the effect of axial interaction between the skewed steps is stronger compared with the end-effect.

This can be further perceived by observing Figure 5.6, which depicts the absolute value of z-axis flux density component (B_z) at 2D cut planes located at the step-skew boundaries and ends of the machine. It is evident that drastically higher values are exhibited at the skew boundaries compared with the machine ends. To determine the extent of the axial leakage flux, the cut planes at the step-skew boundaries are displaced 5mm axially toward the machine ends as illustrated in Figure 5.7, which demonstrates that B_z reduces significantly at the selected distance. Clearly, the reduction in airgap flux density due to the 3D effects will ultimately extend into a decrease of the flux linked by the stator coils; particularly for the case of the skewed machine.
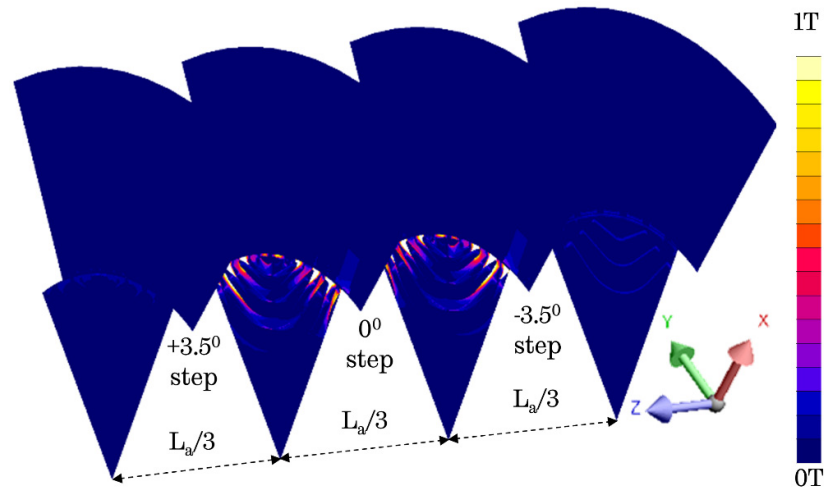
Figure 5.6. Absolute z-axis flux density component (B_z) at machine ends and step-skew boundaries.
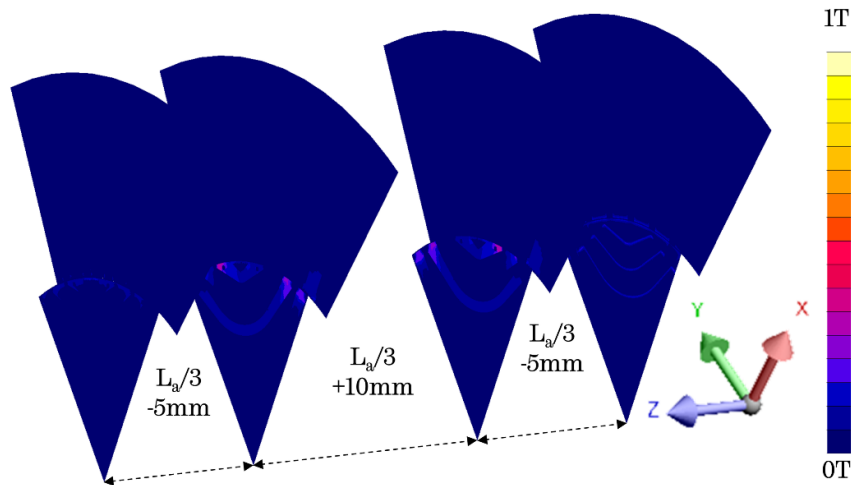
Figure 5.7. Absolute z-axis flux density component (B_z) at cut planes displaced 5mm away from step-skew boundaries, toward the machine ends.

Figure 5.8 shows the back-EMF harmonic spectra of the skewed and unskewed machines, predicted by 2D and 3D FEA. Table 5.1 lists the percentage reduction of the fundamental back-EMF component due to skew. When skew is modeled using 2D FEA, the percentage reduction of the fundamental back-EMF component is only ~1.1%. In the case where skew is modeled using 3D FEA, however, the percentage reduction grows to a considerable ~3.9% indicating the strong axial interaction between adjacent skew steps that cannot be predicted by the multi-slice 2D FEA model.
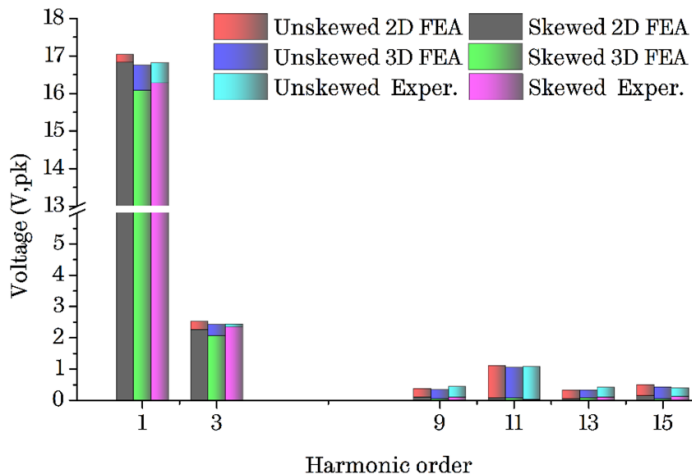
Figure 5.8. Spectra of critical phase back-EMF harmonics obtained via 2D FEA, 3D FEA and experimental tests at base speed (2100r/min).

Table 5.1. Percentage reduction of fundamental back-EMF component due to skew

Evaluation method	Percentage reduction of 1st back-EMF harmonic
2D FEA	-1.1%
3D FEA	-3.9%
Experiment	-3.2%

Measurements acquired from experimental tests using step-skewed and unskewed shafts in the rotor (as shown in Figure 5.9) are also provided in Figure 5.8 for the purpose of validating the foregoing findings. The measurements have been undertaken at a temperature close to room temperature (i.e., 20°C). It can be seen that the 3D FEA-predicted percentage reduction of the fundamental back-EMF harmonic due to skew agrees reasonably well with the measured reduction of ~3.2%. The slight difference in the measured and 3D FEA-predicted reduction can be attributed to the fact that the contact surface between adjacent skew steps may not be prefect in the prototype (due to geometrical tolerances) as is the case with the 3D model. This, in turn, can lead to a slight decrease in the axial leakage flux between the skewed parts.
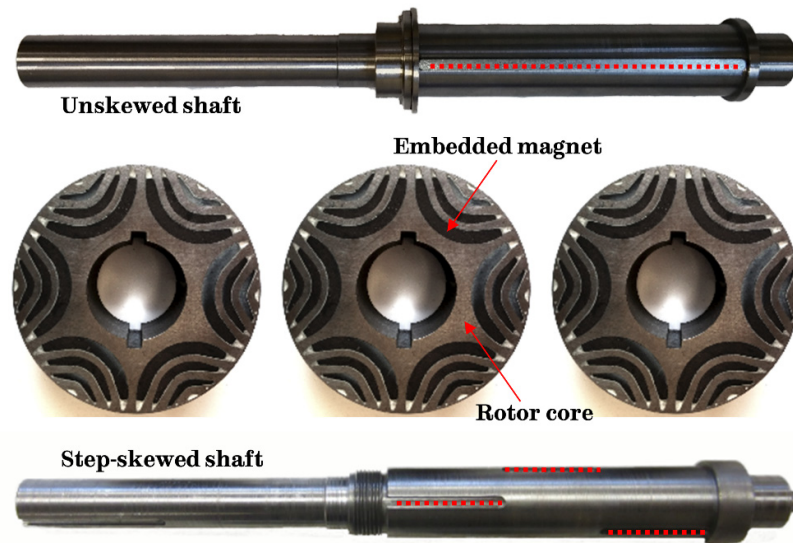
Figure 5.9. Prototype rotor stacks with embedded magnets, 3-step-skewed and unskewed rotor shafts.

5.3 Influence of 3D effects under load conditions.

The axial variations in saturation, introduced by skew, result in changes of both the phase and magnitude of torque along the axial direction [86]. In fact, this is the mechanism underlying the effectiveness of skew in reducing the electromagnetic torque ripple. It is, therefore, interesting to observe how the 3D effects will influence the torque behaviour of the machine by comparing 2D and 3D FEA predictions.

Figure 5.10 and Figure 5.11 show the instantaneous torque, predicted by 2D and 3D FEA, at a maximum-torque-per-ampere operating point corresponding to a high level of magnetic saturation, for the cases of the unskewed and skewed machines, respectively. The difference between the 2D and 3D average torque of the unskewed machine is ~1.5%, and can be attributed to the end-effects associated with the magnet and armature reaction fields. For the case of the skewed machine, the difference in the prediction of torque between the 2D multi-slice and 3D FEA increases to 2.5%. This is due to the additional effect of axial interaction between adjacent skewed steps, which results in reduction of magnet flux and saliency deviations. Note that for the case of PMA SynRM, the magnets only contribute about 20-30% to the total torque.
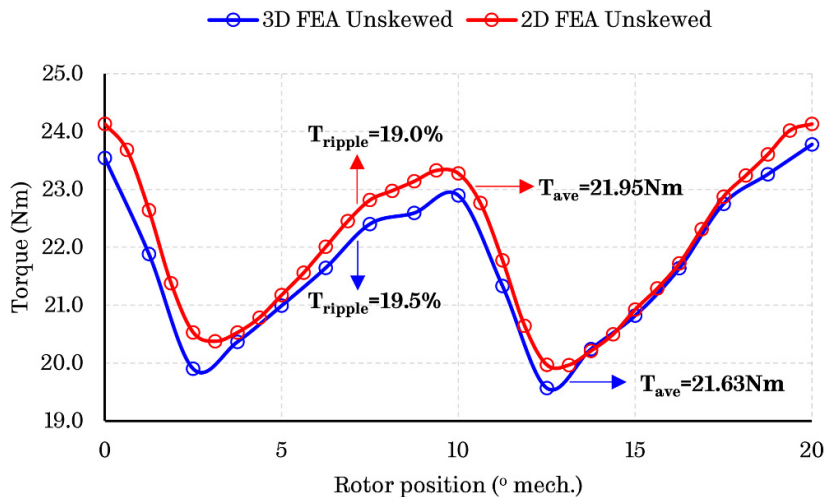
Figure 5.10. Unskewed torque waveform predicted by 2D and 2D FEA at arbitrary load between nominal and peak current (I=70A, γ=53°).
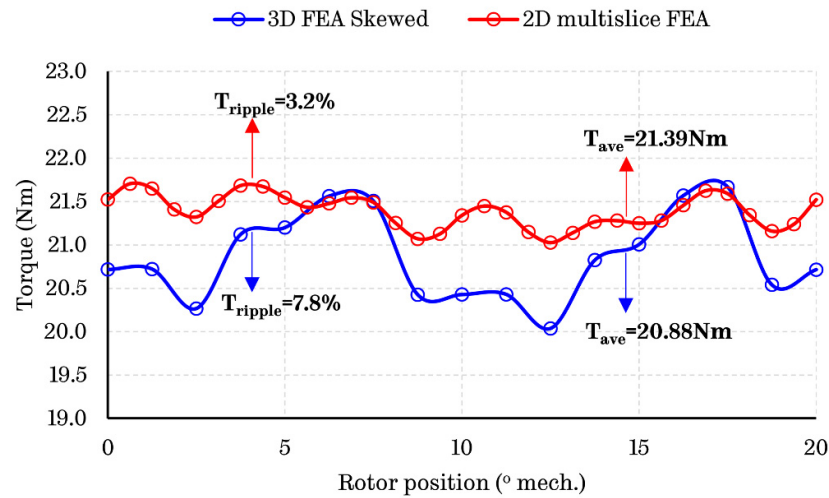
Figure 5.11. Skewed torque waveform predicted by 2D multi-slice and 3D FEA at arbitrary load between nominal and peak current (I=70A,γ=53°).

Figure 5.10 indicates that the torque ripple of the unskewed machine is barely influenced by the presence of the end-effects. In the case of the skewed machine however, the torque ripple predicted by 3D FEA becomes ~2.5 times of that obtained from the 2D multi-slice FEA, as can be seen from Figure 5.11. This implies that the axial interactions between skewed steps, which significantly influence the axial variation of flux density, render the effectiveness of step-skew to be reduced in the actual machine. To establish a more consistent trend, other load points exhibiting higher (I=42A, γ=0°), or lower (I=40A, γ=46°) magnetic saturation were investigated and the results are listed in Table 5.2. It can be seen that the torque ripple predicted by 3D FEA is always about two times higher compared with the 2D multi-slice FEA, indicating the inability of 2D-based techniques in accurately predicting the torque behavior of the machine.

In [108], apart from a reduction in average torque, no significant difference was found between 2D and 3D FEA-predicted torque ripple for a step-skewed surface mounted PM machine. For the PMA SynRM investigated in this paper, the findings show otherwise as the machine has an embedded-magnet rotor type and is characterised by a high degree of magnetic anisotropy. Based on the foregoing

findings, future research will focus on the investigation of skew effectiveness on torque ripple through dedicated 3D FEA analysis and experimental torque ripple characterisation.

Table 5.2. Torque characteristics of skewed machine predicted by 2D multi-slice and 3D FEA

Excitation	Multi-slice 2D FEA		3D FEA	
	T_{ave} (Nm)	T_{ripple} (%)	T_{ave} (Nm)	T_{ripple} (%)
I=70A, γ=53°	21.4	**3.2%**	20.9	**7.8%**
I=42A, γ=0°	5.0	**10.4%**	4.7	**18.8%**
I=40A, γ=46°	11.2	**4.5%**	11.1	**10.4%**

5.4 Remarks

The 3D effects of rotor step-skews in PMA SynRMs have been analysed. It has been shown that the axial interaction between the skewed steps in the vicinity of their interface boundaries gives rise to additional leakage flux and results in a lower back-EMF and torque capability. While the amount of average torque reduction due to these effects is modest, the resultant torque ripple is significantly increased. Thus, the optimal skew angle may have to be assessed by 3D FEA to minimize the torque ripple by employing the rotor step-skews.

Chapter 6

Effect of Laser Cut on the Performance of Permanent Magnet Assisted Synchronous Reluctance Machines

This chapter investigates the effect of laser cutting the stator lamination on the performance of a Permanent Magnet Assisted Synchronous Reluctance machine (PMA SynRM). A technique for the modelling of the B-H curves of electrical steel laminations is described. It takes into account the extent of degradation of the magnetic properties caused by laser cutting, reported in the literature, and assumes that the degree of damage is determined by the distance between the cut edges or the width of the strip. The technique is employed to predict the performance of the PMA SynRM, which exhibited significant discrepancies between measured and predicted performance assuming the ideal manufacturer's B-H curve. In the analysis, the machine is subdivided into regions characterized by the distance between the edges, and each region is assigned a corresponding B-H curve. Through comparisons between experimental measurements and predictions, the chapter highlights the potential adverse impact of laser cutting on the performance of electrical machines, especially those exhibiting a large cutting length per steel area. Therefore, it demonstrates the necessity of incorporating such effects into the modeling in order to improve prediction accuracy.

It is well established that various electrical machine manufacturing steps induce stresses which affect the magnetic properties of electrical steel laminations [110]. Some of these stresses, such as those associated with the cutting of the laminations, result in irreversible changes. In fact, punching and laser cutting, are frequently identified as the most severe cause of magnetic degradation [111], [112]. Recent studies show that punching and laser cutting exhibit different deterioration mechanisms due to the nature of internal stresses they induce [113]–[118]. Namely, punching causes plastic deformation near the cut edge, whereas laser induces thermal stresses during cutting. In [113], [114], the experimental characterisation of the spatial distribution (i.e., edge-to-edge) of the magnetic

degradation from the two cutting processes revealed that for punching a significant drop in permeability occurs near the cut edge. Whereas, in the case of laser cutting the damage seems to extend further from the edge due to the temperature gradient during processing, resulting in a substantial permeability reduction over the total sample width.

The intensity of magnetic degradation was strongly influenced by the geometry of the sample, i.e., the strip width and thickness. Therefore, it is important to understand and model such complex phenomena in order to predict their influence on the performance of electrical machines. Discrepancies between predictions and measurements of electrical machines are frequently observed and reported in the literature. For instance, for the case of iron loss these are reported as "built-factors". Such an approach neglects to reflect the link between the machine design geometrical details and the degree of electrical steel degradation during manufacturing [111]. The quantification of the effects of the magnetic degradation of electrical steel laminations on the machine's flux or back-EMF has received little attention in the literature to date.

Accordingly, this chapter discusses the effect of the laser cutting of the electrical steel lamination employed for the manufacture of the core of a traction permanent magnet assisted synchronous reluctance machine (PMA SynRM). A technique for the modelling of the B-H curves of electrical steel laminations is proposed. The technique takes into account of the extent of degradation of the magnetic properties caused by laser cutting, reported in [113], [114], and assumes that the degree of damage is determined by the distance between the edges or the width of the strip. Subsequently, the technique is employed to predict the performance of the PMA SynRM, which, as has already been shown in Chapter 4, exhibited significant discrepancies between measured and predicted performance, when the ideal manufacturer's B-H curve is employed for the modelling.

6.1 Effect of laser cutting on the magnetic properties of electrical steel

Figure 5.1 shows the variation of the flux density from an edge to another for a given applied magnetic field in a strip of M330-35 Silicon iron lamination [113].

Spatially resolved neutron grating interferometry technique enabled the experimental characterization of the spatial degradation profile resulting from cutting [113], [114]. It can be seen that there is a difference in the flux density between the two edges, with the edge being cut last, having the lowest flux density (*B*) and hence exhibiting the largest damage. Unlike cutting by employing mechanical means, such as stamping, the damage caused by laser cutting is predominantly of thermal origin, and hence resulting in the difference between the edges, which are not simultaneously cut.
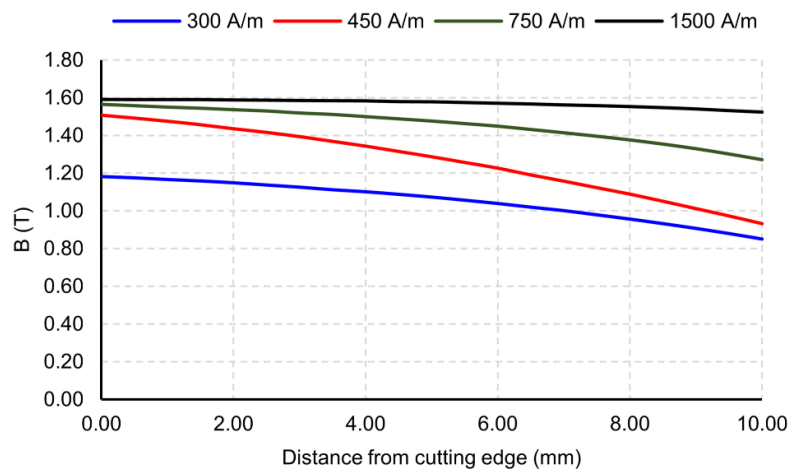
(a) Spatial degradation for 10mm strip.
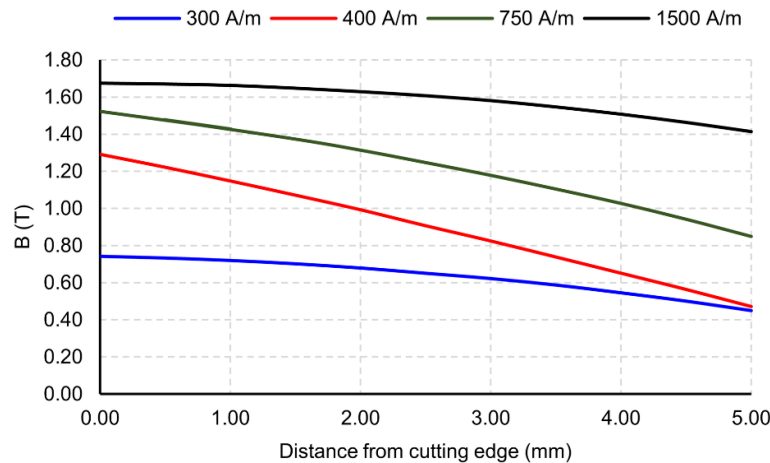
(b) Spatial degradation for 5mm strip.

Figure 6.1. Spatial degradation of flux density in laser cut strips of different width [113].

Figure 6.2 compares the variations of the average flux density (*B*) with the applied magnetic field [113], [114] for an annealed strip, and laser cut strips of 5mm and 10mm, where it can be seen that the size of the strip has a significant effect on its magnetic properties. Naturally, with smaller strip widths, the magnetic degradation becomes substantially higher since for the same laser power level, the energy from the cut is absorbed by a smaller steel mass.
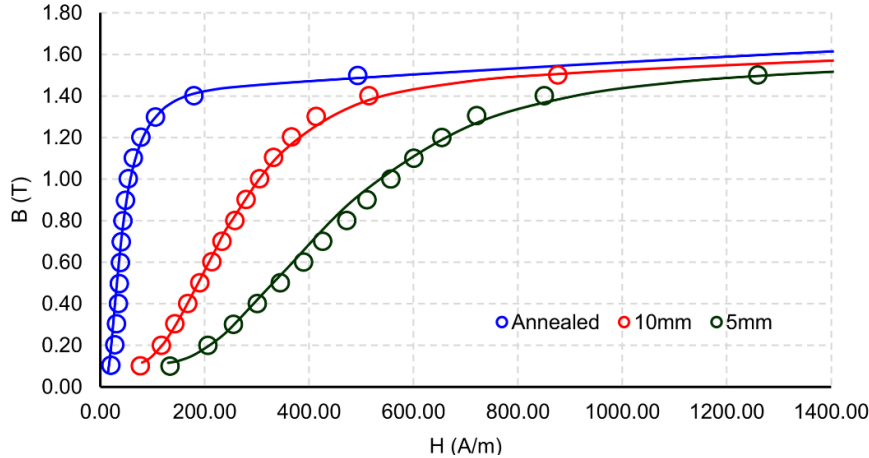
Figure 6.2. B-H curves derived from measurements in [113], [114], fitted (solid line) with proposed equation (6.43).

Furthermore, it can also be seen that the B-H curves obtained from the experiments in [113], [114] can be accurately fitted with the following equation (6.43):

$$B(H) = -A_0 \left(\frac{H}{H_0}\right)^2 e^{-\frac{H}{H_0}} + A_1 \left(1 - e^{-\frac{H}{H_1}}\right) + (B_s - A_1)\left(1 - e^{-\frac{H}{H_2}}\right) + \mu_0 H \qquad (6.43)$$

where A_0, A_1, H_0, H_1 and H_2, are constant coefficients, B_s is assumed to be the saturation flux density (i.e., 2T), and μ_0 is the permeability of free space. The tests presented in [113] and [114] are undertaken on the rolling direction. Thus, in order to estimate the effect of the damage due to laser cutting, the typical manufacturer's initial magnetization curve of an M330-35 grade Silicon steel, which is an average between the rolling and cross-rolling directions, is adjusted for 5 and 10 mm strips by introducing the additional applied magnetic field required to achieve the

average flux density in the rolling direction (Figure 6.3). As it can be observed, the additional applied magnetic field (*H*) required for the laser cut samples reduces toward increasing magnetic induction (*B*) levels, where saturation starts to occur.

Figure 6.4 shows the B-H curves for the silicon steel lamination employed in the manufacture of the PMA SynRM, where the manufacturer B-H curves are compared with those of 5mm and 10mm strips when the effect of laser cutting is accounted based on the measurement data reported in [113], [114]. It can be seen that equation (6.43) fits the B-H curves very well. Table 5.2 provides the respective values of the equation's coefficients resulting from the fitting of each B–H curve.
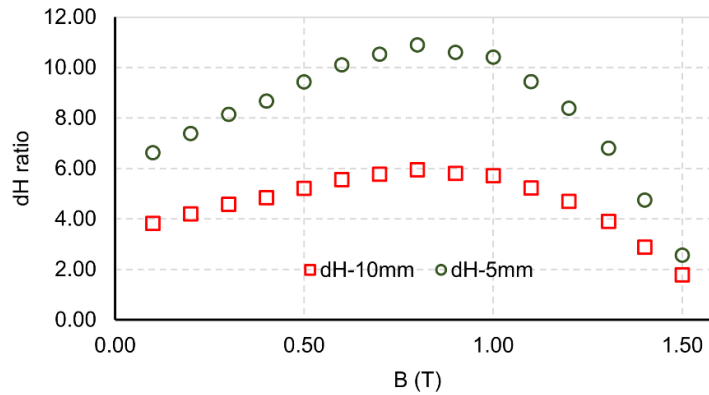
Figure 6.3. dH ratio variation with flux density for 10 and 5 mm strips relative to the annealed sample (derived from data in Figure 6.2).
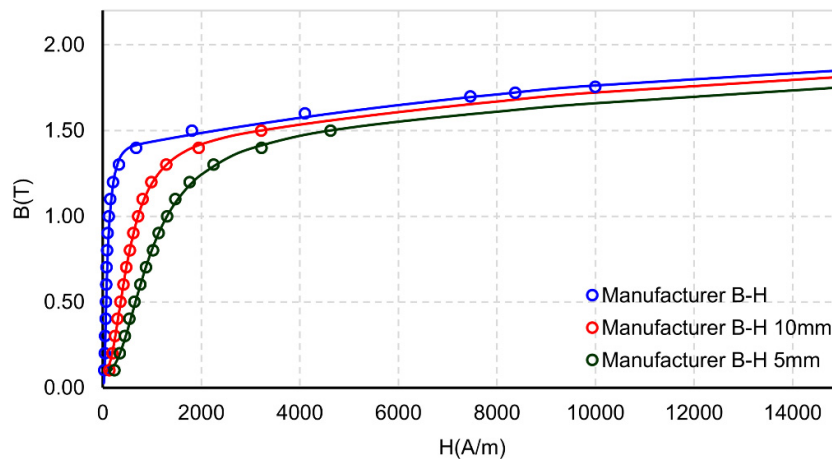
Figure 6.4. Manufacturer's B-H curves fitted (solid line) using the proposed equation (6.43).

Table 6.1. Coefficients from curve-fit of manufacturer's B-H curves

Coefficient	Annealed (Ideal)	10mm	5mm
A_0	0.50	0.50	0.50
A_1	1.40	1.35	1.34
H_0	18.0	122.0	220.0
H_1	115.0	550.0	980.0
H_2	11500.0	12000.0	15500.0

For a given data set of B-H curves corresponding to laser cut strips of different widths, the coefficients of equation (6.43) vary with the width of the strip (x), as indicated in Table 5.2, and the following functions describe these variations:

$$H_0(x) = \frac{a_0}{x^{b_0}} + H_{0\infty} \qquad (6.44)$$

$$H_1(x) = \frac{a_1}{x^{b_1}} + H_{1\infty} \qquad (6.45)$$

$$H_2(x) = \frac{a_2}{x^{b_2}} + H_{2\infty} \qquad (6.46)$$

$$A_1(x) = \frac{a_3 x}{b_3 + x} + \left(A_{1\infty} - \frac{a_3}{b_3} \right) \qquad (6.47)$$

where a_n and b_n ($n = 1, \dots, 3$) are constants, and $H_{0\infty}$, $H_{1\infty}$, $H_{2\infty}$, and $A_{1\infty}$ are the values of H_0, H_1, H_2, and A_1 for an annealed sample (shown in Table 5.2). The constants a_n and b_n are determined by a curve of best fit through the corresponding data of Table 5.2. Each coefficient of equation (6.43) is now a function of the strip width (x), and as $x \to \infty$, the coefficient's value tends to that of the annealed sample [denoted by the ∞ subscript in (6.44) - (6.47)]. This, in turn, would allow for flexible modelling of the material degradation due to laser cutting in finite element analysis (FEA) tools, and B–H curves for strip width different to the measured ones can be generated. For instance, Figure 6.5 shows the variation of the coefficient H_0 with the width of the strip (x), where it can be seen that equation (6.44) represent the variation of the coefficient with strip width well.
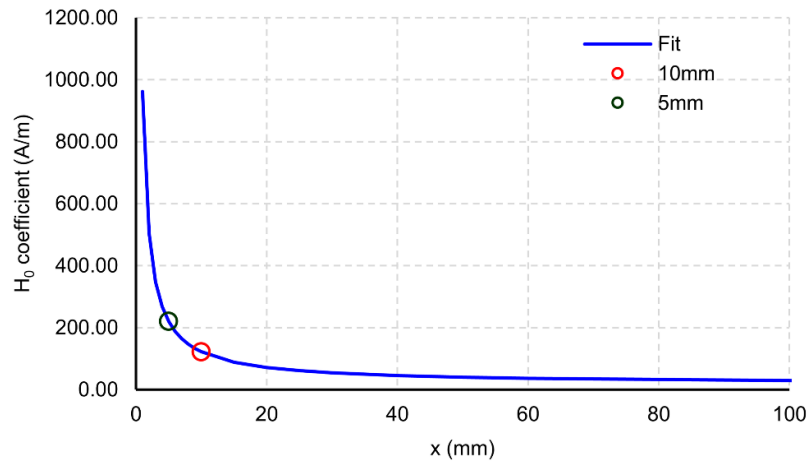
Figure 6.5. H_0 coefficient variation with strip width using function (6.44).

6.2 Effect of laser cutting on the performance of the PMA SynRM machine

Now that the technique for the modelling of B-H curves, taking into account of the electrical steel magnetic degradation due to laser cutting, has been demonstrated, its application for the performance prediction (via FEA) of the PMA SynRM, which exhibited significant discrepancies between predictions and experimental measurements (viz., Chapter 4), will be investigated.

Figure 6.6 shows the stator and rotor schematics of the PMA SynRM. Figure 6.7 shows pictures of the physical rotor and stator laminations including detailed microscope images of the back iron and teeth indicating the insulation burn-marks resulting from the laser cutting. The rotor laminations were cut using electrical discharge machining (EDM), resulting in negligible damage to the magnetic properties of the rotor laminations [119]. However, the stator laminations were cut by CO_2 laser, and therefore, variations in their magnetic properties are expected as discussed in the previous section. In the FEA modelling the stator is subdivided into three regions as indicated in Figure 6.6(a), viz. the back-iron (region 1), tooth body (region 2) and tooth tips (region 3). For each of the defined regions a B-H curve is generated employing equation (6.43), whose coefficients are determined using equations (6.44)-(6.47).
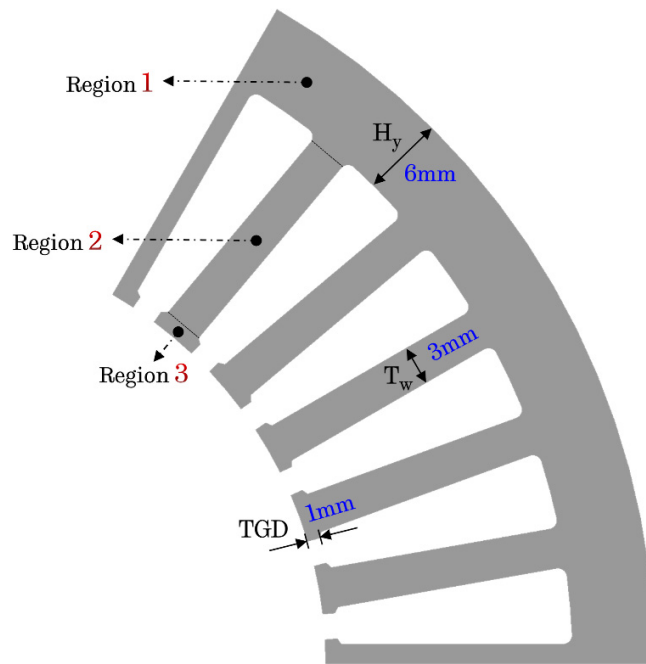
(a) Laser cut stator schematic.
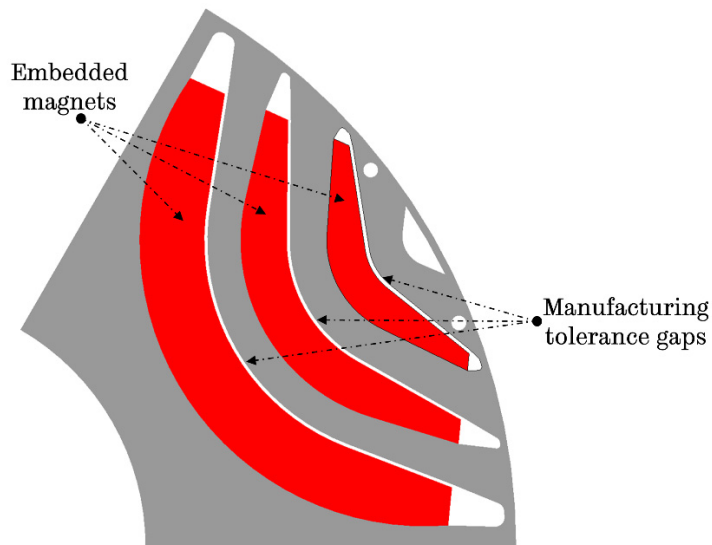
(b) Wire eroded rotor with embedded magnets schematic.

Figure 6.6. PMA SynRM schematics.
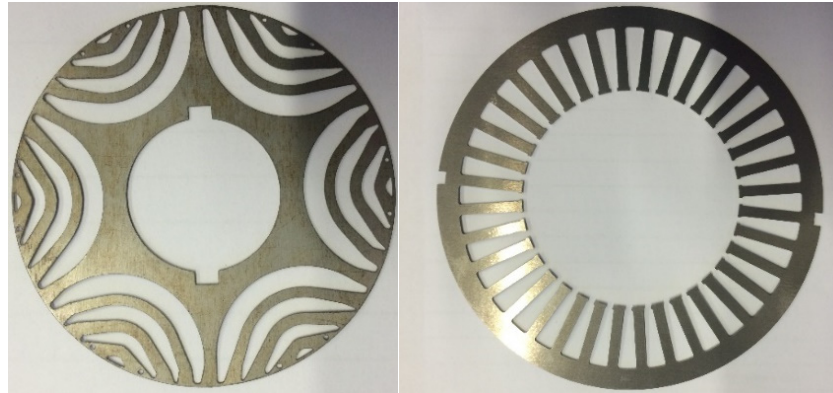
(a) Wire eroded rotor (left) and laser cut stator (right) lamination.
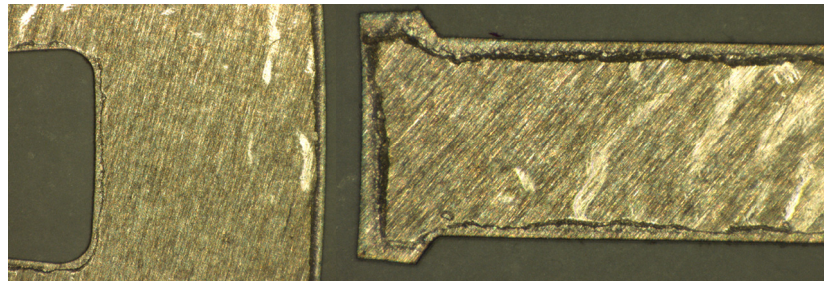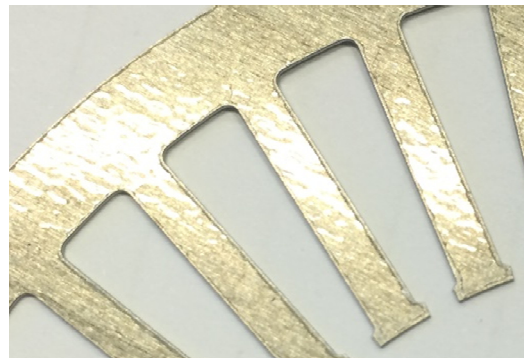
(b) Magnified stator lamination indicating the insulation burn-marks resulting from laser cutting (viz., black lines around the cut edge).

Figure 6.7. Physical machine lamination.

For the back iron and tooth body regions, B-H curves corresponding to 6mm and 3mm laser cut strips are assumed according to their respective widths, H_y and T_w, as illustrated in Figure 6.6(a). For the case of the tooth tip region, a B-H curve corresponding to a 2mm strip is assumed based on the ratio of cut length per steel area between the tooth tips and tooth body regions. Figure 6.8 shows the generated B-H curves corresponding to each region of the subdivided stator in FEA, along with the ideal manufacturer's B-H curve as a reference.
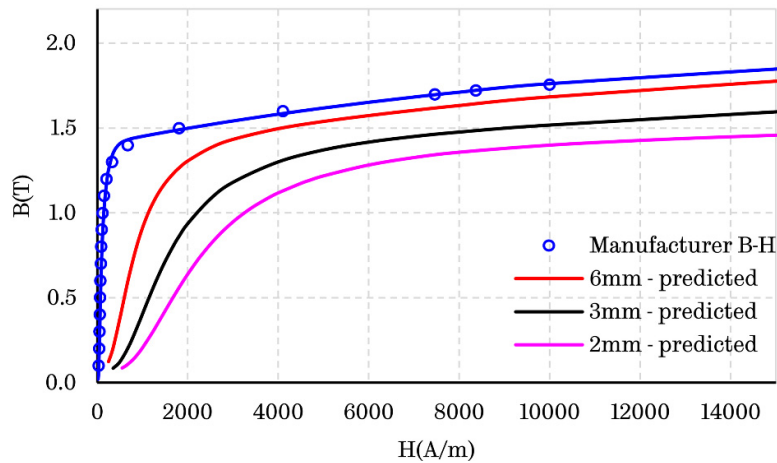
Figure 6.8. Generated B-H curves corresponding to each different region of the sub-divided stator in FEA.

Both 2D and 3D FEA have been employed for the prediction of the key design parameters of the machine. It should also be noted that other manufacturing factors potentially influencing the prototype's performance, such as manufacturing tolerances (viz., Figure 6.6(b)), magnet B-H properties and dimensions have been experimentally characterised and are considered in the FEA model. Further, since the machine has a 3-step-skewed rotor, the use of 3D FEA allowed to factor in the end-effects and the axial interactions between adjacent skewed steps that cannot be predicted by the commonly employed multislice 2D FEA (viz., Chapter 5). As has been shown in Chapter 5, such axial leakage flux components (i.e., 3D) can result in a (~3%) reduction in the fundamental back-EMF harmonic component.

Figure 6.9 illustrates a comparison between the experimentally measured and predicted phase back-EMF. It can be seen that a combination of 3D effects, and more importantly the damage caused by the laser cutting of the stator laminations has resulted in significant reduction in the fundamental component of the back-EMF. It is worth mentioning that the damage resulting from laser cutting depends on the laser power and feed rate, the material's thermal conductivity and thickness, and other processing parameters, which determine the temperatures experienced by the samples, and hence the degree of the damage [114]. Since the laser cut effects are influenced by many processing parameters, it is expected that the cutting

conditions in [113] and [114] may not necessarily be replicated. Consequently, the degree of magnetic degradation experienced by the laminations employed in the investigated machine may be slightly different, which could partially explain the remaining difference between the measurements and predictions of the back EMF. In addition, other manufacturing processes, such as the stator shrink fitting, which is employed for the manufacture of the machine, can also cause stresses that affect the magnetic properties [120] and the performance of the machine. However, these are not considered in this investigation.
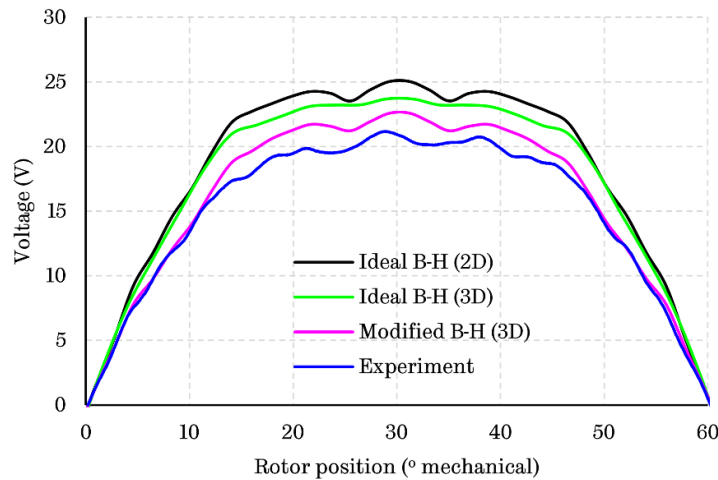
(a) Back-EMF variation with rotor position (over half mechanical cycle).
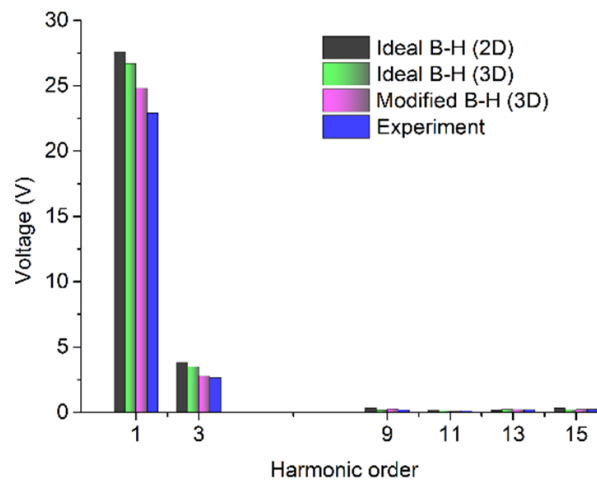
(b) Harmonic spectra of critical back-EMF components.

Figure 6.9. Phase back-EMF at base speed (i.e., 2100rpm).

Figure 6.10 shows the variation of the electromagnetic torque with the q-axis component of phase current (I_q), at different levels of the d-axis component of the phase current (I_d). Again, employing the modified B-H curves, which take into account of the damage caused by laser cutting, results in significantly improved predictions of the torque under various load conditions spanning from low to high saturation levels.
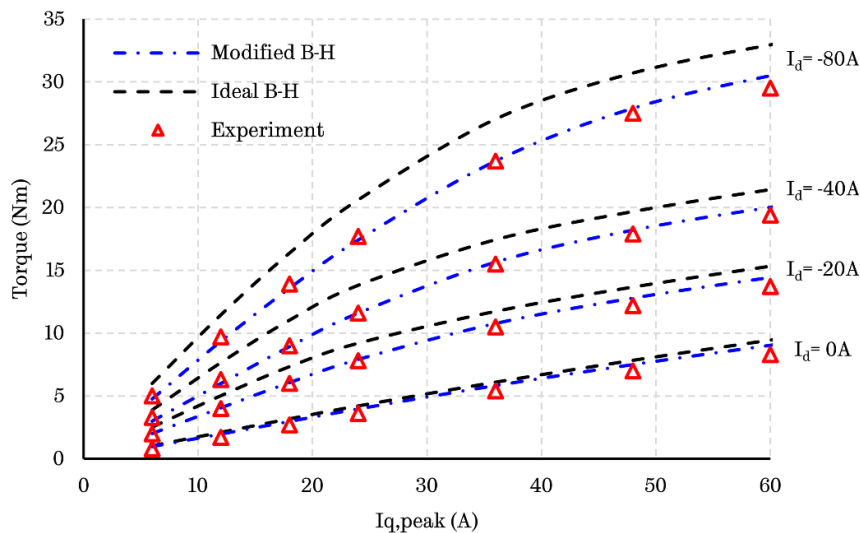
Figure 6.10. Comparisons of average output torque against q-axis current (I_q), at various d-axis currents (I_d).

Lastly, Figure 6.11 shows the variation of the q-axis component of the inductance (L_q) with the q-axis current (I_q), when the direct axis current (I_d) equals zero. Likewise, employing a modified B-H curve results in significantly improved predictions, particularly in the region of lower I_q excitation, where the machine with ideal B-H curve exhibits substantial deviations compared with the measurements. Naturally, towards higher I_q excitation, which is conducive to higher core saturation, differences between measured and predicted results are reduced. The adverse effects emanating from laser cutting may be more pronounced in machine topologies characterized by a large number of stator teeth, or in general, where the ratio of cut length to steel area is high. This is typically the case with machine topologies employing distributed windings, such as the investigated PMA SynRM.
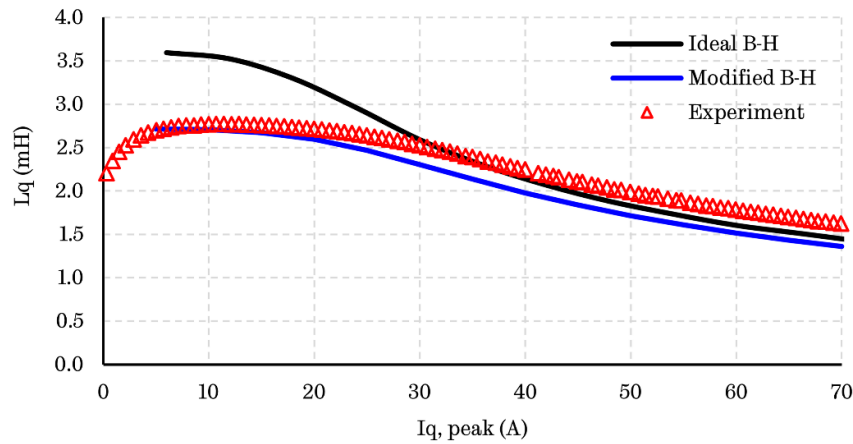
Figure 6.11. Comparisons of q-axis inductance (L_q) against q-axis current (I_q), at d-axis current equal to zero (I_d=0A).

6.3 Remarks

The chapter has investigated the effects of the laser cutting of lamination stacks on the performance of electrical machines. It is shown that the performance of a PMA SynRM, which is equipped with a laser cut stator lamination stack, and characterized by a relatively large cut length per steel area, has been significantly affected. Consequently, the finite element predictions employing ideal manufacturer supplied B–H curves exhibit very large discrepancies with the measurements. A technique for the modeling of the B-H curves taking into account of the effects of laser cutting has been described. The derived B-H curves are employed in finite element analysis (FEA) and reasonably good agreement with measurements is achieved.

Chapter **7**

Topologic and Parametric Multi-physics Design Optimization of PMA SynRM for EV Traction Applications

Permanent magnet assisted synchronous reluctance machines (PMA SynRMs) have the potential to substantially reduce or even eliminate the use of rare-earth magnets, which are currently characterised by a volatile market price and availability issues that are fuelling increasing concerns in the automotive industry. Accordingly, this chapter conducts a comprehensive investigation into topologic and parametric design optimisations of PMA SynRMs for electric vehicle (EV) traction applications, providing useful insights regarding their design for the specific application.

The design optimisations are conducted via an effective and computationally efficient optimisation platform, which facilitates fast multi-physics performance evaluations by using a set of finite-element (FE)-characterised analytical machine models without sacrificing accuracy. It also enables multiple design optimisations characterised by a large number of design parameters (>10) to be executed in a timely efficient manner through the integration of distributed computing capabilities. The employed optimisation platform maximises the system (machine + inverter) energy efficiency against a given driving cycle by systematically evaluating a defined set of electrical, thermal and mechanical design constraints.

Against this background, the multi-physics design optimisation and performance of traction PMA SynRMs employing distributed windings and characteristically different magnet materials in the rotor (i.e., sintered NdFeB and ferrites) is comprehensively investigated. Optimal rotor structures that most effectively utilise the employed magnet material, while leaving the remaining performance virtually unaffected, are identified for each magnet type. Further, the multi-physics design optimisation of PMA SynRMs using fractional-slot windings is also investigated and benchmarked with the optimal configuration with a distributed winding. The attained optimal PMA SynRM designs are comprehensibly evaluated and compared against multiple indicative performance metrics, including the energy efficiency against characteristically different driving cycles, reluctance torque capability, thermal behaviour, torque/power density and cost, with the aim of assessing their viability for (EV) traction applications.

It is shown that a ferrite PMA SynRM design can comprise a competitive solution for EV traction considering the trade-off between performance and cost. In

fact, when its performance is optimised and evaluated against standardised driving cycles (such as the NEDC and WLTP), where the machine is expected to operate over its lifetime most frequently, it exhibits little or even none demerits to the NdFeB PMA SynRM counterpart. Moreover, it is demonstrated that a PMA SynRM employing distributed windings exhibits superior overall performance than the fractional-slot counterpart, primarily due to its superior reluctance torque capability and inherently lower iron losses. This trend persists even if the active axial length of the fractional-slot design is extended to consider the longer end-windings of the distributed winding counterpart.

Parts of this chapter are published by the author in [65].

Current conventional transportation systems, powered by ICE propulsion powertrains, are characterised by extremely low energy efficiencies resulting in the majority of fuel burned for propulsion to be wasted (i.e., in fact, ~80-90%) [121]. The wasted fuel contributes to the generation of carbon and heat emissions and has a high economic impact. Considering that about 1 billion vehicles exist today, consuming ~70% of oil production [121], raises severe concerns about air pollution and fossil fuel abundance. Based on the above notion, lawmakers imposed strict regulations on fuel-efficiency and resulting emissions standards to the automotive industry. This, in turn, has propelled a significant amount of research into traction electrification, as it forms the key to improve the energy efficiency of transportation while leading to a drastic reduction on the reliance on fossil fuels and the resulting carbon and heat emissions. Electric vehicles (EVs) are, without a doubt, becoming an emerging reality and have the potential to offer an ultimate solution for sustainable personal mobility, especially if powered by electrical energy harvested from renewable energy sources.

As an intrinsic part of any EV powertrain, electric traction machines being the only tractive source in the vehicle exhibit the most substantial energy loss [15], and thus significantly influence the system's energy efficiency. The selection of the most energy-efficient and cost-effective electric machine technology and topology for EV tractions forms a primary challenge, given their highly demanding design requirements regarding energy efficiency, torque/power density, wide constant power speed range, overload capacity and cost-effectiveness [19], [20].

A vast majority of currently available commercial EVs employ traction machines that utilise high energy density NdFeB permanent magnets (PMs) [38],

offering high torque and power density and relatively wide high efficiency operating region. However, the ever-growing demand for high energy density rare earth PMs in the EV traction and wind power applications has caused increasing concerns regarding the price volatility and future availability of rare-earth magnet materials [2], [23]. As a result, the industrial EV market is now striving towards more sustainable, rare-earth-less or rare-earth-free solutions with the aim of minimising the reliance on rare earth magnet materials, which are characterised by price instability and supply chain issues. Maintaining, however, the high efficiency and torque/power density performance, that rare earth PM traction machines (such as the interior PM machines) typically offer, forms a key challenge.

While induction machines (IMs) offer the lowest cost, high technological maturity, simple construction, and extensive operating speed range with high reliability, they exhibit a lower torque density, inferior power factor, and relatively less efficiency compared to PM synchronous machines (PMSMs) [48], despite the use of enhanced loss minimization control algorithms [42]. Likewise, switched reluctance machines (SRMs) are more robust and more cost-effective than PMSMs. However, they are characterised by noise and vibration harshness issues and inferior power factor which leads to oversizing of the inverter and, hence, an increase in the powertrain cost. The typically inferior energy efficiency of IMs and SRMs directly influences the attainable EV range and the required battery size and cost.

The PM-assisted synchronous reluctance machine (PMA SynRM), is a PMSM topology that facilitates substantial rare-earth PM volume reduction, but also enables the use of cheaper, low-remanence bonded NdFeB or ferrite PMs (in higher volume). This is due to the fundamental torque production mechanism of PMA SynRM, that fundamentally relies on the reluctance torque component resulting from its highly anisotropic multi-layer rotor structure [35], [71], [122]–[124]. Further, the inherently high reluctance torque capability of the PMA SynRM enables an extended constant power speed range and high overload capacity, while having a relatively low PM amount and hence lower back-EMF at high-speed operation [74]. Considering the trade-off between performance and cost, PMA

SynRM has, therefore, the potential to resolve some of the conflicting design challenges currently characterising the EV automotive industry.

The design and performance of PMA SynRMs considered for EV/HEV traction has been examined for sintered NdFeB and ferrite magnets in [48], [72], [122], [123], [125]–[128] and [37], [69], [89], [93], [129]–[132], respectively. A re-design procedure of the rotor of the 2nd generation TOYOTA Prius IPMSM into a PMA SynRM with the aim of enhancing the reluctance torque contribution is carried out in [37], and the performance of the optimal PMA SynRM is compared to the Prius IPMSM benchmark at the rated operating condition. An analytical process aimed at the minimisation of the PM quantity in a NdFeB PMA SynRM by modifying the surface area (i.e., height and width) of the magnet blocks embedded in the rotor layers, while leaving the remaining performance unaffected and being robust towards demagnetisation, has been presented in [125] and validated by means of FEA.

The optimisation of PM volume to maximise the performance of a PMA SynRM against the rated operating conditions at the base and maximum speed has been investigated in [75]. However, all geometrical design parameters of the machine were kept fixed, and only the magnet remanence was varied in the process, the value of which determines the required PM volume according to a given magnet material type. Such an approach does not reflect the link between the energy density of a particular magnet type (e.g., ferrite or NdFeB) and the rotor lamination shape required to accommodate the magnets, which is likely to influence the magnetic anisotropy and remaining performance of the machine.

The design of PMA SynRM in the majority of studies in the literature, however, generally relies on the conventional design approaches based on the rated operating envelopes of the traction machine without considering the corresponding mission profile of the vehicle in the optimisation process. The current-state-of-art PMA SynRMs for EV traction are typically designed to achieve high efficiency around the rated and/or peak operating points at the base and/or maximum operating speed. As has been demonstrated in Chapter 2, [41] a traction machine optimised against the rated operating conditions may not yield optimal results against a driving cycle. During typical urban or suburban driving,

represented by various legislative driving cycles, the EV traction machine most frequently operates in the low-load operating region [15], [41], [47], which is located far from the rated operating conditions that are primarily utilised in short transients for hill-climbing or acceleration purposes.

The mismatch between the operating regions where high energy consumption is concentrated over driving cycles, and the locations of the rated operating points, clearly highlights the significance of incorporating representative driving cycles into the design optimisation process of traction machines. Doing so will enable to acquire designs exhibiting optimal active material usage and superior energy efficiency against driving conditions pertaining to their real-world operation, which is in turn critical for the enhancement of the EV driving range or the reduction of battery capacity and cost. Against this context, the author's work in [65] has investigated the influence of characteristically different driving cycles on the design optimisation and performance of a low remanence PMA SynRMs with distributed windings for EV traction. It has demonstrated that characteristically different sets of leading machine design parameters are attained when the optimisation objective is switched between different driving cycles (i.e., NEDC and AUDC), since the energy loss of each cycle is concentrated in different areas within the torque-speed operating range.

This chapter expands the scope of Chapter 3 and the author's work published in [65], by taking a holistic approach to the design and optimisation of PMA SynRMs with the aim of comprehensively assessing their viability for EV traction applications. It considers several topologic and parametric modifications in the design optimisation process of PMA SynRMs, which now incorporates systematic evaluation of multi-physical design constraints.

The design optimisation of traction machines is characterised by many challenges and complexities, which stem from their highly demanding design requirements. These involve the energy efficiency maximisation over driving cycles while satisfying the required peak torque-speed operating envelope, subject to stringent multi-physical design constraints – viz., electrical, thermal and

mechanical constraints that need to be systematically evaluated during an optimisation. Incorporating multi-physical design constraints into the design optimisation process of traction machines is imperative to ensure a representative global optimum design.

In the case of PMA SynRM, which employs a multi-layer rotor with embedded magnets, high mechanical stress is typically localised at the multiple rotor bridges that should be as narrow as possible to reduce leakage flux. However, a mechanical stress level that exceeds the mechanical strength of the employed electrical steel can result in failure of the rotor bridges to retain the magnets at high rotating speeds. It is, therefore, important to systematically evaluate the mechanical stress level in the rotor during the optimisation process. This will enable proper adjustment of the bridge thicknesses during the optimisation process, and thus ensure the mechanical integrity of the rotor at high operating speeds. The bridge thickness modification, however, influences the electromagnetic performance of the PMA SynRM in terms of reluctance torque capability and achievable power factor [93], [125].

Further, given that in PMA SynRM the magnets have only an assistive role, and the torque production primarily relies on injected current excitation, systematic monitoring of the temperature during the optimisation process is then critical to ensure a robust design for a given cooling setup and copper insulation class. The systematic evaluation of multi-physics constraints for hundreds of design samples using FEAs would enormously scale the computational time, rendering the multi-physics global optimisation process unfeasible. Therefore, to realise multi-physics design optimisations against driving cycles in a computationally efficient manner, without compromising accuracy, a number of solutions were employed. These involve the use of analytical and semi-analytical models characterised from FEAs to describe the behaviour of the machine in the multi-physics domain (i.e., electromagnetic, thermal and mechanical), as well as the use of efficient optimisation tools and algorithms dedicated for optimisations of FE models [133].

Owing to the complex rotor structure, and hence a high degree of freedom associated with the design of PMA SynRM, multiple design parameters need to be optimised to obtain a maximum energy efficiency over a cycle, while satisfying the multi-physical design constraints. A large number of tuning parameters (e.g., ≥10) automatically translates to a vast design space, which requires the FEA evaluation of a large number of design samples to properly search and identify a global optimum solution. This leads to a drastic increase in computation time despite the use of computationally efficient multi-physics performance evaluation models. Thus, to realise several, multi-parameter design optimisations for the topologic and parametric PMA SynRM design investigation within reasonable computational times, a distributed computing cluster has been integrated with the optimisation platform.

Through this powerful design optimisation platform, which maximises the system (machine plus inverter) energy efficiency against a given driving cycle while systematically evaluating a defined set of multi-physical design constraints, this chapter comprehensively investigates various topologic and parametric design aspects on the performance of PMA SynRMs for EV traction applications. To date, no such comprehensive study on the PMA SynRM design has been demonstrated in the literature. The chapter investigates the multi-physics design optimisation and performance of PMA SynRMs employing distributed windings and characteristically different magnet materials in the rotor (i.e., sintered NdFeB and ferrites), for design cases with identical and different axial lengths.

It identifies optimal rotor structures that most efficiently utilise each magnet material type, while leaving the remaining performance virtually unaffected. Further, the multi-physics design optimisation of a PMA SynRM topology using a novel fractional-slot winding configuration [68] is also investigated and benchmarked with the optimal PMA SynRM configuration with distributed windings, where both designs use ferrite magnets. During the study, the optimised PMA SynRM designs are comprehensibly evaluated and compared against multiple indicative performance metrics, including the energy efficiency against characteristically different driving cycles, reluctance torque capability, thermal behaviour, torque/power density and cost, which assist in assessing their viability

in the considered EV traction application. The same EV application and its design specification employed in Chapter 3 are used for the design investigation conducted in this chapter.

7.1 EV and traction machine specification

Figure 7.1 illustrates the schematic of the Hi-Wi EV, which has been described in Chapter 3. The distributed traction drivetrain of the Hi-Wi comprises of three motors, with one motor mounted on the front axle and contributing nominal 40% of the total traction power, and two identical motors mounted on the rear axle, each providing 30% nominally. All three motors are coupled to their corresponding axle via a differential with a gear ratio of 1:4 and 1:7 for the front and rear motors, respectively. Detailed vehicle parameters are given in Table 7.1.
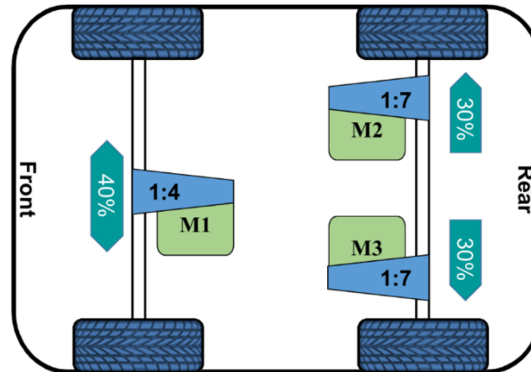
Figure 7.1. Electric vehicle drivetrain schematic – class 2 vehicle.

Table 7.1. Electric vehicle specification

Parameter	Value
Tire size	165/50 R15
Radius of wheels (m)	0.273
Vehicle mass (kg)	800
Rolling resistance coefficient	0.007
Product of drag coefficient and front area (m^2)	0.350
Air density (kg/m^3)	1.250
Efficiency of differential	0.980
Gear Ratio	1:7 rear/ 1:4 front
Maximum vehicle speed (km/h)	120.0

7.1.1 Torque-speed envelopes and driving cycles

This chapter investigates the design of the rear motors of the Hi-Wi EV with a 1:7 reduction gear. Based on a vehicle dynamics model established from the data of Table 7.1, and the requirements regarding the vehicle acceleration and hill-climbing ability, the peak and continuous torque-speed profiles for each of the rear traction motors are derived, as shown in Figure 7.2, following the process described in Chapter 2. The requirements for the design of the traction machine are established from Figure 7.2, and they are listed in Table 7.2 together with other volumetric, electrical and thermal design specification.

Owing to the dynamically varied torque-speed combinations in traction applications, which significantly influence the traction machine's energy efficiency and hence attainable EV range, it is essential to incorporate representative driving cycles, such as the NEDC, Artemis, or WLTP, into the design optimisation process of the traction PMA SynRM. As described in Chapter 2, this will enable to acquire designs exhibiting superior energy efficiency against driving conditions pertaining to real-world operation [41], [65]. The incorporation of driving cycles in the design optimisation process, however, imposes prohibitive computational time costs, particularly when high fidelity finite element (FE) evaluations over the hundreds of cycles' operating points are needed. To evaluate the machine performance over driving cycles within realistic computational times, the energy consumption over the driving cycles under consideration (i.e., AUDC and NEDC) is characterised into a finite number of representative operating points ("energy gravity centres") using the technique proposed in Chapter 2 [41].

The acquired representative operating points are shown under the operating envelopes of Figure 7.2 for comparative purposes. Each of the operating points of Figure 7.2 represents a torque-speed combination at which a specific amount of energy, referred to as energy weight, is consumed over a driving cycle. The energy weight of each representative point is represented by its equivalent marker diameter, which is normalised to the point with the maximum energy weight over both driving cycles. As a result, a systematic machine design optimisation against driving cycles can be realised against these representative

points with drastically reduced FEA computation time without compromising accuracy in energy loss representation over the cycle.
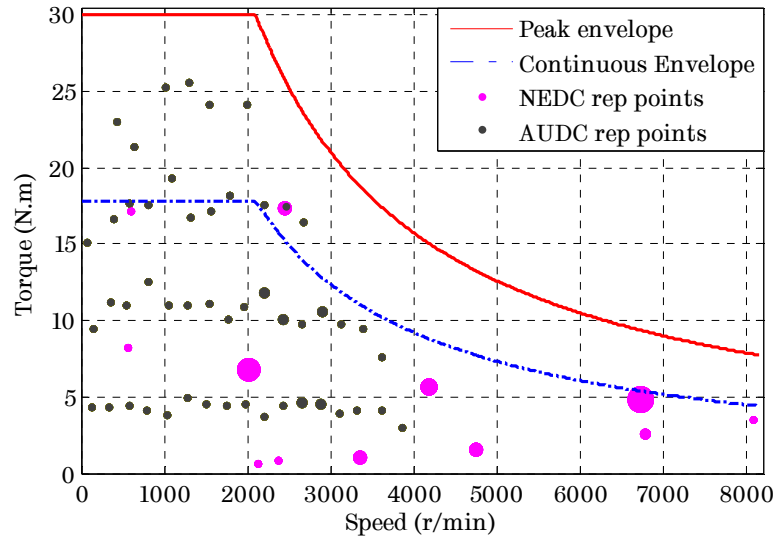
Figure 7.2. Torque-speed envelope overlaid by NEDC and AUDC representative points.

Table 7.2. Traction machine design specification

Parameter	Symbol	Value
Active length (mm)	L_s	105
Stator outside diameter (mm)	D_o	120
Base speed (rpm)	ω_b	2100
Maximum cruise speed (rpm)	ω_{ms}	8200
Peak torque below and at base speed for 120 s	T_{pk}	30.0
Continuous torque below and at base speed (N.m)	T_c	17.0
Peak torque at maximum cruise speed (N.m)	T_{ms}	7.4
Continuous torque at maximum cruise speed	T_{cms}	4.4
Peak power (kW)	P_{pk}	6.6
Continuous power below and at base speed	P_c	3.75
Nominal DC link voltage (V)	V_{dc}	120
Maximum inverter current (A)	A_{pk}	120
Maximum permissible line-to-line voltage (V)	E_{max}	<250
Ambient Temperature (ºC)	T_{amb}	40
Thermal limit for continuous operation (ºC)	-	120
Maximum thermal limit (ºC)	-	150
Cooling method	-	Air-cooled

As can be seen from Figure 7.2, the two considered driving cycles are emulating different driving modes, which are reflected by the energy consumption distribution of each cycle within the defined torque-speed operating range. The majority of operating points for both driving cycles are covered by the continuous operating envelope, implying that the machine could be continuously operated over NEDC and AUDC without exceeding its rated thermal limit. The mismatch between the operating regions where high energy consumption is concentrated over the two driving cycles, and the locations of the machine's rated and peak operating points (i.e., T_{pk}, T_c, T_{ms}, T_{cms}), which are primarily utilised in short transients during driving for acceleration and hill-climbing purposes, can be clearly observed. This highlights the significance of incorporating representative driving cycles into the design optimisation process of traction machines, which is in turn important for the enhancement of the driving range or the reduction of battery capacity.

The distinct characteristics of the two driving cycles will, therefore, influence the outcome of the design optimisation process. Indeed, as has been demonstrated by the author's work in [65], different trends of the leading design parameters are obtained when the optimisation objective is switched between NEDC and AUDC, owing to the fact that the energy loss of each cycle is distributed in different areas within the torque-speed operating range. It has been found that a PMA SynRM design optimised against the NEDC utilises a considerably lower magnet amount than a design optimised against the AUDC while exhibiting a relatively competitive AUDC energy efficiency compared with the AUDC-optimised design.

Without loss of generality, the NEDC has been selected as the reference cycle against which the design optimisations will be conducted for the purposes of this comparative study, as until recently it formed the certification standard for micro-sized vehicles in the automotive industry of Europe [7], [52]. However, it is acknowledged that NEDC has been criticised as not being able to emulate real-world driving conditions, particularly when it comes to the acceleration and stop-and-go activities of the vehicle (related to urban driving). For this reason, similar to Chapter 3, the energy efficiency over the AUDC [76], which better represents

these driving conditions, is also considered as a metric for the performance evaluation of the investigated machine designs. The energy efficiency evaluation over AUDC acts as an indicative marker of the machine's versatility when operated against different, more aggressive, driving conditions in contrast to those found in the more moderate NEDC (i.e., optimisation objective).

The WLTP has recently been introduced by the members of the 1998 UN/ECE with the aim of improving upon the more moderate NEDC regarding the representation of more realistic driving behaviours [7]. At the time of conducting this study the WLTP was unavailable, and hence the NEDC has been used as a target cycle during the optimisation process. Nonetheless, the performance of the acquired optimal designs are also evaluated over the newly available WLTP, for comparative purposes, based on data corresponding to a class-2 vehicle.

7.2 Design optimisation procedure incorporating multi-physics performance evaluation capabilities

The design optimisation of traction machines is characterised by many challenges and complexities, which stem from their highly demanding design requirements, involving the energy efficiency maximisation over driving cycles subject to stringent multi-physical design constraints (viz., electrical, thermal and mechanical) which need to be systematically evaluated during an optimisation. The incorporation of multi-physics design constraints into the design optimisation process (which are expected to impact the outcome of the optimisation) infers repetitive multi-physics FEA evaluations over hundreds of design samples comprising the optimisation's design space. This, in turn, scales the computation time enormously, and thus renders the multi-physics optimisation unfeasible even with state-of-art computing resources. This situation is further exacerbated for the case of PMA SynRM, which is characterised by a highly non-linear magnetic behaviour and a complex rotor structure comprising of multiple design parameters.

On the other hand, incorporating multi-physical design constraints into the design optimisation process of traction machines is of paramount importance in

order to yield a representative global optimum design pertinent to its real-world operating conditions. In the case of PMA SynRM, the use of multi-layer rotor with embedded magnets, operated at high rotating speeds, necessitates monitoring of the mechanical stress level typically localised at the multiple rotor bridges, and accordingly the adjustment of the bridge thicknesses to ensure robust mechanical integrity for safe operation at high rotating speeds. The rotor bridge thickness modification, however, considerably influences the PMA SynRM's electromagnetic performance. Especially if employed with low remanence embedded magnets, as it impacts the saliency ratio and power factor of the machine (i.e., due to magnet and armature flux required to saturate the bridges) [93], [125].

Further, since in PMA SynRM the magnets have only an assistive role, and the output torque mainly relies on current excitation, the systematic evaluation of the temperature rise against critical operating conditions is mandatory during the optimisation process to ensure a robust design for a given cooling setup and copper insulation class. This is also particularly useful when PMA SynRM designs employing different slot/pole combinations are to be optimised and evaluated, where the different slot geometry can considerably influence the copper hot-spot temperature. To realise systematic multi-physics design optimisations against driving cycles in a computationally efficient manner, without compromising accuracy, several solutions were exploited. These involve the use of analytical and semi-analytical models characterised from FEAs to represent the multi-physical behaviour of the machine (i.e., electromagnetic, thermal and mechanical), and the use of dedicated optimisation tools with state-of-the-art optimisation algorithms and techniques.

Moreover, the characterisation of driving cycles into a finite number of representative points against which the energy loss is evaluated further contributes to the reduction in computation time. These solutions are combined to form a powerful, yet computationally efficient, multi-physics optimisation methodology against driving cycles, which is employed for the analyses conducted later on in this chapter. A flowchart that illustrates the design optimisation process is shown in Figure 7.3. The different steps involved in the optimisation process will be described in the following sections.
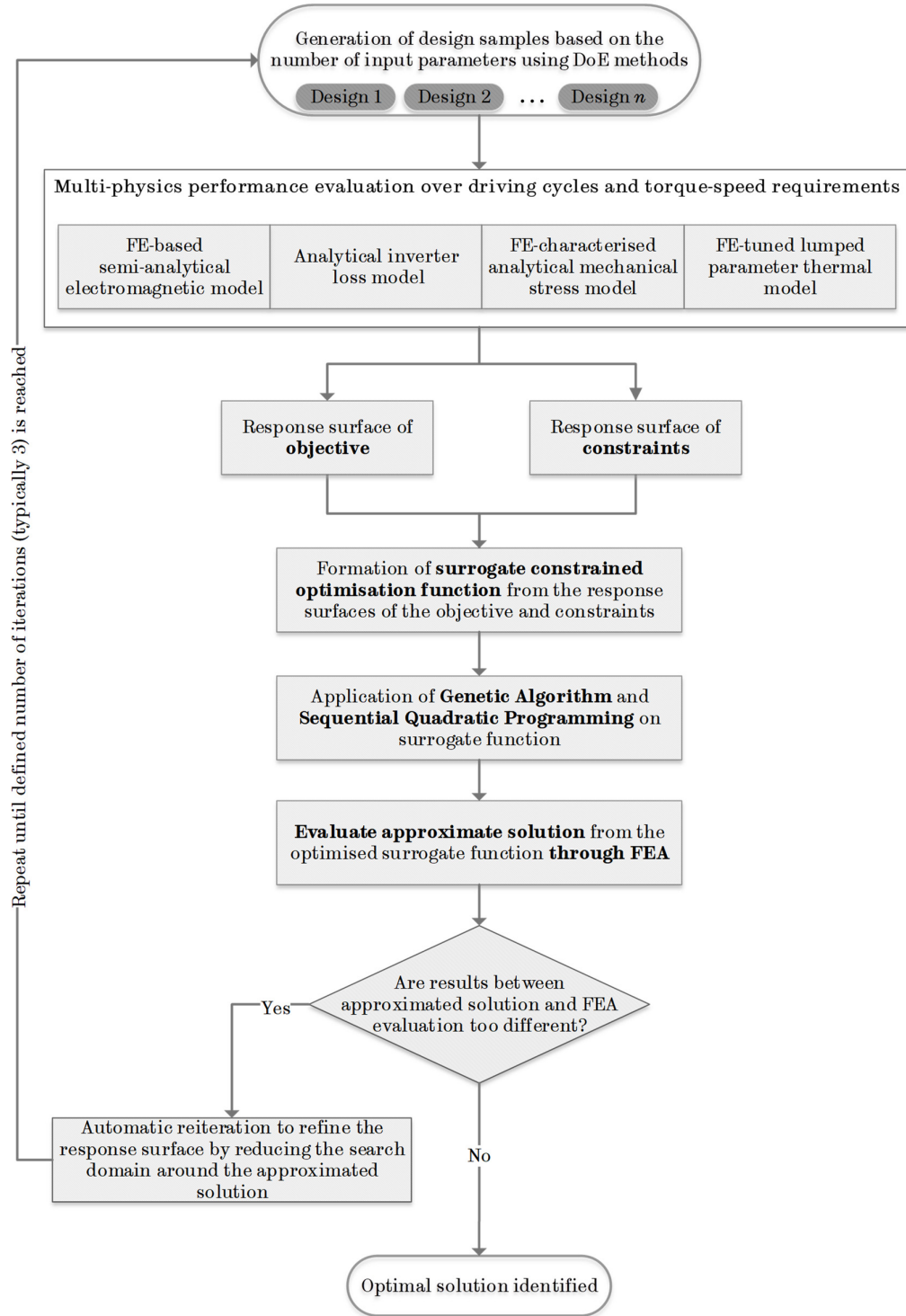
Figure 7.3. Multi-physics design optimisation flowchart.

7.2.1 Optimisation tools and algorithms

A dedicated optimisation tool, GOT-It, created by CEDRAT is employed in the multi-physics optimisation procedure. GOT-It comprises of multiple state-of-the-art optimisation algorithms and design of experiment techniques capable of solving complex multi-parameter, mono- or multi-objective optimisation problems subject to a set of defined constraints (if any). It provides parameter-screening capabilities for model order reduction by enabling to determine the most influential design parameters. It also offers robustness analyses tools to check how robust the optimal design yielded from the algorithm is, by introducing perturbations in the vicinity of the optimal parameters. It makes use of both deterministic algorithms (algorithmic), which are computationally cheap but prone to getting trapped in local optima, and stochastic algorithms (random), which are computationally expensive but gradient-free and capable of efficiently searching the design space to identify the global optimum in functions containing multiple modes. It provides the designer with full flexibility to tune the parameters of each algorithm and the possibility of combining different algorithms (such as Differential Evolution, Genetic Algorithms, Niching, Sequential Quadratic Programming etc.) for a particular optimisation problem.

GOT-It tool is essentially meant for coupling with CEDRAT's electromagnetic FEA software (FLUX) for optimisation of FE models, where the relationship between the input parameters of the model and its output behaviour are unknown, and evaluations of the model are computationally costly. It, therefore, proposes the use of optimisation methods (such as the Sequential Surrogate Optimiser – SSO) dedicated to the optimisation of numerical FE models. The proposed optimisation method relies on the response surface methodology (RSM) by building quadratic approximations of the original objective function from a finite number of well-selected sample points (or experiments), which are then interpolated. This indirect optimisation approach facilitates substantial computational time saving by optimising a response surface of the objective function (i.e., a surrogate) rather than the original objective function, which is computationally expensive to evaluate (especially when considering repeated FEA calls from the optimisation algorithm).

The response surface methodology was initially developed for modelling responses from experimental data [134], and have since gained increasing interest regarding the modelling and optimisation of numerical experiments (such as FEA)[135], including the field of electromagnetic devices [136]. A response surface is a mathematical technique that provides an approximation of a function's behaviour (that is generally unknown) in relation to its input parameter set $(x_1, \ldots, x_n)$ and typically takes the form of a second order polynomial [135], [136]

$$f(x_1, \ldots, x_n) = \alpha_0 + \sum_{i=0}^{n} \alpha_i x_i + \sum_{i=1}^{n} \alpha_{ii} x_i^2 + \sum_{i=1}^{n} \sum_{j=i+1}^{n} \alpha_{ij} x_i x_j \qquad (7.48)$$

Where α, signified with a subscript, are the polynomial tuning parameters to be calculated. The response surface function can represent the behaviour of any design objective or constraint (e.g., energy efficiency or voltage limit) with respect to the variation of the input parameters (e.g., machine geometrical parameters). The polynomial coefficients can be calculated based on a relatively small number of well-selected design samples of the defined input parameter set. Interpolations of the obtained response surface can then provide a close approximation of the function's behaviour. The developed response surface can, therefore, be used in the optimisation instead of the original function resulting in a simplified and faster process. The selection process of the design samples (or experiments) to be evaluated, however, is of critical importance in order to capture the maximum amount of information regarding the function's response from the lowest possible number of computationally costly FEA sample evaluations.

The SSO algorithm in GOT-It optimisation tool, which was primarily developed for optimisation of FEA models, automatically facilitates this process. The selection of the design samples is conducted based on Design of Experiment (DoE) techniques, where factorial design, central composite design (CCD), and Box-Behnken technique are the most frequently employed DoE ones for building response surfaces, and estimating the main and interaction effects of the input parameters [137], [138]. GOT-It applies the central composite design principle for the selection of the design samples based on the number and value range (i.e., 2-level – min and max values) of the input parameters using the principle shown in

(7.49). The CCD approach provides an effective solution, which is extensively employed, for building the quadratic (second order) response surfaces during the optimisation process [137].

$$N_{samples} = 2^{k-p} + 2k + 1 \qquad (7.49)$$

Where k is the number of input parameters, and p is a coefficient that takes values from zero onwards to make first term of (7.49) a full, one-half, one-quarter or one-eighth 2^k factorial based on the value of k. The data listed in Table 7.3 demonstrate the use of the central composite design principle in GOT-It based on different number of input parameters (k).

Table 7.3. Generation of design samples based on central composite design in GOT-It

No. of input parameters (k)	Central composite design type	Generated design samples ($N_{samples}$) per iteration
3	Central composite full ($p = 0$)	15
5	Central composite half ($p = 1$)	27
7	Central composite half ($p = 1$)	79
9	Central composite quarter ($p = 2$)	147
10	Central composite eighth ($p = 3$)	149

Now that the principle of sample (or experiment) selection in GOT-It has been demonstrated, the steps to set up the constraint optimisation problem, as well as the way GOT-It tool couples with the electromagnetic FEA (i.e., FLUX) to execute the optimisation process will be described. Firstly, a fully parameterised (viz., with geometrical and physical parameters) 2D/3D electromagnetic FEA model of an electrical machine is created in FLUX software. To exchange data between FLUX and GOT-It in the form of geometrical and physical parameters, as well as results (such as the torque output or voltage), a dedicated interface, namely Flux communicator, is employed. The exchange process between the two software is illustrated in Figure 7.4. The desired parameters required to formulate the optimisation problem, in terms of input parameters, objectives and constraints, should first be defined in the parameterised FLUX model of the physical device to

be optimised. Once this is done, the FLUX communicator interface makes the parameters defined in the FEA model available in GOT-It tool, where they can be utilised by the user to set up the optimisation problem.
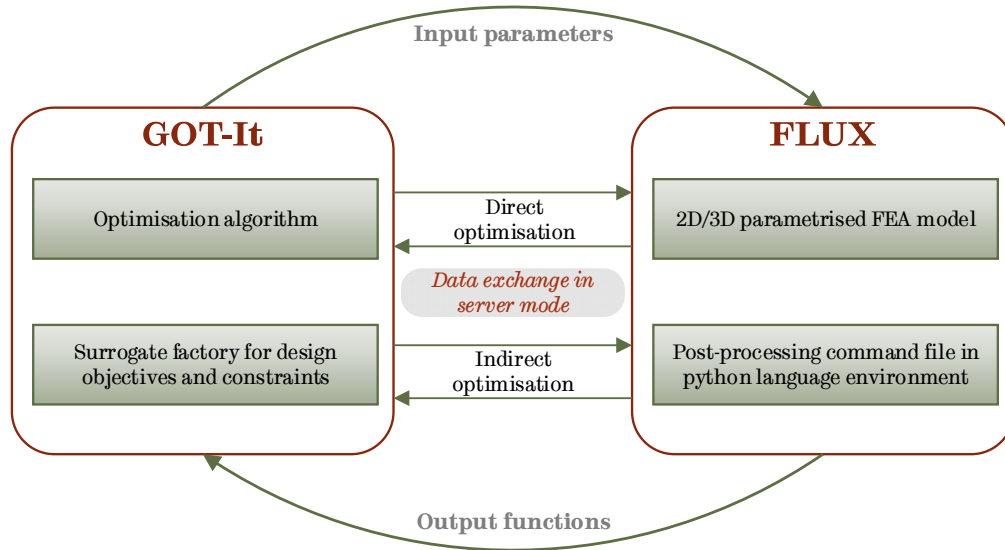
Figure 7.4. Coupling and exchange of data between FLUX and GOT-It software.

After configuring the FLUX communicator, GOT-It can automatically control FLUX (which now operates in server mode) by passing instructions to it. This enables GOT-It to send and receive parameters to and from the FLUX FEA model to be processed by its built-in algorithm during the optimisation process. More complex functions and command sequences in the form of a macro can be implemented in a post-processing file written in python language, which is executed every time GOT-It requests an FEA evaluation of the model. This post-processing file enables to conduct powerful analysis and manipulations on the results acquired from an FEA evaluation. Further, it allows the incorporation of other multi-physical models in the optimisation process. The results from the post-processing are stored in the parameters already defined in the FEA model in FLUX and are then passed to GOT-It. The process repeats as the optimisation progresses.

The following steps are sequentially executed to set up an optimisation problem in GOT-It:

- Definition of the input parameters, their type (discrete or continuous)

and their variation range in terms of minimum and maximum values.

- Definition of the optimisation objective(s) and constraint(s).
- Selection of the appropriate optimisation algorithm to be employed for the problem at hand (in this case, the sequential surrogate optimiser) and tuning of its settings (e.g., number of iterations).
- Execution of the optimisation.
- Analysis and plotting of results to identify patterns and gain physical insights.

It is a good practice to perform a parameter screening before the execution of the optimisation to identify the most influential design parameters and achieve a model order reduction with reduced variation parameters, which leads to computational cost savings. In this study, only singe-objective constrained optimisation problems are considered. The objective to be optimised is always the energy efficiency over a defined driving cycle, which for the considered application, primarily influences the attainable EV range and the battery size and cost. Other design requirements, like the dc-link voltage limit, the maximum inverter current, temperature limits, mechanical stress limits, demagnetisation, torque ripple, and the required torque-speed range, are treated as constraint functions that need to be respected during the optimisation. Once the optimisation is configured and executed in GOT-It, the SSO algorithm generates the initial design space populated by a number of samples determined based on the central composite design described previously.

The samples are evaluated in the multi-physical domain through FEA and the post-processing macro that contains analytical and semi-analytical electromagnetic, thermal and mechanical stress models (which are described in more detail in a subsequent section). After the evaluation of the initial sample population is completed, the SSO substitutes the original objective and constraint functions with analytical response surfaces (surrogates) in the form of second-order polynomials. The approach that GOT-It uses for the creation of the response surfaces is described in [139]–[141]. The developed surrogate functions of the objective and constraints are then combined to formulate an equivalent mono-

objective constrained surrogate optimisation function (G) as shown in equation (7.50).

$$G = f + \sum_{j=1}^{n} p_j \, \text{Max}(0, CTRT_i - LIMIT_i) \qquad (7.50)$$

where f is the optimisation's single objective, $CTRT_i$ is the ith design constraint and $LIMIT_i$ is its corresponding design limit value, and p_i the penalty factor of a particular design constraint. The penalty factor is applied when a design constraint is not satisfied, leading to the penalisation of the objective function (G). This makes the minimisation of the objective harder, and leads to avoiding certain parts of the design space by excluding particular combinations of the input parameters.

Now, the SSO applies a computationally costly genetic algorithm (configured with 1000 generations and 30 individuals) on the formulated surrogate optimisation function (G) to identify the optimal set of values for the input design parameters. Since the optimisation objective is now represented by a computationally inexpensive, analytical response surface, the GA can yield an approximate global optimum solution rapidly by avoiding numerous FEA evaluations. A sequential quadratic programming (SQP) algorithm is thereafter implemented on the result from the GA to inspect the robustness of the obtained solution. The value of the solution from the optimised surrogate function is then compared to that of the original function, after performing an FEA evaluation for it. If the results from the comparison are not satisfactory, the SSO automatically repeats the process to improve the response surface by shrinking the search domain around the approximated optimal solution obtained from the surrogate model.

The SSO then generates another population of trial designs in the evolved, reduced search domain for the next iteration, where a refined surrogate function is constructed. The described process repeats by further shrinking the search space until the SSO converges to a robust global optimum solution. Typically, three iterations were found to be adequate for the algorithm to converge to a robust solution. If, however, the yielded solution is not robust enough, it is possible to increase the iteration number, and the SSO will naturally proceed from where it

left off. An example of an optimisation case of a representative PMA SynRM traction machine aiming to maximise the system (machine + inverter) energy efficiency over the NEDC, subject to several multi-physical design constraints, has been executed using the described optimisation process to demonstrate its effectiveness.

Figure 7.5 demonstrates the evolution of the objective function and the input design parameters as the SSO proceeds through multiple iterations (in this case 3) to converge to the global optimum solution. It can be observed that by the end of the third iteration the optimisation objective only varies within the range of about 0.5%, indicating the convergence of the algorithm to a robust global optimum solution. Multiple optimisations such as the demonstrated case are performed for the purposes of the analysis described in the subsequent sections of this chapter.
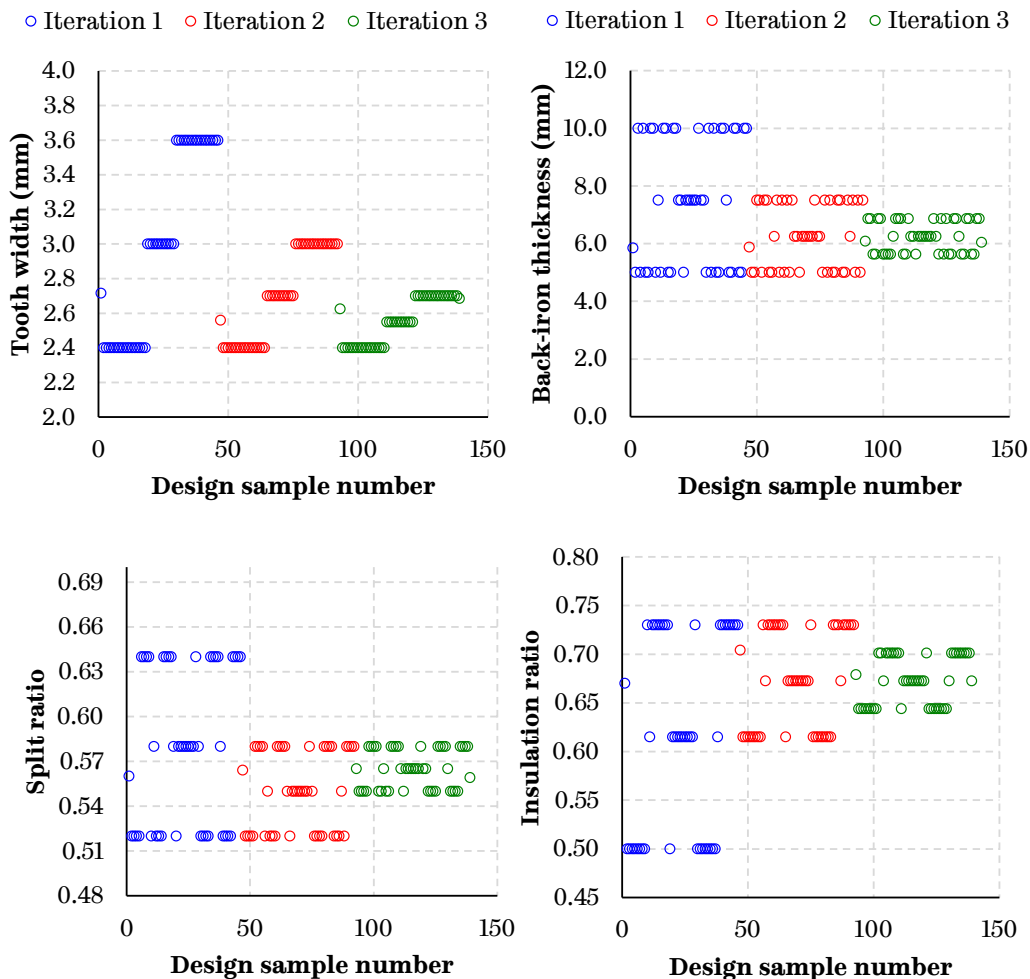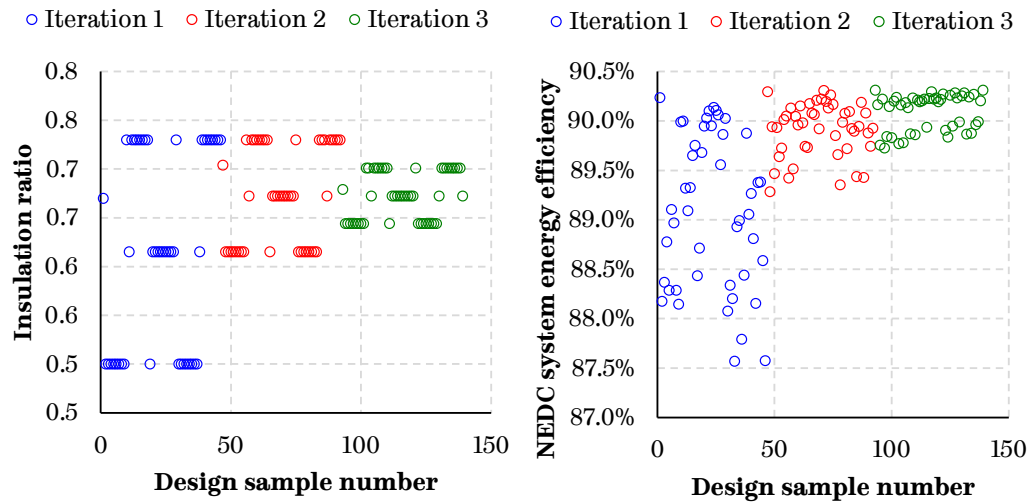
Figure 7.5. Example of optimisation with SSO in GOT-It– convergence of defined input parameters and objective function after 3 iterations.

7.2.2 Distributed computing cluster

Owing to the complex rotor structure, and hence high degree of freedom associated with the design of PMA SynRM, as well as the high non-linearity due to its high anisotropy, multiple design parameters need to be optimised to attain the maximum cycle energy efficiency and optimal active material usage while satisfying the defined multi-physical design constraints. A large number of influential design parameters occurs, despite a parameter screening process, leading to a vast design space to be explored by the algorithm. Referring back to Table 7.3, one can see that the number of samples for one iteration becomes ~5.5 times larger when the number of input design parameters increases from 5 to 10. The large design space, however, necessitates numerous FEA evaluations of trial design samples so that the optimisation algorithm can build response surfaces that adequately represent the behaviour of the model under optimisation. This, in turn, results in a drastic increase of computation time, despite the advantages emanating from the use of computationally-efficient multi-physics evaluation models and optimisation algorithms.

For instance, a 10-parameter optimisation problem would require the FEA evaluation of ~450 samples in three iterations using the SSO algorithm. This approximates to a total computation time of ~225 hours (i.e., ~9.5 days), assuming

~30 minutes for the performance evaluation of each design sample through FEA. The situation worsens if one considers that the computational time linearly scales when several machine topologies are to be optimised during a design investigation process, as is the case of this holistic study. Thus, to realise several multi-parameter design optimisations for the topologic and parametric design investigation within a realistic time-frame, a high-performance computing (HPC) cluster was implemented using CEDRAT's distribution engine (CDE) that couples with GOT-It and FLUX. The HPC cluster facilitates distributed (parallel) computations by simultaneously solving several design samples. This approach erodes a substantial amount of time from the total computation time compared with conventional sequential computing.

The analogy between the two approaches is demonstrated in the diagrams of Figure 7.6. Note that the reduction in computational time is approximately linear to the number of CPU cores involved in the process. This suggests that the resulting ~64 hours of computation time can potentially reduce further to almost half (~ 32 hours) if an additional 4-core CPU is incorporated in the cluster configuration and so forth. Having defined and demonstrated the optimisation software tools and algorithms involved in the devised optimisation process, the subsequent section will delve into the description of the computationally efficient models used for the multi-physics evaluation of each design sample during the optimisation.
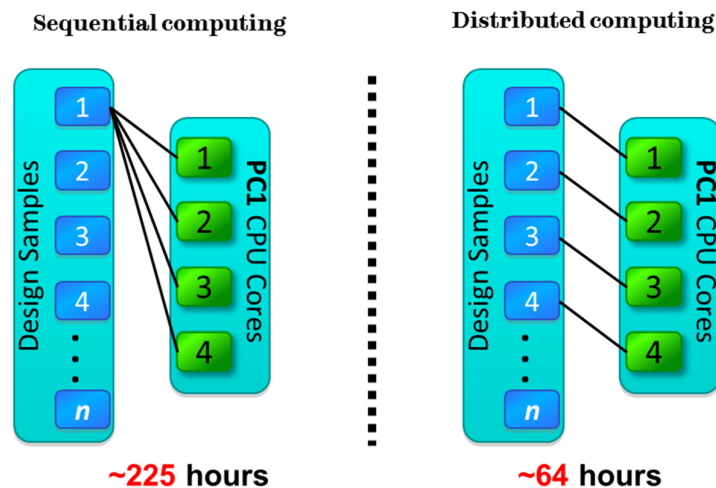
Figure 7.6. Sequential vs distributed computing optimisation times (with 10 optimisation parameters).

7.2.3 Multi-physics performance evaluation models for the PMA SynRM

The multi-physics performance evaluation block (see the diagram of Figure 7.3) consists of computationally efficient models, which can provide accurate electromagnetic, thermal and mechanical stress evaluations for each design sample of the optimisation process swiftly. An analytical inverter loss model is also included, enabling the evaluation of system (i.e., machine plus inverter) energy efficiency over driving cycles. The employment of such computationally efficient evaluation models constitutes an additional step towards the realisation of an effective multi-physics optimisation environment of traction machines over driving cycles.

7.2.3.1 Electromagnetic performance evaluation models

This section describes the methods employed to enable swift predictions of the electromagnetic performance of a design sample over the whole torque-speed operating range with high accuracy. The employed methods are premised on the classical d- and q- axes modelling system (with the d-axis being aligned with the magnetisation direction of the magnets).

The electromagnetic behaviour of a design sample is characterised by analytical response surface functions of the d- and q-axis flux-linkage, constructed from a limited number of FEA solutions over a uniform grid of d- and q-axis current samples. It has been identified that only a 6 by 7 grid of d- and q-axis current combinations is required to adequately represent the magnetic non-linearity and cross-coupling effects (between the d- and q- axes) [99], [101] characterising the PMA SynRM topology under investigation. Experimentation with other machine topologies, exhibiting less magnetic non-linearity in contrast to the investigated PMA SynRM, has indicated that even a 4 by 5 grid of d- and q-axis current samples was adequate to accurately represent the electromagnetic behaviour of a single-layer v-shaped IPM.

All things considered, the trade-off between the minimum number of d- and q-axis current combinations, and the accuracy of the model in representing the electromagnetic behaviour of a particular machine under study, should be

considered prior to commencing the optimisation process to guarantee the best possible reduction in computation time. The models representing the variations of d- and q-axis flux-linkage with the d- and q-axis currents are expressed in the form of high-order polynomials (7.51), the coefficients of which, are obtained from fitting their corresponding response surface.

$$\Psi_{d,q}(I_d, I_q) = \sum_{i=0}^{m} \sum_{j=0}^{n} \alpha_{ij} I_d^m I_q^n \qquad (7.51)$$

The number of coefficients for the polynomial with two independent variables is given by $(m+1)(n+1)$. Where $\Psi_{d,q}$ is the average d- or q-axis flux-linkage over one electrical cycle, m and n are the polynomial order numbers assigned for I_d and I_q, respectively. In this study, the selection of $m = 3$ and $n = 4$ in the bivariate polynomial of (7.51) yields an accurate fit for the finite set of data samples obtained from FEA. The goodness-of-fit from the surface fitting process of the flux-linkages of a representative PMA SynRM model is demonstrated in Figure 7.7, where the black dots indicate the raw data samples from FEA.
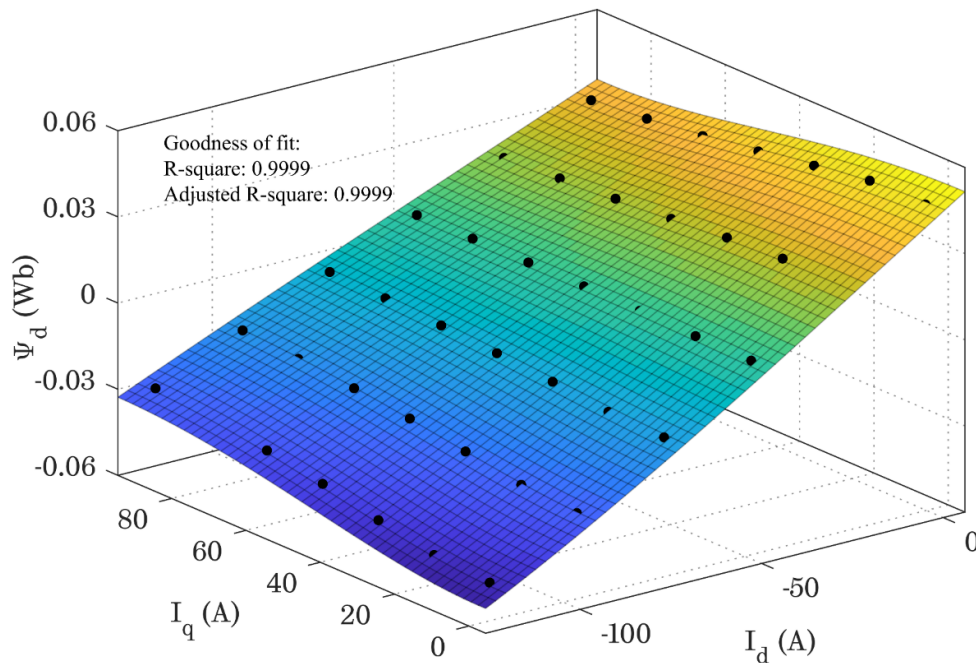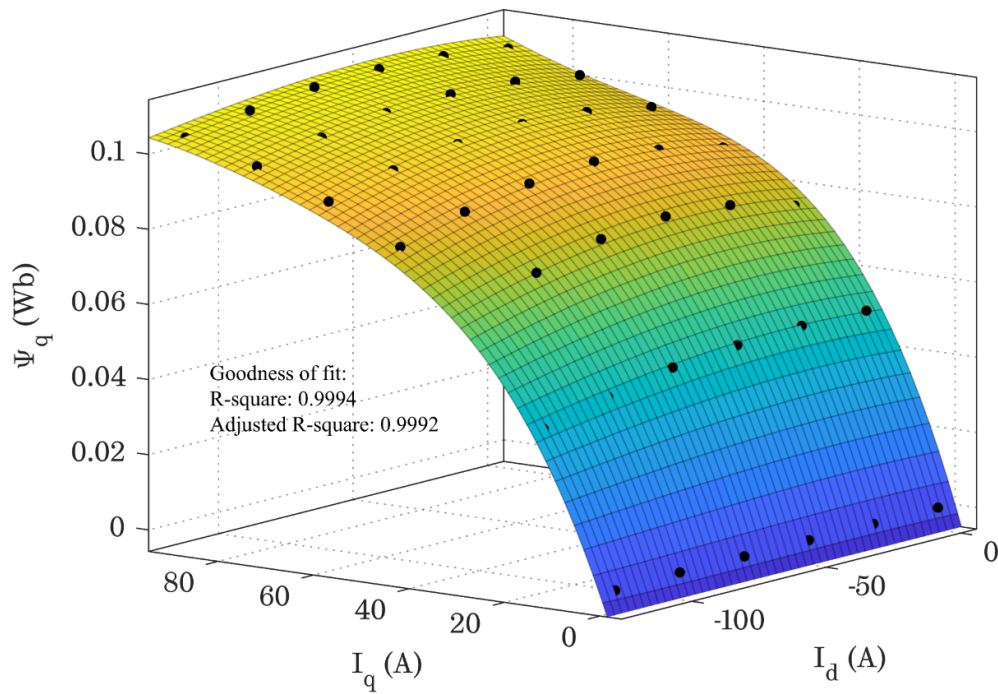
Figure 7.7. Surface fitting of $\Psi_d(I_d, I_q)$ and $\Psi_q(I_d, I_q)$ data obtained from FEA.

Typically, multi-static angle-rotated or transient FEA solution over an electrical cycle (or one-sixth of the cycle in the case of a balanced 3-phase system) are required to obtain the average flux-linkage. It is possible, however, to considerably reduce the computation time for these evaluations by performing only two magneto-static FEA solutions to accurately predict the average flux-linkage for each current combination [133]. The angular displacement between the two rotor positions at which the magneto-static FEA solutions should conducted can be derived based on the harmonic content of the *d*- and *q*-axis flux-linkages over one electrical cycle. Once the dominant harmonic that dictates the shape of the waveform is identified, the displacement angle between the two rotor positions is set to half the period of the dominant harmonic. FEA evaluations over these two rotor position samples can quite accurately provide the average flux linkage. This approach enables to calculate relatively more *d*- and *q*-axis flux-linkage samples to better represent the electromagnetic behaviour of the machine, without compromising the time-efficiency of the optimisation process.

The obtained flux-linkage models are utilised for prediction of the torque and voltage as described by the conventional equations (7.52) and (7.53).

$$T_{em} = \frac{m}{2} p (\Psi_d I_q - \Psi_q I_d) \tag{7.52}$$

$$V = \omega_e \sqrt{\Psi_d^2 + \Psi_q^2} \leq V_{lim} \tag{7.53}$$

where T_{em} is the electromagnetic torque, V is the phase voltage, ω_e is the electrical angular speed, and V_{lim} is the maximum available voltage from the inverter. With these information, it is now possible to determine the optimal values of the I_d and I_q for a particular operating point within the defined torque-speed range. This is a constraint optimisation problem, where the torque (7.52) should be maximised subject to the available inverter voltage (V_{lim}) and current (I_{lim}) as described by (7.52) and (7.53), respectively. An alternative approach to obtain the otpimal I_d and I_q is to switch the optimisation target to the minimisation of the machine's power losses (i.e., copper and iron losses), and set the torque as an additionanl constraint to the optimisation problem. This approach is frequently expressesed as maximum-torque-per-power (MTPP), whereas the former approach is expressed as maximum-torque-per-amp (MTPA) subject to the voltage and current constraints.

$$I = \sqrt{I_d^2 + I_q^2} \leq I_{lim} \tag{7.54}$$

where I is the peak phase current of the machine.

This constraint optimisation problem can be solved by employing an established non-linear optimisation algorithm, such as the Bisection and Newton-Rahson technique (or any of their improved-modified versions). The results obtained from the execution of this optimisation problem for the case of a representative PMA SynRM (characterised with high saliency) are demonstrated in Figure 7.8 and Figure 7.9. Figure 7.8 shows the variation of power loss and voltage with I_d for an operating point located in the low-speed region. The trends obtained from using both the MTPA and MTPP approaches are illustrtated for comparative purposes. It can be seen that for the low-speed operating point, where the voltage did not reach the limit, the optimal current combination is almost identical.
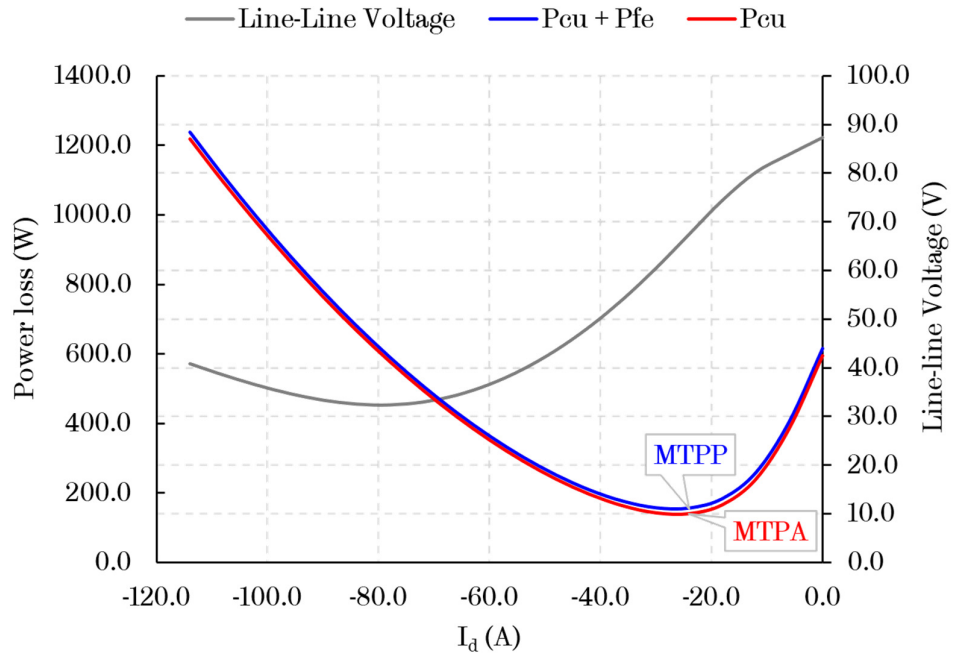
Figure 7.8. *Variation of power loss and voltage with I_d for a given operating point located in the low-speed region – Note: P_{cu} and P_{fe} are the copper and iron loss.*
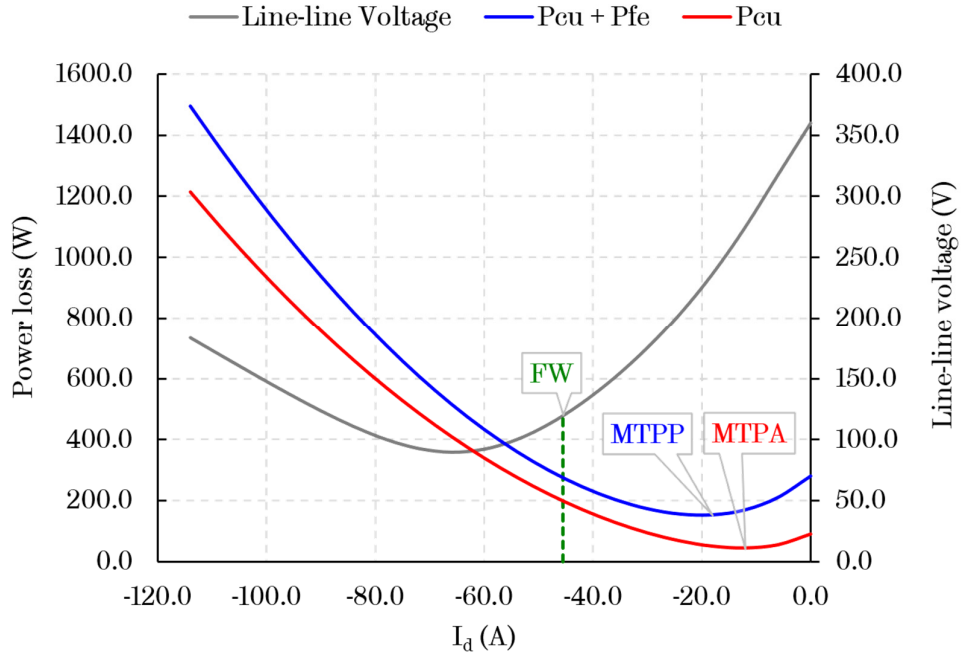
Figure 7.9. *Variation of power loss and voltage with I_d for a given operating point located in the high-speed region – Note: P_{cu} and P_{fe} are the copper and iron loss.*

Figure 7.9 shows the same type of results, but for an operating point located in the high-speed region, thus, representing the field-weakening (FW) operation (where the voltage of the machine exceeds the voltage limit and the field from the magnets must be weakened by advancing the current angle [124]). In this case, it can be observed that the MTPP approach, which also considers the iron loss variation, yields a different optimal current combination to the MTPA approach. This difference indicates that the effect of iron loss is more dominant during high-speed operation where FW is involved. For this reason, the MTTP approach is employed when the voltage limit is reached in FW mode.

Using the described process it is possible to establish the variation of the maximum available torque of the machine, subject to the voltage and current limits, over the entire speed range up to the defined maximum rotating speed. Figure 7.10 illustrates the maximum torque variation up to the maximum speed, along with the peak and continuous torque-speed envelope requirements for the design of the representative PMA SynRM.
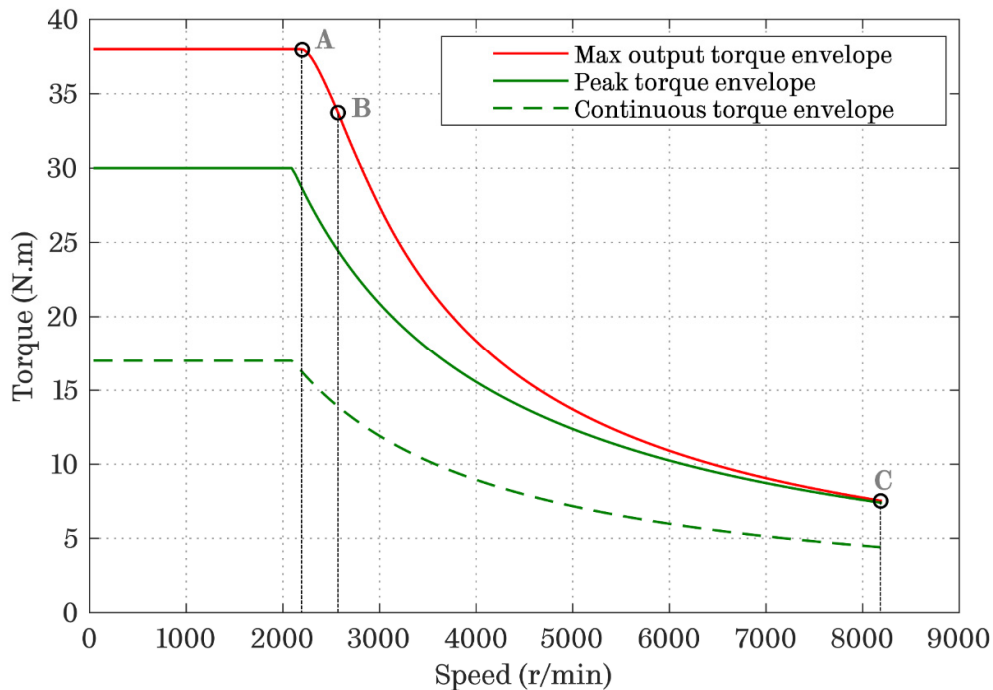
Figure 7.10. Torque-speed characteristics of representative PMA SynRM.

The *d*- and *q*-axis current loci required to produce the torque-speed characteristics illustrated in Figure 7.10 are shown in the plot of Figure 7.11. Note that the colour of the loci in Figure 7.11 corresponds to the colour of the torque-speed envelopes in Figure 7.10. The effect of the imposed current and voltage limits cause three characteristic modes of operation to occur while operating along the maximum torque speed envelope as indicated by points A, B and C in Figure 7.10. The first section (from speed equal to zero until point A) is bound by the maximum current constraint represented by the current circle in magenta colour in Figure 7.11. In this section the *d*- and *q*-axis currents are selected based on the MTPA approach as can be seen from the first part of the current loci (until point A), which corresponds to the variation of torque from zero to maximum.

As the speed increases, the second section (from point A to B) becomes bound from both the maximum current and voltage limits, and is rather short for the investigated PMA SynRM. At this point FW starts, as the field from the magnet needs to be weakened to meet the voltage constraint. Consequently, the torque is reduced. This region is represented as mode I of FW operation. Moving to further higher speed leads to section three (from point B to C), where it becomes impossible to keep using the maximum available current, and the machine essentially operates under maximum-torque-per-volt (MPTV) since now the voltage limit dictates the maximum achievable torque. This region of operation is denoted as FW mode II. The optimal current combinations in the two FW modes are selected based on the MTPP approach due to the reasons described above.

Figure 7.11 also contains iso-torque loci for a number of defining points of the torque-speed envelopes, such as the maximum torque at maximum speed (T_{cms} at ω_{ms}). It can be seen that the optimal current combination to realise this operating point is obtained from the intersection of the ellipse representing the voltage limit at maximum speed and the iso-torque loci representing that particular point. The current loci for the required peak and continuous torque-speed envelopes also stem from the current loci of the maximum operating envelope and follow the same principles, albeit without mode I of FW as the maximum inverter current is never used.
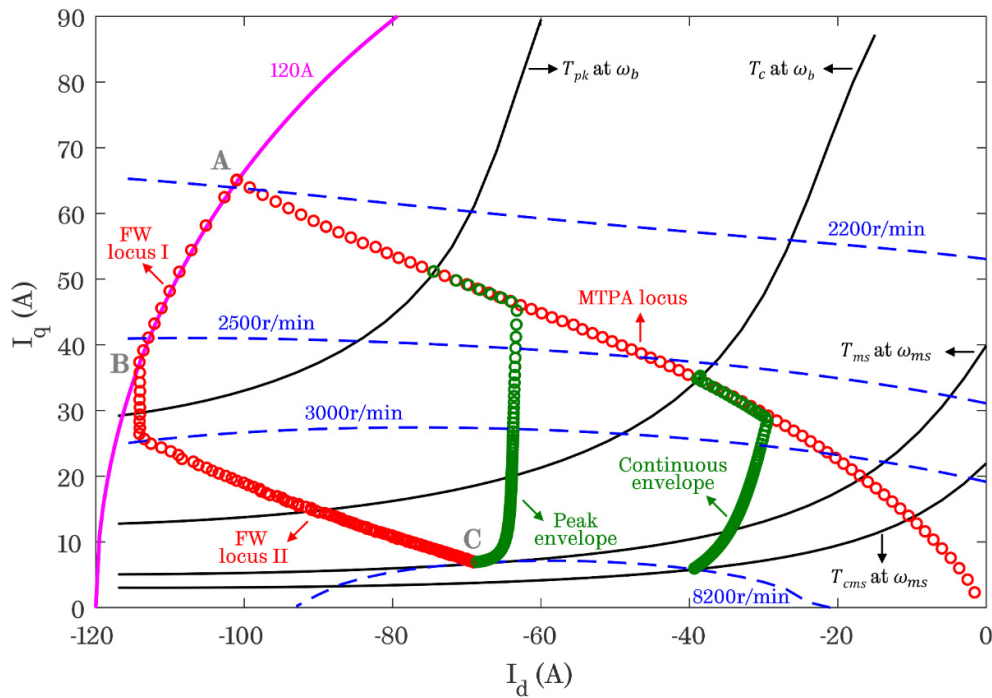
Figure 7.11. I_d and I_q loci representing the operation along the torque-speed envelopes of Figure 7.10.

The next part concerning the computationally efficient modelling of the electromagnetic performance of the machine regards the iron loss prediction, which is required to calculate the efficiency of the machine (given that copper losses can be calculated based on the already established d- and q-axis currents and phase resistance). As commonly known, to predict the iron loss of the machine at a particular working point an FEA evaluation over one electrical cycle is necessary. Performing this FEA evaluation, however, for several operating points would significantly increase the total computation time. To eliminate this problem, a computationally efficient iron loss model [142] capable of accurately predicting the iron loss at a given operating point has been incorporated in the electromagnetic modelling process. The method exhibits a relatively high accuracy in iron loss prediction (compared with FEA) as demonstrated in [142] and [143],[144] for a non-salient and salient PMSM, respectively. The incorporation of the iron loss model further accelerates the optimisation process, especially when combined with the representative operating points derived in Chapter 2 for evaluations over driving cycles. It should be noted, however, that this model is only applicable to PMSMs.

The fact that the predicted iron loss, even if obtained purely from FEA, can significantly deviate from the actual measurements due to impurities in the rolled sheet, internal stresses, cutting/punching process, pressing process, and welding process, constitutes an additional reason favouring the incorporation of this model in the optimisation process. The method for the iron loss calculation in the employed FEA package (FEA) relies on the Bertotti model [145], [145], [146], where for a given frequency, f, the total average iron losses are segregated into three components as shown in (7.55) and (7.56) for sinusoidal excitation.

$$P_{fe}(f) = P_h(f) + P_e(f) + P_{ex}(f) \tag{7.55}$$

$$P_{fe} = \left[\int k_h B_m^2 f + \sigma \frac{\pi^2 d^2}{6} (B_m f)^2 + k_e (B_m f)^{\frac{3}{2}} \right] k_f \tag{7.56}$$

where k_h and k_e are the hysteresis and excess loss coefficients, respectively, B_m is the maximal flux density, σ is the material conductivity, d is the lamination thickness, and k_f is the lamination stacking factor. The iron loss coefficients and material properties are obtained through processing of the manufacturer-provided datasheet.

The employed iron loss model [142], [143] is based on two transient FEA solutions at open-circuit $(I_d = I_q = 0)$ and short-circuit $(I_q = 0, I_d = -I_{sc} \rightarrow I_d$ where $\Psi_d = 0)$ conditions at a reference rotating speed. The open-circuit condition represents the magnetising path, whereas the short-circuit condition represents the demagnetising path of the electromagnetic circuit. The contribution of each of the two components to the total iron loss is represented by the magnetising (V_m) and demagnetising (V_{dem}) voltages as described in (7.57) to (7.60) for each of the iron loss components.

$$P_h = \frac{V_m}{V_{oc}} P_{h_{oc}} + \frac{V_{dem}}{V_{oc}} P_{h_{sc}} \tag{7.57}$$

$$P_e = \left(\frac{V_m}{V_{oc}} \right)^2 P_{e_{oc}} + \left(\frac{V_{dem}}{V_{oc}} \right)^2 P_{e_{sc}} \tag{7.58}$$

$$P_{ex} = \left(\frac{V_m}{V_{oc}}\right)^{\frac{3}{2}} P_{ex_{oc}} + \left(\frac{V_{dem}}{V_{oc}}\right)^{\frac{3}{2}} P_{ex_{sc}} \qquad (7.59)$$

$$V_m = \omega_e \sqrt{\Psi_d\left(I_d, I_q\right)^2 + \Psi_q\left(I_d, I_q\right)^2}$$
$$V_{dem} = -\omega_e\left(\Psi_d(I_d, I_q) - \Psi_m(0, I_q)\right) \qquad (7.60)$$

where V_{oc} is the open-circuit (no-load) back-EMF, and Ψ_m is the flux-linkage contributed by the magnets.

As the machine performance and inverter loss are interrelated, the inverter loss is also included in the performance evaluation by using a loss model reported in [62]. The incorporation of the inverter loss model enables to factor in the influence of inverter loss on the design optimisation trend of the machine. Based on conducted optimisation case studies, it has been identified that a design optimisation, which does not consider inverter losses, will yield a different global optimum compared with an optimisation that does consider the inverter loss. The combination of the above models enables the prediction the machine's electromagnetic performance and the system energy efficiency over driving cycles.

7.2.3.2 Thermal model

The steady-state thermal behaviour of the machine is evaluated using an analytical thermal model developed based on the lumped parameter method. The analytical model, albeit with some simplifications, can provide sufficiently accurate temperature predictions based on validations with Motor-CAD's lumped parameter and FEA modules (viz., dedicated thermal analyses software for electrical machines[92]). The thermal resistances of the analytical model are derived based on the machine's geometrical features and the employed material properties [147], and its heat sources are the copper and iron losses obtained from the electromagnetic parameter models. Since forced air is the cooling means of the machines investigated in this study, resulting from the movement of the vehicle, the cooling frame resistance is obtained from Motor-CAD. The air-velocity at the maximum rotating speed (ω_{ms}) is assumed at 10m/s. This air velocity was selected based on the wheel velocity for the considered EV at 120km/h, which amounts to

33.3 m/s. Since the traction machine is mounted at the bottom of the chassis, only portion of the air velocity will be available to provide effective cooling. Hence, the air velocity in the thermal simulation was assumed at only about one-third of the maximum vehicle velocity at 120 km/h.

To account for the variation of air velocity with rotating speed, the cooling frame resistance is defined as a function of the rotating speed based on data obtained from Motor-CAD. A similar calibration can be performed with respect to the outside diameter and axial stack length of the machine, for the case where either or both are set as variable parameters in the optimisation process. It is important to note that, in general, the analytical thermal model should always be calibrated based on a reference machine design for the topology under investigation. Table 7.4 compares the copper hot-spot, and rotor temperatures predicted by the analytical thermal model and Motor-CAD FEA modules [92] against some operating points located on the machine's continuous torque-speed envelope (indicated in Figure 7.2). As can be observed, sufficient accuracy is achieved over the entire operating range, with the maximum temperature error being ~1°C and ~4°C for the copper and rotor temperatures, respectively.

Table 7.4. Comparison of temperature predictions between the analytical thermal model and Motor-CAD

Torque - Speed operating point	Copper		Rotor	
	Model	Motor-CAD	Model	Motor-CAD
17 N.m - 2100 r/min	101.8 °C	101.7 °C	100.8 °C	100.3 °C
8.9 N.m - 2100 r/min	62.7 °C	62.6 °C	68.2 °C	66.5 °C
6.0 N.m - 2100 r/min	59.0 °C	60.1 °C	68.9 °C	67.5 °C
4.4 N.m - 2100 r/min	59.9 °C	60.9 °C	76.0 °C	71.8 °C

7.2.3.3 Mechanical stress model

Similar to IPM machines, PMA SynRMs use flux barriers to limit the leakage flux originating from the embedded magnets. In turn, this leads to quite narrow rotor bridges, which are conducive to high mechanical stress levels due to the centrifugal force developed at high rotating speeds. The trade-off between mechanical stress level and magnet flux leakage suggests that the bridge thickness

should be optimised to attain the minimum leakage flux, while avoiding failure of the rotor bridges at high rotating speeds. As already explained above, this is of high importance for the design of PMA SynRM due to the multiple embedded magnet layers.

The mechanical stress level at the multiple rotor bridges of the PMA SynRM should normally be a function of the rotor design parameters, as well as the bridge thicknesses (b_1, b_2, b_3) indicated in the rotor schematic of Figure 7.12. This approach, however, would lead to a drastic increase in computational time as repeated calls of FEA would be required to evaluate the maximum mechanical stress level of different design samples from the optimisation's design space. To simplify the mechanical stress model, without compromising accuracy, the maximum mechanical stress $(S_{n\,max})$ exhibited at a rotor bridge can be modelled as a function of the bridge thickness (b_n) and the equivalent rotor core mass density $(m_{n\,eqv})$ – in the form $S_{n\,max} = f(b_n, m_{n\,eqv})$. The subscript n denotes the function's parameters for a particular rotor layer and its corresponding bridge (i.e., $n = 1 \dots 3$, for the PMA SynRM rotor configuration shown in Figure 7.12). The equivalent mass density $m_{n\,eqv}$ is calculated using (7.61):

$$m_{n\,eqv} = \rho_{fe}\,A_{n\,fe} + \rho_m\,A_{n\,mag} \qquad (7.61)$$

where,

- ρ_{fe} and ρ_m are the rotor iron core and employed magnet material mass densities respectively,
- $A_{n\,fe}$ represents the total area of the iron core flux guides located above a particular magnet layer that corresponds to one pair of bridges,
- and $A_{n\,mag}$ represents the area of a particular magnet layer that corresponds to one pair of bridges and the area of the magnet layers located above it (if any), in one rotor pole as shown in Figure 7.12.

For example, for the equivalent mass density, $m_{1\,eqv}$, calculation of the innermost magnet layer in Figure 7.12, $A_{n\,fe}$ would include the areas of all iron flux guides (fg_1 to fg_3), and $A_{n\,mag}$ would include the areas of all three magnet layers

in the rotor. The maximum mechanical stress at each pair of the rotor bridges is modelled by the following quadratic polynomial function (7.62).

$$S_{n\ max} = m_{n\ eqv} \left[C_{n0} + C_{n1} \frac{1}{b_n} + C_{n2} \left(\frac{1}{b_n} \right)^2 \right] \qquad (7.62)$$

where, C_{n0}, C_{n1}, and C_{n2} are the polynomial coefficients for the mechanical stress function of the rotor bridges. The coefficients are obtained from a curve of best fit through data acquired from mechanical stress FEA calculations of a reference design with varying bridge thicknesses. Note that the non-linear contact between the magnets and the rotor iron is taken into account in the FEA model (shown in Figure 7.13).
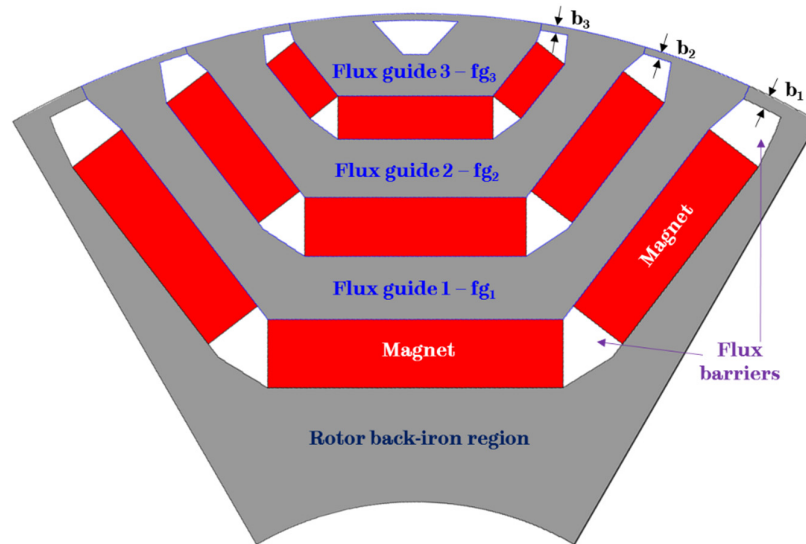
Figure 7.12. Reference rotor pole structure of a PMA SynRM with three embedded magnet layers.

The model is employed to predict the maximum mechanical stress of a PMA SynRM design with different bridge thicknesses and rotor design parameters, which in essence translates to substantially varied equivalent mass densities, compared with the reference design. The results from the analytical mechanical stress model are in reasonable agreement with the data obtained from FEA, despite neglecting the variation of the polynomial coefficients with the remaining rotor design parameters (other than the rotor bridges) [133]. Note that the model needs to be calibrated when applied to machine designs employing different embedded-

magnet rotor configurations, by following the previously described process. As the model facilitates fast estimation of the maximum mechanical stress exhibited at the rotor bridges, with sufficient accuracy, it can, therefore, be incorporated into the machine design optimisation process.
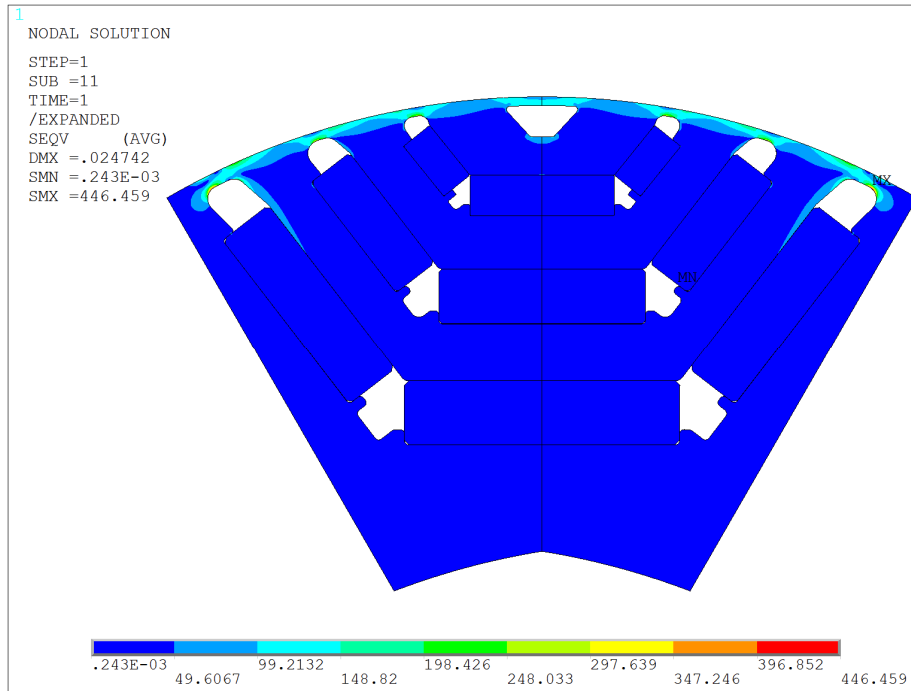
Figure 7.13. Mechanical stress FEA solution of reference design model.

Since the objective is to achieve the minimum bridge thicknesses that satisfy the mechanical stress limit of the employed electrical steel lamination material, the technique is used to automatically determine the optimal rotor bridge thicknesses of each design sample during the optimisation process. It should be noted that the optimal bridge thicknesses are indirectly dependent on the remaining rotor design parameters that in fact determine the iron core flux guide and magnet areas, and hence the equivalent iron core and magnet mass densities (m_{eqv}) used in the model.

Ultimately, the combination of the above multi-physics modelling techniques and optimisation tools has provided a versatile and effective optimisation procedure allowing for the rapid evaluation of the complete design space of EV traction machines that are characterised by many design challenges.

This will, in turn, enable to obtain a holistic perspective on the design and optimisation of PMA SynRMs dedicated for traction applications. Against this background, the design and optimisation of the PMA SynRM topology will be comprehensively investigated in the following sections of this chapter.

7.3 Design optimisation and performance evaluation of PMA SynRMs with different magnet materials employed in the rotor

A great majority of the existing commercial EVs use traction machines that employ high energy density NdFeB permanent magnets (PMs)[38]. However, the ever-growing demand for high energy density PMs has fuelled increasing concerns regarding the price volatility and availability of rare-earth materials. As a result, the industrial EV market is now striving towards rare-earth-less or rare-earth-free solutions with the aim of minimising the reliance on the price-and-abundance-unstable rare earth magnet materials. Maintaining, however, the high efficiency and torque/power density performance that rare earth traction machines typically offer forms a primary challenge. The PMA SynRM is a topology that facilitates substantial rare earth PM reduction, but also enables the use of cheaper bonded NdFeB and ferrite PMs, due to its intrinsic torque production mechanism that fundamentally relies on the reluctance torque component. PMA SynRM has, therefore, the potential to resolve some of the challenges currently characterising the industrial EV market.

Accordingly, this section delves into the design, optimisation and performance evaluation of the PMA SynRM topology against the investigated EV application (via the devised multi-physics optimisation platform), when two characteristically different PM materials are employed in its rotor. A more expensive, high energy-density sintered NdFeB PM material, typically used in conventional PM machines, i.e., N35-EH, and a cheaper, low energy-density ferrite PM material, which is classified as one of the strongest ferrite PM grades, i.e., NMF-12F developed by Hitachi. The key properties of the PM materials employed in this study are listed in Table 7.5.

The conventional distributed winding configuration (with integral slot per pole per phase), which is known to exhibit superior magnetic anisotropy compared with the fractional-slot winding counterparts [80], [81], has been selected for the design optimisation and performance evaluation considering the different magnet materials in the rotor of the PMA SynRM. Based on the findings of this section, the study will investigate the design of a fractional slot PMA SynRM using a novel slot/pole configuration [68], [148], and will compare it against the distributed winding counterpart in the subsequent sections of the chapter.

Table 7.5. Employed magnet material properties

Parameter	NdFeB	Ferrite
Magnet remanence at 100ºC - Br (T)	1.07	0.37
Coercivity at 100ºC - H_c (kA/m)	820.0	285.0
Max. temperature (ºC)	~150.0	~300.0
Knee-point flux density (T) at critical temperature	0.1 at 140ºC	0.1 at -40ºC
Mass density (kg/m³)	7500	5000
Cost per kg ($/kg) [37], [38]	90-130.0	8.0

7.3.1 PMA SynRM design optimisation objective and constraints

Without loss of generality, the optimisation objective is to maximise the energy efficiency (or minimise the energy losses) over the defined driving cycle (i.e., NEDC in this case), while satisfying the required torque-speed operating range and a given set of electrical, thermal, mechanical and other volumetric constraints. The selection of a global optimum design is, ultimately, subjected to the fulfilment of interrelated multi-physical design constraints. The machine should deliver the peak (overload) torque at both ω_b and ω_{ms} within the specified inverter VA rating, i.e., 120 A_{pk} and 120 V dc-link, whilst not exceeding the maximum line-line back-EMF limit of 250 V_{pk} at maximum speed in order to ensure safety in the case of an intermittent inverter fault. The machine should deliver constant power over a wide speed range, i.e., ~4 times the base speed.

The rotor magnets should endure irreversible demagnetisation against the worst-case overload condition of the defined operating range (i.e.,T_{pk}, ω_b orT_{ms}, ω_{ms}), while operating under their corresponding critical temperature

condition where the demagnetisation knee-point is more evident (viz., high temperature for sintered NdFeB, whereas sub-zero temperature for ferrites). The mechanical stress exhibited at the rotor bridges, when the rotor is rotated at 1.5 times the maximum speed (ω_{ms}), should not exceed the yield strength limit (450 Mpa) of the employed lamination electrical steel grade, namely M270-35A, to avoid the rotor deformation which would compromise the airgap. The thickness of the multiple rotor bridges, which are responsible to retain the embedded magnets within the rotor, is automatically adjusted during the design optimisation process, through the technique described in §7.2.3.3, in order to satisfy the specified yield strength limit. Note that the minimum bridge thickness is limited to 0.3 mm to ensure a robust manufacturability of the rotor, since the employed lamination material has a thickness of 0.35 mm.

The traction machine of the investigated EV application is air-cooled, enclosed by a radial-finned aluminium jacket with an ambient temperature of 40°C. The copper winding and magnet temperatures should be limited below 120°C (in alignment with the selected insulation class) when operating over the entire continuous torque-speed envelope, where the worst-case operating conditions typically reside at the extremities of the envelope, i.e., T_{pk}, ω_b or T_{ms}, ω_{ms}. The machine temperatures are systematically evaluated via the analytical thermal model, described in §7.2.3.2, during the global design optimisation process.

The torque ripple exhibited by the machine should be sufficiently low to ensure passenger comfort. The percentage of peak-peak torque ripple over the peak torque at the worst operating condition should be limited below 5%, according to the specification released for a next generation EV (Freedom car 2020) [78]. Intrinsically high torque ripple is one of the demerits of the PMA SynRM topology due to its highly salient nature that underlies its operating principle. However, numerous techniques are now available that can rectify the high torque ripple by means of skewing, flux barrier pairing and shaping [36],[37], [87]–[89], as well as the introduction of features into the rotor [90], whilst leaving the remaining performance virtually unaffected (since torque ripple is more sensitive to minor geometrical modifications, such as the flux barrier opening angles). The aforementioned techniques can also be combined for more effective torque ripple

reduction. Therefore, the torque ripple minimisation is considered as a post-process, applied once the design sample that exhibits optimal performance with respect to the defined design objectives and constraints has been identified. Based on the above assertions, the torque ripple minimisation is beyond the scope of investigation of this chapter.

7.3.2 Leading design parameters of PMA SynRM

A three-phase transversally laminated PMA SynRM with 6-pole, and 36-slot configuration was selected for the design investigation of the distributed winding topology employing different magnet materials in the rotor. This slot/pole configuration was chosen considering the trade-off between high torque production capability at low speed and low iron loss generation at high speed [79]. The lack of low order space harmonics, combined with the multilayer rotor, lead to low iron loss production under high-speed operation. The selection of three embedded layers and a cutout in the rotor leads to enhanced magnetic anisotropy [84], and hence reluctance torque capability while ensuring good structural integrity and manufacturability of the rotor based on the given machine space envelope. Further, the selection of three layers allows for thick enough magnets capable of withstanding irreversible demagnetisation during overload. A schematic of on of the investigated PMA SynRM topologies is illustrated in Figure 7.14.

As already explained, owing to the complex rotor structure of the PMA SynRM, a large number of leading design parameters need to be incorporated to the optimisation process to enhance its performance and ensure an optimal design that delivers the maximum driving cycle energy efficiency, while satisfying the defined multi-physical design constraints. The schematic of Figure 7.14 illustrates the leading design parameters selected for the design optimisation process. The motors were optimised with respect to 11 design parameters, as listed below,

- the tooth width, T_w,
- the back iron width, H_y,
- the ratio of rotor radius to stator outer radius abbreviated as split ratio, $\frac{R_i}{R_o}$,

- the coil turn number, TN,

- the magnet pole angle, β_m,

- the side magnets width w_{m_i},

- the magnet depth, d_m,

- the span of the middle barrier section, α_m,

- and the insulation ratios (i.e., the ratio of air/PM to iron) for the middle, k_{ins_mid}, and side, k_{ins_side}, flux barrier sections which are described by the following two equations:

$$k_{ins\_mid} = \frac{\sum_i h_{b_i}}{d_m} \qquad\qquad (7.63)$$

$$k_{ins\_side} = \frac{\sum_i h_{m_i}}{d_m} \qquad\qquad (7.64)$$

where the subscript i denotes the rotor layer number. The insulation ratio is a critical parameter to the design of the PMA SynRM as it regulates the saturation level in the rotor and it is responsible for the enhancement of magnetic anisotropy (i.e., d- and q-axis inductance difference), and hence the reluctance torque capability of the machine. The insulation ratio should be optimised in alignment with the back iron and tooth thickness, which define the flux density levels in the stator lamination, to fine-tune the flux circulation between the rotor and stator iron cores for optimal electromagnetic performance [69].

Unlike the conventional SynRM, parts of the flux barriers of the PMA SynRM are occupied by magnets, which assist in the torque production and alleviate the poorer efficiency and power factor characterising the SynRM. In this case, since both magnet and air occupy the same space in the flux barrier, the insulation ratio defines the ratio of air and magnet to iron (instead of only air to iron in the case of SynRM). Its optimal value will be dependent on the energy density of the employed magnet material and its arrangement in the rotor. It is therefore important to introduce a high degree of freedom in the design optimisation process of the PMA SynRM. Doing so will avoid any conflict between the optimal sizing of the flux barrier shape and that of the magnet, as the two may not coincide with the case where only one insulation ratio that dictates the shape

of the whole flux barrier is selected. This, in turn, justifies the definition of two rotor insulation ratio parameters for the middle and side sections of the flux barrier, respectively.
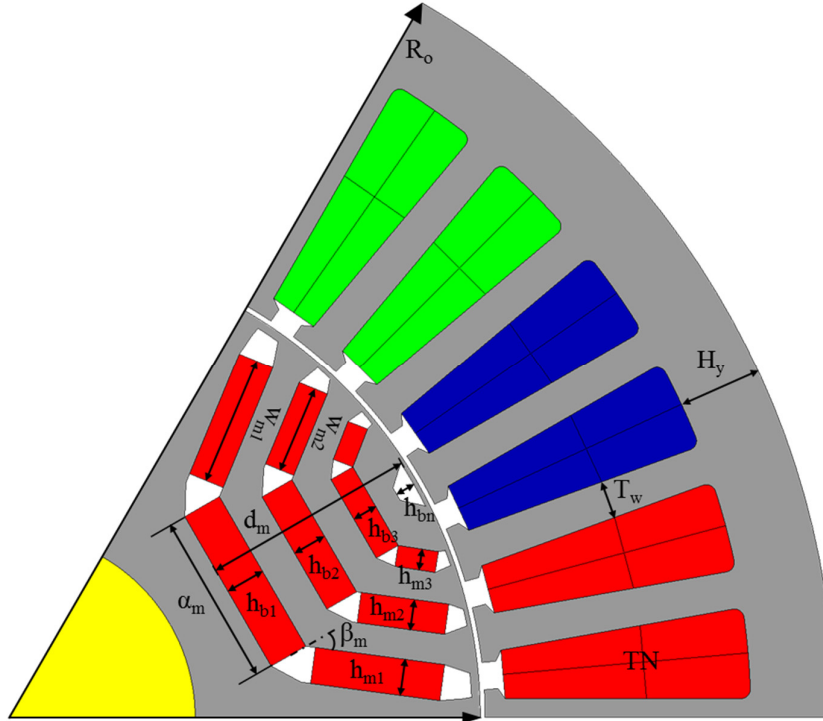
Figure 7.14. Leading design optimisation parameters of a typical PMA SynRM schematic with rectangular magnets embedded in the rotor.

These ratios in combination with the magnet width parameters will allow for the optimal fine-tuning of rotor lamination geometry and magnet volume, regardless of the energy density of the employed magnet material and its arrangement in the rotor, as will be shown in the following sections of the chapter. Against this background, a parametric and topologic design optimisation of the PMA SynRM is conducted via the developed computationally efficient optimisation platform, enabling to obtain a holistic view of the performance of PMA SynRMs employing the two characteristically different magnet materials in EV traction applications. The optimal machine designs acquired from the global optimisation process will be evaluated and compared against a number of indicative performance markers. These include the system (machine plus inverter) energy efficiency over the two defined driving cycles, the mass and cost of active materials,

the VA rating, torque/power density, reluctance torque capability and thermal behaviour.

7.3.3 PMA SynRM structures employing sintered NdFeB magnets

This section deals with the design of PMA SynRMs with sintered NdFeB magnets embedded in the rotor. Owing to the high energy density characterising sintered NdFeB magnets, only a small amount of PMs need be inserted in the rotor flux barriers to assist in the torque production, to avoid the magnetic saturation of the rotor and stator iron cores. The fact that only a small amount of NdFeB magnets is required to fill parts of the flux barriers implies increased flexibility regarding their arrangement inside the rotor, which will in turn influence the magnetic flux distribution in the iron core of the machine and hence, the flux linked by the stator coils. This section aims to identify such rotor structure that enables the most efficient utilisation of the employed magnet material, which translates to the minimisation of PM volume, and hence cost of the expensive rare-earth material while maintaining optimal output performance with respect to the defined objectives and constraints.

For manufacturability purposes, rectangular magnet blocks are considered, which in turn determine the flux barrier shape that incorporates them. The machine aspect ratio is fixed according to Table 7.2. Figure 7.15 shows three PMA SynRM cross sections each employing different arrangements of the sintered NdFeB magnets in the rotor flux barriers. The three models share the same stator and rotor lamination geometries as well as coil turn number. The reference design, denoted as "NdFeB-1", employs a single magnet block in the middle section of each rotor flux barrier. The remaining two designs, denoted as "NdFeB-2" and "NdFeB-3", employ the same magnet volume as the NdFeB-1 design, but re-arranged in more magnet blocks at different locations inside the flux barriers. Table 7.6 lists the obtained no-load back-EMF of the three models and compares them to the reference, NdFeB-1, design. Note that in all three designs the flux density working point is located on the linear section of the lamination's B-H curve, indicating that no saturation occurs under no-load operating conditions (apart from the rotor bridges).
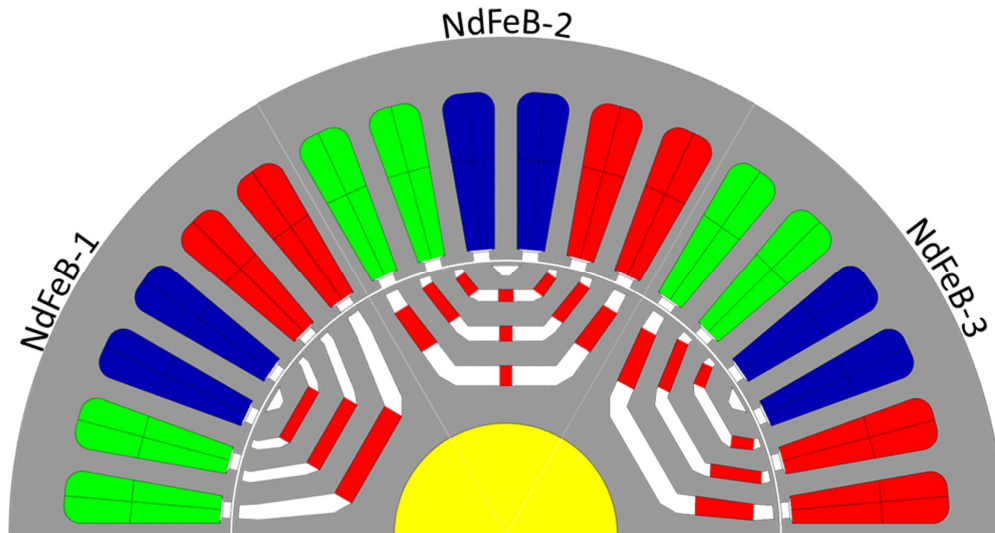
Figure 7.15. PMA SynRM structures with sintered NdFeB magnets.

Table 7.6. Comparison of back-EMF between the PMA SynRM topologies employing identical sintered NdFeB amount

Parameter	NdFeB-1	NdFeB-2	NdFeB-3
PM-mass (kg)		0.27	
Line-Line back-EMF fundamental component at ω_{ms} (V,pk)	182.5	213.0	221.5
Back-EMF ratio normalised to NdFeB-1	1.0	1.17	1.22

As can be observed from Table 7.6, the rearrangement of the same magnet volume with two magnet blocks at the side-sections of each flux barrier (i.e., NdFeB-3 design) brings about 22% more back-EMF compared with the reference design (i.e., NdFeB-1), which employs only a single magnet block inserted to the middle section of each flux barrier. Based on the fact that no saturation occurs under no-load operation, this translates to a proportional percentage reduction (i.e., ~22%) in magnet material usage for design NdFeB-3. The substantial magnet reduction of NdFeB-3 can be attributed to the fact that this magnet configuration makes use of the flux-focusing effect, which concentrates the flux in the airgap and also arranges all the magnets to be closer to the airgap leading to less flux loss due to leakage flux (viz., the rotor bridges are saturated more effectively).

NdFeB-2 design, which combines the magnet configurations of NdFeB-1 and NdFeB-3 topologies, uses magnet blocks in all sections of each flux barrier. Being the in-between configuration, NdFeB-2 yields a certain amount of magnet saving. However, it is not as substantial when compared with the magnet saving attained by NdFeb-3. Further, the fact that design NdFeB-2 uses three magnet blocks per rotor layer, and thus requires six different magnet shapes to be machined per pole, would result in additional complexity of the manufacturing process (in contrast to the more straightforward NdFeB-1 topology). Based on the above factors, design NdFeB-2 is disregarded from the design optimisation process of the NdFeB PMA SynRM.

Designs NdFeB-1 and NdFeB-3 have been optimised via the developed multi-physics global optimisation process, with respect to the leading design parameters defined in §7.3.2, against the design objectives and constraints described in §7.3.1. Once the optimal design, which delivers the maximum driving cycle efficiency while satisfying the multi-physics design constraints is attained, a secondary (refining) optimisation process is executed with the aim of minimising the magnet material usage of the optimal design which, in the case of NdFeB, largely influences the cost of the machine. The acquired energy efficiency of the optimal design is now set as an additional design constraint, and the magnet volume is set as the optimisation objective. The stator design parameters and split ratio of the optimal design obtained from the primary optimisation round are now fixed, and only the rotor internal design parameters are varied.

An additional design parameter, defined as the magnet distribution ratio (k_{mag_distr}), is introduced in the secondary optimisation process, which essentially redistributes the magnet thickness in the rotor flux barriers. By way of example, if $k_{mag\_distr} = 1$, all magnet layers have the same thickness, if $k_{mag\_distr} > 1$ the magnet thickness becomes progressively larger from the inner-most towards the outer-most layer, and vice versa for the case where $k_{mag\_distr} < 1$. The additional design parameter in combination with the remaining internal rotor design parameters, provide increased flexibility in tuning the PM surface area, enabling to minimise the PM usage while maintaining the optimal energy efficiency acquired from the primary optimisation process.

The flux emanating from the magnets contributes to the saturation of the rotor bridges, leading to the reduction of the input current (for a given torque) and the enhancement of power factor. The remaining magnet flux crosses the airgap and becomes linked by the stator coils (i.e., PM flux linkage - ψ_m), influencing the torque production (hence efficiency) and the field-weakening (FW) capability. The effectiveness of the magnets in producing flux depends on the magnet grade remanence (B_r) and the PM surface orthogonal to the magnetisation direction [75]. The distribution of the magnets thickness with respect to their position in the rotor also contributes to more effective magnet material utilisation.

Ultimately, the design parameters involved in the secondary optimisation round enable to minimise the surface of the PMs by optimising their shape (i.e., width and thickness) and position in the rotor (i.e., distance from the airgap) while satisfying all multi-physical design constraints and leaving the optimal cycle energy efficiency virtually unaffected. It has been found that for the same PM surface area, a PM with larger span and smaller thickness produces significantly higher flux compared with a thicker but narrower PM. Hence, a substantial PM usage reduction was achieved via the secondary optimisation process, where the thickness of the magnet was reduced, and their span was slightly increased to reach the desired PM flux linkage level. Further, for the case of the NdFeB designs, k_{mag_distr} is > 1, which indicates that larger thickness is attributed to the outer magnet layers that are positioned closer to the airgap. This allows for more effective utilisation of the magnet material as less flux is lost due to leakage (viz., the outer magnets have less reluctance in the path towards the stator).

It should be noted, however, that the PM-minimisation process forms a trade-off with the robustness towards demagnetisation under overload operation, which has been monitored during the process. As a result, the design with the minimum magnets may not always be feasible, since the magnet layers should all have sufficient thickness to endure irreversible demagnetisation under overload conditions. This trend is in alignment with the findings reported in [125]. Despite this trade-off, a significant magnet usage reduction can still be achieved. The cross-sections of the two NdFeB designs optimised through the described optimisation process, i.e., NdFeB-1 and NdFeB-3, are illustrated side-by-side in Figure 7.16. The

key performance metrics of the optimal designs are listed in Table 7.7, including their energy efficiency over the NEDC and AUDC. The energy loss components over the two characteristically different driving cycles are also compared between the two designs in Figure 7.17.
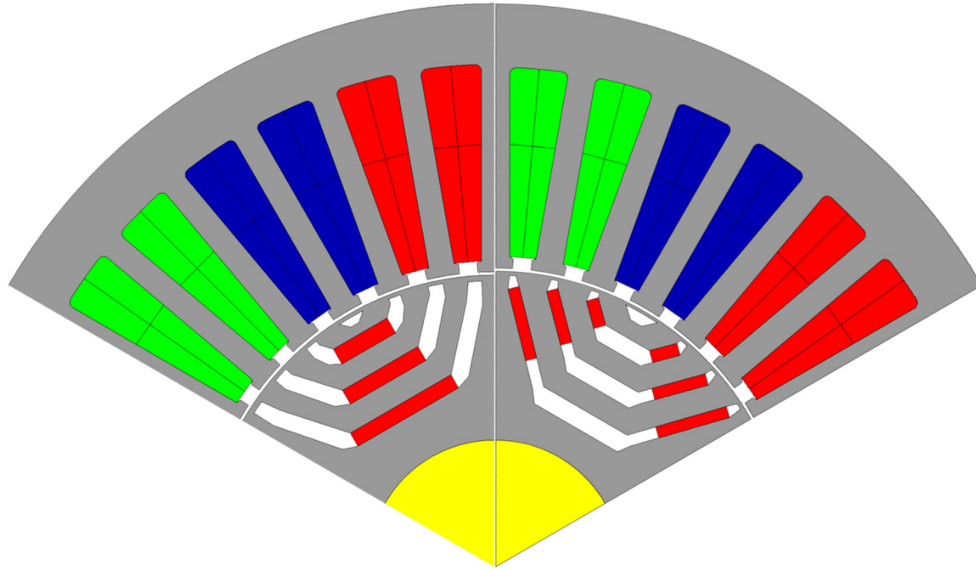
Figure 7.16. PMA SynRM structures with sintered NdFeB magnets optimised against the NEDC.

Table 7.7. Key performance metrics of optimal designs with straight- and side-PM arrangements in the rotor

Parameter	NdFeB-1	NdFeB-3
PM mass (kg)	**0.22**	**0.185**
Inductance difference at rated point (mH)	1.59	1.72
Saliency ratio at rated point	3.54	3.41
Peak current at T_{pk} , ω_b (A$_{pk}$)	94.41	90.21
Rated current at T_c , ω_b (A$_{pk}$)	54.65	52.05
Line-Line back-EMF at ω_{ms} (V)	186.0	207.5
Characteristic current (A$_{pk}$)	58.7	56.5
I_{ch}/I_{rated} ratio	1.07	1.08
Copper/rotor temperature at T_c , ω_b (ºC)	96.6 / 96.3	93.3 / 92.8
System energy efficiency over NEDC	**90.42%**	**90.54%**
System energy efficiency over AUDC	**87.53%**	**88.0%**
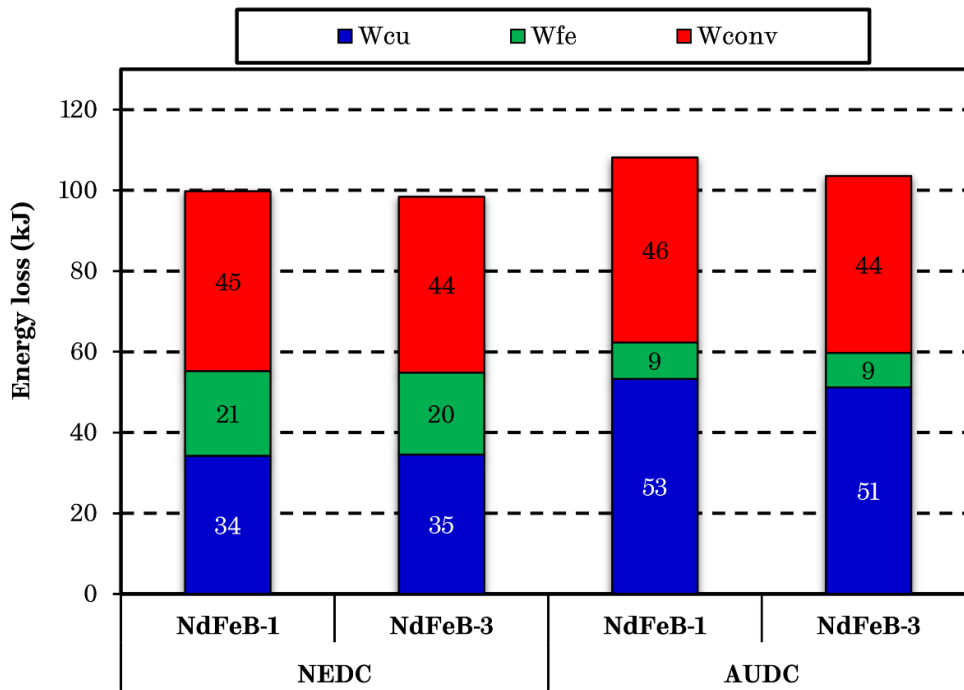
Figure 7.17. Comparison of driving cycle energy loss components between optimal designs employing sintered NdFeB magnets.

As can be observed from Figure 7.16, apart from the inner rotor geometry configuration (i.e., unique magnet arrangement and flux barrier shape), the two optimal designs have similar geometries. The distinct flux barrier shapes of the two configurations justify the selection of two insulation ratios (i.e., k_{ins_mid} and k_{ins_side}) for the optimisation process, which allow to regulate the PM-flux and volume, as well as enhance the magnetic anisotropy. It can be seen that design NdFeB-3 has thinner flux barrier sides, where the magnets are located, so as to avoid saturating the *q*-axis (high permeance) flux guides, but has thicker middle sections of the barriers in order to provide more insulation in the *d*-axis (low permeance) and enhance the magnetic anisotropy.

Design NdFeB-1, on the other hand, has relatively thick middle sections of the flux barriers to regulate the PM-flux and also insulate the *d*-axis, but also has thicker side flux barrier sections in order to limit the leakage flux from the magnets. This however, forms a trade-off since the thickness of the flux barrier sides cannot be made very thick as this will lead to saturation of the *q*-axis flux

guides, and thus a reduction in L_q. It is evident from Table 7.7 that design NdFeB-1 uses ~19% more magnet material while producing ~11% lower no-load back-EMF for the same coil turn number (i.e., *TN*=7). The effectiveness of the NdFeB-3 magnet arrangement is clearly manifested when compared with design NdFeB-1.

The rated and peak phase current of NdFeB-3 design are slightly lower than those of NdFeB-1 design, leading to lower copper loss and hence slightly lower temperatures under continuous operation (viz., this is the worst operating condition for the thermal evaluation of PMA SynRM). Further, the two optimal designs exhibit comparable FW capability as can be seen from their characteristic current (I_d at which $\psi_d = 0$) normalised to their rated current (I_{ch}/I_{rated}). Notice that the I_{ch} of NdFeB-3 design is slightly lower compared to that of design NdFeB-1, despite the considerably higher back-EMF. This implies that the L_d of design NdFeB-3 is higher than that of NdFeB-1 to compensate for the higher PM-flux. Meanwhile, design NdFeB-3 maintains a comparable, or even slightly higher inductance difference (viz., indicative of the reluctance torque production capability), which indicates that its L_q is also higher than that of design NdFeB-1.

Both designs exhibit comparable energy efficiency against the NEDC (i.e., the optimisation objective), where high energy consumption predominantly occurs during the low-torque, middle-to-high speed operation. This can be confirmed by comparing the energy loss components generated by the two designs over the NEDC (Figure 7.17), where design NdFeB-3 produces marginally lower energy loss. However, when evaluated over the AUDC, where high energy consumption occurs in the middle-to-high torque and low-speed region, design NdFeB-3 exhibits ~0.5% higher system energy efficiency primarily owing to its stronger PM-flux emanating from its magnet arrangement. The higher PM-flux leads to lower current per given torque, and hence the current-induced losses, i.e., the copper and inverter losses are lower for design NdFeB-3 as can be seen from   Figure 7.17.

Based on the comparisons between the two configurations, which have both been optimised via the same process, it can be concluded that design NdFeB-3 is superior to NdFeB-1 as it delivers the same, or even higher performance, with a substantially reduced PM-amount, while satisfying all multi-physical design

constraints. This is a highly desirable attribute in applications, such as EV traction. While the magnet reduction resulting from NdFeB-3 topology indeed translates to a substantial reduction of the machine's active materials cost (primarily dominated by the NdFeB cost), it arguably slightly increases the manufacturing complexity, and indirectly the production costs, since two magnet blocks need to be inserted into each of the flux barriers in the rotor, compared to only one in the case of NdFeB-1. Note, however, that the number of different magnet blocks that need to be machined is identical for the two configurations due to the rotor symmetry. Nevertheless, this trade-off remains to be resolved by mass production industrial manufacturers.

For this study, NdFeB-3 topology configuration is considered as the most suitable candidate for the use of sintered NdFeB in PMA SynRM, based on the previous findings, which demonstrated that design NdFeB-3 enables better exploitation of the NdFeB magnet material in contrast to the other arrangements. The machine and system efficiency maps of the optimal NdFeB-3 design, overlaid by the driving cycles operating points are provided for reference in Figure 7.18. Where it can be seen that high efficiency is distributed over a high and wide torque speed region covering the majority of NEDC (target cycle) representative points, as well as a large amount of operating points from the more aggressive AUDC.
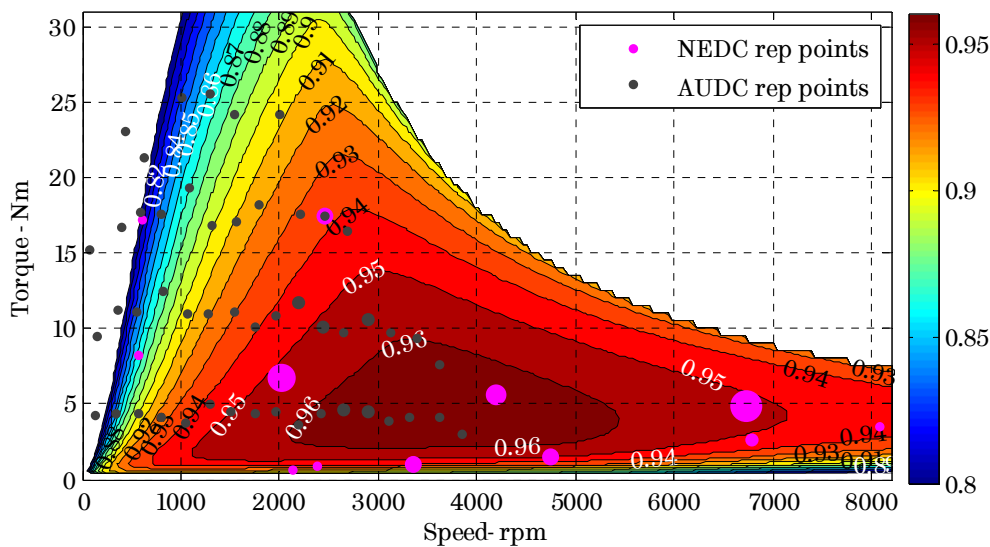

(a) Machine efficiency map
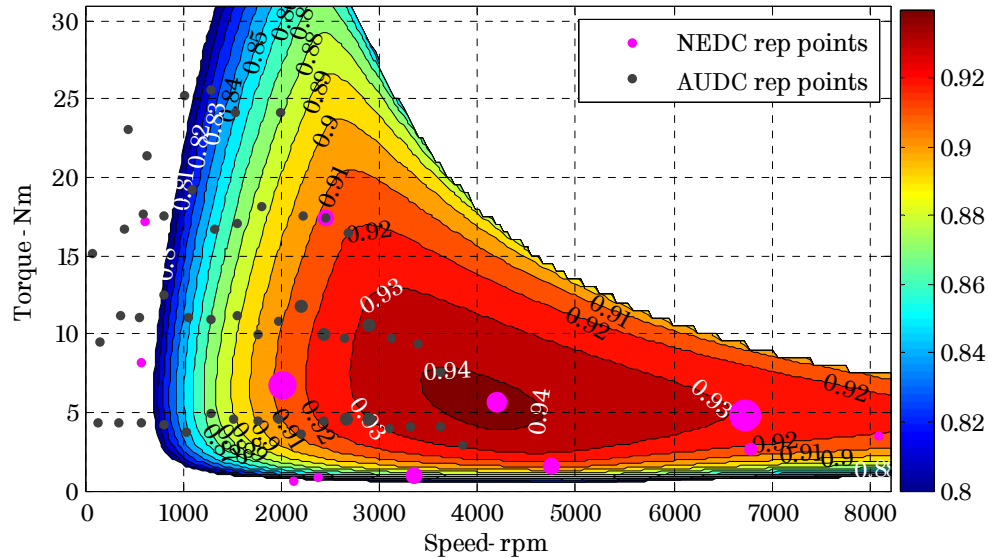
(b) System (machine + inverter) efficiency map

Figure 7.18. Efficiency maps of optimal sintered NdFeB-3 PMA SynRM design, overlaid by the driving cycle's representative operating points.

7.3.4 PMA SynRM structures employing ferrite magnets

Against the same background described in §7.3.3, which deals with the design of PMA SynRM with sintered NdFeB, this section investigates the design of PMA SynRMs employing ferrite magnets (viz., magnet properties are given in Table 7.5 – NMF-12F). Owing to the low energy density characterising ferrite magnets, it becomes necessary to fill most of the flux barrier area with PMs to enhance the performance and achieve a competitive efficiency against that of the PMA SynRM employing sintered NdFeB. In the case of ferrite PMA SynRM, the conflict between the magnet and iron areas in the rotor is more evident. The two form a trade-off, which needs to be balanced during the optimisation process to maximise the machine's electromagnetic performance (i.e., magnetic anisotropy and PM-flux contribution).

Two rotor configurations are investigated for the case of PMA SynRM employing ferrite magnets – one with circular flux barrier layout [36], [130] (reminiscent of the conventional transversally laminated SynRM rotor) denoted as "Ferrite-Circ.", and one with rectangular flux barrier layout denoted as "Ferrite-

Rect.". The two designs were optimised following the same process described in the previous section, i.e., the system energy efficiency over NEDC is maximised and then set as a constraint for the secondary optimisation process, which minimises the PM volume while maintaining the optimal energy efficiency and satisfying the multi-physical design constraints. The cross-sections of the optimal ferrite designs with circular and rectangular flux barrier shapes are illustrated side-by-side in Figure 7.19 for comparison. The key performance metrics of the two designs are listed in Table 7.8. Their system energy efficiencies over the NEDC and AUDC are also provided in Table 7.8, and their major energy loss components are compared in Figure 7.20.
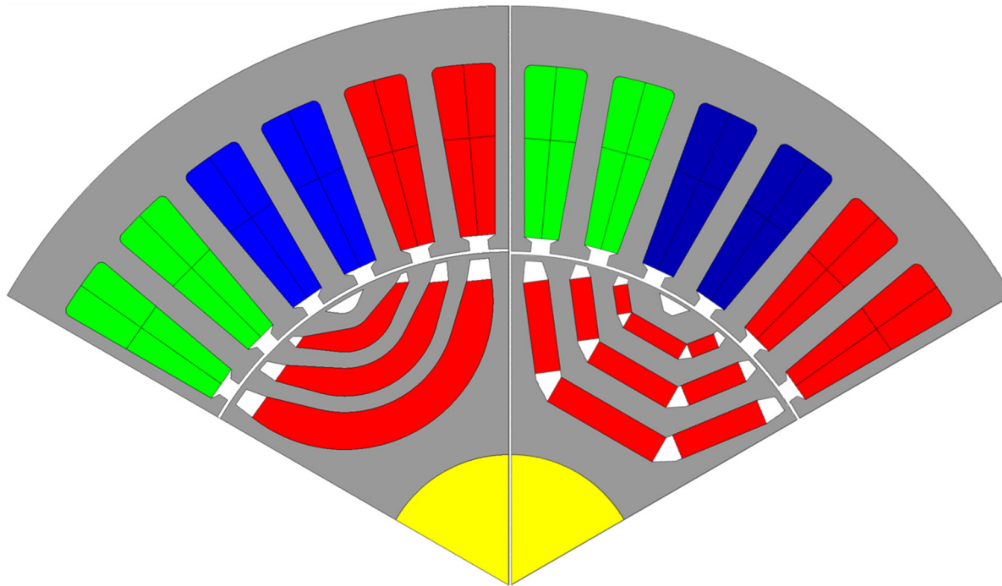
Figure 7.19. PMA SynRM rotor structures with ferrite magnets optimised against the NEDC.

Similar to the case of the optimal PMA SynRMs with sintered NdFeB, the two optimal ferrite designs share comparable stator geometries and split ratio, with differences mainly appearing in the inner rotor geometry. It is evident from Table 7.8 that Ferrite-Circ. design uses ~30% more magnet material and produces ~18% lower back-EMF compared with the Ferrite-Rect. design, for the same coil turn number (i.e., TN=7). This can be attributed to two reasons – first, the PM surface area perpendicular to the magnetisation direction is inherently lower for the Ferrite-Circ. design due to its circular shape. Both designs employ parallel

magnetisation for simplicity, as other magnetisation patterns would complicate manufacturing. Second, the Ferrite-Rect. design makes use of the flux focusing effect, which concentrates the flux in the airgap leading to more efficient utilisation of the magnet material. The rectangular flux barrier design leads to relatively thinner flux barriers and allows relatively more space for the iron flux guides as can be observed from Figure 7.19.

Table 7.8. Key performance metrics of optimal ferrite designs with circular and rectangular flux barrier shapes in the rotor

Parameter	Ferrite-Circ.	Ferrite-Rect.
PM mass (kg)	**0.65**	**0.50**
Inductance difference at T_c , ω_b (mH)	1.85	1.78
Saliency ratio at T_c , ω_b	4.44	4.01
Peak current at T_{pk} , ω_b (A,pk)	99.0	96.8
Rated current at T_c , ω_b (A,pk)	57.0	55.7
Line-Line back-EMF at ω_{ms} (V,pk)	**129.5**	**157.2**
Characteristic current I_{ch} (A,pk)	49.7	53.8
I_{ch}/I_{rated} ratio	0.87	0.97
Copper/rotor temperature at T_c , ω_b (ºC)	104.7 / 103.0	101.8 / 100.8
System energy efficiency over NEDC	**90.4%**	**90.5%**
System energy efficiency over AUDC	**86.5%**	**86.9%**

During the magnet minimisation process (i.e., secondary optimisation) of the ferrite designs it has been observed that $k_{mag\_distr} < 1$, which indicates that more thickness is attributed to the magnets of the inner rotor layers, in contrast to the trend observed with the sintered NdFeB designs (i.e., $k_{mag\_distr} > 1$). This can be explained by the fact that the product of PM remanence and the PM surface area perpendicular to the magnetisation direction of the innermost magnets, is higher for the case of the ferrite magnet designs compared with those employing sintered NdFeB. This is due to the significantly lower energy density of the ferrite magnets. The span of the inner magnets is inherently much larger compared with the outer layers in the ferrite designs, since almost all the flux barrier is filled by magnets, and their surface area is inherently larger. Hence more weight/thickness is attributed to the inner magnets during the optimisation, which appear as more

effective in maximising the PM-flux of the machine. Naturally, there is a trade-off with the demagnetisation withstanding, which has also been monitored during the process. The magnet layers must be sufficiently thick to avoid irreversible demagnetisation, which for the case of ferrites occurs at sub-zero temperatures in contrast to the NdFeB magnets [93].

The stronger PM-flux characterising the Ferrite-Rect. design leads to slightly lower rated and peak phase current, and hence lower copper loss. The copper and rotor temperatures during continuous operation at base speed are, therefore, a few degrees lower compared with design Ferrite-Circ. (i.e., ~3°C). The FW capability is comparable between the two designs, as can be seen from the ratio I_{ch}/I_{rated}. The L_d of the Ferrite-Rect. design is slightly higher, though, in order to compensate for its higher PM-flux. This is reflected by its thinner middle-section magnets, which in turn reduce the insulation in the d-axis. This results in a marginally lower inductance difference and saliency ratio for the Ferrite-Rect. design, as L_q is nearly identical between the two designs.
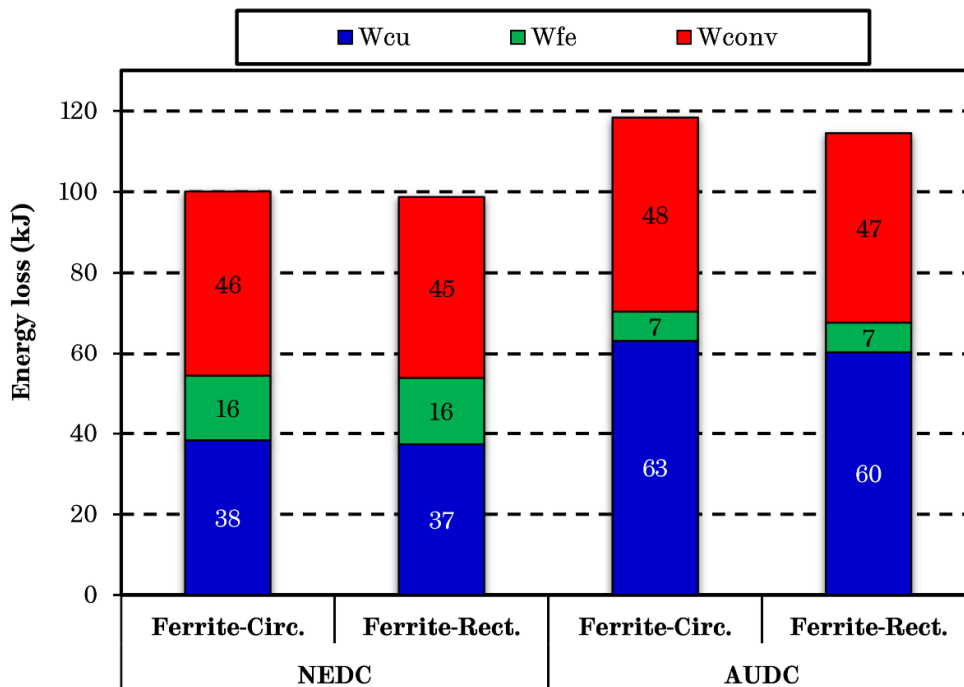
Figure 7.20. Comparison of driving cycle energy loss components between optimal designs employing ferrite magnets.

Overall, the system energy efficiency of the optimal ferrite designs is comparable, as can be verified by the comparison of the energy loss components in Figure 7.20. The marginal efficiency improvement (i.e., ~0.1%) of Ferrite-Rect. design is attributed to its lower current-related losses (i.e., copper and inverter losses), due to its higher PM-flux. For the same reason, the Ferrite-Rect. design achieves a higher efficiency (by ~0.4%) over the AUDC, where the current-related losses are more dominant in contrast to the NEDC. The iron loss trend remains very similar between the two designs over both driving cycles.

Based on the previous investigation, design Ferrite-Rect. achieves marginally improved electromagnetic performance compared with the Ferrite-Circ. design, but most importantly, it substantially reduces the PM-amount of the machine. Whereas this may not be as significant regarding cost reduction, as was the case of the NdFeB PMA SynRM (due to the order-of-magnitude lower price of ferrite), a decrease in PM amount is still desirable. Further, the circular flux barrier design imposes complications in manufacturing, as ferrite magnets are difficult to machine with proper tolerances in circular shape [129]. On the other hand, while the rectangular shaped magnets of design Ferrite-Rect. are easier to machine, it still requires six different magnet shapes to be machined, and three times the number of magnet blocks that need to be magnetised and inserted into the rotor during the assembly process. Again, this is a trade-off that remains to be resolved by industrial manufacturers.

It is considered that the Ferrite-Circ. rotor configuration could be particularly attractive for cases where injection molded bonded NdFeB magnets (which can be produced in any shape with ease) are used in the rotor, due to its relatively simpler manufacturing and the fact that still retains the typical configuration of the conventional transversally laminated SynRM. Such topology has been investigated in Chapter 3 and [65]. For the purposes of this study, the Ferrite-Rect. design is considered the most suitable topology to accommodate ferrite magnets in PMA SynRM, based on the preceding findings. Hence, this configuration will be used for the performance comparisons in later sections of this chapter. The machine and system efficiency maps of the optimal Ferrite-Rect. design (overlaid by the representative operating points of both driving cycles) are

provided in Figure 7.21, where it can be seen that high-efficiency regions extend over a high-speed range, and particularly in the low torque operating region due to the inherently low iron losses of the ferrite design.
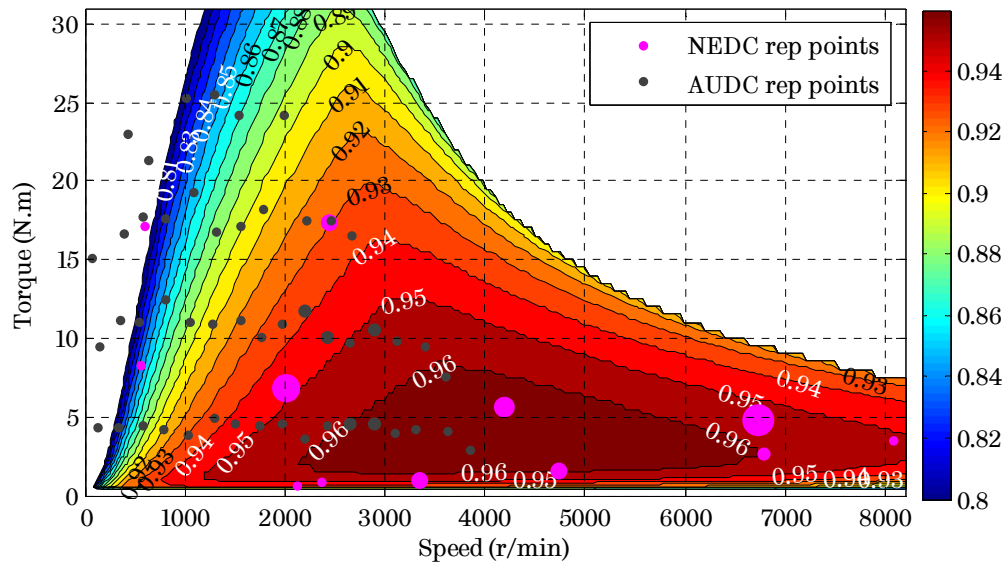
(a) Machine efficiency map
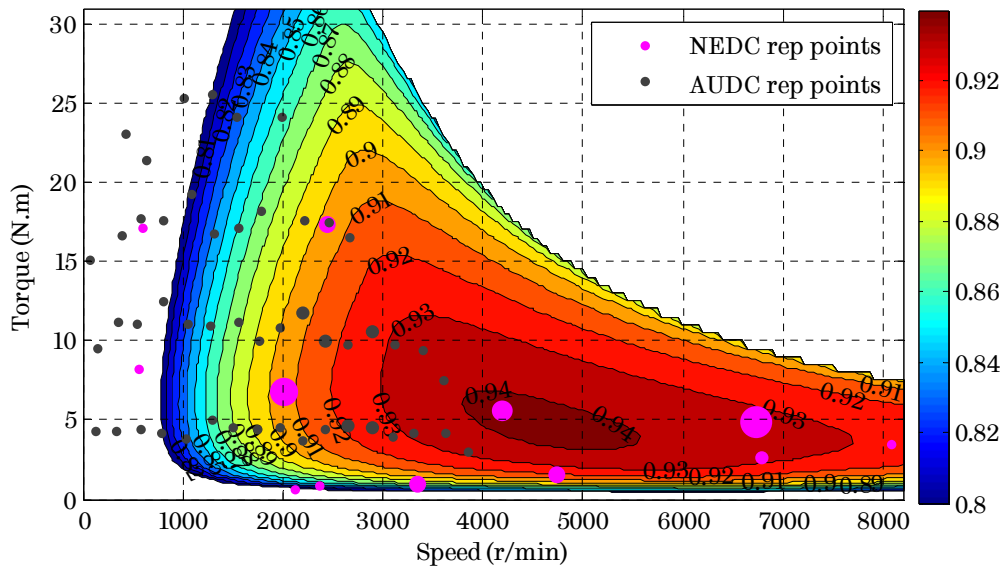
(b) System (machine + inverter) efficiency map

Figure 7.21. Efficiency maps of optimal ferrite PMA SynRM design, overlaid by the driving cycles' representative operating points.

7.3.5 Performance comparisons between optimal designs employing sintered NdFeB and ferrite magnets

Now that the optimal topology configurations of PMA SynRMs using sintered NdFeB and ferrite magnets have been identified (i.e., NdFeB-3 and Ferrite-Rect.), this section will evaluate and compare their performance against a number of indicative performance metrics. Ultimately, this will enable to acquire a holistic view regarding their viability in traction applications. The cross-sections of the two optimal designs, which have been optimised via the described multi-physics optimisation process against the same objective (i.e., NEDC), are illustrated side-by-side in Figure 7.22 for comparative purposes.
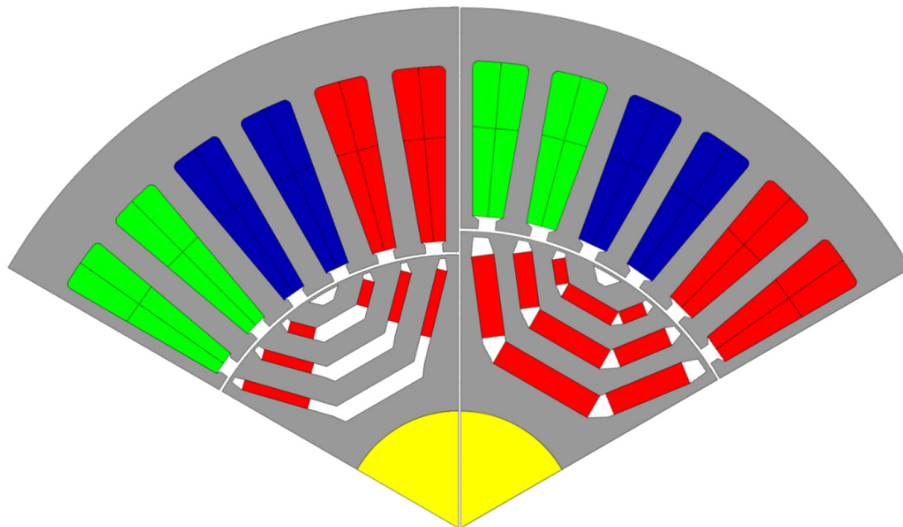
Figure 7.22. Cross sections of optimal NdFeB (left) and ferrite (right) PMA SynRM designs.

Both designs satisfy all multi-physical design constraints, have an optimised (i.e., minimised) PM amount, and have been evaluated against irreversible demagnetisation against their respective worst-case operating condition. It is evident from Figure 7.22 that, for the same optimisation objective, the use of the two characteristically different magnet materials in the rotor influences the selection of the leading design parameters during the design optimisation process of the PMA SynRMs, which, in turn, define the electromagnetic behaviour of the machines. The leading design parameters and critical performance metrics of the optimal designs are listed in Table 7.9.

Table 7.9. Key design parameters and performance metrics of optimal NdFeB and ferrite PMA SynRM designs

Parameter	NdFeB-3	Ferrite
Outside diameter (mm)	120.0	
Active axial length (mm)	105.0	
Tooth width - T_w (mm)	2.95	2.75
Bick iron thickness - H_y (mm)	6.75	6.10
Split ratio	0.525	0.5705
Magnet depth - d_m (mm)	14.40	15.9
Magnet angle span - β_m (º elec.)	165.0	166.5
Middle section insulation ratio - k_{ins_mid}	0.411	0.456
Side section insulation ratio - k_{ins_side}	0.264	0.402
Middle barrier section span - α_m (mm)	10.3	12.5
Bridge thicknesses – inner towards outer (mm)	0.4, 0.3, 0.3	0.6, 0.3, 0.3
Coil turn number - TN	7.0	
PM mass (kg)	0.185	0.50
L_d at T_c , ω_b (mH)	0.714	0.591
L_q at T_c , ω_b (mH)	2.43	2.37
Inductance difference at T_c , ω_b (mH)	1.72	1.78
Saliency ratio at T_c , ω_b	3.41	4.01
Phase resistance at 120ºC - R_{ph} (mΩ)	62.1	63.2
Peak current - I_{pk} (A,pk)	90.21	96.8
Rated current - I_{rated} (A,pk)	52.0	55.7
Line-Line back-EMF at ω_{ms} (V,pk)	207.5	157.2
Characteristic current - I_{ch} (A,pk)	56.5	53.8
I_{ch}/I_{rated} ratio	1.09	0.97
Copper/rotor temperature at T_c , ω_b (ºC)	93.3 / 92.8	101.8 / 100.8
Copper/rotor temperature at T_{cms} , ω_{ms} (ºC)	61.6 / 76.2	59.9 / 76.9

As can be observed from Table 7.9, the NdFeB PMA SynRM design produces significantly higher back-EMF (i.e., ~32%) for the same coil turn number by using only a fraction of the PM surface used in the ferrite design. Indeed, this stems from the substantially higher energy density of sintered NdFeB. The magnet mass of the NdFeB design is 63% lower, despite the 1.5 times higher mass density of the NdFeB magnet material (viz., Table 7.5). This, in turn, results in a smaller split ratio for the

NdFeB design, and hence more space for the stator coils (viz., taller slots). In addition, the bridge of the inner rotor layer is considerably thinner (i.e., 0.4 mm) compared with that of the ferrite design (i.e., 0.6 mm), which further contributes to its higher back-EMF. To accommodate the higher flux (and hence higher flux density level), however, the stator teeth and back iron, as well as the rotor flux guides, of the NdFeB design are thicker compared with the ferrite design, as can be observed from Figure 7.22 and the data of Table 7.9.

On the other hand, to maximise the flux linkage due to the PMs, the ferrite PMA SynRM design uses a higher split and insulation ratios to accommodate more magnets in the rotor, while at the same time maintaining thick-enough flux guides for enhanced reluctance torque production (viz., insulation ratio regulation of the middle and side sections of the flux barriers). Despite its substantially higher PM surface area, its PM-flux is still lower owing to the low energy density of the ferrite magnets. Hence, its tooth width and back iron are made thinner during the optimisation process against the NEDC, resulting in comparable phase resistance with that of the NdFeB design (viz., ~1.8% higher).

The system energy losses and efficiencies of the two optimal designs against the distinct driving cycles, i.e., the NEDC and AUDC, are evaluated and listed in Table 7.10 and Table 7.11, respectively. Their energy loss components are also compared in Figure 7.23. The analysis of the system energy losses against the considered driving cycles will assist in evaluating the influence of the different magnet materials on the design and performance of the PMA SynRMs for the investigated EV traction application.

As already explained the design optimisation objective is the system energy efficiency (machine plus inverter) over the NEDC. Accordingly, during the optimisation process, the leading design parameters of the two designs are tuned to minimise the system energy losses over the representative driving cycle operating points, which for the case of the NEDC are predominantly located in the low-torque, middle-to-high speed operating region. As can be seen from the data of Table 7.10, the two optimal designs deliver comparable energy efficiencies over the NEDC, despite the much lower magnet flux of the ferrite design. The total system

energy loss figures are similar between the two designs (viz., Figure 7.23), although the loss distribution is slightly different.

Table 7.10. Energy loss components and efficiency of optimal NdFeB and ferrite PMA SynRM designs against NEDC

Parameter	NdFeB-3	Ferrite
Total energy copper loss (kJ)	34.56	37.40
Low-speed energy copper loss (kJ)	21.60	25.65
High-speed energy copper loss (kJ)	12.96	11.75
Total energy iron loss over NEDC (kJ)	20.30	16.40
Low-speed energy iron loss (kJ)	12.87	9.50
High-speed energy iron loss (kJ)	7.43	6.90
Total energy inverter loss (kJ)	43.61	44.96
Machine energy efficiency	94.50%	94.60%
System energy efficiency	90.54%	90.51%

Table 7.11. Energy loss components and efficiency of optimal NdFeB and ferrite PMA SynRM designs against AUDC

Parameter	NdFeB-3	Ferrite
Total energy copper loss (kJ)	51.28	60.4
Low-speed energy copper loss (kJ)	49.15	58.83
High-speed energy copper loss (kJ)	2.13	1.57
Total energy iron loss (kJ)	8.51	7.31
Low-speed energy iron loss (kJ)	7.89	6.83
High-speed energy iron loss (kJ)	0.62	0.48
Total energy inverter loss (kJ)	43.82	46.78
Machine energy efficiency	92.70%	91.81%
System energy efficiency	88.00%	86.90%

Owing to its higher PM-flux, which elevates the flux density levels in the iron core, the NdFeB design generates a higher iron loss compared with the ferrite design despite the slightly thicker tooth and back iron. However, this is compensated by a lower inverter and copper loss (particularly in the lower speed operating region). The two designs exhibit comparable FW capabilities based on their respective ratio of I_{ch}/I_{rated} indicated in Table 7.9. The d-axis inductance (L_d)

of each design is regulated during the optimisation process so as to compensate for their respective PM flux linkage level, while at the same time maintaining a high L_q and, hence high magnetic anisotropy (viz., inductance difference), which is conducive to enhanced reluctance torque production.
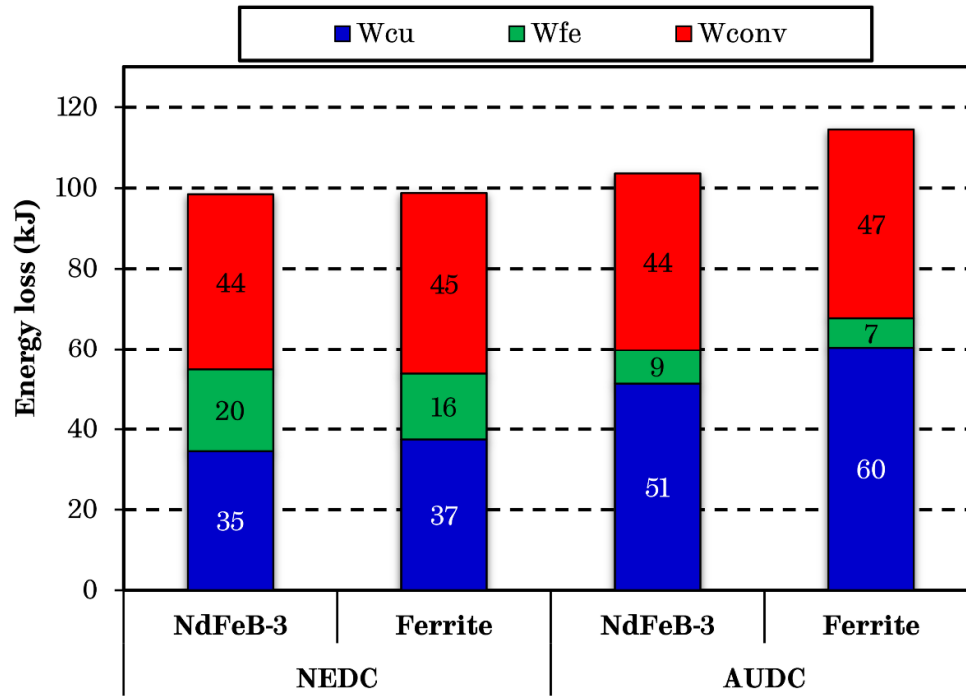
Figure 7.23. Comparison of driving cycle energy loss components between optimal NdFeB and ferrite PMA SynRM designs.

This is indeed regulated by tuning the split ratio and the insulation ratios in the rotor of the two designs in alignment with the grade of the employed magnet material. Therefore, the NdFeB design has a smaller split ratio and insulation ratios (viz., $k_{ins\,side}$ is about half of the $k_{ins\,mid}$) to balance the ratio of PM-flux and L_d and at the same time maintain a high enough L_q, where the two form a trade-off. This has resulted in ~21% higher L_d compared with that of the ferrite design, compensating for its higher PM-flux. Conversely, the ferrite design uses a higher split ratio and higher insulation ratios to maximise the surface area of the weak ferrites, while simultaneously introducing a higher insulation in the d-axis (particularly by using a higher $k_{ins\,mid}$). This leads to more effective saturation of

the rotor bridges, and enables to reduce L_d to its optimal level with respect to its PM-flux level.

The characteristic current (I_{ch}) of the ferrite design is slightly lower, resulting in lower high-speed copper loss (i.e., produced during FW operation) as can be seen from Table 7.10. Its copper loss during low-speed operation, however, is considerably higher compared with the NdFeB design due to the inherently lower PM-flux contribution. In the literature, excellent field weakening capability is frequently associated with the condition where $I_{ch} = I_{rated}$ during the design process of PMA SynRM [35], [74], [75], [125], [127]. However, this condition corresponds to the machine's operation along the continuous torque-speed envelope, which translates to continuous delivery of the rated power during cruise (i.e., flat constant power curve). As has been shown, the location of the high operating duty driving cycle operating points within the torque-speed range is different to that of the continuous envelope. Therefore, when driving cycles are incorporated to the design optimisation process with the aim of maximising energy efficiency over the cycle, the condition $I_{ch} = I_{rated}$ does not necessarily apply [65]. As has been demonstrated (viz., Table 7.9), the I_{ch}/I_{rated} ratio of the two optimal PMA SynRM designs, is 0.97 and 1.09 for the ferrite and NdFeB designs, respectively.

When evaluated over the AUDC, the energy efficiency difference between the two PMA SynRM designs grows considerably. As can be observed from Table 7.11, the NdFeB design exhibits ~1.1% higher system energy efficiency compared with the ferrite counterpart, which translates to ~10% lower system energy loss (viz., Figure 7.23). Albeit the energy efficiency over the NEDC is set as the optimisation objective, as already explained, the energy efficiency evaluation over AUDC serves as an indicative marker of the machine's versatility when exhibited to driving conditions which are different (more aggressive) to those imposed by the more moderate NEDC.

The AUDC is a suitable choice, as its energy consumption distribution is characteristically different from that of NEDC – i.e., high energy consumption is concentrated in the low-speed region with rapid variations of torque ranging from

low towards the peak torque of the machine. Under these driving conditions, a high current is often required to produce the torque needed for hard accelerations and stop-and-go activities of the vehicle during low-speed driving. As a result, the current-induced losses (i.e., copper and inverter loss) are the most dominant loss components during AUDC driving. Therefore, the inherently higher PM-flux contribution of the NdFeB design enables it to gain higher energy efficiency over the AUDC. Further, it can be noticed from Figure 7.23, that for the case of PMA SynRM the current-induced losses are, in fact, the dominant energy loss components over both driving cycles, despite their characteristically different energy consumption distributions.

This can be attributed to the intrinsically low iron losses of the PMA SynRM topology, due to the use of distributed windings (viz., the absence of low and high order asynchronous MMF harmonics) combined with the multi-layered rotor [83] and the inherently low PM-flux contribution. The energy efficiency trends of the two optimal designs over the considered driving cycles can be further perceived by observing their system (machine plus inverter) efficiency-difference map, overlaid with the driving cycles' representative energy consumption points and the required torque-speed envelopes, illustrated in Figure 7.24. Note that positive percentage values indicate a higher efficiency for the NdFeB design and vice versa. It can be seen that the regions, where high efficiency-difference is exhibited between the two designs, are located at distinct operating regions within the torque-speed range. More specifically, the NdFeB design exhibits superior efficiency in the low-speed region up to the maximum torque, whereas in the case of the ferrite design higher efficiency is observed in the middle-to-high speed operating region where the torque is very low.

As can be observed from Figure 7.24, the majority of high energy consumption representative operating points of the NEDC are located in regions where the two designs exhibit the least efficiency difference. That is to be expected, as the two designs were optimised against the same objective (i.e., energy efficiency over the NEDC). The remaining of the driving cycle operating points are almost equally distributed in such regions where each design exhibits an approximately equal amount of higher efficiency against the other. Hence, the respective efficiency

gains of each design over these operating points are compensated with respect to each other. This trend, therefore, explains the nearly identical energy efficiency exhibited by the two designs when operated over the NEDC. On the other hand, as already explained, the majority of AUDC's representative operating points are residing in the low speed operating region, where the NdFeB design inherently exhibits superior efficiency to the ferrite design. This, in turn, justifies the considerably higher AUDC energy efficiency exhibited by the NdFeB design.
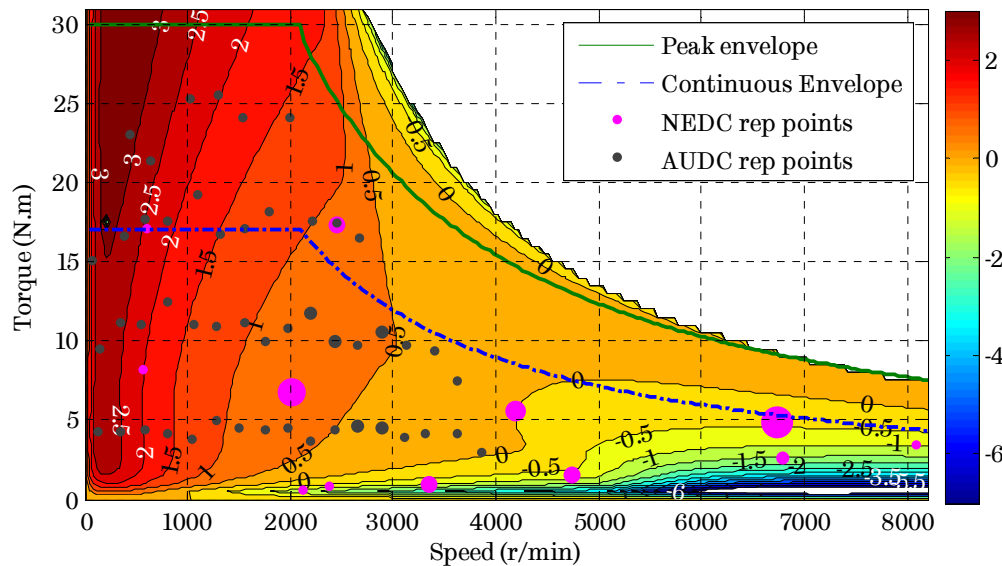
Figure 7.24. System efficiency difference map between optimal NdFeB and ferrite PMA SynRM designs.

The obtained efficiency trends can be further explained by analysing the torque production capability (i.e., magnet and reluctance torque contributions) of the two optimal designs in alignment with their design characteristics. It is well known in the literature [36], [71], [74], [127], [131], that for the case of embedded magnet machines, such as the PMA SynRM, a high reluctance torque contribution brings forth a number of advantages. These include enhanced torque and power densities, as well as improved overload and FW capabilities, all of which are conducive to energy efficiency improvement. Ideally, to accurately segregate the torque contributing components of an embedded magnet machine, the frozen permeability method should be employed [149], [150], which involves several processing steps. However, this is beyond the scope of this study, and since the

objective is the relative comparison between different designs, the use of the classical torque equation is considered adequate to estimate the torque contributing components of each design for simplicity.

The classical torque equation of a three-phase interior PM (IPM) machine formulated in the d-q axis frame is given below as a function of d- and q-axis currents,

$$T_e(I_d, I_q) = \frac{3}{2}p\{\psi_m(0, I_q)I_q + [L_d(I_d, I_q) - L_q(I_d, I_q)]I_d I_q\} \qquad (7.65)$$

where, p is the pole pair number, ψ_m is the PM flux linkage, I_d and I_q, and L_d and L_q are the d- and q-axis currents and inductances, respectively. Note that the d-axis is aligned with the low permeance axis, and that the cross-coupling effect between the d- and q-axis is taken into account in the torque calculation. The first term in the bracket of (7.65) represents the magnet-related torque component, known as alignment torque, whereas the second bracketed term represents the reluctance torque component, resulting from the rotor magnetic anisotropy (i.e., d- and q-axis inductance difference).

The variation of the PM-flux linkage (ψ_m) with I_q for the optimal designs is illustrated in Figure 7.25. As can be observed, the NdFeB design consistently produces about 1.25~1.3 times higher ψ_m than the ferrite design, even after considering the d-q axis cross-coupling. Hence, for the same I_q input, the NdFeB design would produce the same amount of higher magnet torque than the ferrite design according to the first term of (7.65). To evaluate the reluctance torque production capability of the two designs, the d- and q-axis inductance difference $(L_d - L_q)$ over the I_d and I_q operating range is used as an indicative metric according to the second term of (7.65). Therefore, for a given I_d, I_q input, the design that exhibits a higher inductance difference will accordingly produce a proportional amount of higher reluctance torque.
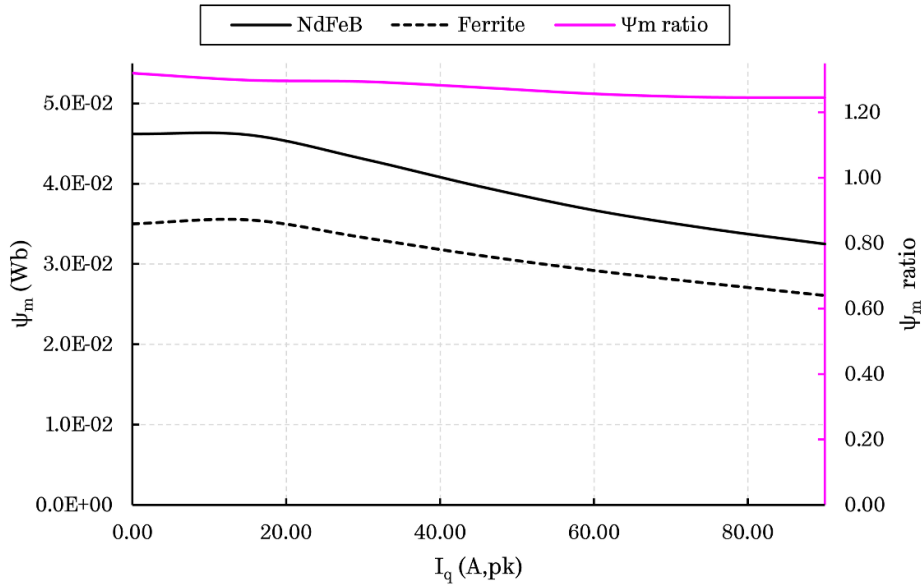
Figure 7.25. Variation of ψ_m with I_q (when $I_d = 0A$) for the optimal designs, including the ratio of ψ_m between the NdFeB and ferrite PMA SynRM designs (right-hand axis).

Figure 7.26 demonstrates the ratio of absolute inductance difference between the ferrite and the NdFeB designs over the I_d and I_q range, where values >1 indicate higher inductance difference for the NdFeB design and vice versa. The d-q axis current trajectories of the two designs over the continuous and peak torque-speed envelopes are also illustrated in the inductance difference ratio map for comparative purposes. The region A to B on the current trajectories is associated with the maximum torque per ampere (MPTA) operation in the low-speed section of the torque-speed envelope, whereas region B to C is associated with the FW operation over the higher speed section of the envelope, where the maximum torque is limited by the inverter voltage and/or current limits.

As can be seen from Figure 7.26, the inductance difference varies little with I_d but changes drastically with I_q, which defines the saturation level in the lamination. It can also be observed that the ferrite design achieves a higher inductance difference than the NdFeB design in the lower I_q operating region, which indicates that it can produce a higher reluctance torque for the same input current. As the I_q increases, and hence the magnetic saturation in the lamination, the inductance difference ratio between the two designs approaches unity. At significantly higher I_q levels, it even surpasses unity indicating a superior

inductance difference for the NdFeB design. However, this is beyond the operational current range of the machines as indicated by the current trajectories over the continuous and peak operating envelopes.
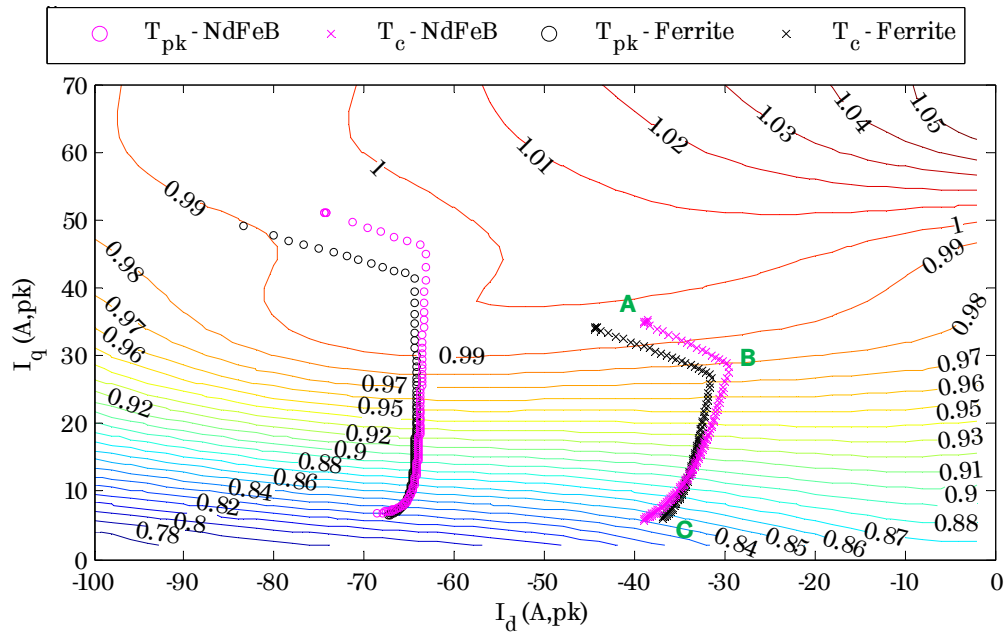
Figure 7.26. Ratio of absolute inductance difference between NdFeB and ferrite PMA SynRM designs, overlaid by current trajectories over the T-N operating envelopes.

This behaviour can be explained based on the trend of the leading design parameters of the two optimal designs, which as previously described is influenced by the employed magnet material. Hence, the larger split and insulation ratios of the ferrite design enable it to achieve superior magnetic anisotropy in the lower current region. However, the resulting thinner flux guides, stator teeth and back iron of the ferrite design, start to saturate at relatively lower input current. This leads to a reduction in L_q, and eventually to a reduced inductance difference. On the other hand, the thicker flux guides, stator teeth and back iron of the NdFeB design do not saturate at the same rate with the increase of input current (as the ferrite design does) – which justifies the established inductance difference trend.

Based on the established inductance difference trend, it can be deduced that the ferrite design compensates for its lower magnet torque (due to its lower PM-flux) with superior magnetic anisotropy in the lower I_q operating region. This

region covers most part of the FW region as can be seen from Figure 7.26, which explains the nearly identical current of the two designs during FW operation where the torque is low. When higher torque is required during drive (i.e., MTPA operation in lower speeds), however, the required I_q levels become higher. This in turn is conducive to higher saturation, leading to the inductance difference between the two designs to become nearly identical (viz., hence identical reluctance torque capability for the same input current). At the same time, the magnet torque contribution is now becoming more significant according to the first term of the classical torque equation (due to the higher I_q).

Therefore, the inherently higher PM-flux of the NdFeB design enables it to use a lower current than the ferrite design to achieve the same torque demand, which in turn leads to lower current-induced losses and improved efficiency under these operating conditions. For this reason, the NdFeB design achieves ~8 °C lower steady-state temperature at T_c, ω_b, as can be observed from Table 7.9. Since this is, thermally, the worst-case operating condition for the investigated PMA SynRMs, it can be inferred that the NdFeB design may achieve a longer lifespan due to reduced thermal stresses on the winding insulation. The steady-state temperature of the two designs at T_{cms}, ω_{ms}, which corresponds to continuous driving at 120 km/h, is nearly identical since as already explained the two designs use similar current and exhibit comparable losses at that operating condition.

Figure 7.27 shows the *d-q* axis current trajectories of the two designs when operated over the investigated driving cycles, i.e., NEDC and AUDC, overlaid on the inductance difference ratio map. Given that the two designs have comparable phase resistance, an inherently low iron loss, and the fact that the major energy loss components over both driving cycles are the current-induced losses, their energy efficiency trends can be explained based on their torque production capability, which in turn defines their operating currents.

It can be seen that the majority of the NDEC's *d-q* axis operating currents reside in the region where the ferrite design exhibits superior magnetic anisotropy than the NdFeB design, compensating for its lower PM-flux. For the low-torque, high-speed NEDC operating points the ferrite design uses lower currents than the

NdFeB design, whereas the opposite occurs for the higher torque, low-speed operating points. For the remaining NEDC operating points the current of the two designs are nearly identical. This in turn justifies the comparable NEDC energy efficiency exhibited by the two optimal designs. In the case of the AUDC, it can be observed that the majority of *d-q* axis operating currents are located in the higher I_q region where the two designs have almost identical inductance difference, and hence similar reluctance torque capability for the same input current.
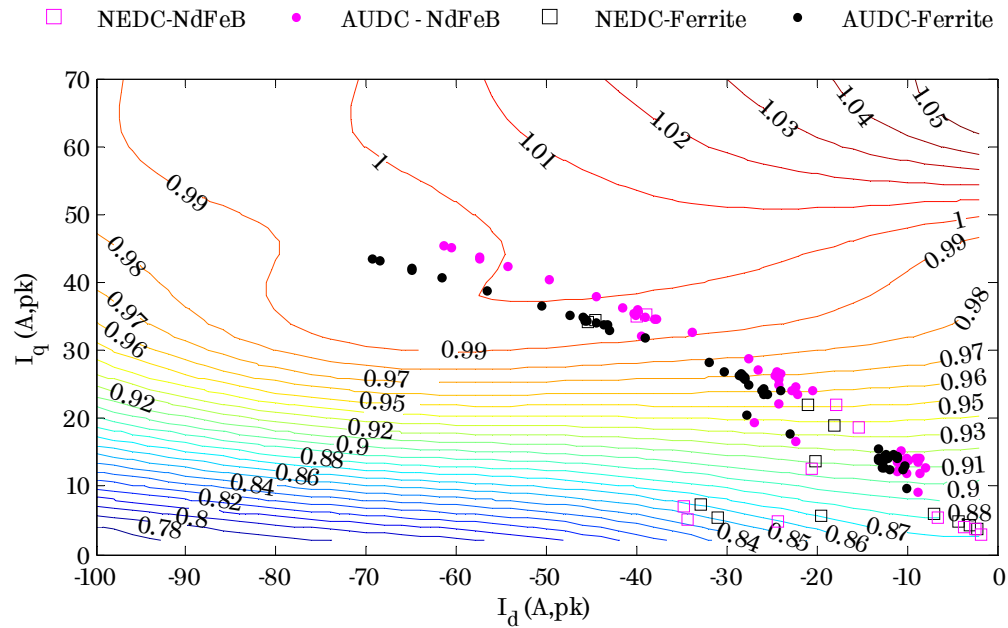
Figure 7.27. Ratio of absolute inductance difference between NdFeB and ferrite PMA SynRM designs, overlaid by current trajectories over NEDC and AUDC.

Clearly, the operating currents over AUDC are larger, since the torque demand is higher compared to the NEDC. Similar to the MTPA region, explained before, the inherently higher PM-flux of the NdFeB design enables it to deliver the same torque with a lower input current. Again, this leads to lower current-induced energy losses (which dominate the total loss over AUDC) for the NdFeB design, which achieves ~1.1% higher system energy efficiency over AUDC than the ferrite design. The power factor of the two optimal designs over the continuous and peak torque-speed envelopes is illustrated in Figure 7.28. As can be observed both designs exhibit a relatively high power factor, which exceeds 0.8 over the complete operating range due to their enhanced magnetic anisotropy [127]. The

power factor over the peak operating envelope is nearly identical for the two designs. The same applies to the low-speed part of the continuous envelope (i.e., MTPA operation). The slight difference in the power factor of the two designs over the higher-speed part of the continuous envelope can be attributed to the different I_{ch}/I_{rated} ratio of the two designs (i.e., 1.09 for the NdFeB design and 0.97 for the ferrite design, as indicated in Table 7.9).
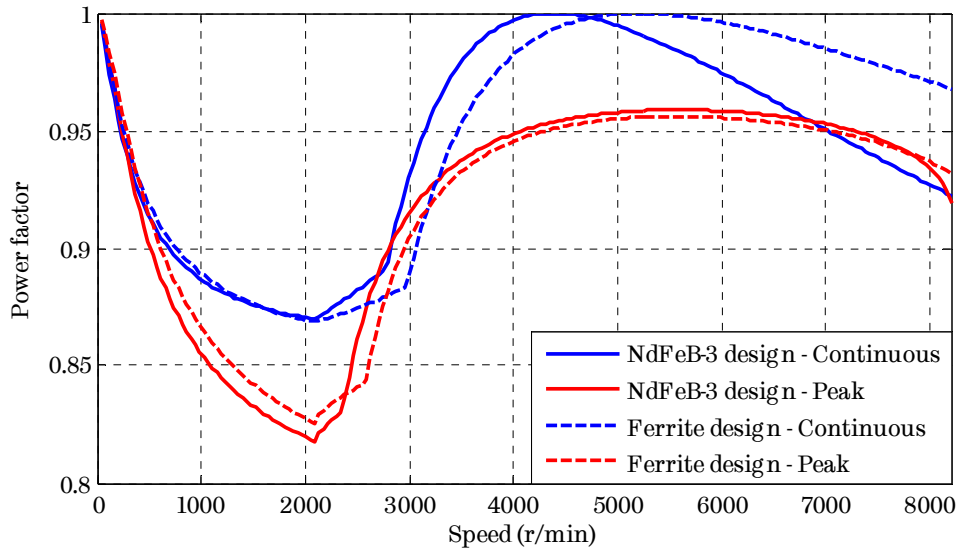
Figure 7.28. Power factor comparison between NdFeB and ferrite PMA SynRM design, along the continuous and peak T-N envelopes.

The mass and estimated cost of the active materials used in the two optimal designs are given in Table 7.12 for comparison. As can be observed, the two designs have a comparable total active weight. The total active material cost of the machines is estimated based on typical market prices available in the literature. Further, to reflect the rapid fluctuations recently characterising the price of NdFeB magnets, [38], a minimum and maximum value has been considered. As shown in Table 7.12, the total estimated cost of active materials for the NdFeB design is 1.7~2.1 times higher than that of the ferrite design. This is due to the substantially inflated price of NdFeB magnets, which in fact contribute about 50~60% to the total material cost in the case of the NdFeB design (despite the minimised magnet usage). This is, indeed, a penalising factor pertaining to the viability of the NdFeB design for automotive applications, where cost (just as performance) is of paramount importance.

Table 7.12. Active material mass and cost comparison of optimal NdFeB and ferrite PMA SynRM designs

Parameter	NdFeB-3	Ferrite
Stator steel mass (kg)	3.76	3.32
Rotor steel mass (kg)	1.48	1.54
Copper mass - active (kg)	1.25	1.23
Magnet mass (kg)	0.185	0.50
Total active mass (kg)	**6.67**	**6.59**
Silicon iron cost ($) at 1.3 $/kg	6.81	6.32
Copper cost ($) at 6.6 $/kg	8.25	8.12
Magnet cost ($)	16.7-24.0 (at 90-130 $/kg)	4.0 (at 8 $/kg)
Total cost - active materials ($)	**31.7-39.1**	**18.4**

7.3.5.1 Torque/Power density evaluation with different magnet materials

In the previous sections of this chapter both the NdFeB and ferrite PMA SynRM designs were optimised against the maximum available axial length and outside diameter (imposed by the OEM as part of the Hi-Wi project) for the purpose of exploiting their maximum energy efficiency potential. To acquire a holistic view regarding the performance comparison of the two design configurations, namely the NdFeB and ferrite PMA SynRMs, this section evaluates and compares their maximum achievable torque density. Accordingly, the described optimisation process is repeated for varying axial length until the respective minimum axial length that satisfies the defined multi-physical design constraints is acquired, for each of the design configurations. Note that the objective of each optimisation is still the energy efficiency maximisation over the NEDC. The key design parameters of the optimal NdFeB and ferrite designs with minimised axial length are summarised in Table 7.13.

It is evident from the data of Table 7.13 that the two optimal designs with minimum axial length have been pushed towards their extreme design limits – i.e., both designs have been pushed close to the defined continuous thermal limit of 120^oC, whereas the ferrite design has also reached the defined current constraint of 120A. Further, it can also be observed that the NdFeB design satisfies all design

constraints by using 10mm lower axial length than the ferrite design. This, in turn, translates to about 12% higher torque/power density for the NdFeB design, owing to the higher energy density of the sintered NdFeB magnets which enables it to produce a considerably higher back-EMF despite its shorter axial length. Moreover, the NdFeB design achieves ~11% higher specific torque/power density than the ferrite design due to its lower active mass. The energy loss components and efficiency over driving cycles are shown in Figure 7.29 for the optimal NdFeB and ferrite designs with minimum axial length.

Table 7.13. Key design parameters and performance metrics of optimal NdFeB and ferrite PMA SynRM designs with minimum axial length

Parameter	NdFeB	Ferrite
Outside diameter (mm)	120.0	
Active axial length (mm)	85.0	95.0
Coil turn number - TN	8.0	7.0
PM mass (kg)	0.22	0.59
Total active mass (kg)	5.31	5.87
Inductance difference at T_c , ω_b (mH)	1.53	1.50
Saliency ratio at T_c , ω_b	3.44	4.18
Phase resistance at 120ºC - R_{ph} (mΩ)	64.7	52.1
Rated - I_{rated} / Peak current - I_{pk} (A,pk)	56.0 / 100.3	65.5 / 119.0
Line-Line back-EMF at ω_{ms} (V,pk)	191.2	113.7
Characteristic current - I_{ch} (A,pk)	61.6	49.9
I_{ch}/I_{rated} ratio	1.1	0.76
Rated / Peak Efficiency at ω_b	91.9% / 86.7%	91.2% / 85.2%
Copper/rotor temperature at T_c , ω_b (ºC)	117.0 / 113.8	119.9 / 115.8

The two designs exhibit comparable energy efficiency over the NEDC (i.e., the optimisation target). An identical copper loss is produced by the two designs over the NEDC, albeit distributed in different operating regions for each design – i.e., the NdFeB design produces a relatively lower copper loss during MTPA operation whereas the ferrite design produces a relatively lower copper loss during FW operation and vice versa. The considerably higher PM-flux of the NdFeB design enables it to produce lower copper loss during MTPA, despite its much higher

phase resistance. However, owing to its higher PM-flux, the NdFeB design requires a higher current during FW, which combined with its higher phase resistance leads to a relatively higher copper loss under these operating conditions. The contrary occurs in the case of the ferrite design due to the low energy density of the ferrite magnets. This trend is reflected by the characteristic current and I_{ch}/I_{rated} ratio of the two optimal designs.
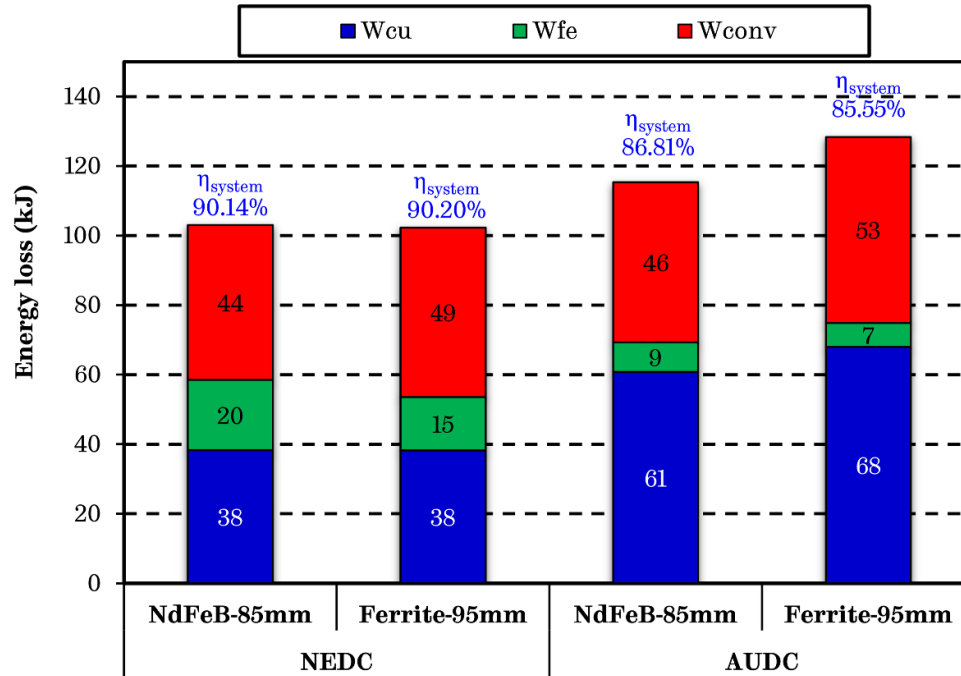
Figure 7.29. Comparison of driving cycle energy loss components between optimal NdFeB and ferrite PMA SynRM designs with minimised axial length.

Further, due to the weak ferrite magnets, the ferrite design produces lower iron losses over the cycle despite its longer axial length, but on the other hand it generates higher converter losses than the NdFeB design. When evaluated over the AUDC, where most energy consumption occurs in the low speed and middle-to-high torque region, the NdFeB design produces ~1.3% higher system energy efficiency than the ferrite design, despite its shorter axial length and higher phase resistance. Again, this is due to the considerably higher PM-flux of the NdFeB design, which leads to lower current-induced losses that comprise the most dominant energy loss components over the AUDC. A similar trend occurs for the rated and peak efficiency of the optimal designs at base speed (ω_b).

In summary, the design optimisations of the two PMA SynRM configurations with minimised axial length have demonstrated that the NdFeB design can achieve ~12% higher torque/power density and ~11% higher specific torque/power density than the ferrite design, owing to the high energy density of the NdFeB magnets. Both designs exhibit comparable energy efficiency over the NEDC, whereas the NdFeB design produces ~1.3% higher energy efficiency over the AUDC, despite its reduced active volume. The resulting loss trends over the driving cycles remain similar to those obtained from the previous comparison, where both design configurations utilise the full available space envelope. The energy loss over the NEDC is nearly the same between the NdFeB and ferrite designs with full axial length as well as the NdFeB and ferrite designs with minimised axial length. Whereas, in the case of the AUDC, the NdFeB designs with maximum and minimised axial length produce ~10-11% lower energy losses compared with their ferrite counterparts, respectively.

However, as expected, both the NdFeB and ferrite designs with minimised axial length produce ~4% and ~11% higher energy losses than their full-axial-length counterparts over the NEDC and AUDC, respectively. It can be noticed that the energy loss-increase for the designs with minimised axial length is relatively small under low-load operation (such as the NEDC), but increases drastically toward higher load conditions (such as those found in AUDC). Albeit the NdFeB design with minimised axial length exhibits higher torque and power density than the ferrite counterpart due to the high energy density of the sintered NdFeB magnets, this does not translate to the same amount of active material cost reduction.

Owing to the substantially higher price of sintered NdFeB magnets, the estimated total cost of the NdFeB PMA SynRM design remains about 1.7~2 times higher than that of the ferrite design, despite its lower active mass and volume. Clearly, this is due to the fact that the total active material cost of the NdFeB design is primarily dominated by the price of the sintered NdFeB magnets, which is approximately 11~16 times higher than that of the ferrites. Similar to the design comparison with full axial length, the performance improvement of the NdFeB PMA SynRM design over the ferrite counterpart forms a trade-off with the machine's cost, which is difficult to justify.

7.3.5.2 Overall figure of merits comparison

The multi-physics design optimisation and performance of traction PMA SynRMs employing conventional distributed winding in the stator, and characteristically different magnet materials (i.e., NdFeB and ferrite) in the rotor, have been coherently analysed against driving cycles in the previous sections of this chapter. This section will provide the overall figure of merits stemming from the findings obtained through the comparisons between the optimal PMA SynRM designs employing sintered NdFeB and ferrite magnets. A set of key performance indicators are summarised for the two PMA SynRM configurations in the spider chart of Figure 7.30, which assists in assessing their viability for traction applications from a multi-perspective point of view.
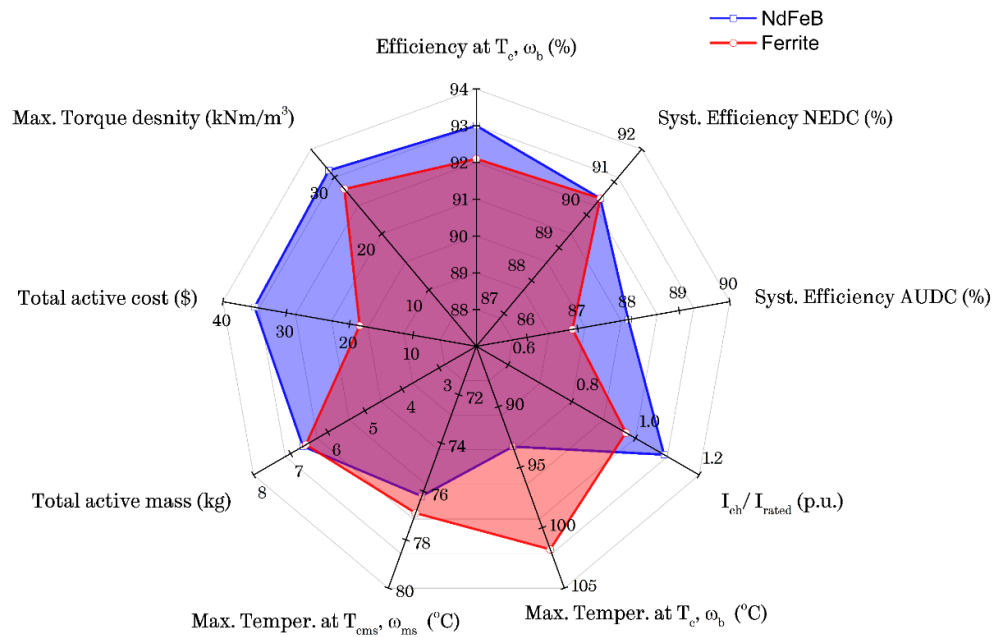
Figure 7.30. Comparison of key indicative performance metrics between the optimal NdFeB and ferrite PMA SynRM designs.

Based on the foregoing analysis it can be seen that the PMA SynRM design employing ferrites can, indeed, comprise a competitive solution for EV traction applications when its performance is evaluated and optimised against driving cycles (viz., where the traction machine most frequently operates over its lifetime), rather than a few points located close to the rated operating conditions. In fact,

when optimised and evaluated against the NEDC, which until recently has formed the certification standard for light-duty vehicles in the EU, the optimal ferrite design can deliver nearly identical system energy efficiency as the optimal NdFeB design despite the much lower energy density of the ferrite magnets. As has been demonstrated, this can be attributed to its superior magnetic anisotropy under these operating conditions, which is conducive to enhanced reluctance torque capability that compensates for the low energy density of the ferrites.

On the other hand, when evaluated against driving conditions characteristically different to the optimisation objective (i.e., NEDC), such as the more aggressive AUDC, the NdFeB design exhibits superior versatility by producing ~1.1% higher system energy efficiency than the ferrite design. This translates to ~10% lower system energy loss and can be attributed to the larger energy density of the sintered NdFeB magnets, which enables the NdFeB design to produce higher PM-flux for the same design space envelope. Additionally, the NdFeB design can achieve ~12% higher torque/power density than the ferrite design (as described in §7.3.5.1). However, this is at the expense of a considerably higher active material cost, which amounts to 1.7~2.1 times of that of the ferrite design, due to the substantially inflated price of NdFeB magnets. The total active mass of the two designs is almost equal, at ~6.5 kg, indicating an identical specific torque and power density when compared against the same design space envelope.

The optimal NdFeB and ferrite designs exhibit comparable FW capability over the continuous operating envelope, as can be observed from their respective I_{ch}/I_{rated} ratio (which is very close to unity). Since their current trajectories and losses during the deep FW region are very similar, the two designs exhibit comparable thermal behaviour under continuous operation at maximum cruise speed (T_{cms}, ω_{ms}). However, for the case of the PMA SynRM, the worst thermal condition occurs under continuous operation in the low speed region (T_c, ω_b). Under these circumstances, the NdFeB design produces ~8°C lower copper hot-spot temperature than the ferrite design, due to its inherently higher PM-flux that enables it to produce the same torque with a reduced input current leading to reduced copper losses. This, in turn, may translate to a potentially longer lifespan for the NdFeB design.

For the sake of completeness, the performance of the optimal NdFeB and ferrite designs is also evaluated over the WLTP cycle, which will soon form the new certification standard in the automotive industry by replacing the NEDC. The representative operating points of the WLTP cycle corresponding to a class-2 vehicle are established and compared with those of the NEDC in Figure 7.31. Note that the WLTP class-2 cycle does not include the extra-high-speed portion, and thus the maximum vehicle speed is limited to 90 km/h.
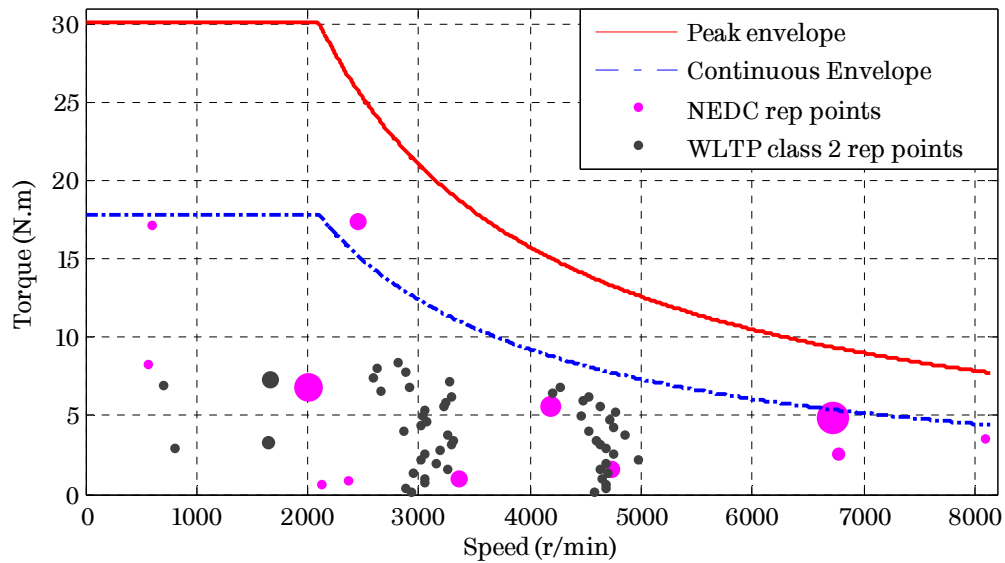
Figure 7.31. Torque-speed envelope overlaid by NEDC and WLTP (class-2) representative operating points.

It can be seen that the locations of most representative operating points of the two cycles reside in similar regions of the torque-speed operating range, i.e., low-torque, middle-high speed. It can also be seen that in the WLTP the torque variation is more significant due to the more dynamic nature of this cycle, which emulates more realistic worldwide driving patterns than its predecessor the NEDC. Further, owing to the more dynamic nature of WLTP, more representative points are required (i.e., 55) to accurately represent the cycle's energy consumption than the NEDC. Based on the fact that many of the representative energy consumption points of the two cycles are located in similar operating regions, it is anticipated that the designs optimised against the NEDC may exhibit near-optimal energy efficiency over the WLTP as well. The obtained energy loss components and

efficiencies of the optimal NdFeB and ferrite PMA SynRM designs (viz., with full axial length – 105mm), when operated over the WLTP-class 2 cycle, are listed in Table 7.14.

Table 7.14. Energy loss components and efficiency of optimal NdFeB and ferrite PMA SynRM designs against WLTP (class 2)

Parameter	NdFeB-3	Ferrite
Total energy copper loss (kJ)	26.99	31.13
Low-speed energy copper loss (kJ)	19.64	25.59
High-speed energy copper loss (kJ)	7.34	5.54
Total energy iron loss over (kJ)	25.25	20.03
Low-speed energy iron loss (kJ)	17.56	15.84
High-speed energy iron loss (kJ)	7.68	4.19
Total energy inverter loss (kJ)	59.50	61.87
Machine energy efficiency	95.33	95.42
System energy efficiency	**90.52%**	**90.42%**

It can be seen that, although not optimised against the WLTP, the NEDC-optimised NdFeB and ferrite designs exhibit near identical system energy efficiency when evaluated against the WLTP. As expected, the acquired energy efficiency and loss distribution trend is similar to that obtained for the NEDC. The preceding findings of the study demonstrate that, by following the same multi-physics design optimisation process, the PMA SynRM design employing sintered NdFeB magnets is a better overall performer than the ferrite design for the investigated traction application for a number of reasons. It provides improved versatility when exhibited to more aggressive driving conditions (viz. often imposed by the driver), different to the optimisation target, by producing a wider high-efficiency region. Further, it exhibits improved thermal behaviour against the worst-case operating conditions, and has the potential to offer ~12% higher torque/power density than the ferrite design.

When the cost of active materials is factored in, however, the viability of the NdFeB design for EV traction is largely penalised due to the substantially inflated price of the sintered NdFeB magnets. The nearly twice active material cost of the NdFeB design is considered not adequate to justify its performance improvement

over the ferrite PMA SynRM, particularly if the volatile NdFeB market continues to exist. Therefore, considering the trade-off between performance (i.e., energy efficiency) and cost, the ferrite PMA SynRM design can indeed comprise an attractive alternative solution to its NdFeB counterpart for EV traction applications. Notably, by considering that it delivers nearly identical system energy efficiency as the NdFeB counterpart over the previous and new certification standard driving cycles (i.e., NEDC and WLTP), where in fact the traction machine most frequently operates throughout its lifetime.

The above assertion infers that the ferrite PMA SynRM has little or even none demerits against its NdFeB counterpart when its performance is optimised and evaluated against these standardised driving cycles. It should be noted, however, that regarding manufacturability, the ferrite design might be more complicated and/or costly to manufacture, as it requires three more different magnet pieces per pole to be cut and assembled, compared with the NdFeB design.

7.4 Performance evaluation of PMA SynRMs with respect to different stator winding configurations

The previous sections of this chapter have investigated the design optimisation of PMA SynRMs employing distributed windings in the stator and characteristically different magnet materials in the rotor via the developed multi-physics optimisation process. The performance of the attained optimal design configurations has been evaluated against multiple performance indicators, where it has been demonstrated that the PMA SynRM design employing ferrites can comprise a competitive solution for EV traction considering the trade-off between performance and cost. As a next step, this section will deal with the multi-physics design optimisation of PMA SynRMs employing a ferrite rotor structure, but a fractional-slot winding configuration. Ultimately, the performance of the optimal ferrite PMA SynRM with fractional-slot windings will be compared against that of the optimal ferrite PMA SynRM employing distributed windings, with the aim of evaluating their feasibility for EV traction applications.

7.4.1 Distributed and fractional-slot PMA SynRM characteristics

In the literature, the PMA SynRM, being an evolution of SynRM and IPM topologies, is typically associated with distributed windings, which exhibit enhanced reluctance torque production. Fractional-slot winding configurations, on the other hand, are well known for their distinctive advantages in manufacturability (due to the use of concentrated coils), short end-winding length, high slot-fill factor, and excellent field weakening capability which can be well-calibrated by design [58], [59], [151], [152]. When applied, however, to machine topologies having anisotropic rotor structures, such as the IPM, fractional-slot windings appear to diminish the reluctance torque production [80]–[82]. For this reason, few studies are available investigating their applicability on PMA SynRMs, except the configuration with slot-per-pole-per-phase (q) equal to 0.5 that appears not to harm the reluctance torque capability [148], [153].

However, it is possible that particular fractional-slot winding configurations, when paired with a multi-barrier rotor containing magnets (such as PMA SynRM), may exhibit considerable reluctance torque contribution and competitive overall performance. The performance of three fractional-slot PMA SynRMs, namely, with 12-slot/10-pole ($q = 2/5$), 12-slot/6-pole ($q = 0.5$) and 18-slot/8-pole ($q = 3/4$) configurations, has been comprehensively evaluated in [148]. It has been found that the PMA SynRM with 12-slot/10-pole (viz., one of the most popular fractional-slot configurations) produced, albeit considerable, the least reluctance torque contribution. This can be attributed to the fact that the MMF harmonics of this winding configuration, travelling asynchronously to the fundamental harmonic, compromise the insulation between the d- and q-axis, despite the multi-barrier rotor structure (which enhances magnetic insulation in the low permeance d-axis). This pertains to a poor magnetic anisotropy (i.e., d-q axis inductance difference) and consequently to inferior reluctance torque capability.

Further, the high total harmonic distortion in the MMF of this configuration has resulted in excessive iron losses, which penalise its performance and give rise to thermal issues at high speed operation. The 12-slot and 8-pole PMA SynRM configuration, although exhibiting high reluctance torque contribution,

has an inherently high torque ripple which is difficult to alleviate without compromising its performance. The 18-slot/8-pole configuration appeared as the best fractional slot PMA SynRM performer due to the high winding factor, low torque ripple, high reluctance torque contribution and low total harmonic distortion, which is conducive to lower iron loss production.

Against this background, the 18-slot/8-pole PMA SynRM configuration has been selected for design optimisation and performance comparison against the optimal ferrite PMA SynRM benchmark, established in the previous sections, with 36-slot/6-pole distributed winding configuration. It should be noted that the 18-slot/8-pole is a novel fractional-slot configuration, proposed in [68], which doubles the stator slot/coil number of the conventional 9-slot/8-pole configuration to mitigate undesirable sub- and high-order asynchronous MMF harmonics (typically found in fractional-slot machines). The duplicated winding sets are shifted apart in space by an appropriate phase shift angle and connected in series. The MMF spectra of the fractional-slot and distributed winding configurations are compared in Figure 7.32, where all harmonics are normalised to the fundamental harmonic of the distributed winding, and the harmonic order represents the period number over one mechanical cycle.
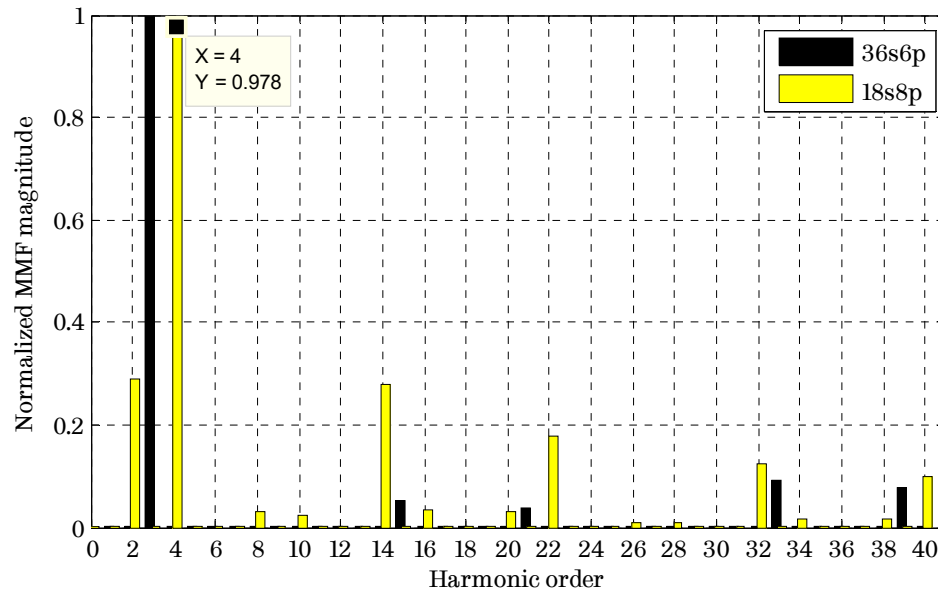
Figure 7.32. MMF spectra comparison between distributed (36s6p) and fractional slot (18s8p) winding configurations – normalised to 1st harmonic of distributed winding.

As can be observed from Figure 7.32, the distributed winding exhibits a lower total harmonic distortion and no sub-harmonics in its MMF spectrum compared with the fractional slot one. Further, it can also be observed that the fundamental (working) harmonic of the 18s8p configuration is slightly lower (viz., 2.2%) than that of the distributed winding.

7.4.2 Design optimisation of 18-slot/8-pole PMA SynRM and performance comparison against 36-slot/6-pole benchmark

The multi-physics design optimisation of the 18-slot/8-pole fractional-slot ferrite PMA SynRM was conducted using the same optimisation objectives and constraints as the distributed winding PMA SynRM. An important point to note is the difference in the phase resistance calculation between the two configurations resulting from their different end-winding length, which in turn influences the copper losses. To achieve a more representative resistance prediction, the end-winding length calculation was calibrated based on results taken from SPEED software [154] (viz., which utilises empirical formulas) for each winding configuration. The same slot-fill factor of 0.4 has been employed in the resistance prediction of the 18-slot/8-pole PMA SynRM since its windings are also overlapping. Being a fractional-slot configuration, the 18-slot/8-pole PMA SynRM has a shorter end-winding length as well as a shorter total axial length (viz., active + end-winding axial lengths) than the distributed PMA SynRM.

It should be emphasized that the different stator layout in the two configurations, i.e. the narrow slots in the distributed winding PMA SynRM and wider slots in the fractional-slot PMA SynRM, will considerably influence their thermal behaviour (viz., the hot-spot temperature of copper wire). Hence, this highlights the significance of incorporating the analytical thermal model in the performance evaluation and design optimisation process, which enables a more effective representation of the thermal behaviour of the two configurations. Further, the semi-analytical mechanical stress model incorporated in the multi-physics design optimisation process has been calibrated for the case of the 18-slot/8-pole PMA SynRM configuration using the method described in §7.2.3.3. This enables monitoring of the maximum mechanical stress level in the rotor of the 18-

slot/8-pole PMA SynRM by appropriately modifying the rotor bridge thicknesses during the optimisation process. The cross-section of the optimal 18-slot/8-pole ferrite PMA SynRM optimised with the same active axial length and outside diameter as the 36-slot/6-pole ferrite PMA SynRM is shown in Figure 7.33. Further, the cross-section of one pole-pair of the optimal 18-slot/8-pole design is compared with that of the 36-slot/6-pole benchmark in Figure 7.34.
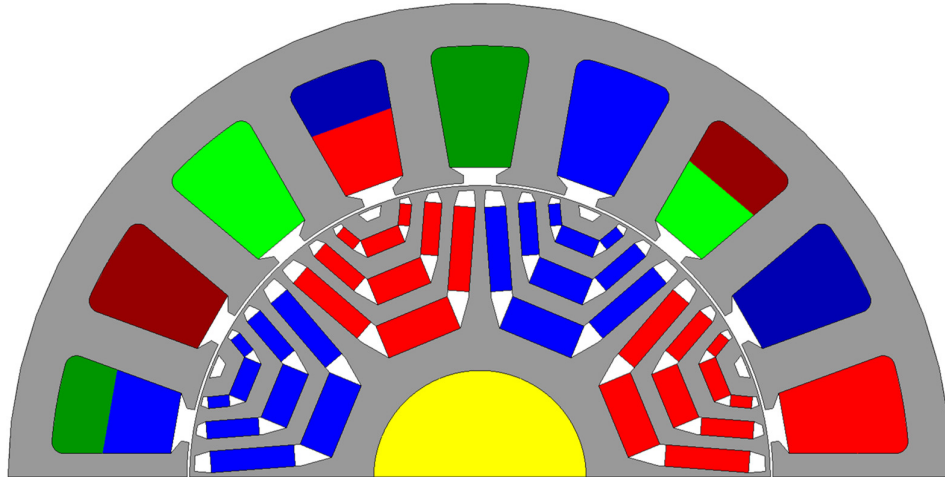
Figure 7.33. Optimised 18-slot/8-pole ferrite PMA SynRM schematic.
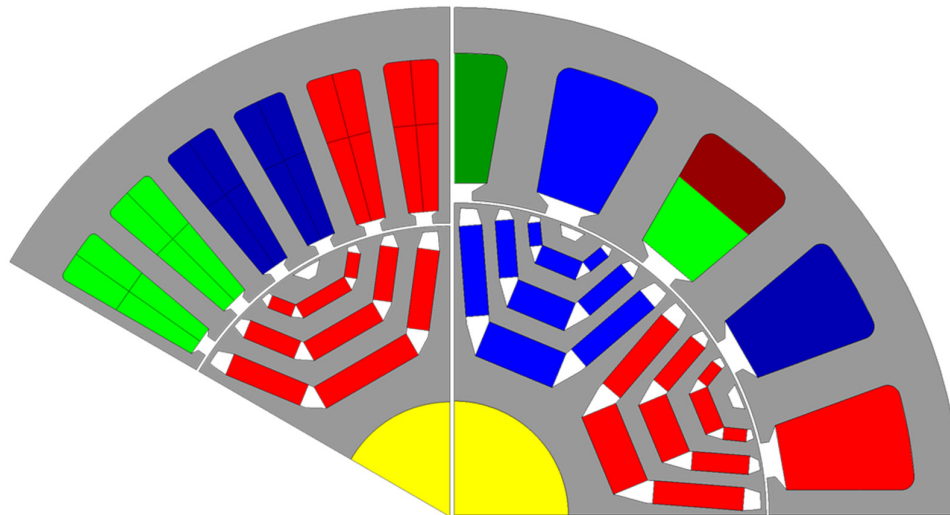
Figure 7.34. Comparison between optimal distributed and fractional-slot PMA SynRM designs with identical active axial length.

The key design parameters and performance metrics of the optimal ferrite PMA SynRM designs with fractional-slot and distributed winding configurations are given in Table 7.15 for comparative purposes. It should be noted that during the

optimisation of the fractional-slot PMA SynRM, half-coil turn numbers were allowed to better regulate the L_d and PM-flux linkage, which influence the FW performance. The slot opening, which influences the slot leakage of the fractional-slot machine, was also included as an additional optimising parameter in order to further fine-tune L_d.

Table 7.15. Key design parameters and performance metrics of optimal distributed and fractional-slot ferrite PMA SynRM designs

Parameter	6p36s	8p18s	8p18s
Tooth width - T_w (mm)	2.75	6.0	6.45
Back-iron thickness - H_y (mm)	6.10	5.40	4.825
Split ratio	0.571	0.615	0.605
Magnet depth - d_m (mm)	15.90	18.53	17.54
Magnet angle span - β_m (º elec.)	166.5	172.5	169.0
Middle section insulation ratio - k_{ins_mid}	0.456	0.550	0.504
Side section insulation ratio - k_{ins_side}	0.402	0.346	0.319
Middle barrier section span - α_m (mm)	12.50	9.82	10.16
Slot opening (mm)	2.0	4.20	4.35
Coil turn number - TN	7.0	6.5	6.0
Active axial length	105.0	105.0	117.0
Axial length including end-winding (mm)	164	152	164
Bridge thicknesses – inner to outer (mm)		0.6, 0.3, 0.3	
PM mass (kg)	0.50	0.74	0.72
L_d at T_c , ω_b (mH)	0.59	0.49	0.50
L_q at T_c , ω_b (mH)	2.37	1.22	1.26
Inductance difference at T_c , ω_b (mH)	1.78	0.73	0.77
Saliency ratio at T_c , ω_b	4.01	2.48	2.54
Phase resistance at 120ºC - R_{ph} (mΩ)	63.2	56.6	50.6
Peak current - I_{pk} (A,pk)	96.8	110.2	108.0
Rated current - I_{rated} (A,pk)	55.7	63.1	62.2
Line-Line back-EMF at ω_{ms} (V,pk)	157.2	180.0	179.0
Characteristic current - I_{ch} (A,pk)	53.8	55.6	55.3
I_{ch}/I_{rated}	0.97	0.88	0.89
Copper/rotor temperature at T_c , ω_b (ºC)	101.8 / 100.8	121.3 / 115.6	104.6/102.1
Copper/rotor temperature at T_{cms}, ω_{ms} (ºC)	59.9 / 76.9	65.8 / 93.5	62.3 /84.2

The energy loss components and efficiency over the NEDC and AUDC are compared in Figure 7.35 and Table 7.16 for the optimal fractional-slot and distributed winding PMA SynRM designs.
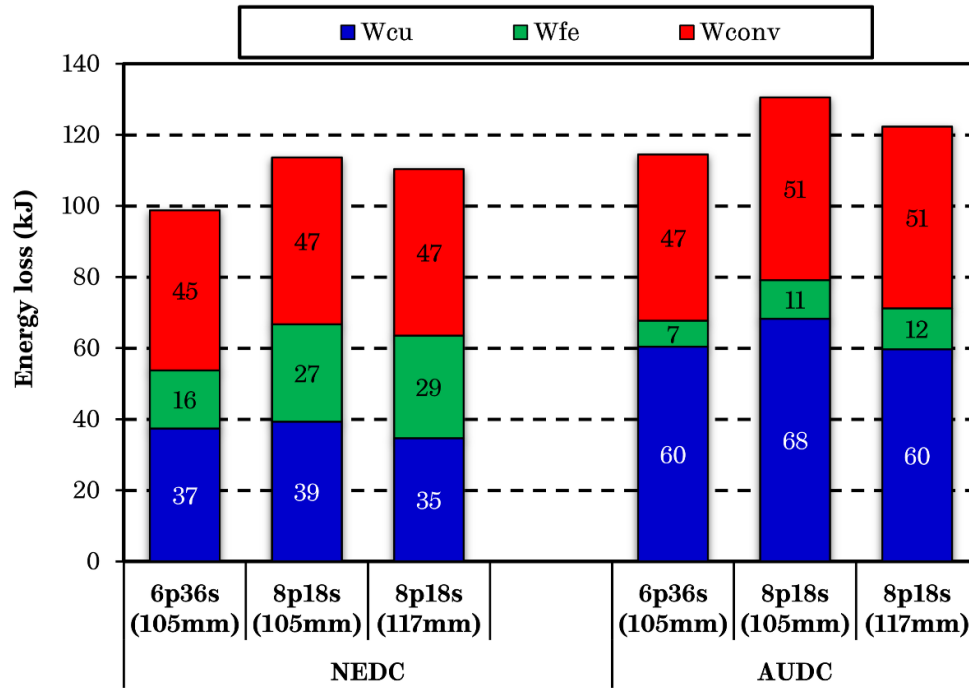
Figure 7.35. Comparisons of driving cycle energy loss components between optimal distributed and fractional-slot designs employing ferrite magnets.

Table 7.16. Energy efficiency comparison of optimal distributed and fractional-slot PMA SynRM designs against NEDC and AUDC driving cycles

Parameter	Ferrite (105mm)	8p18s (105mm)	8p18s (117mm)
Machine energy efficiency over NEDC	94.6%	93.4%	93.7%
System energy efficiency over NEDC	90.5%	89.2%	89.5%
Machine energy efficiency over AUDC	91.8%	90.6%	91.4%
System energy efficiency over AUDC	86.9%	85.3%	86.2%

Evidently, the fractional-slot PMA SynRM, optimised with the same active axial length as the distributed winding benchmark, exhibits ~1.3% and ~1.6% lower system energy efficiency over the NEDC and AUDC, respectively. This translates to

~15% higher energy losses over both driving cycles. The fundamental reasons behind this trend are the inferior reluctance torque capability and higher iron losses of the optimal fractional-slot design, both of which originate from its MMF harmonic content shown in Figure 7.32. Figure 7.36 demonstrates the ratio of absolute inductance difference between the 36-slot/6-pole and 18-slot/8-pole optimal PMA SynRM designs over the I_d and I_q range, where values >1 indicate a higher inductance difference for the 36-slot/6-pole design and vice versa. The d-q axis current trajectories of the two designs over the continuous and peak torque-speed envelopes are also illustrated in the inductance difference ratio map for comparative purposes.
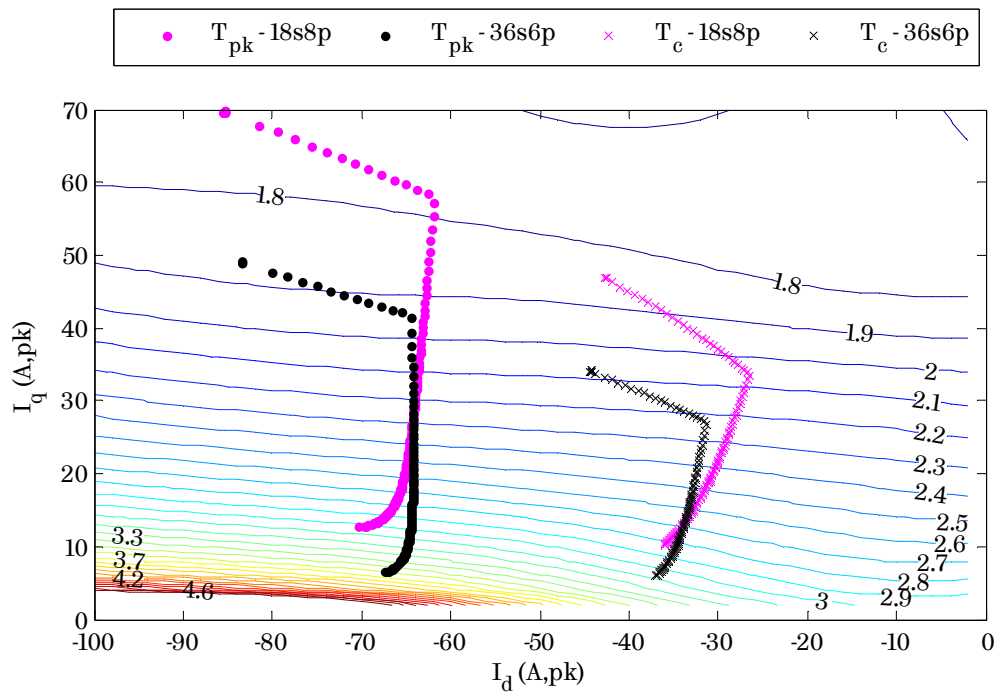
Figure 7.36. Ratio of absolute inductance difference between 36s6p and 18s8p PMA SynRM designs, overlaid by current trajectories over the T-N operating envelopes.

The 36-slot/6-pole PMA SynRM design exhibits superior reluctance torque capability over the entire d-q axis operating current range covering MTPA and FW operation, since for the same input current its inductance difference is about 2 to 3 times larger than the 18-slot/8-pole design. The ratio of inductance difference increases with lower q-axis current and remains virtually unchanged for different

d-axis current. This infers that the reluctance torque capability of the 36-slot/6-pole design becomes increasingly higher during low-load operation (such as in FW). The presence of low and high order asynchronous harmonics in the MMF spectrum of the 18-slot/8-pole design, albeit significantly less than conventional fractional-slot configurations (e.g., $q = 2/5$), pertain to a poor decoupling between the d- and q-axis [16], [36] leading to reduced magnetic anisotropy and inductance difference when compared with the distributed winding 36-slot/6-pole benchmark.

To compensate for the lower reluctance torque capability, the 18-slot/8-pole design uses more magnet material (~48%) than the 36-slot/6-pole design by having a higher split ratio as well as thicker magnets. The higher split ratio maximises the pole area, and apart from allowing for more magnet area, it also helps to enhance the reluctance torque capability. Nevertheless, as can be observed from Figure 7.36, due to its reduced magnetic anisotropy, the 18-slot/8-pole design still requires a higher phase current to deliver the torque demand. This leads to higher current-induced losses in both MTPA and FW modes of operation, despite its higher PM-flux and lower phase resistance.

Being a fractional-slot configuration, the 18-slot/8-pole PMA SynRM design exhibits an inherently high L_d. The inherently high L_d is what makes fractional-slot machines particularly attractive for extended speed applications due to their ability to easier counteract the PM-field by using less current during FW operation. However, this is typically the case with strong PMs, such as NdFeB, which produce a high magnetic flux. When paired with low-remanence magnets, such as ferrites, the fractional-slot machine with inherently high L_d may result entering into the maximum torque per volt (MTPV) mode too early, and thus being unable to deliver the required peak power at maximum cruise speed within the available DC-link voltage limit. Under these circumstances, the characteristic current ($I_{ch} = \psi_m/L_d$) becomes relatively low. On the other hand, due to the inherently poorer reluctance torque capability of the fractional-slot machine the rated current becomes relatively high.

Therefore, it becomes more challenging for the fractional-slot machine to achieve an appropriate I_{ch}/I_{rated} ratio, which is conducive to good FW capability

(that is necessary to achieve the required peak power at maximum cruise speed). This situation was evident in the design optimisation trend of the 18-slot/8-pole PMA SynRM for the investigated traction application. Therefore, to satisfy the required peak torque-speed envelope, the optimal 18-slot/8-pole design uses half turn less per coil than the 36-slot/6-pole benchmark to reduce its L_d (viz., inductance is square proportional to the number of turns), and also maximises the PM-volume in order to increase the PM-flux. In addition, to further reduce the L_d, the 18-slot/8-pole design uses a large slot opening (viz., slightly more than double compared with the 36-slot/6-pole design). The large slot opening, however, further penalises the reluctance torque capability as it limits the q-axis flux linkage and hence, the q-axis inductance.

Apart from satisfying the peak power at maximum cruise speed, the thermal limit under continuous operation at low speed (T_c, ω_b) should also be satisfied. The conflicting design requirements, pertaining to the investigated traction application, have resulted in the optimal 18-slot/8-pole ferrite PMA SynRM design slightly violating (by 1.3°C) the defined thermal limit of 120°C under continuous operation at base speed (viz., Table 7.15), which is thermally the worst operating condition of the PMA SynRM.

Under this operating condition, the 18-slot/8-pole design produces ~45W and ~15W higher copper and iron losses, respectively, than the 36-slot/6-pole benchmark. This is due to its poorer reluctance torque capability, and the combination of its MMF harmonic content and higher PM-flux, respectively. Hence, the higher copper and iron losses combined with the wider slot layout of the 18-slot/8-pole design result in a higher copper hot-spot temperature. It should be noted that if the same amount of losses are assigned to the thermal model of the 36-slot/6-pole design with different slot number and layout, the copper hot-spot temperature turns out ~6.5°C cooler than that of the 18-slot/8-pole design (for the same cooling setup), which validates the above assertion.

It has been demonstrated that for the same active space envelope, the optimal 36-slot/6-pole ferrite PMA SynRM design outperforms the optimal 18-slot/8-pole fractional-slot counterpart primarily due to its superior reluctance

torque capability. The 36-slot/6-pole benchmark produces ~15% lower system energy losses over both considered driving cycles and exhibits ~20°C cooler hot-spot temperature against the worst thermal operating condition, while using ~33% lower magnet material than the 18-slot/8-pole counterpart. Further, the 36-slot/6-pole design has a much lower rotor temperature under continuous operation at maximum cruise speed due to its inherently lower iron losses.

The 18-slot/8-pole design, however, being a fractional-slot configuration has about 12 mm shorter end-winding axial length, as can be seen from Table 7.15. Arguably, when the total machine axial length is considered (i.e., active plus end-winding axial lengths), the 18-slot/8-pole fractional-slot design would produce a higher torque density compared with the 36-slot/6-pole distributed winding benchmark. Therefore, to compare the two design configurations with the same total axial length, an additional design optimisation has been conducted with the 18-slot/8-pole configuration now having 12 mm longer active axial length. The cross-sections of the optimal 18-slot/8-pole designs with nominal (105mm) and extended (117mm) active axial lengths are compared in Figure 7.37. The key design parameters, energy loss components and efficiency over the NEDC and AUDC of the optimal 18-slot/8-pole design with extended active axial length are also given in Table 7.15, Figure 7.35 and Table 7.16 respectively, for comparison.
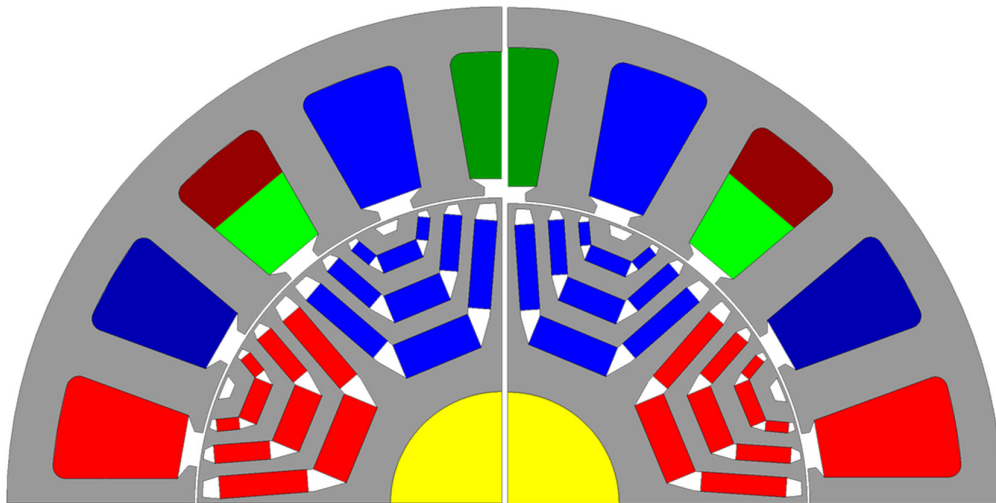
Figure 7.37. Cross-sections of optimal 18-slot/8-pole ferrite PMA SynRM designs with nominal (left) and extended (right) active axial lengths.

It can be observed from Figure 7.37 that the 18-slot/8-pole design with extended active axial length has narrower and taller slots, a smaller split ratio and thinner magnets (i.e., middle and side-section insulation ratios) than the 18-slot/8-pole design with nominal active axial length. The two designs have a comparable PM-usage and back-EMF, as the extended-length design uses half turn less per coil. Due to its lower turn number and a slightly larger slot area, however, the extended-length design exhibits ~11% lower phase resistance, which leads to a proportional decrease in the amount copper losses. The inductance difference of the extended-length design is marginally improved, due to the slightly thicker rotor flux guides. This results in the rated and peak operating phase currents to be marginally lower and is conducive to lower current-induced losses.

Therefore, the lower phase resistance, the slightly improved reluctance torque capability and increased contact surface with the cooling shell, enable the extended-length design to satisfy the worst-case thermal condition with margin as can be observed from Table 7.15. The cross-section of the optimal 18-slot/8-pole PMA SynRM design with extended active axial length is also compared with that of the 36-slot/6-pole benchmark in Figure 7.38. The two designs now have identical total (active plus end-winding) axial lengths. Compared with the distributed winding benchmark, the fractional-slot design still uses a higher split ratio, larger slot openings, a lower coil turn number and ~44% more magnet material.
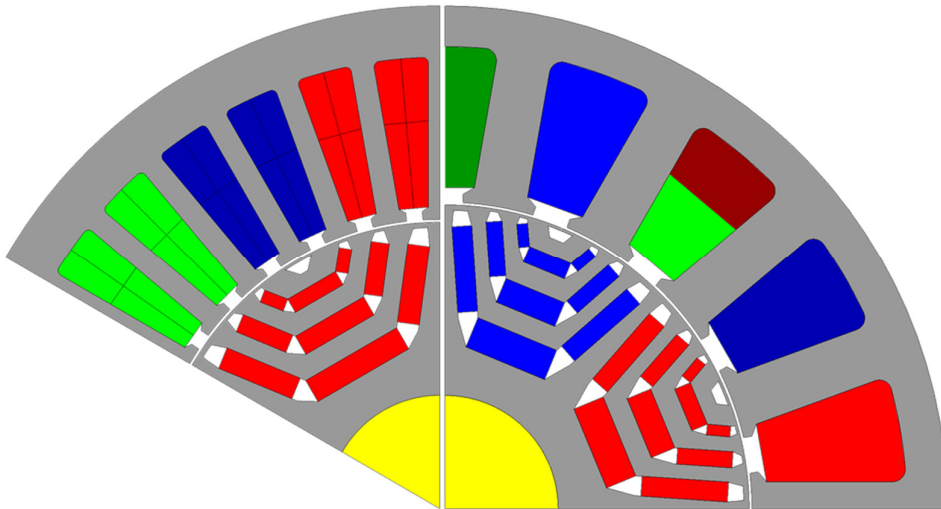
Figure 7.38. Comparison between distributed (left) and fractional-slot (right) optimal ferrite PMA SynRM designs with identical total (active + end-winding) axial length.

Figure 7.39 illustrates the system efficiency difference map between the distributed and extended-length fractional-slot winding PMA SynRM configurations, overlaid with the torque-speed envelopes and driving cycle representative operating points. Note that values higher than one indicate superior efficiency (in percentage) for the distributed winding PMA SynRM, and vice versa.
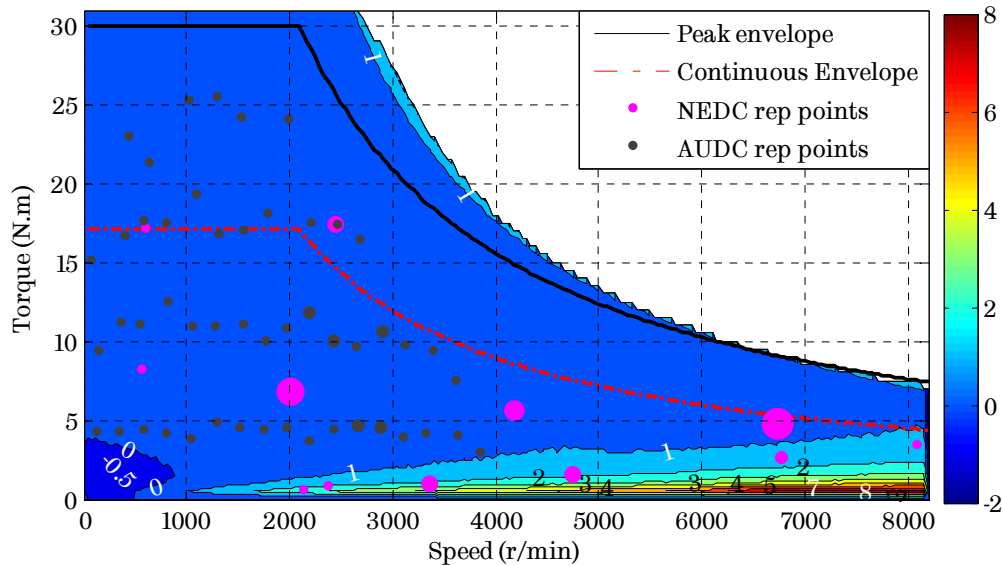
Figure 7.39. System energy efficiency-difference map between distributed and extended axial length fractional slot optimal designs.

It can be seen that the distributed winding benchmark achieves up to 1% higher system efficiency over most of the torque-speed operating range. However, the efficiency difference grows at the low torque, middle-to-high speed operating region, where the distributed winding exhibits inherently lower iron losses (viz., more dominant under these operating conditions), and also superior reluctance torque capability. The fact that half of the NEDC operating points reside in that operating region justifies the ~1% higher system energy efficiency of the distributed winding design over its fractional-slot counterpart, which is penalised by its higher iron losses and inferior reluctance torque capability.

On the other hand, for the case of the AUDC, the majority of representative operating points reside in the region where the efficiency difference is less than 1%, which explains the system energy efficiency difference of ~0.7% between the two

designs. Under these operating conditions, where iron losses are less dominant, the fractional-slot design reduces the efficiency gap against the distributed winding design primarily due to its lower phase resistance (~25%) and higher PM-flux (~14%) that partially compensates for its poorer reluctance torque capability. Nonetheless, the substantially superior reluctance torque capability of the distributed winding PMA SynRM enables it to produce lower inverter losses, which combined with its inherently lower iron losses, lead to a higher AUDC system energy efficiency as can be seen from Figure 7.35 and Table 7.16.

Based on the preceding analysis it can be deduced that the optimal ferrite PMA SynRM with distributed windings exhibits superior overall performance compared with the optimal fractional-slot counterpart for the investigated traction application. It produces higher system energy efficiency against both considered driving cycles while using a substantially lower magnet amount and having a considerably higher phase resistance. Its superior performance stems primarily from its substantially higher reluctance torque capability and inherently lower iron losses. It has been demonstrated that even if the active axial length of the fractional-slot design is extended, so as to achieve the same total axial length (active + end-winding) as the distributed winding counterpart, its performance (albeit slightly improved) is still inferior to the distributed winding PMA SynRM despite the much higher magnet usage. Moreover, it should be emphasised that the specific torque/power density of the extended-length fractional-slot design becomes inferior to that of the distributed winding design, due to the extra iron material, which also leads to an increase in the total machine cost.

7.5 Remarks

A versatile and effective multi-physics optimisation platform, enabling computationally efficient design optimisations of PM traction machines has been described. The optimisation platform maximises the system (traction machine + inverter) energy efficiency against a given driving cycle subject to a defined set of electrical, thermal and mechanical design constraints. It is shown that a multi-parameter (>10 parameters), multi-physics design optimisation can be completed in less than ~64 hours, due to the use of distributed computing, efficient

optimisation algorithms and analytical (FE-characterised) multi-physics evaluation models. The developed multi-physics optimisation platform is employed to conduct comprehensive topologic and parametric design optimisations of PMA SynRMs with the aim of assessing their viability for EV traction. The attained optimal designs are comprehensibly evaluated and compared against multiple indicative performance markers, including the energy efficiency against different driving cycles, reluctance torque capability, thermal behaviour, torque/power density and cost.

The first part of the study has investigated the multi-physics design optimisation of distributed winding PMA SynRMs employing characteristically different magnet materials in the rotor, namely, NdFeB and ferrite. Optimal rotor structures leading to minimisation of magnet usage, while leaving the remaining performance virtually unaffected, are identified for each magnet material type. It is shown that the use of different magnet materials in the rotor significantly influenced the selection of the leading design parameters during the optimisation process. Further, it is demonstrated that the PMA SynRM employing sintered NdFeB magnets is a better performer than the ferrite design for the investigated traction application. It provides a more extensive high-efficiency region leading to improved versatility when exhibited to more aggressive driving conditions. Also, it demonstrates enhanced thermal behaviour against the worst-case operating condition, and can achieve a higher torque/power density.

However, the viability of PMA SynRM with NdFeB for EV traction is largely penalised by the substantially inflated price of NdFeB magnets. The nearly double active material cost of the NdFeB design is not considered adequate to justify its performance improvement over the ferrite counterpart, particularly if the volatile NdFeB market continues to exist. Therefore, considering the trade-off between performance and cost, the ferrite PMA SynRM design, can indeed, comprise an attractive alternative solution for EV traction applications – particularly when its performance is optimised and evaluated against driving cycles, where in fact the traction machine most frequently operates throughout its lifetime. It is demonstrated that the ferrite PMA SynRM actually delivers nearly identical system energy efficiency to that of the NdFeB counterpart over the two standardised

driving cycles, namely, the former NEDC and the new WLTP. This is primarily attributed to its superior reluctance torque capability, under these operating conditions, which compensates for the low energy-density of the embedded ferrite magnets.

Having investigated the influence of different magnet materials in the rotor of the PMA SynRM, the second part of the study examined the viability of fractional-slot winding configurations in traction PMA SynRMs employing ferrite magnets in the rotor. The optimal fractional-slot PMA SynRM designs are compared against the distributed winding benchmark. It is shown that the distributed winding ferrite PMA SynRM exhibits superior overall performance than the fractional-slot counterpart for the investigated EV traction application, by producing a higher system energy efficiency against both considered driving cycles, while using a substantially lower magnet amount. The superior performance of the distributed winding PMA SynRM stems primarily from its considerably higher reluctance torque capability and inherently lower iron losses. Further, it is demonstrated that even if the active axial length of the fractional-slot PMA SynRM is extended, to achieve the same total axial length (active plus end-winding) as the distributed winding counterpart, its performance (albeit slightly improved) remains inferior despite the much higher magnet usage. Moreover, the extended-length fractional-slot design is penalised by a poorer specific torque/power density due to the additional electrical steel, which also leads to an increase in the total cost of the machine.

Chapter 8

General Conclusions and Future Work

8.1 General conclusions

An investigation into the performance of Permanent Magnet Assisted Synchronous Reluctance machines for electric vehicle applications is presented. The various aspects pertaining to the design of traction machines in particular over specified driving cycles are addressed and a computationally efficient technique, which enables to limit the large number of operating points of a driving cycle to a finite number of representative energy points, is proposed in Chapter 2. The technique substantially reduces the numerical FEA computation time required for performance evaluation over a cycle, and is applicable to any driving cycle and any electrical machine technology/topology. It is shown that a design optimised for a particular point, "rated point", may not necessarily correspond to a design optimised over a specific driving cycle. The research employs the specification requirements of small personal mobility city vehicles, and was undertaken as part of EU-funded projects, namely P-MOB and Hi-Wi.

In Chapter 3, a PMA SynRM is designed and optimised to meet the requirements of a small city vehicle (more specifically, FIAT 500). Best design practices pertaining to traction machines in general, and PMA SynRMs in particular are adopted. The multi-physical aspects of machine design/performance, i.e., electromagnetic, mechanical and thermal are considered in an engineer-in-the-loop iterative process. The design is optimised over a driving cycle represented by a finite number of operating points. It is shown that the PMA SynRM can meet the torque and speed requirements while achieving relatively high energy efficiencies over driving cycles, (~94.4% over the NEDC and ~92.8% over the AUDC). When compared to rare earth PM machines, it exhibits a competitive

continuous airgap shear stress of ~22 kPa and a torque density of ~14.3 Nm/Litre for air-cooled conditions.

In Chapter 4, a novel technique for the modelling of skew and the determination of the leading machine electromagnetic parameters is presented. The technique employs a single set of 2D FEA computations for the unskewed machine (i.e., single slice) from which the effect of a number of skew slices can be determined. It is shown that when compared with the so-called 2.5D multi-slice FEA a good agreement is achieved in a fraction of the computational time required for the 2.5D FEA. Furthermore, although the skew is primarily introduced to reduce torque ripple, its effect on the key electromagnetic parameters and performance of the machine are thoroughly investigated. It is shown that as expected skew affects the torque production of the machine, in particular the reluctance component with negligible effects on the PM component of the torque. Furthermore, efficiency is only slightly affected with the maximum of ~0.2% reduction within the continuous torque-speed operating region.

In Chapter 5, the effects of the finite length of the machine are investigated together with the axial leakage occurring after step skewing the rotor of the PMA SynRM machine. It is shown that the axial interaction between the skewed steps in the vicinity of their interface boundaries gives rise to additional leakage flux and results in a lower back-emf and torque capability compared to the 2.5D multislice FEA. Further, the torque ripple is considerably higher than the prediction from multi-slice 2.5D FEA. It is also shown that for the case of the unskewed PMA SynRM the effects of the finite length are much less significant. Therefore, the optimal skew angle may have to be determined using 3D FEA.

In Chapter 6, the effects of laser cutting the electrical steel laminations on the permeability of the stator core of the considered PMA SynRM are investigated. It is shown that thermal stresses exhibited by the lamination during the laser cutting process can have a significant effect on its magnetic properties, and thereby the resulting performance of the machine. It is demonstrated that the effects on the performance of the machine are primarily determined by the ratio of the cut length to the area of the steel. Furthermore, a method for estimating these effects on the

performance of the machine is proposed and a good agreement is reached when comparing between the predictions and measurements. These effects can have a significant impact on the performance of the machine, particularly those with distributed windings, which have a large number of stator teeth, as is the case with the investigated PMA SynRM.

In Chapter 7, a multi-physics approach employing a formal optimisation method is proposed. The method is applied for the topologic and parametric design and optimisation of a PMA SynRM to meet the same specification as the machine described in Chapter 3, which is optimised using best practice design methods. A ~0.5% improvement in energy efficiency over the NEDC can be achieved [65]. Table 8.1 summarises the performance of machines optimised using the manual (Chapter 3) and formal (Chapter 7) optimisation method under the same volumetric and multi-physical design constraints, and torque-speed requirements indicated in Chapters 3 and 7. The same airgap length of 0.35mm is employed for the design of all machine topologies. The schematic of each topology listed in Table 8.1 is shown in Figure 8.1 and Figure 8.2 for reference. It can be seen that a properly optimised PMA SynRM employing ferrite magnets can compete with machine topologies employing rare earth sintered permanent magnets in terms of torque/power density and energy efficiency over distinctively different driving cycles.

Table 8.1. Performance comparison between traction machine topologies optimised against the NEDC using the described formal optimisation method

Parameter	PMASynRM circular manual opt.	PMASynRM circular formal opt.	PMASynRM rectangular ferrite	PMASynRM rectangular sint. NdFeB	IPMSM v-shaped sint. NdFeB
Continuous torque			14.3		
$W_{copper_{NEDC}}$ **(kJ)**	37.0	32.9	37.4	34.6	37.8
$W_{iron_{NEDC}}$ **(kJ)**	19.3	19.1	16.4	20.3	24.5
$W_{converter_{NEDC}}$ **(kJ)**	43.4	44.2	45.0	43.6	44.1
PM material	Bonded NdFeB	Bonded NdFeB	Ferrite	Sintered NdFeB	Sintered NdFeB
PM mass (kg)	0.66	0.58	0.50	0.19	0.28
$\eta_{machine_{NEDC}}$	94.4%	94.8%	94.6%	94.5%	93.8%
$\eta_{system_{NEDC}}$	90.4%	90.7%	90.5%	90.5%	89.9%
$\eta_{machine_{AUDC}}$	92.8%	92.8%	91.8%	92.7%	92.0%
$\eta_{system_{AUDC}}$	88.1%	88.0%	86.9%	88.0%	87.2%

* The results correspond to a magnet temperature of 100ºC and a winding temperature of 120ºC.
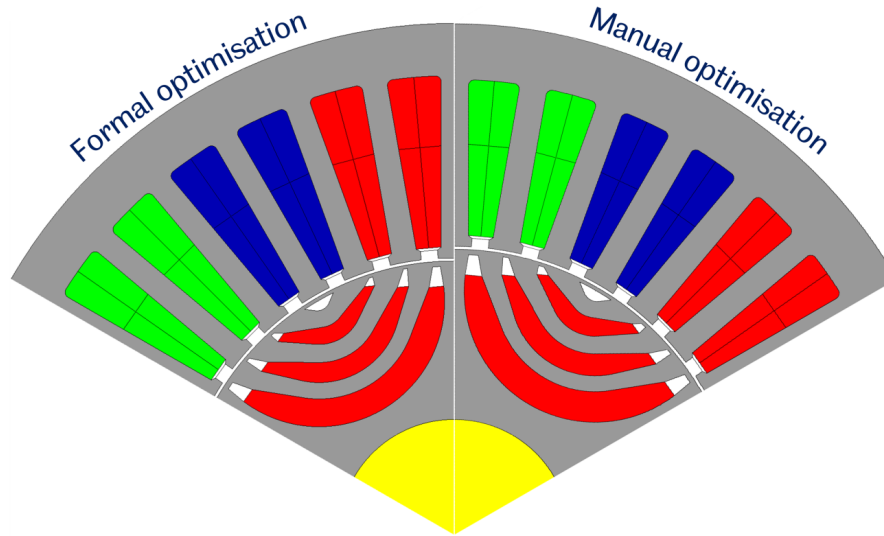
Figure 8.1. Schematics of NEDC-optimised PMA SynRM designs employing bonded NdFeB, obtained from manual and formal optimisation methods.
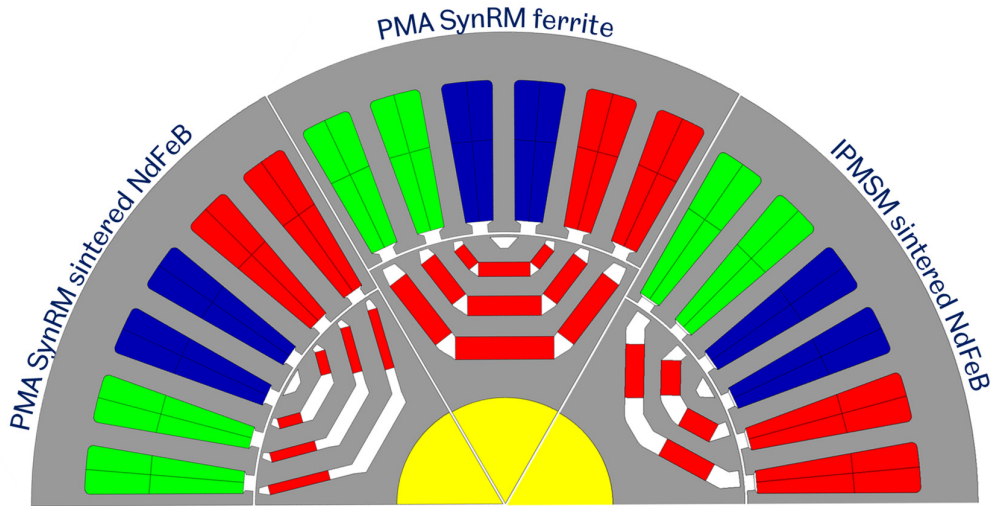
Figure 8.2. Schematics of NEDC-optimised machine topologies with different magnet materials obtained from formal optimisation.

8.2 Future work

The proposed technique for the determination of the energy-representative operating points of a driving cycle still requires manual manipulation. Therefore, a technique, which completely automates the process for any driving cycle and any reference efficiency map, should be developed, for example by employing machine-learning techniques.

The multi-physics optimisation method can be extended to more than one machine in order to cater for distributed traction drivetrain topologies, where the effect of a dynamic torque distribution strategy can be simultaneously taken into consideration in the determination of the optimal energy efficiency of the combined drivetrain.

Investigate the electromechanical interactions between the PMA SynRM and the mechanical components of the drivetrain in order to understand the effects of the operating conditions on the mechanically induced static and dynamic eccentricity and the resulting unbalanced magnetic pull.

Undertake an in-depth investigation on the effects of the cutting processes on the magnetic properties of electrical lamination material and model their effects on the performance of electrical machines. The work should first be experimentally extensive employing a large number of measurement samples obtained through different cutting processes.

References

[1] C. C. Chan, 'An overview of electric vehicle technology', *Proceedings of the IEEE*, vol. 81, no. 9, pp. 1202–1213, Sep. 1993.

[2] C. C. Chan, 'The State of the Art of Electric, Hybrid, and Fuel Cell Vehicles', *Proceedings of the IEEE*, vol. 95, no. 4, pp. 704–718, Apr. 2007.

[3] BP Energy Economics, 'BP Energy Outlook', BP, 2018.

[4] 'BP Statistical Review of World Energy', BP, 66th edition, 2017.

[5] P. J. Landrigan *et al.*, 'The Lancet Commission on pollution and health', *The Lancet*, vol. 391, no. 10119, pp. 462–512, Feb. 2018.

[6] 'Air quality in Europe — 2017 report', European Environment Agency, Air quality in Europe — 2017 report, 2017.

[7] 'Transport in Europe: key facts and trends', European Environment Agency, 2016.

[8] 'Final energy consumption by mode of transport', European Environment Agency, 2017.

[9] 'Monitoring progress of Europe's transport sector towards its environment, health and climate objectives', European Environment Agency, 2018.

[10] 'FROM LABORATORY TO ROAD A 2014 UPDATE OF OFFICIAL AND "REAL-WORLD" FUEL CONSUMPTION AND CO2 VALUES FOR PASSENGER CARS IN EUROPE', ICCT, TNO, IFEU, 2014.

[11] C. C. Chan, 'The State of the Art of Electric, Hybrid, and Fuel Cell Vehicles', *Proceedings of the IEEE*, vol. 95, no. 4, pp. 704–718, Apr. 2007.

[12] C. C. Chan, A. Bouscayrol, and K. Chen, 'Electric, Hybrid, and Fuel-Cell Vehicles: Architectures and Modeling', *IEEE Transactions on Vehicular Technology*, vol. 59, no. 2, pp. 589–598, Feb. 2010.

[13] 'Electric vehicles and the energy sector - impacts on Europe's future emissions', European Environment Agency, 2017.

[14] 'Global EV outlook 2017', International Energy Agency, 2017.

[15] Xibo Yuan and Jiabin Wang, 'Torque Distribution Strategy for a Front- and Rear-Wheel-Driven Electric Vehicle', *IEEE Transactions on Vehicular Technology*, vol. 61, no. 8, pp. 3365–3374, Oct. 2012.

[16] Y. Honda, T. Nakamura, T. Higaki, and Y. Takeda, 'Motor design considerations and test results of an interior permanent magnet synchronous motor for electric vehicles', 1997, vol. 1, pp. 75–82.

[17] H. Neudorfer, N. Wicker, and A. Binder, 'Comparison of three different electric powertrains for the use in hybrid electric vehicles', 2008.

[18] H. Neudorfer, 'Comparison of three different electric powertrains for the use in high performance Electric Go-Kart', 2007, pp. 21–26.

[19] K. T. Chau, C. C. Chan, and C. Liu, 'Overview of permanent-magnet brushless drives for electric and hybrid electric vehicles', *Industrial Electronics, IEEE Transactions on*, vol. 55, no. 6, pp. 2246–2257, 2008.

[20] Z. Q. Zhu and D. Howe, 'Electrical Machines and Drives for Electric, Hybrid, and Fuel Cell Vehicles', *Proceedings of the IEEE*, vol. 95, no. 4, pp. 746–765, Apr. 2007.

[21] Morrison, A. Binder, B. Funieru, and C. Sabirin, 'Drive train design for medium-sized zero emission electric vehicles', in *13th European Conference on Power Electronics and Applications*, Barcelona, Spain, 2009, pp. 1–10.

[22] C. C. Pavel *et al.*, 'Role of substitution in mitigating the supply pressure of rare earths in electric road transport applications', *Sustainable Materials and Technologies*, vol. 12, pp. 62–72, Jul. 2017.

[23] S. Kozawa, 'Trends and Problems in Research of Permanent Magnets for Motors-Addressing Scarcity Problem of Rare Earth Elements', *Science and Technology Trends*, vol. Quarterly Review, no. 38, pp. 40–54, 2011.

[24] Y. Zhang *et al.*, 'Coercivity enhancement of Nd–Fe–B sintered magnets with intergranular adding (Pr, Dy, Cu)–Hx powders', *Journal of Magnetism and Magnetic Materials*, vol. 399, pp. 159–163, Feb. 2016.

[25] J. D. Widmer, R. Martin, and M. Kimiabeigi, 'Electric vehicle traction motors without rare earth magnets', *Sustainable Materials and Technologies*, vol. 3, pp. 7–13, Apr. 2015.

[26] K. Bourzac, 'The Rare-Earth Crisis', MIT Technology Review, 2011.

[27] A. Brumme, *Wind energy deployment and the relevance of rare earths: an economic analysis*, Aufl. 2014. Wiesbaden: Springer Gabler, 2014.

[28] K. Smith Stegen, 'Heavy rare earths, permanent magnets, and renewable energies: An imminent crisis', *Energy Policy*, vol. 79, pp. 1–8, Apr. 2015.

[29] J. M. Miller, 'Electric Motor R&D', Oak Ridge National Laboratory, 2013 U.S. DOE Hydrogen and Fuel Cells Program and Vehicle Technologies Program Annual Merit Review and Peer Evaluation Meeting, 2013.

[30] A. M. Bazzi, 'Electric machines and energy storage technologies in EVs and HEVs for over a century', 2013, pp. 212–219.

[31] 'Global Analysis of Electric Traction Motor Technologies for Electric and Hybrid Vehicles', Frost & Sullivan, Market Research Report, 2016.

[32] P. Harrop and J. Harrop, 'Electric Motors for Electric Vehicles 2018-2028 Traction motors, motor generators, boost recuperation machines, BSG, ISG for 48V MH, strong hybrid, pure electric, EIV: land, water, air', IDTechEx, 2018.

[33] S. Constantinides, 'Market Outlook for Ferrite, Rare Earth and other Permanent Magnets', in *International forum on magnetic applications*, Jacksonville, FL, 2016.

[34] J. D. Pedarnig, 'Application of laser-induced breakdown spectroscopy to the analysis of secondary materials in industrial production', in *Laser Spectroscopy for Sensing*, Elsevier, 2014, pp. 496–521.

[35] S. Morimoto, M. Sanada, and Y. Takeda, 'Performance of PM-assisted synchronous reluctance motor for high-efficiency and wide constant-power operation', *IEEE Transactions on Industry Applications*, vol. 37, no. 5, pp. 1234–1240, Sep. 2001.

[36] S. Ooi, S. Morimoto, M. Sanada, and Y. Inoue, 'Performance Evaluation of a High-Power-Density PMASynRM With Ferrite Magnets', *IEEE Transactions on Industry Applications*, vol. 49, no. 3, pp. 1308–1315, May 2013.

[37] H. Cai, B. Guan, and L. Xu, 'Low-Cost Ferrite PM-Assisted Synchronous Reluctance Machine for Electric Vehicles', *IEEE Transactions on Industrial Electronics*, vol. 61, no. 10, pp. 5741–5748, Oct. 2014.

[38] I. Boldea, L. N. Tutelea, L. Parsa, and D. Dorrell, 'Automotive Electric Propulsion Systems With Reduced or No Permanent Magnets: An Overview', *IEEE Transactions on Industrial Electronics*, vol. 61, no. 10, pp. 5696–5711, Oct. 2014.

[39] T. Buress, 'Benchmarking State-of-the-Art Technologies', Oak Ridge National Laboratory, 2013.

[40] M. Kimiabeigi, J. D. Widmer, N. J. Baker, R. Martin, B. C. Mecrow, and A. Michaelides, 'Three-Dimensional Modelling of Demagnetization and Utilization of Poorer Magnet Materials for EV/HEV Applications', *IEEE Transactions on Energy Conversion*, vol. 31, no. 3, pp. 981–992, Sep. 2016.

[41] P. Lazari, J. Wang, and L. Chen, 'A Computationally Efficient Design Technique for Electric-Vehicle Traction Machines', *IEEE Transactions on Industry Applications*, vol. 50, no. 5, pp. 3203–3213, Sep. 2014.

[42] V. T. Buyukdegirmenci, A. M. Bazzi, and P. T. Krein, 'Evaluation of Induction and Permanent Magnet Synchronous Machines Using Drive-Cycle Energy and Loss Minimization in Traction Applications', *IEEE Transactions on Industry Applications*, vol. 50, no. 1, pp. 395–403, 2014.

[43] Z. Q. Zhu and C. C. Chan, 'Electrical machine topologies and technologies for electric, hybrid, and fuel cell vehicles', in *Proceedings of the IEEE VPPC Conference*, 2008, pp. 1–6.

[44] S. Kreuawan, F. Gillon, and P. Brochet, 'Comparative study of design approach for electric machine in traction application', *International Review of Electrical Engineering*, vol. 3, no. 3, pp. 455–465, Jun. 2008.

[45] J. de Santiago *et al.*, 'Electrical Motor Drivelines in Commercial All-Electric Vehicles: A Review', *IEEE Transactions on Vehicular Technology*, vol. 61, no. 2, pp. 475–484, Feb. 2012.

[46] E. Sulaiman, T. Kosaka, and N. Matsui, 'Design and Performance of 6-slot 5-pole PMFSM with Hybrid Excitation for Hybrid Electric Vehicle Applications', presented at the International Power Electronics Conference, 2010, pp. 1962–1968.

[47] D. Gerling, G. Dajaku, and K. Muhlbauer, 'Cost-Effective Electric Traction Drive with High Efficiency at Low-Load Operation', 2010, pp. 1–6.

[48] G. Pellegrino, A. Vagati, B. Boazzo, and P. Guglielmi, 'Comparison of Induction and PM Synchronous Motor Drives for EV Application Including Design Examples', *IEEE Transactions on Industry Applications*, vol. 48, no. 6, pp. 2322–2332, Nov. 2012.

[49] A. R. Tariq, C. E. Nino-Baron, and E. G. Strangas, 'Design and analysis of PMSMs for HEVs based upon average driving cycle efficiency', in *Electric Machines & Drives Conference (IEMDC), 2011 IEEE International*, 2011, pp. 218–223.

[50] E. Hoang, M. Lecrivain, S. Hlioui, and M. Gabsi, 'Hybrid excitation synchronous permanent magnets synchronous machines optimally designed for hybrid and full electrical vehicle', in *IEEE 8th International Conference on Power Electronics and ECCE Asia (ICPE & ECCE)*, 2011, pp. 153–160.

[51] P. H. Nguyen, E. Hoang, and M. Gabsi, 'Performance Synthesis of Permanent-Magnet Synchronous Machines During the Driving Cycle of a Hybrid Electric Vehicle', *IEEE Transactions on Vehicular Technology*, vol. 60, no. 5, pp. 1991–1998, 2011.

[52] 'Emission Test Cycles for the Certification of Light Duty Vehicles in Europe', in *EEC Directive 90/C81/01*, 2009.

[53] X. Chen, 'Modelling and Design of Permanent-magnet Machines for Electric Vehicle Traction', PhD thesis, The University of Sheffield, 2015.

[54] S. Shahidinejad, E. Bibeau, and S. Filizadeh, 'Statistical Development of a Duty Cycle for Plug-in Vehicles in a North American Urban Setting Using Fleet Information', *IEEE Transactions on Vehicular Technology*, vol. 59, no. 8, pp. 3710–3719, Oct. 2010.

[55] W. Rui and S. M. Lukic, 'Review of driving conditions prediction and driving style recognition based control algorithms for hybrid electric vehicles', in *IEEE Vehicle Power and Propulsion Conference (VPPC)*, 2011, pp. 1–7.

[56] A. Jaafar, B. Sareni, and X. Roboam, 'A Systemic Approach Integrating Driving Cycles for the Design of Hybrid Locomotives', 2013.

[57] G. Souffran, L. Miegeville, and P. Guerin, 'Simulation of Real-World Vehicle Missions Using a Stochastic Markov Model for Optimal Powertrain Sizing', *IEEE Transactions on Vehicular Technology*, vol. 61, no. 8, pp. 3454–3465, Oct. 2012.

[58] A. M. EL-Refaie and T. M. Jahns, 'Optimal flux weakening in surface PM machines using fractional-slot concentrated windings', *IEEE Transactions on Industry Applications*, vol. 41, pp. 790–800, 2005.

[59] J. Wang, X. Yuan, and K. Atallah, 'Design Optimization of a Surface-Mounted Permanent-Magnet Motor With Concentrated Windings for Electric Vehicle Applications', *IEEE Transactions on Vehicular Technology*, vol. 62, no. 3, pp. 1053–1064, Mar. 2013.

[60] Jiabin Wang, K. Atallah, Z. Q. Zhu, and D. Howe, 'Modular Three-Phase Permanent-Magnet Brushless Machines for In-Wheel Applications', *IEEE Transactions on Vehicular Technology*, vol. 57, no. 5, pp. 2714–2720, Sep. 2008.

[61] A. M. EL-Refaie and T. M. Jahns, 'Scalability of Surface PM Machines With Concentrated Windings Designed to Achieve Wide Speed Ranges of Constant-Power Operation', *IEEE Transactions On Energy Conversion*, vol. 21, no. 2, pp. 362–368, 2006.

[62] J. Wang and D. Howe, 'Design Optimization of Radially Magnetized, Iron-Cored, Tubular Permanent-Magnet Machines and Drive Systems', *IEEE Transactions on Magnetics*, vol. 40, no. 5, pp. 3262–3277, Sep. 2004.

[63] J. Wang, K. Atallah, R. Chin, W. M. Arshad, and H. Lendenmann, 'Rotor Eddy-Current Loss in Permanent-Magnet Brushless AC Machines', *IEEE Transactions on Magnetics*, vol. 46, pp. 2701–2707, 2010.

[64] N. Bianchi, S. Bolognani, and E. Fornasiero, 'An Overview of Rotor Losses Determination in Three-Phase Fractional-Slot PM Machines', *IEEE Transactions on Industry Applications*, vol. 46, pp. 2338–2345, 2010.

[65] P. Lazari, J. Wang, L. Chen, and X. Chen, 'Design optimisation and performance evaluation of a rare-earth-free Permanent Magnet Assisted Synchronous Reluctance Machine for electric vehicle traction', presented at the 7th IET International Conference on Power Electronics, Machines and Drives (PEMD 2014), 2014, pp. 1–6.

[66] L. Chen, P. Lazari, and J. Wang, 'Optimal power split ratio of a distributed electric vehicle traction system', in *7th IET International Conference on Power Electronics, Machines and Drives (PEMD 2014)*, 2014, pp. 1–6.

[67] L. Chen, D. Hopkinson, J. Wang, A. Cockburn, M. Sparkes, and W. O'Neill, 'Reduced Dysprosium Permanent Magnets and Their Applications in Electric Vehicle Traction Motors', *IEEE Transactions on Magnetics*, vol. 51, no. 11, pp. 1–4, Nov. 2015.

[68] J. Wang, V. I. Patel, and W. Wang, 'Fractional-Slot Permanent Magnet Brushless Machines with Low Space Harmonic Contents', *IEEE Transactions on Magnetics*, vol. 50, no. 1, pp. 1–9, Jan. 2014.

[69] M. Ferrari, N. Bianchi, and E. Fornasiero, 'Analysis of Rotor Saturation in SynchronousReluctance and PM Assisted Reluctance Motors', *IEEE Transactions on Industry Applications*, vol. PP, no. 99, pp. 1–1, 2014.

[70] N. Bianchi, 'Synchronous reluctance and interior permanent magnet motors', 2013, pp. 75–84.

[71] H. Murakami, Y. Honda, Y. Sadanaga, Y. Ikkai, S. Morimoto, and Y. Takeda, 'Optimum design of highly efficient magnet assisted reluctance motor', 2001, vol. 4, pp. 2296–2301.

[72] J. H. Lee, J. C. Kim, and D.-S. Hyun, 'Effect analysis of magnet on Ld and Lq inductance of permanent magnet assisted synchronous reluctance motor using finite element method', *Magnetics, IEEE Transactions on*, vol. 35, no. 3, pp. 1199–1202, 1999.

[73] T. M. Jahns and V. Caliskan, 'Uncontrolled generator operation of interior PM synchronous machines following high-speed inverter shutdown', *IEEE Transactions on Industry Applications*, vol. 35, no. 6, pp. 1347–1357, Dec. 1999.

[74] G. Pellegrino, A. Vagati, and P. Guglielmi, 'Design Tradeoffs Between Constant Power Speed Range, Uncontrolled Generator Operation, and Rated Current of IPM Motor Drives', *IEEE Transactions on Industry Applications*, vol. 47, no. 5, pp. 1995–2003, Sep. 2011.

[75] M. Barcaro, N. Bianchi, and F. Magnussen, 'Permanent-magnet optimization in permanent-magnet-assisted synchronous reluctance motor for a wide constant-power speed range', *Industrial Electronics, IEEE Transactions on*, vol. 59, no. 6, pp. 2495–2502, 2012.

[76] M. André, 'The ARTEMIS European driving cycles for measuring car pollutant emissions', *Science of The Total Environment*, vol. 334–335, pp. 73–84, Dec. 2004.

[77] M. André, R. Joumard, R. Vidon, P. Tassel, and P. Perret, 'Real-world European driving cycles, for measuring pollutant emissions from high- and low-powered cars', *Atmospheric Environment*, vol. 40, no. 31, pp. 5944–5953, Oct. 2006.

[78] E. Carraro and N. Bianchi, 'Design and comparison of interior permanent magnet synchronous motors with non-uniform airgap and conventional rotor for electric vehicle applications', *IET Electric Power Applications*, vol. 8, no. 6, pp. 240–249, Jul. 2014.

[79] T. Tokuda, M. Sanada, and S. Morimoto, 'Influence of rotor structure on performance of permanent magnet assisted synchronous reluctance motor', 2009, pp. 1–6.

[80] J. K. Tangudu and T. M. Jahns, 'Comparison of interior PM machines with concentrated and distributed stator windings for traction applications', 2011, pp. 1–8.

[81] J. K. Tangudu, T. M. Jahns, and A. El-Refaie, 'Unsaturated and saturated saliency trends in fractional-slot concentrated-winding interior permanent magnet machines', 2010, pp. 1082–1089.

[82] P. B. Reddy, A. M. El-Refaie, K.-K. Huh, J. K. Tangudu, and T. M. Jahns, 'Comparison of Interior and Surface PM Machines Equipped With Fractional-Slot Concentrated Windings for Hybrid Traction Applications', *IEEE Transactions on Energy Conversion*, vol. 27, no. 3, pp. 593–602, Sep. 2012.

[83] S.-H. Han, W. L. Soong, T. M. Jahns, M. K. Güven, and M. S. Illindala, 'Reducing Harmonic Eddy-Current Losses in the Stator Teeth of Interior Permanent Magnet Synchronous Machines During Flux Weakening', *IEEE Transactions on Energy Conversion*, vol. 25, no. 2, pp. 441–449, Jun. 2010.

[84] K. Wang, Z. Q. Zhu, G. Ombach, M. Koch, S. Zhang, and J. Xu, 'Optimal slot/pole and flux-barrier layer number combinations for synchronous reluctance machines', 2013, pp. 1–8.

[85] T. Matsuo and T. A. Lipo, 'Rotor Design Optimization of Synchronous Reluctance Machine', p. 7.

[86] W. Q. Chu and Z. Q. Zhu, 'Investigation of Torque Ripples in Permanent Magnet Synchronous Machines With Skewing', *IEEE Transactions on Magnetics*, vol. 49, no. 3, pp. 1211–1220, Mar. 2013.

[87] P. Alotto, M. Barcaro, N. Bianchi, and M. Guarnieri, 'Optimization of Interior PM Motors With Machaon Rotor Flux Barriers', *IEEE Transactions on Magnetics*, vol. 47, no. 5, pp. 958–961, May 2011.

[88] N. Bianchi, S. Bolognani, D. Bon, and M. Dai Pre, 'Rotor Flux-Barrier Design for Torque Ripple Reduction in Synchronous Reluctance and PM-Assisted Synchronous Reluctance Motors', *IEEE Transactions on Industry Applications*, vol. 45, no. 3, pp. 921–928, 2009.

[89] M. Obata, S. Morimoto, M. Sanada, and Y. Inoue, 'Performance evaluation of high power and low torque ripple structure of rare-earth free PMASynRM with ferrite magnet', 2013, pp. 714–719.

[90] Y. Kano, T. Terahai, T. Kosaka, N. Matsui, and T. Nakanishi, 'A new flux-barrier design of torque ripple reduction in saliency-based sensorless drive IPM motors for general industrial applications', 2009, pp. 1939–1945.

[91] C. M. Spargo, B. C. Mecrow, and J. D. Widmer, 'A Seminumerical Finite-Element Postprocessing Torque Ripple Analysis Technique for Synchronous Electric Machines Utilizing the Air-Gap Maxwell Stress Tensor', *IEEE Transactions on Magnetics*, vol. 50, no. 5, pp. 1–9, May 2014.

[92] *Motor-CAD version 8.3.8 user manual*. Motor Design Limited, 2015.

[93] A. Vagati, B. Boazzo, P. Guglielmi, and G. Pellegrino, 'Design of Ferrite-Assisted Synchronous Reluctance Machines Robust Toward Demagnetization', *IEEE Transactions on Industry Applications*, vol. 50, no. 3, pp. 1768–1779, May 2014.

[94] P. Lazari, B. SEN, J. Wang, and X. Chen, 'Accurate d-q Axis Modeling of Synchronous Machines With Skew Accounting for Saturation', *IEEE Transactions on Magnetics*, vol. 50, no. 11, pp. 1–4, Nov. 2014.

[95] F. Piriou and A. Razek, 'A model for coupled magnetic-electric circuits in electric machines with skewed slots', *Magnetics, IEEE Transactions on*, vol. 26, no. 2, pp. 1096–1100, 1990.

[96] S. Williamson, T. J. Flack, and A. F. Volschenk, 'Representation of skew in time-stepped two-dimensional finite-element models of electrical machines', *IEEE Transactions on Industry Applications*, vol. 31, no. 5, pp. 1009–1015, Oct. 1995.

[97] H. De Gersem, K. Hameyer, and T. Weiland, 'Skew interface conditions in 2-D finite-element machine models', *IEEE Transactions on Magnetics*, vol. 39, no. 3, pp. 1452–1455, May 2003.

[98] Y. S. Chen, Z. Q. Zhu, and D. Howe, 'Calculation of d- and q-axis inductances of PM brushless ac machines accounting for skew', *IEEE Transactions on Magnetics*, vol. 41, no. 10, pp. 3940–3942, Oct. 2005.

[99] G. Qi, J. T. Chen, Z. Q. Zhu, D. Howe, L. B. Zhou, and C. L. Gu, 'Influence of Skew and Cross-Coupling on Flux-Weakening Performance of Permanent-Magnet Brushless AC Machines', *IEEE Transactions on Magnetics*, vol. 45, no. 5, pp. 2110–2117, May 2009.

[100] S. Williamson and C. I. McClay, 'The effect of axial variations in saturation due to skew on induction motor equivalent-circuit parameters', *IEEE Transactions on Industry Applications*, vol. 35, no. 6, pp. 1323–1331, Dec. 1999.

[101] E. C. Lovelace, T. M. Jahns, and J. H. Lang, 'A saturating lumped-parameter model for an interior PM synchronous machine', *IEEE Transactions on Industry Applications*, vol. 38, no. 3, pp. 645–650, Jun. 2002.

[102] P. Lazari, J. Wang, and B. Sen, '3-D Effects of Rotor Step-Skews in Permanent Magnet-Assisted Synchronous Reluctance Machines', *IEEE Transactions on Magnetics*, vol. 51, no. 11, pp. 1–4, Nov. 2015.

[103] H.-S. Chen, D. G. Dorrell, and M.-C. Tsai, 'Design and Operation of Interior Permanent-Magnet Motors With Two Axial Segments and High Rotor Saliency', *IEEE Transactions on Magnetics*, vol. 46, no. 9, pp. 3664–3675, Sep. 2010.

[104] N. Bianchi and S. Bolognani, 'Design techniques for reducing the cogging torque in surface-mounted PM motors', *IEEE Transactions on Industry Applications*, vol. 38, no. 5, pp. 1259–1265, Sep. 2002.

[105] R. Islam, I. Husain, A. Fardoun, and K. McLaughlin, 'Permanent-Magnet Synchronous Motor Magnet Designs With Skewing for Torque Ripple and Cogging Torque Reduction', *IEEE Transactions on Industry Applications*, vol. 45, no. 1, pp. 152–160, 2009.

[106] 'Klausnitzer and Moeckel - 2013 - Methods for calculation of skewed permanent magnet.pdf'. .

[107] *FLUX version 11.2 user manual*. CEDRAT, 2013.

[108] W. Q. Chu and Z. Q. Zhu, 'Reduction of On-Load Torque Ripples in Permanent Magnet Synchronous Machines by Improved Skewing', *IEEE Transactions on Magnetics*, vol. 49, no. 7, pp. 3822–3825, Jul. 2013.

[109] P. Lazari, K. Atallah, and J. Wang, 'Effect of Laser Cut on the Performance of Permanent Magnet Assisted Synchronous Reluctance Machines', *IEEE Transactions on Magnetics*, vol. 51, no. 11, pp. 1–4, Nov. 2015.

[110] W. M. Arshad *et al.*, 'Incorporating lamination processing and component manufacturing in electrical machine design tools', 2007, pp. 94–102.

[111] M. Bali, H. De Gersem, and A. Muetze, 'Finite-Element Modeling of Magnetic Material Degradation Due to Punching', *IEEE Transactions on Magnetics*, vol. 50, no. 2, pp. 745–748, Feb. 2014.

[112] A. Schoppa and J. Schneider, 'Influence of the manufacturing process on the magnetic properties of non-oriented electrical steels', *Journal of Magnetism and Magnetic Materials*, p. 5, 2000.

[113] R. Siebert, J. Schneider, and E. Beyer, 'Laser Cutting and Mechanical Cutting of Electrical Steels and its Effect on the Magnetic Properties', *IEEE Transactions on Magnetics*, vol. 50, no. 4, pp. 1–4, Apr. 2014.

[114] R. Siebert, A. Wetzig, E. Beyer, B. Betz, C. Grunzweig, and E. Lehmann, 'Localized investigation of magnetic bulk property deterioration of electrical steel: Analysing magnetic property drop thorough mechanical and laser cutting of electrical steel laminations using neutron grating interferometry', in *Electric Drives Production Conference (EDPC), 3rd International*, 2013, pp. 1–5.

[115]   G. Loisos and A. J. Moses, 'Effect of mechanical and Nd:YAG laser cutting on magnetic flux distribution near the cut edge of non-oriented steels', *Journal of Materials Processing Technology*, vol. 161, no. 1–2, pp. 151–155, Apr. 2005.

[116]   J. Schneider, A. M. Fernandez, E. Gomes, M. Schmidtchen, and Y. Houbaert, 'Deterioration of the magnetic properties in fesi strips after cutting by laser or by mechanical cutting', in *Proceedings ICPNS*, 2010, pp. 1–6.

[117]   S. Steentjes, G. von Pfingsten, and K. Hameyer, 'An Application-Oriented Approach for Consideration of Material Degradation Effects Due to Cutting on Iron Losses and Magnetizability', *IEEE Transactions on Magnetics*, vol. 50, no. 11, pp. 1–4, Nov. 2014.

[118]   E. G. Araujo, J. Schneider, K. Verbeken, G. Pasquarella, and Y. Houbaert, 'Dimensional Effects on Magnetic Properties of Fe-Si Steels Due to Laser and Mechanical Cutting', *IEEE Transactions on Magnetics*, vol. 46, no. 2, pp. 213–216, Feb. 2010.

[119]   V. Mənescu, G. Paltanea, G. Horia, and G. Scutaru, *The effect of mechanical and electrical discharge cutting technologies on the magnetic properties of non-oriented silicon iron steels*, vol. 60. 2015.

[120]   K. Ali, K. Atallah, and D. Howe, 'Prediction of mechanical stress effects on the iron loss in electrical machines', *Journal of Applied Physics*, vol. 81, no. 8, p. 4119, 1997.

[121]   R. Reisinger and A. Emadi, 'Sensible Transportation Electrification : Get rid of inefficient powertrain designs.', *IEEE Electrification Magazine*, vol. 1, no. 2, pp. 6–12, Dec. 2013.

[122]   P. Niazi, H. A. Toliyat, D.-H. Cheong, and J.-C. Kim, 'A low-cost and efficient permanent-magnet-assisted synchronous reluctance motor drive', *Industry Applications, IEEE Transactions on*, vol. 43, no. 2, pp. 542–550, 2007.

[123]   I. Boldea, L. Tutelea, and C. I. Pitic, 'PM-Assisted Reluctance Synchronous Motor/Generator (PM-RSM) for Mild Hybrid Vehicles: Electromagnetic Design', *IEEE Transactions on Industry Applications*, vol. 40, no. 2, pp. 492–498, Mar. 2004.

[124]   W. L. Soong and T. J. E. Miller, 'Field-weakening performance of brushless synchronous AC motor drives', *Electric Power Applications, IEE Proceedings -*, vol. 141, no. 6, pp. 331–340, Nov. 1994.

[125]   P. Guglielmi, B. Boazzo, E. Armando, G. Pellegrino, and A. Vagati, 'Permanent-Magnet Minimization in PM-Assisted Synchronous Reluctance Motors for Wide Speed Range', *IEEE Transactions on Industry Applications*, vol. 49, no. 1, pp. 31–41, Jan. 2013.

[126]   K. Khan, S. Haghbin, M. Leksell, and O. Wallmark, 'Design and performance analysis of a permanent-magnet assisted synchronous reluctance machine for an integrated charger application', 2010, pp. 1–6.

[127]   G. Pellegrino, A. Vagati, P. Guglielmi, and B. Boazzo, 'Performance Comparison Between Surface-Mounted and Interior PM Motor Drives for Electric Vehicle Application', *IEEE Transactions on Industrial Electronics*, vol. 59, no. 2, pp. 803–811, Feb. 2012.

[128]   E. Armando, P. Guglielmi, G. Pellegrino, and A. Vagati, 'Accurate magnetic modelling and performance analysis of IPM-PMASR motors', 2007, pp. 133–140.

[129]   M. Obata, S. Morimoto, M. Sanada, and Y. Inoue, 'Performance of PMASynRM With Ferrite Magnets for EV/HEV Applications Considering

Productivity', *IEEE Transactions on Industry Applications*, vol. 50, no. 4, pp. 2427–2435, Jul. 2014.

[130] S. Morimoto, S. Ooi, Y. Inoue, and M. Sanada, 'Experimental Evaluation of a Rare-Earth-Free PMASynRM With Ferrite Magnets for Automotive Applications', *IEEE Transactions on Industrial Electronics*, vol. 61, no. 10, pp. 5749–5756, Oct. 2014.

[131] M. Barcaro and N. Bianchi, 'Interior PM Machines using Ferrite to Replace Rare-Earth Surface PM Machines', *IEEE Transactions on Industry Applications*, vol. 50, no. 2, pp. 979–985, Mar. 2014.

[132] E. E. Montalvo-Ortiz, S. N. Foster, J. G. Cintron-Rivera, and E. G. Strangas, 'Comparison between a spoke-type PMSM and a PMASynRM using ferrite magnets', 2013, pp. 1080–1087.

[133] L. Chen, X. Chen, J. Wang, and P. Lazari, 'A computationally efficient multi-physics optimization technique for permanent magnet machines in electric vehicle traction applications', 2015, pp. 1644–1650.

[134] G. E. P. Box and N. R. Draper, *Empirical model-building and response surfaces*. New York: Wiley, 1987.

[135] G. Gary Wang, Z. Dong, and P. Aitchison, 'ADAPTIVE RESPONSE SURFACE METHOD - A GLOBAL OPTIMIZATION SCHEME FOR APPROXIMATION-BASED DESIGN PROBLEMS', *Engineering Optimization*, vol. 33, no. 6, pp. 707–733, Aug. 2001.

[136] Y. Duan and D. M. Ionel, 'A Review of Recent Developments in Electrical Machine Design Optimization Methods With a Permanent-Magnet Synchronous Motor Benchmark Study', *IEEE Transactions on Industry Applications*, vol. 49, no. 3, pp. 1268–1275, May 2013.

[137] D. C. Montgomery, *Design and analysis of experiments*. 2017.

[138] M. Cavazzuti, *Optimization methods: from theory to design ; scientific and technological aspects in mechanics*. Heidelberg: Springer, 2013.

[139] P. Alotto, M. Gaggero, G. Molinari, and M. Nervi, 'A" design of experiment" and statistical approach to enhance the" generalised response surface" method in the optimisation of multiminima problems', *IEEE Transactions on magnetics*, vol. 33, no. 2, pp. 1896–1899, 1997.

[140] M. C. Costa, J.-L. Coulomb, Y. Maréchal, and S. I. Nabeta, 'An adaptive method applied to the diffuse element approximation in optimization process', *IEEE Transactions on magnetics*, vol. 37, no. 5, pp. 3418–3422, 2001.

[141] M. C. Costa, J.-L. Coulomb, Y. Maréchal, Á. B. Dietrich, and S. I. Nabeta, 'Diffuse-element method and quadtrees: two" ingredients" for an adaptive response surface', *IEEE transactions on magnetics*, vol. 38, no. 2, pp. 1085–1088, 2002.

[142] P. H. Mellor, R. Wrobel, and D. Holliday, 'A computationally efficient iron loss model for brushless AC machines that caters for rated flux and field weakened operation', 2009, pp. 490–494.

[143] J. Goss, P. H. Mellor, R. Wrobel, D. A. Staton, and M. Popescu, 'The design of AC permanent magnet motors for electric vehicles: a computationally efficient model of the operational envelope', 2012.

[144] L. Chen, J. Wang, P. Lazari, and X. Chen, 'Optimizations of a permanent magnet machine targeting different driving cycles for electric vehicles', 2013, pp. 855–862.

[145]   G. Bertotti, A. Boglietti, M. Chiampi, D. Chiarabaglio, F. Fiorillo, and M. Lazzari, 'An improved estimation of iron losses in rotating electrical machines', *IEEE Transactions on Magnetics*, vol. 27, no. 6, pp. 5007–5009, 1991.

[146]   F. Fiorillo and A. Novikov, 'An improved approach to power losses in magnetic laminations under nonsinusoidal induction waveform', *IEEE Transactions on Magnetics*, vol. 26, no. 5, pp. 2904–2910, 1990.

[147]   J. Wang, W. Wang, and K. Atallah, 'A Linear Permanent-Magnet Motor for Active Vehicle Suspension', *IEEE Transactions on Vehicular Technology*, vol. 60, no. 1, pp. 55–63, Jan. 2011.

[148]   X. Chen, J. Wang, P. Lazari, and L. Chen, 'Permanent magnet assisted synchronous reluctance machine with fractional-slot winding configurations', 2013, pp. 374–381.

[149]   X. Chen, J. Wang, V. I. Patel, P. Lazari, L. Chen, and P. Lombard, 'Reluctance torque evaluation for interior permanent magnet machines using frozen permeability', in *7th IET International Conference on Power Electronics, Machines and Drives (PEMD 2014)*, 2014, pp. 1–6.

[150]   W. Q. Chu and Z. Q. Zhu, 'Average Torque Separation in Permanent Magnet Synchronous Machines Using Frozen Permeability', *IEEE Transactions on Magnetics*, vol. 49, no. 3, pp. 1202–1210, Mar. 2013.

[151]   N. Bianchi, S. Bolognani, M. D. Pré, and G. Grezzani, 'Design considerations for fractional-slot winding configurations of synchronous machines', *IEEE Transactions on Industry Applications*, vol. 42, no. 4, pp. 997–1006, Jul. 2006.

[152]   A. M. EL-Refaie, 'Fractional-Slot Concentrated-Windings Synchronous Permanent Magnet Machines: Opportunities and Challenges', *IEEE Transactions on Industrial Electronics*, vol. 57, no. 1, pp. 107–121, Jan. 2010.

[153]   M. Gamba, G. Pellegrino, and A. Vagati, 'A new PM-assisted Synchronous Reluctance machine with a nonconventional fractional slot per pole combination', presented at the 2014 International Conference on Optimization of Electrical and Electronic Equipment (OPTIM), 2014, pp. 268–275.

[154]   *SPEED - Software for Electric Machine Design and Analysis version 9.04.012 user manual*. Siemens (CD-adapco), 2015.

Table of Figures

List of Tables